THE PROPERTIES OF ADVANCED ALUMINIUM ALLOY SYSTEMS

FRANK LESLIE HADDLETON

Doctor of Philosophy

THE UNIVERSITY OF ASTON IN BIRMINGHAM

October 1987

THE UNIVERSITY OF ASTON IN BIRMINGHAM

THE PROPERTIES OF ADVANCED ALUMINIUM ALLOY SYSTEMS

FRANK LESLIE HADDLETON
Doctor of Philosophy

October 1987

SUMMARY

2XXX and 7XXX series aluminium alloys have been the accepted materials for airframe construction for many decades. However, only minor improvements in properties have been possible by the development of these alloys since the early 1970's. The constant need to reduce weight in aircraft has therefore led to a resurgence in the research for higher performance aluminium alloys.

The reason for this investigation was to evaluate possible alternatives for the existing conventional aluminium alloy 2014 for aircraft wheel applications. Three new technologies in alloy development were considered: a metal matrix composite, an aluminium-lithium alloy and a powder metallurgical alloy.

The basic mechanical properties of these advanced materials have already been established to an extent, but their fatigue behaviour has yet to be fully understood. The purpose of this work was to investigate the fatigue properties of the materials concerned, in both air and an aerated 3.5% NaCl solution, and compare these properties to 2014-T6. As well as the basic mechanical properties, fatigue crack propagation data is presented for all of the materials concerned. Additionally, fatigue crack initiation data is presented for the aluminium-lithium alloy and 2014. The D.C. electrical potential method was used to monitor crack growth.

Of the materials investigated, the most promising was the aluminium-lithium alloy. However, short transverse properties need to be increased and the commercial cost of the material needs to be decreased before it can be considered as a direct replacement for 2014 for aircraft structural applications. It was considered that the cost of the powder metallurgical alloy would limit its further use. The metal matrix composite material proved to be unsuitable for most ambient temperature applications.

Key Words: Aluminium Alloys, Metal Matrix Composites, Fatigue, Corrosion Fatigue.

ACKNOWLEDGEMENTS

I would like to express my sincere gratitude to both of my supervisors, initially Prof.J.T.Barnby and subsequently Dr.S.Murphy, for their help and encouragement during the period this work was carried out. Thanks are extended to T.J.Griffin, of Dunlop Ltd. (Aviation Division), for his valuable guidance and Dr.D.S.McDarmaid, of RAE Farnborough, for helpful discussions. I would also like to thank the staff of the Mechanical and Production Engineering Department of Aston University.

This work was carried out with the financial support of the Science and Engineering Research Council (SERC) and Dunlop Ltd. (Aviation Division), to whom I am grateful.

Finally, I would like to thank my parents, to whom I dedicate this work, for their help over the years.

CONTENTS

FIGURES

TABLES

1. INTRODUCTION

In the aircraft industry, where high strength-to-weight ratio is of prime importance, aluminium alloys have been the accepted material for airframe construction since the mid-1930's. The Al-Cu-Mg alloys (Durals) were the first to be developed, and have been followed by Al-Zn-Mg-Cu (7XXX series) and Al-Cu-Mg-Si (2XXX series) alloys. In this area, alloys 7075 and 2024 have been established as the basic aluminium alloys.

By the early 1970's the development of these alloys had been reduced to minor improvements in the existing alloys, resulting in the improvement of most properties with the exception of strength (1). However, due to the rapid escalation in fuel prices in the mid-1970's, and the need to reduce weight in military aircraft, there has been a resurgence in the research for higher performance aluminium alloys.

This research has resulted in several new technologies in alloy development. This research involves three of them:

(i) The potential for metal matrix composites is impressive. These materials, which are basically solid metals strengthened by fibres of another material, have high temperature capability, high thermal conductivity, low thermal expansion and high specific stiffness. Such properties make metal-matrix composites appealing lightweight alternatives to conventional aluminium alloys.

(ii) Development of aluminium-lithium alloys is attractive because they can achieve intermediate to high strengths and they have low density, high elastic modulus, good corrosion behaviour and the potential to be more resistant under cyclic loading conditions than other conventionally cast and fabricated aluminium alloys.

(iii) The powder metallurgical route generally results in appreciably improved properties compared with an ingot metallurgy alloy of the same composition, largely due to the inherent rapid solidification route. Properties particularly improved by the powder metallurgy route are fatigue performance and stress corrosion resistance.

Metal fatigue is an expression designed to indicate the behaviour of metals subjected to frequently repeated stresses over a particular range. It arises from the initiation and propagation of very fine cracks under these conditions of fluctuating stress. It has long been

recognised that a metal subjected to fatigue will fail at a lower stress than that required to cause fracture by a single application of load, and for this reason typically 90% of reported mechanical failures are due to fatigue.

Fatigue is of more critical concern in aircraft than any other machine or structure (2), with the possible exception of the nuclear power industry. The outcome of failure of a primary load-bearing component in an aircraft will usually be catastrophic, often resulting in loss of life as well as the hardware and possible damage to ground structures. For this reason the fatigue, as well as corrosion fatigue, properties of these materials are of importance. One of the purposes of this research is to evaluate these properties.

The fatigue resistance of metals can be profoundly affected by interactions with environmental conditions, changing crack initiation and/or propagation. Corrosion fatigue results from the combined action of repeated or fluctuating stresses and a corrosive environment. An aggressive environment results in failure in fewer stress cycles than would have been the case in an inert environment. Almost all corrosive environments affect crack initiation in some way. Corrosion fatigue cracking of primary structures is a major cause of shortened aircraft life. Salt spray and high humidity environments accelerate crack initiation and propagation.

2. MATERIALS

2.1. 2XXX AND 7XXX SERIES

Since their introduction, high mechanical strength aluminium alloys have been mainly used in aircraft applications (1). One of the first examples is the use of Duralumin, an Al-Cu-Mg alloy, in Zeppelin airships as early as 1914. Later, after 1940, Al-Zn-Mg-Cu alloys were developed, having even greater mechanical properties.

The 2XXX (Al-Cu-Mg-Si) type of alloy, although being the first heat-treatable alloy to be discovered (Duralumin) still finds wide application for many general engineering and aircraft structural purposes in the form of forgings, extrusions, sheet, plate, tube and rivets. The alloys belonging to this group (AA2XXX series) have good fracture toughness and find usage for temperatures up to about 120°C. The ones used in aerospace applications are mainly 2014, 2024 and 2618 for the structural components and 2017 (formerly 'Duralumin') for rivets (3).

The 7XXX (Al-Zn-Mg-Cu) series of alloys have the highest strength of all aluminium alloys and are used mainly in aircraft structural applications in the form of clad sheet, forgings and extrusions. Strengths of the order of 600 MPa are achieved by the stronger of the alloys. The basic alloy, 7075, is still used in all possible semi-fabricated forms, though with changes in chemical composition and improvements introduced by new thermochemical treatments. Its purer versions, 7175 and 7475, offer better fracture toughness, and double ageing provides better stress corrosion and exfoliation corrosion resistance. However, some alloys (for example, 7079) still suffer from stress corrosion proneness, and are little used because of this.

Development has led to alloys such as 7050 which offers good stress corrosion resistance. Among alloys under examination for aerospace applications are 7010 and 7012.

2.1.1. EFFECT OF ALLOY PRECIPITATION (4)

(i) Secondary intermetallic particles

In high strength aluminium alloys, the formation of secondary intermetallic particles is by

eutectic decomposition of the liquid solution on casting. Soaking the ingot at elevated temperatures (below the solidus) dissolves all or most of the intermetallic compounds of zinc, magnesium or copper. The impurity elements, iron and silicon, combine with other elements and separate as intermetallic-phase particles during solidification. These particles, because they cannot be taken into solid solution, are virtually unaffected by ingot heat treatment. They are fractured during subsequent fabrication to a size of about 30μm in the largest dimension, but they remain segregated. Al_7Cu_2Fe and Mg_2Si are the common particles of this kind.

Similar types of reactions occur with both 7XXX and 2XXX alloys, depending on the composition. These coarse, secondary intermetallic particles do not contribute to strength, but because they are brittle they either fracture or separate from the matrix when the local strain exceeds a critical value. Therefore, decreasing the volume fraction of secondary intermetallic particles below the level found in the older alloys increases fracture toughness and resistance to fatigue crack propagation.

(ii) Dispersoids

Dispersoids are formed by solid state precipitation. Either chromium (up to 0.25%), manganese (up to 0.8%) or zirconium (up to 0.15%) is added to high-strength aluminium alloys to form these intermetallic particles. They control recrystallisation in hot worked products by modifying dynamic recovery processes. They also refine the grain size in products cold worked prior to solution heat treatment. The elements are retained in supersaturated solid solution in the ingot, and precipitate out as $Al_{12}Mg_2Cr$, $Al_{20}Mn_3Cu_2$ or Al_3Zr during subsequent thermal treatments. Chromium and manganese produce large (0.02 - 0.5μm in the longest dimension), incoherent dispersoids, whereas Al_3Zr is a smaller (<0.01μm in the longest dimension), coherent particle.

These dispersoids provide insignificant particulate strengthening, but they can influence strength indirectly by their ability to suppress recrystallisation.

(iii) Metastable precipitates

As a result of quenching from above the solvus temperature and holding at either room temperature (natural ageing) or elevated temperature (artificial ageing) below a critical temperature, a transition structure called Guinier-Preston (G-P) zones is formed in these

high strength aluminium alloys. These zones increase in number and size with ageing, accompanied by an increase in strength of the alloy. Continued artificial ageing of the alloy transforms these zones into a metastable precipitate, followed by a stable precipitate.

In the case of Al-Zn-Mg alloys, strengthening is in the form of certain proportions of G-P zones and metastable precipitates. Copper is added to stimulate this precipitation throughout the matrix and so increase strength. The precipitation sequence on ageing can be summarised as follows:

$$\text{Supersaturated solid solution} \rightarrow \text{G-P zones} \rightarrow \eta' \rightarrow \eta \qquad \ldots.(2.1.)$$

The metastable precipitate η' is partly coherent with the matrix. Persistent ageing produces the incoherent η precipitate, $MgZn_2$, resulting in a drop in strength.

In the case of Al-Cu-Mg-Si alloys a similar precipitation sequence occurs:

$$\text{Supersaturated solid solution} \rightarrow \text{G-P zones} \rightarrow S'' \rightarrow S' \rightarrow S\ (Al_2CuMg) \qquad \ldots.(2.2.)$$

Peak strength is associated with the partly coherent S' precipitates.

In aluminium alloys, these precipitates nucleate onto structural defects within the structure, such as dislocations or grain boundaries. 2XXX series alloys can be cold worked after quenching and prior to ageing to increase their yield strength, by increasing the number of nucleation sites present (in the form of a dislocation network) to produce a higher volume fraction of hardening precipitate.

2.2. COMPOSITE MATERIALS

With the ever increasing performance requirements for advanced aerospace applications, the mechanical properties of monolithic materials are being pushed to their limit. In an effort to enhance these properties one approach which has been taken is the development of metal matrix composites (5, 6). Metals with good ductility and strength are combined with fibres which have low ductility, higher strength and stiffness, and lower density. The two dissimilar materials are combined in order to optimise the properties of the individual constituents.

Graphite, boron, glass, silicon carbide and alumina are the principal reinforcement materials (7). The fibres may be long and continuous or they may be discontinuous.

Metals and polymers have been used as matrix materials (7). So far, glass fibre-reinforced polymers have been the most common fibre-strengthened materials. However, one of the problems of resin-based composites is that their properties in directions normal to the fibres or in shear parallel with the fibres often leave a lot to be desired. Low thermal conductivity and chemical stability are also problems. Metal matrix composites do not suffer this disadvantage to the same extent. The most common metal matrices, aluminium alloys, are structural materials in their own right, and so offer much better transverse strength and elastic modulus, better shear properties and good compression strength. They also provide higher thermal conductivity and greater chemical stability.

The most widely exploited metal matrix composite system uptil now has been boron fibre/aluminium alloy (8, 9). Filaments are produced by the chemical vapour deposition of boron on tungsten filaments. Boron fibres for metal matrix composites generally have a diameter of 100-150μm. Borsic fibres are boron fibres having a surface coating of silicon carbide to provide higher temperature capability in aluminium or titianium, by acting as a diffusion barrier.

Carbon (or graphite) fibre reinforcement is also common. The graphite fibres are produced from rayon, polyacrylonitrile or petroleum pitch. Ceramic fibres are also now available for metal matrix fabrication, continuous silicon carbide and α-alumina fibres being the most promising due to their greater inertness. Aramid organic fibres, Kevlar being the best known trade name, are widely used in the aerospace, marine and sports goods industry

and have many other applications. Silicon nitride is another lesser known fibre reinforcement.

However, all of these fibres are costly, and usually require a very expensive fabrication route, and so commercial viability is difficult to achieve (10). Aluminium alloys reinforced with whisker forms of silicon carbide are potentially cheaper than the fibre-based materials, and the material offers enhanced stiffness, elevated strength and wear properties (11), but the cost is still much higher than that of conventional alloys.

It can be seen that the progress towards an industrial application for metal matrix composites has been slowed down by the lack of availability of a low cost fibre meeting the required technical specifications and of an economic composite fabrication method.

2.2.1. METAL MATRIX COMPOSITES USING ALUMINA FIBRES

The most notable of the ceramic base reinforcements being developed is probably alumina (Al_2O_3) filaments. It has inherent resistance to oxidation, very good strength retention up to about 1350°C, room temperature tensile strength ranging from 1700 to 2100 MPa and a tensile modulus ranging from 300 to 380 GPa, depending upon fabrication method and purity.

Following early enthusiasm for and disillusionment with sapphire whiskers for reinforcing metals (12), attempts have been made to produce cheaper polycrystalline alumina fibres. High temperature mechanical properties of these Al_2O_3/Al composites are very promising. Their use raises the temperature capability of aluminium sufficiently for automotive engine applications (13, 14). Alumina reinforcement also brings the coefficient of expansion of aluminium close to that of steel. They have potential applications for aircraft structural parts, automotive engine parts, electrical equipment and radar transparent structures.

Alumina in continuous fibre form is produced by several companies. The Du Pont Company has developed the FP fibre, which is polycrystalline α-Al_2O_3 (15, 16, 17). It is essentially 99% α-Al_2O_3, the filaments having an elastic modulus of about 380 GPa, comparable with those of boron and carbon, and a minimum tensile strength of about 1400 MPa (15). However, the combination of aluminium and alumina is complicated by the non-

wetting characteristics of the system, and either coatings or alloying additions have had to be used to promote interactions between the matrix and the filaments. It has been reported (18) that wetting by liquid aluminium may be achieved only if small additions of lithium are made to the matrix alloy. This is clearly a limitation to FP fibre, although they are attractive in that they are more inert than boron or carbon and do not support corrosion processes.

However, FP fibres still have the disadvantage of being costly. In response to the need for a lower priced reinforcing fibre, ICI Mond Division introduced in 1982 a new grade of 'Saffil' alumina fibre. The RF grade has been specifically designed for use in advanced composites (19), in which the fibres are randomly oriented in a plane. It is a short staple fibre consisting of polycrystalline δ-alumina (its main constituents are 96-97% Al_2O_3 and 3-4% SiO_2). The relevant properties of the fibre are compared to those of other fibres for use in metal matrix composites in table 1.

Saffil has a tensile strength approximately 45% higher than continuous filament alumina fibre. Its delta-alumina crystal phase and incorporated silica promote easy wetting by a wide variety of aluminium alloy melts and good bonding to the matrix. It has been suggested (20) that the silica is instrumental in enhancing the initial wetting of the fibre. This solves the problem encountered with α-alumina fibres, where lithium has to be added as a wetting agent (18), as previously described.

Saffil's complete resistance to oxidation allows for easier high temperature processing than for carbon - it can be used up to 1600°C before its properties deteriorate. Because of its chemical inertness it does not suffer any deterioration in strength when in contact with molten aluminium alloys, unlike some silicon carbide fibres. However, its greatest advantage over other advanced reinforcement fibres is its price, up to ten times cheaper than continuous alumina fibres, for example.

In 1983, Toyota announced the development of a piston for use in high performance internal combustion engines, with fibre reinforcement using Saffil (14). Ringland reinforcement produced an increase in wear resistance, and on the crown there was an increase in hot strength of up to five times giving greater resistance to crown cracking. It can be seen that the most significant advantages of Saffil reinforcement will be realised at high

Fibre	Density (g/cm^3)	Fibre Diameter (μm)	Youngs Modulus (GPa)	Tensile Strength(GPa)
"Saffil" δ-alumina	3.3	3	300	2.0
FP α-alumina	3.95	20	380	1.38
Boron	2.6	100-150	400	3.4
Carbon				
(i) High tensile	1.7	7-10	200	3.0-3.5
(ii) High modulus	2.0	7-10	400	2.0-2.5
Silicon Carbide				
(i) Whisker	3.2	1-50	480	Upto 7.0
(ii) Continuous Filament.	3.2	15	245-400	3.0-3.5

Table 1: Properties of fibres for metal matrix composites.

temperatures, and this is likely to lead to other applications in other parts of the engine.

Apart from the excellent wear and erosion resistance, the two most important properties conferred on aluminium alloys by Saffil reinforcement are a 20-40% increase in modulus and retention of strength at temperatures upto 300°c (21, 22). However, little or no enhancement to room temperature strength has been given by reinforcement, due to the low ductility of the system.

2.2.2. MECHANICS OF FIBRE REINFORCEMENT

In fibre strengthening, the high modulus fibres carry almost all of the load. The matrix serves to transmit the load to the fibres, to protect fibres from surface damage and to separate the individual fibres and blunt cracks which arise from fibre breakage. It would therefore be preferable to have good fibre-matrix bonding, which is usually the case with fibre- reinforced metals.

In order to describe the principles of fibre reinforcement, it is easier to consider a composite containing unidirectional continuous fibres oriented parallel to the stress axis. The uniaxial tensile stress-strain curves show many stages, as shown in figure 1. In stage 1, if there is no slipping at the interface both fibres and matrix undergo the same elastic deformation. The Young's modulus of a fibre reinforced material, E_c, can be determined by the rule of mixtures (24).

$$E_c = E_f V_f + E_m V_m = E_f V_f + E_m(1 - V_f) \qquad \text{....(2.3.)}$$

where V_f and V_m are the volume fractions of the fibre and matrix, respectively. Kelly and Davies (25) have shown that this rule works experimentally.

If the composite is loaded so that the yield stress of the matrix is exceeded then E_m is no longer the relevant term in the above expression. This is stage 2, where the matrix deforms plastically and the fibre is still elastic. The slope of the matrix stress/strain curve under these conditions at a given value of fibre strain (ε_f) is given by $(d\sigma_m/d\varepsilon_m)_{\varepsilon_f}$ and so:

$$E_c = E_f V_f + (d\sigma_m/d\varepsilon_m)_{\varepsilon_f} . V_m \qquad \text{....(2.4.)}$$

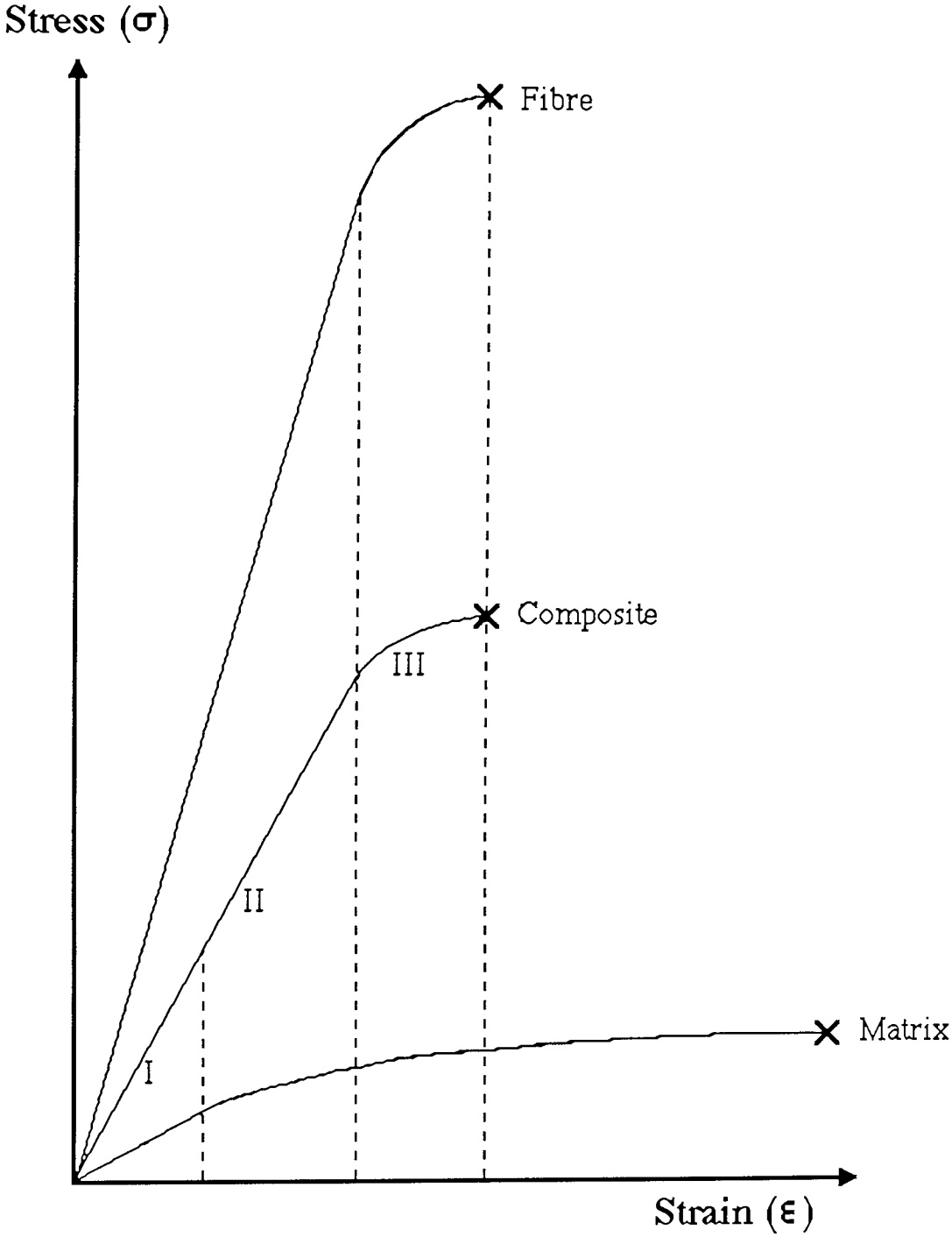

Figure 1: Stress-strain behaviour of composite materials.

where σ_m is matrix stress and ε_m is matrix strain.

In stage 2, when the composite is unloaded the fibres return to their original length but the matrix is deformed into compression.

On further straining a composite with ductile fibres, the fibres themselves deform plastically (stage 3). However, since most of the high strength, high modulus fibres are brittle they fracture on entering stage 3, effectively bypassing it. Finally, in stage 4, the fibres fracture and the composite as a whole soon fractures.

The ultimate tensile strength, σ_c, of the composite loaded into stage 2 is given by (25):

$$\sigma_c = \sigma_f V_f + \sigma_m'(1 - V_f) \qquad \text{....(2.5.)}$$

where σ_f is the tensile strength of the fibres and σ_m' is the tensile stress in the matrix when the fibres are strained to their tensile strength. Since very strong fibres will have little ductility, the strain at which σ_m' is evaluated is low and $\sigma_m' << \sigma_f$.

A critical fibre volume, V_{crit}, has to be exceeded for fibre strengthening to occur:

$$V_{crit} = \frac{\sigma_u - \sigma_m'}{\sigma_f - \sigma_m'} \qquad \text{....(2.6.)}$$

where σ_u is the strength of the strain hardened matrix. It is assumed that this critical volume fraction has been exceeded for the metal matrix composites under investigation.

All of the equations quoted so far in this section apply to continuous fibres. The situation for discontinuous is more complex. Since the fibres in a composite are loaded via interfacial shear stresses the end portions of discontinuous fibres are under lower tensile stress than the central portion. But the higher shear stresses at the ends of the fibre mean that a metal matrix will flow plastically above some critical value. Therefore, in order to utilise fully the high strength of the fibre it is necessary that the plastic zone in the matrix does not extend from the fibre ends to its midlength before the strain in the fibre reaches its failure strain. A critical fibre length, L_c, can be derived (26) for a given diameter, d, below which the fibre is not fully loaded by the interfacial shear stresses and reinforcement is inefficient:

$$L_c = \frac{\sigma_f . d}{2\tau_0} \qquad \ldots.(2.7.)$$

where τ_0 is the shear yield stress of the matrix. The longer the fibre length, L, the more the stress/strain behaviour approximates to that of continuous fibre composites.

For these discontinuous fibre composites, the tensile strength is given by:

$$\sigma_c = \sigma_f . V_f \left(1 - (1 - \beta)\frac{L_c}{L}\right) + \sigma_m' (1 - V_f) \qquad \ldots.(2.8.)$$

where, in this case, β is a constant 0.5. It can be seen that the reinforcement obtained with discontinuous fibres is less than that obtained with continuous fibres, but if L_c/L is small the difference is negligible.

A unidirectional array of fibres in a matrix is a highly anisotropic material. If parallel fibres are oriented at an angle to the stress axis then a rapid reduction in strength results. The failure mode changes with increased loading angle, from flow parallel to the fibres (failure stress = σ_c) to failure by shear in the matrix or at the fibre-matrix interface (failure stress = τ_s), to failure of the composite in a direction normal to the fibres (failure stress = σ_s). The effect of these three failure modes can be seen in figure 2.

The transverse strength, σ_s, of a fibre reinforced composite is dependent upon the properties of the interface and the fibre volume fraction, and is reasonably high in the case of metal matrix composites. The reduction in strength is usually compensated for in practice by using laminated sheets in which the fibres have a different orientation in each layer. Under these conditions the minimum strength in any direction should exceed one third of the unidirection strength.

The behaviour of random fibre oriented composites are only partly understood. With a planar random fibre orientation, the same principles as those applied to unidirectional composites are relevant. A simplified approximation for the Young's modulus of these composites has been produced (27) by considering a case where all of the fibres are aligned in one direction and averaging the value of modulus over all angles between the axis of alignment and the direction of the applied load. A modified form of the rule of mixtures has

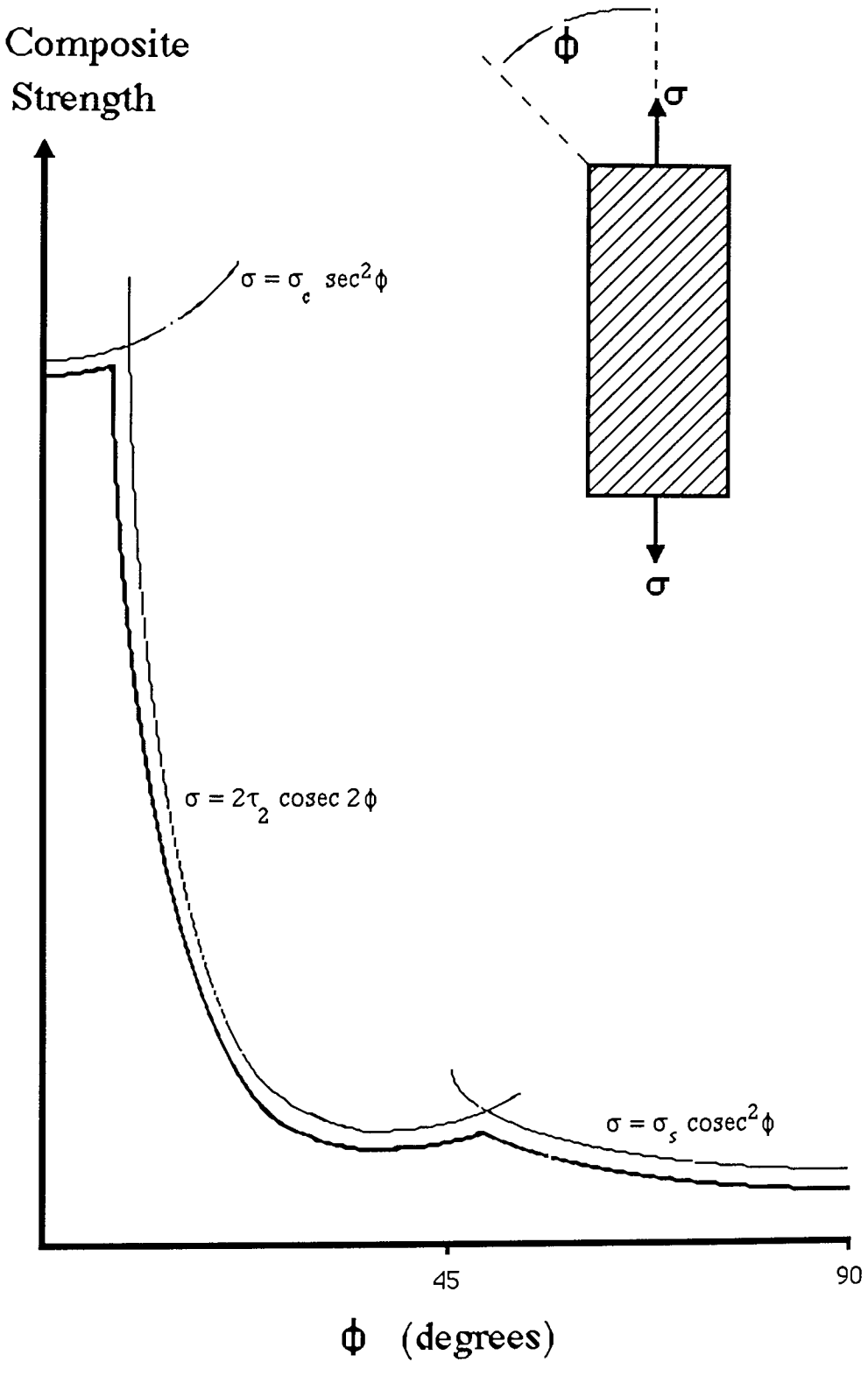

Figure 2: Variation of composite strength with fibre orientation.

been used to express the strength properties of planar random fibre oriented composites (28):

$$\sigma_c = \alpha.V_f.\sigma_f + V_m.\sigma_m \qquad \ldots.(2.9.)$$

where α is a coefficient which takes account of changes in fibre orientation, fibre-matrix bonding, etc.

Yield and the initial stages of work hardening in Saffil reinforced aluminium alloys have been shown to be controlled by the development of long range internal stresses, and fracture to initiate at small groups of closely spaced fibres (29). Failure then occurs by the development of a critical crack size, caused by the fracture of individual fibres due to loading above their tensile strength, after which the crack advances rapidly with damage being nucleated ahead of it. The matrix material plays a big part in the resultant composite strength (30, 23). The ultimate tensile strength can show improvements or a decrease from fibre reinforcement, depending on the matrix alloy used. Fibre-matrix interface strength and matrix ductility seem to be the major factors in dictating ultimate strength (31).

The toughness of fibre-reinforced materials is a property that can arise from the ductility of the matrix in its ability to blunt cracks or notches by flow, or from delamination in which the fibre-matrix interface fails, resulting in a large work of fracture (32). When a crack is present in a fibre-reinforced composite a transverse tensile component of stress exists ahead of the crack tip. This component of stress exerts a major effect on toughness by causing the opening up of weak interfaces with fibres parallel to the stress axis. The crack is therefore deflected along the interface.

2.3. ALUMINIUM-LITHIUM ALLOYS

Since 1973 the rapid escalation of fuel costs has accelerated the research on developing more fuel-efficient aircraft, and one way to achieve this is to reduce their weight (33). Recent aerospace system studies have shown that low density and high modulus are the material properties most desirable for weight reduction in future aircraft. Since aluminium alloys comprise about 80wt.% of the airframe, most development is in this area. Besides beryllium, which has associated manufacturing and health related problems, lithium is the only known metal which improves both modulus and density when alloyed with aluminium. Aluminium-lithium alloys have again become of great interest for aircraft components because of this combination of properties (34, 35, 36).

Lithium, with a density of only 534 kg/m^3, is by far the lightest metallic element. In combination with aluminium, with a density of 2700 kg/m^3, it offers the prospect of extremely light alloys. An addition as small as 2 to 3 weight per cent is sufficient to significantly improve the specific modulus and reduce the density of the alloy. Each weight per cent lithium (for up to 4% Li) added reduces the density approximately 3% and increases the elastic modulus approximately 6%.

The development of aluminium-lithium alloys is also attractive because they can achieve high strengths, have good corrosion behaviour and the potential to be more resistant under cyclic loading conditions than other conventionally cast and fabricated aluminium alloys (4). However, the levels of lithium additions that result in these desirable properties also result in poor toughness properties and increased difficulties in ingot casting and fabrication (37, 38).

One additional benefit of the use of aluminium-lithium alloys for aircraft is that the aircraft constructor can use the new material without incurring the expense and time required in employing other new materials such as reinforced plastic composites. The existing fabrication processes and labour would not need to change significantly. Many established routines and practices, including those of inspection and repair will continue to apply.

Research on aluminium-lithium alloys so far has focused on binary Al-Li (39), ternary Al-Cu-Li (40) and Al-Mg-Li (41) and quaternary Al-Li-Cu-Mg (42, 43).

The development of aluminium-base alloys containing lithium began in the early 1920's

in Germany with the introduction of the Scleron alloys (Al-Zn-Cu-Li) (44). In the late 1950's metallurgists at Alcoa recognised that lithium increased the elastic modulus of aluminium and they developed the high strength Al-Cu-Li alloy 2020. However, this alloy had low ductility and fracture toughness in the maximum strength temper. These limitations, as well as production problems, led to its withdrawal as a commercial alloy in 1969. Later work (45) showed that a more careful choice of thermomechanical processing route can improve these properties. In the mid-1960's the Al-Mg-Li alloy, 01420, was developed in the USSR (44). Although its specific modulus is better than those of conventional alloys, its specific strength levels are only comparable with the commonly used 2XXX series aluminium alloys, so that weight saving can only be achieved in stiffness-critical structures.

The development of aluminium-lithium alloys has evolved slowly for a number of reasons. Melting and ingot casting of alloys containing lithium are complicated by the reactivity of lithium, making it undesirable to the producer. This, and the high price of aluminium-lithium alloys, has resulted in slow progress.

However, more development has been devoted to these alloys in the last ten years than any other aluminium alloy. There have been special techniques developed to melt, degas and cast the alloys. Also, the wide gap between the properties of the lithium-containing alloys and the lithium-free alloys has been minimised by cold rolling or stretching before ageing. The effect of embrittlement has been minimised by alloy development and thermomechanical treatment (45).

While early alloy development was mostly concerned with Al-Cu-Li or Al-Mg-Li alloys, recent work has concentrated on Al-Li-Cu-Mg alloys (42, 43, 46). Joint alloy development at RAE and British Aluminium produced a series of Al-Li-Cu-Mg alloys with compositions designed to optimise density, strength and fracture toughness, for substitution of existing conventional alloys. The materials have shown a simultaneous 10% density reduction, 10% increase in elastic modulus and strength properties to match established aircraft alloys, while achieving toughness levels only marginally lower. These alloys have been designated the AA specifications 8090 and 8091 (46).

A comparison of the yield strength and ductility of various aluminium-lithium alloys in sheet form is shown in figure 3.

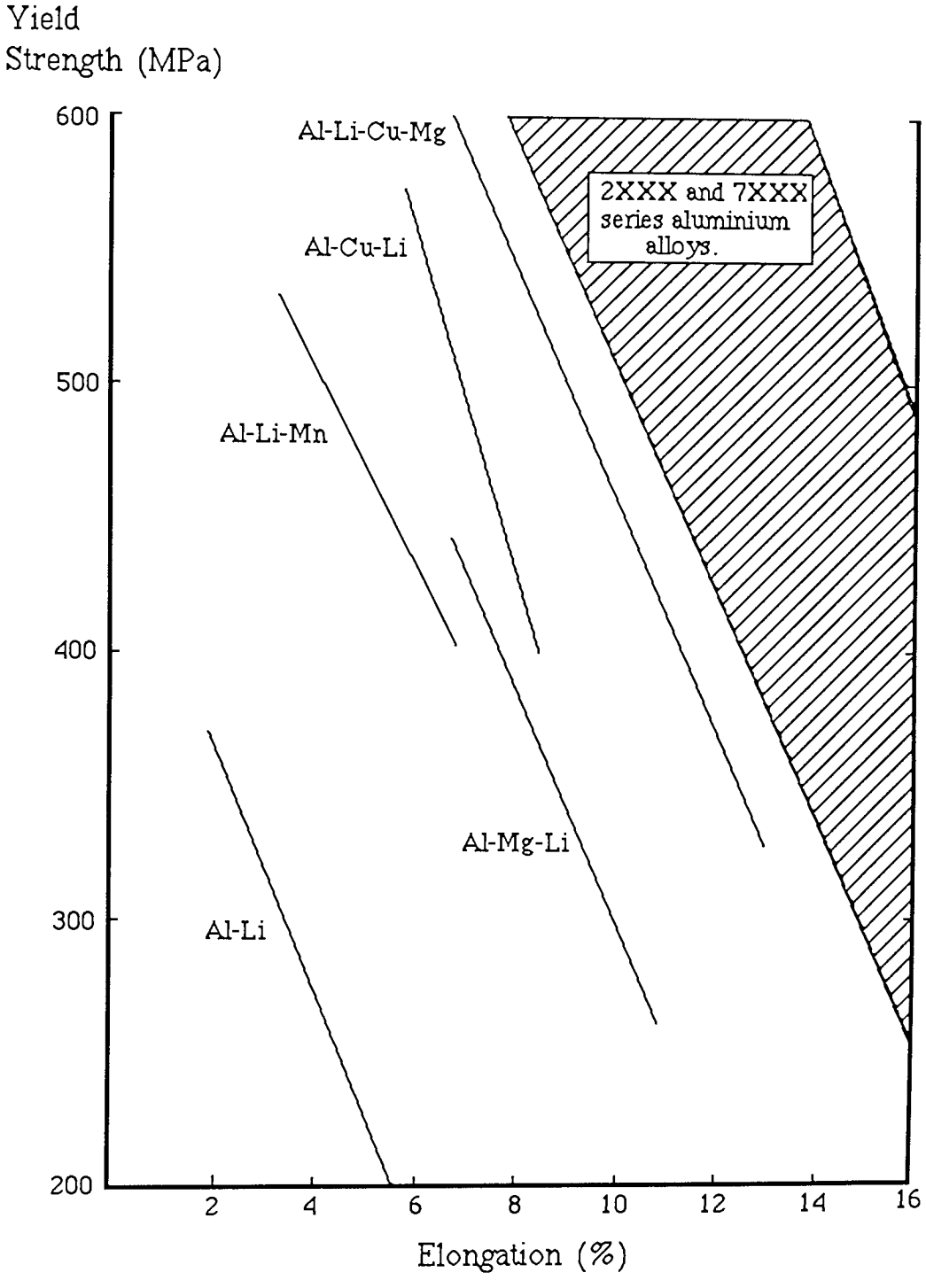

Figure 3: Comparison of yield stength and ductility of various aluminium-lithium alloys.

2.3.1 STRENGTHENING MECHANISMS IN ALUMINIUM-LITHIUM ALLOYS

The aluminium-lithium phase diagram, shown in figure 4, indicates that alloys containing up to 4.5 wt.% lithium would exhibit classical age-hardening behaviour (47). The rapid increase in solid solubility of lithium in aluminium over the temperature range 0° to 500°C results in an alloy system that can be precipitation hardened to achieve strength levels comparable with some of the currently used aluminium alloys.

When aluminium-lithium alloys with sufficient solute (more than 1 wt.% lithium) are quenched from the single phase field and subsequently aged at a temperature in the two phase field, below the metastable solvus line (48), decomposition of the supersaturated solid solution occurs by homogenous precipitation of the ordered metastable phase Al_3Li (δ').

Once the nucleation process has occurred, the growth rate is governed by the transport of solute to the precipitates. The particle size increases following a $time^{1/3}$ behaviour, (Lifshitz-Wagner relationship)(48). However, preferential δ' coarsening occurs at structural defects, such as dislocations or grain boundaries. Eventually, these coarse δ' precipitates transform to δ (AlLi) with prolonged ageing below the δ' solvus. Although aluminium-lithium alloys derive their strength from homogenous precipitation of δ', heterogenous precipitation of the δ phase is always possible below the solvus temperature. Since all grain boundaries lower the surface and strain energies involved with the precipitate, nucleation of this stable, incoherent phase occurs preferentially. It has been proposed (49) that δ nucleates independently of δ' and grows by dissolution of the surrounding metastable δ'. This results in a lithium depleted precipitate-free zone (PFZ) adjacent to the grain boundary. This zone is weaker than the matrix and can be a site for preferential deformation, leading to high stress concentrations at grain boundary triple points. Cracks then nucleate either at these triple points or at the AlLi grain boundary precipitates, and propagate intergranularly within the PFZ.

The basic strengthening mechanism of aluminium-lithium alloys is the formation of this metastable precipitate $\delta'(Al_3Li)$, the atomic arrangement of which is analogous to the ordered Cu_3Au (Ll_2) structure (49). The similarity in structure and parameter between δ' and the alpha aluminium matrix results in a cube/cube relationship with only a small lattice misfit

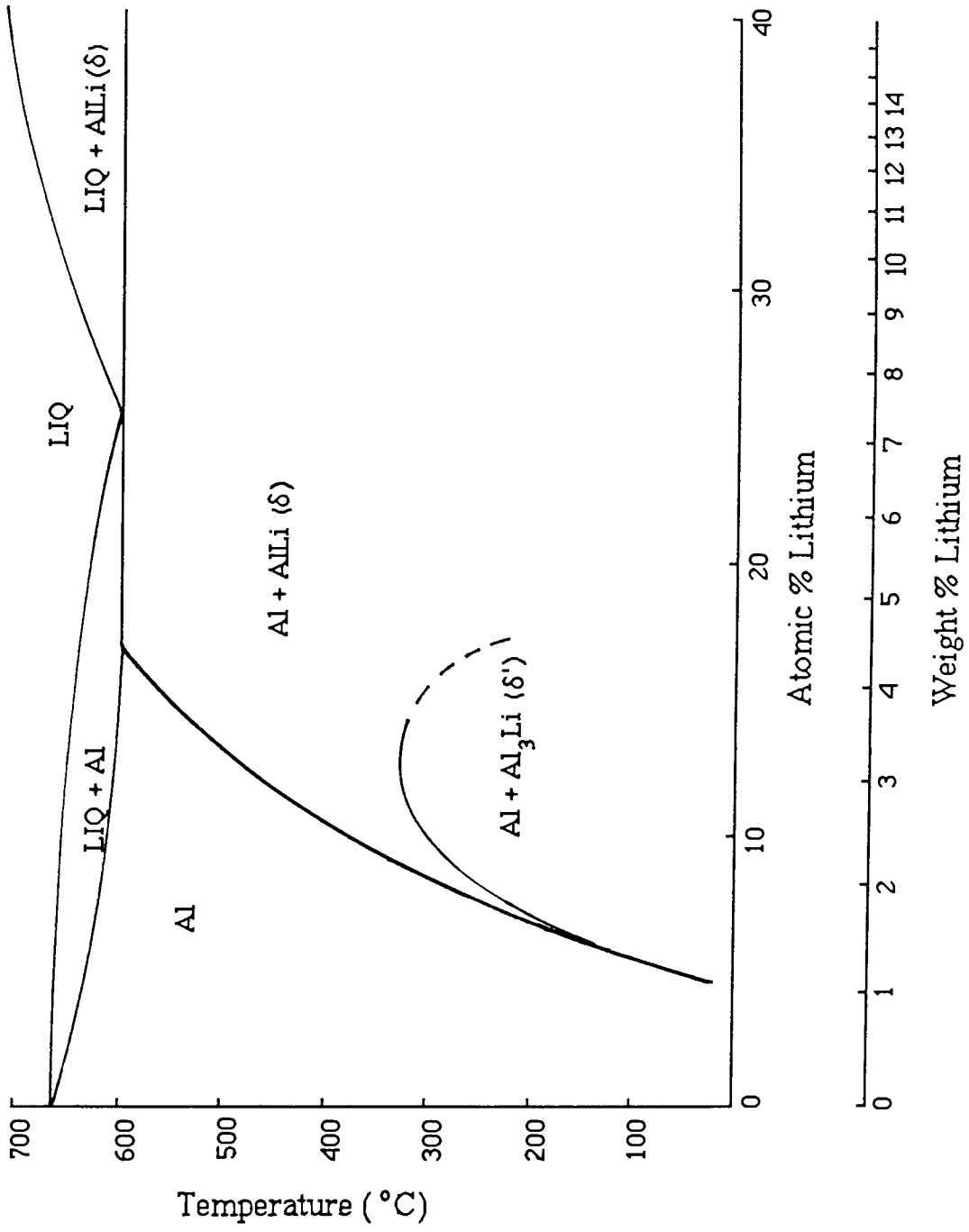

Figure 4: Aluminium-lithium phase diagram.

(0.18%) (47, 48), and leads to a homogenous distribution of coherent, spherical δ' precipitates.

It can be seen that the age-hardening in aluminium-lithium alloys is a two stage process (47):

$$\text{Supersaturated Solid Solution} \longrightarrow \delta'\,(Al_3Li) \rightarrow \delta\,(AlLi) \qquad \text{....(2.10.)}$$

The ageing sequence of ternary aluminium-magnesium-lithium alloys in the early stages is similar to an aluminium-lithium alloy:

$$\text{Supersaturated Solid Solution} \longrightarrow \delta'\,(Al_3Li) \rightarrow Al_2MgLi \qquad \text{....(2.11.)}$$

The Al_3Li metastable phase is still the precipitate that is responsible for strengthening, as it is unaltered by the presence of magnesium (50). However, analogous to the Al-Li system continued artificial ageing below the δ' solvus results in preferential coarsening at grain boundaries, the transformation of δ' to Al_2MgLi and the development and growth of PFZ's (41).

Precipitation in the aluminium-copper-lithium alloys follows the parallel sequence:

$$\begin{array}{l} \text{Supersaturated} \\ \text{Solid Solution} \end{array} \begin{array}{l} \nearrow \\ \searrow \end{array} \begin{array}{l} \text{GP zones} \rightarrow \theta'' \rightarrow \theta' \rightarrow \theta\,(Al_2Cu) \\ \delta'\,(Al_3Li) \rightarrow \delta\,(AlLi) \end{array} \begin{array}{l} \nearrow T_1\,(Al_2CuLi) \\ \\ \end{array} \qquad \text{....(2.12.)}$$

The copper precipitates independently of lithium and follows the sequence that occurs in the Al-Cu binary system, while at the same time lithium precipitates as Al_3Li.

The peak strength in the commercial alloy 2020 has been attributed to the coprecipitation of θ" and δ'.

The Al-Li-Cu-Mg alloys show a combination of reactions from the two ternary alloys (43):

$$\begin{array}{l} \text{Supersaturated} \\ \text{Solid Solution} \end{array} \begin{array}{l} \nearrow \\ \searrow \end{array} \begin{array}{l} \delta'\,(Al_3Li) \rightarrow \delta\,(AlLi) \\ \text{GP zones} \rightarrow \theta'' \rightarrow \theta' \rightarrow \theta\,(Al_2Cu) \end{array} \begin{array}{l} \\ \nearrow S\,(Al_2CuMg) \\ \searrow T_1\,(Al_2CuLi) \end{array} \qquad \text{....(2.13.)}$$

With the Al-Li-Cu-Mg alloys concerned (8090) there is a combined precipitation of the δ', S and T_1 phases.

The grain structure of the Al-Li-Cu-Mg is controlled mainly by the addition of zirconium. Al_3Zr forms by solid-state precipitation, as a small coherent particle. It serves to control recrystallisation in hot worked products and to maintain fine grain size in products cold worked prior to solution treatment (4).

The improvements in elastic modulus and density in aluminium-lithium alloys occur whether lithium is present in solid solution or in the δ' precipitate. However, improvement in strength accompanies the nucleation and growth of δ', and the magnitude of the effect increases with its volume fraction and size, as expected for coherent precipitates.

The strength of an alloy is related to the resistance to the motion of dislocations. Plastic deformation in precipitation hardened aluminium alloys like aluminium-lithium occurs through motion of dislocations on {111} close packed planes, in close packed directions. The strength and microdeformation characteristics of these alloys are dominated by the interaction of the mobile dislocations with zones and precipitates. Coherent particles, such as Al_3Li, may be penetrated by dislocations, since the slip systems of the precipitate and matrix are coincident. In this case, where particle shearing is the dominant dislocation - precipitate reaction, there are a number of possible mechanisms that can contribute to alloy strengthening. The strength will depend on the degree of coherency, modulus difference between the matrix and precipitate, particle size and distribution, volume fraction and the degree of ordering of the precipitates. Order hardening and modulus hardening seem to contribute the most towards alloy strengthening (51).

When the particle size is increased, by overageing, the dislocations begin to loop the precipitates, in which case the alloy strength is dominated by volume fraction and interparticle spacing.

The shearing of δ' precipitates by dislocations results in disorder, in the form of an antiphase boundary (APB) on the part of the slip plane within the particles. Because a second dislocation restores the order, it is attracted to the particle. Deformation therefore occurs by the motion of identical pairs of unit dislocations (called superdislocations).

However, the passage of a dislocation pair through a coherent particle reduces its

effective radius on that slip plane, so reducing the resistance to passage of following pairs. So once deformation has occurred on a particular slip plane, deformation on that plane is favoured. This leads to a tendency toward localised planar slip (45). Such concentrated slip results in premature fracture in the intense slip bands, or produces stress concentrations across grain boundaries which enhance intergranular failure, especially in ingot processed aluminium-lithium alloys where the grain sizes are large and so there are long dislocation pile-ups at grain boundaries (52). This is the main cause of the low ductility of aluminium-lithium alloys in the underaged and peak-aged conditions, as shown in figure 5a. In the overaged condition, PFZ's form at the grain boundary due to the formation of AlLi(δ) (45), as shown in figure 5b. Cracks then nucleate at these stress concentrations, and propagate intergranularly within the PFZ.

A third possible cause of the poor toughness of Al-Li alloys is the precipitation at the grain boundaries of certain impurity elements, namely sodium, potassium and sulphur (37, 53).

Improvements can be made in the ductility and toughness of these alloys by grain refinement and the addition of incoherent dispersoids. The magnitude of the stress concentrations at grain boundaries depend on the number of dislocations that can be accommodated on a given slip plane, so reducing grain size is very effective in reducing strain localisation (54). It also alleviates the effects of PFZ's and coarse grain boundary precipitates. A small grain size can be achieved by thermal mechanical treatments or by powder metallurgy.

Manganese, chromium and zirconium have been added to aluminium- lithium alloys to form small incoherent dispersoids during solidification and solution treatment. They are primarily used to control grain size and shape, but they also disperse slip and so inhibit the formation of intense slip bands (55), so delaying crack formation. Zirconium precipitates, in the form of Al_3Zr, have been shown to have two beneficial effects in aluminium-lithium alloys. It produces a finer as-cast structure than do manganese or chromium additions. The precipitate also retards recrystallisation in wrought aluminium-lithium alloys.

Since the presence of PFZ's and sheared coherent precipitates weaken the structure by

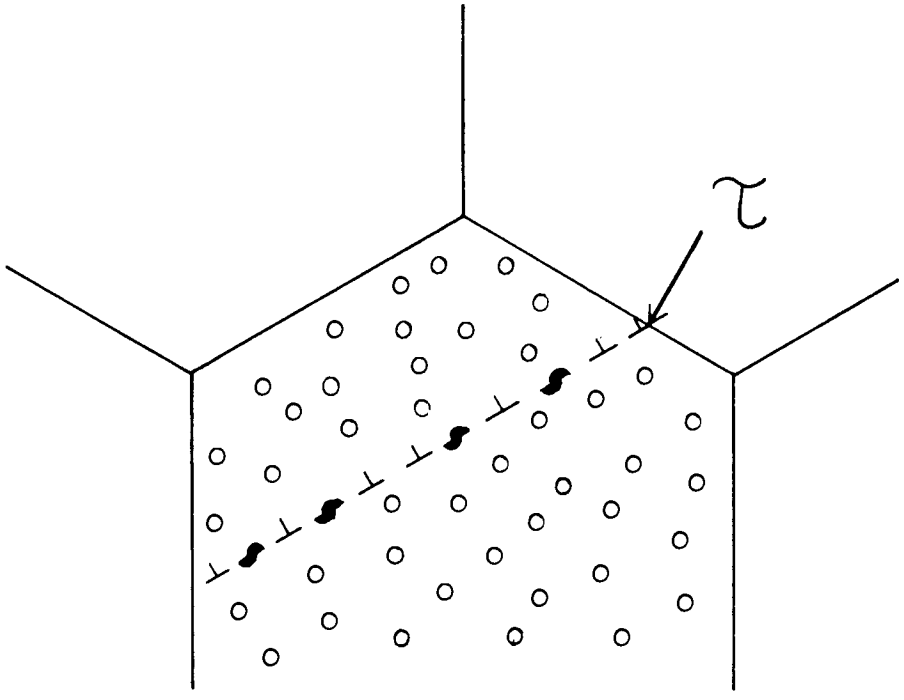

(a) Slip band fracture.

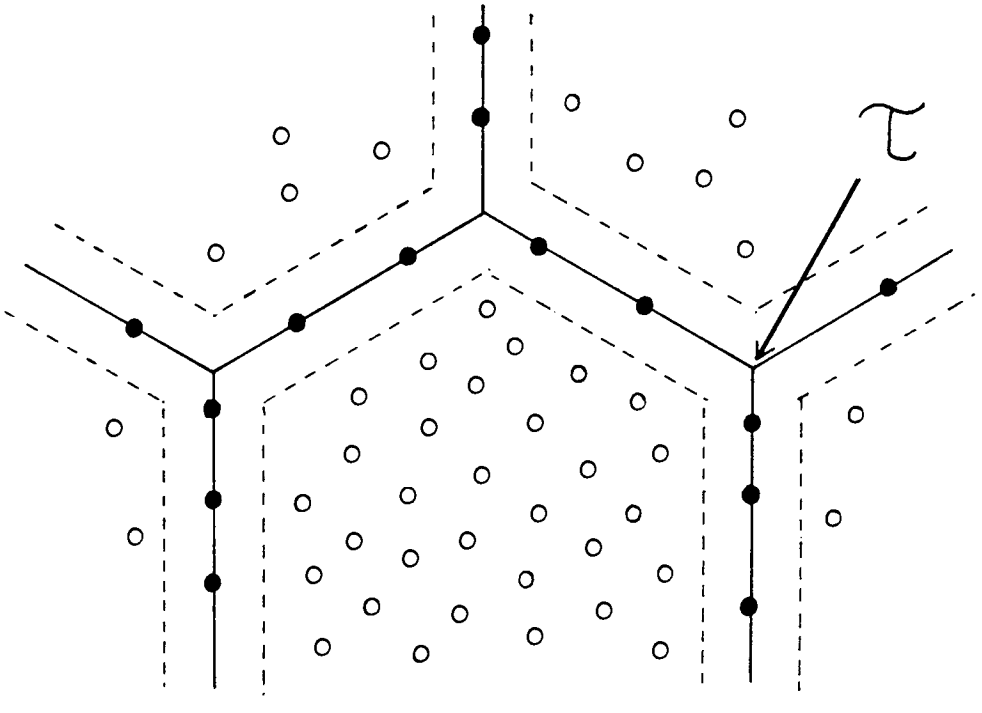

(b) Grain boundary fracture (PFZ).

Figure 5: Tensile deformation and crack nucleation mechanisms in aluminium-lithium alloys.

causing strain localisation, it would be advantageous to produce solid solution strengthening and further precipitation strengthening. Lithium additions to aluminium produce very little solid solution strengthening (51) and so the addition of magnesium and/or copper is made.

Magnesium contributes to the strength in two ways (50) - it adds a component of solid solution strengthening and increases the volume fraction of δ' by reducing the solid solubility of lithium in aluminium. However, it has also been shown to suppress the $\delta' \rightarrow \delta$ reaction.

The addition of copper to aluminium produces the precipitation of θ'' as well as δ', and so precipitation strengthening is much higher. When added to Al-Li-Mg alloys, copper increases the strength, homogenises slip, suppresses the $\delta' \rightarrow \delta$ transformation at grain boundaries, decreases the PFZ width and increases the strength near the grain boundaries.

A small amount of cold deformation prior to ageing has been shown to be beneficial to the fracture properties of aluminium-lithium alloys (56). Ductility and fracture toughness properties of most high strength aluminium alloys degrade with strength enhancement, and thermomechanical treatments (TMT) are used to improve damage tolerance and strength properties simultaneously. For aluminium-lithium alloys, TMT involves mechanical deformation after solution heat treatment and prior to ageing. Modification of the slip behaviour in Al-Li-Cu-Mg alloys can be induced by the precipitation of S' (Al_2CuMg) phase. However, the precipitation of S' phase during normal age hardening treatments is sparse, due to the low density of quenched-in defects to act as nucleation sites. A pre-ageing stretch of 1 to 3% introduces a dislocation substructure into the matrix, resulting in a relatively uniform heterogenous precipitation of fine laths of S' phase and a reduction in the size of PFZ's. This increased volume fraction and more uniform nature of the S' phase leads to a change in failure mechanism from long range planar shear to large amounts of ductile tearing.

One of the most interesting characteristic of aluminium-lithium alloys for aerospace applications is its high stiffness. A 3 wt.% addition of lithium to aluminium increases the specific Young's modulus by about 30%. The major contribution to the modulus increase has been shown to be due to lithium in solid solution (57), its effect being to modify the electronic structure of the alloy.

2.4. POWDER METALLURGICAL ALUMINIUM ALLOYS

In recent years, the achievement of higher levels of balanced properties by development of alloy chemistry has been increasingly difficult in conventional aluminium alloys produced by an ingot metallurgy (IM) route, due to the limited equilibrium solubility of alloying additions to these alloys. Powder metallurgy (PM) aluminium alloys provide the opportunity to overcome this problem of limited alloy solubility by using recently developed technologies such as rapid solidification (58) or mechanical alloying (59).

Powder metallurgy (PM) is the production, processing and consolidation of fine particles to produce a solid metal. It is already well established in iron, nickel and copper-base materials, where cost reduction has been the main aim (60). However, the development of the PM process has offered the opportunity to achieve material properties for demanding applications such as in the aerospace industry (58).

The conventional ingot metallurgy (IM) route for the production of aluminium alloys usually involves a chill casting or a direct-chill (DC) casting process, using water cooled moulds. Cooling rates in the range of 10^{-2} to 10°C per second are attained, depending upon the size of the ingot produced. The ingots are then hot and/or cold worked to product form and given an appropriate heat treatment. Since the original Alcoa patent on vertical direct chill casting in 1942, this continuous casting method has been dominant in the production of aluminium alloys for aerospace applications.

The PM route for the production of aluminium alloys involves the use of pre-alloyed powders, which are packaged into metallic cans and cold compacted. After vacuum degassing, the compact is hot consolidated to 100% density by hot isostatic pressing (HIP) to produce a billet of fine grain size. The solid PM billet at this stage is essentially identical to a cast ingot, and is followed by the same hot work and heat treatment procedures as an IM alloy, using the same equipment (61).

PM aluminium alloys offer the possibility of improved mechanical and corrosion properties, due to the rapid solidification (RS) technique (58). RS extends the solubility limits of alloying elements, so permitting alloying of elements that cannot be alloyed by conventional IM and enabling the creation of new metastable strengthening phases.

Microstructural features such as grain size and constituent particle size are refined by the RS technique, which also allows oxide and carbide dispersion strengthening. A further advantage that can result from rapid cooling is an increased tolerance to tramp elements compared to IM material due to the greatly reduced segregation, especially at sites such as grain boundaries. A lack of texture in most PM alloys can also be an advantage, where short transverse strength is poor in IM alloys.

The disadvantages of PM aluminium alloys in comparison with IM alloys include its higher cost, the limitation in the size of billets that can be produced at present and the small number of production facilities available (62). Also, defects in PM aluminium alloys have affected product reliability. Defects involving ceramic or metallic inclusions have not been satisfactorily eliminated for any of the current powder making approaches, and can be very destructive to engineering properties.

2.4.1. THE PRODUCTION OF PM ALUMINIUM ALLOYS

The two most commonly used methods of aluminium alloy powder production for the PM route are rapid solidification (RS) (58) and mechanical alloying (MA) (59). RS of a melt is the powder process being given the most consideration. Cooling rates in the range of 10^3 to 10^6°C per second produce powders with varying micromorphologies. Alloying elements which are miscible in the melt are retained as metastable, supersaturated solid solutions. The MA technique subjects elemental or partially prealloyed particles of the desired alloy chemistry to a high energy mixing process, producing powder with a uniform chemical and dispersoid distribution. Both of these methods produce fine powders with a relatively uniform matrix chemistry with controlled, supersaturated levels of alloying elements and fine, uniformly spaced, stable dispersoids (oxides or intermetallics). The PM material under investigation utilised RS powder.

(i) Rapid Solidification.

Powder is most often produced by RS techniques such as atomisation or ribbon casting (63). RS techniques rely on cooling rates upto 10^6°C per second to produce powders with increased alloying element concentrations through supersaturated solid solution, and small dispersoid and grain sizes. Equilibrium cooling reactions are suppressed, resulting in an

extension of the solubility of most alloying elements. The resulting uniform distribution of dispersoids and alloying elements provides higher room temperature strength, fracture toughness and corrosion resistance and improved elevated temperature mechanical properties when compared to IM alloys (58).

Atomisation is the most common and economic method of producing RS aluminium alloys, and is the preferred technique in the production of reactive alloy powders because it offers control of alloy chemistry, cleanliness, size and shape. Gas atomisation processes rely on high energy gas streams to fragment a coaxially impinging liquid metal stream (63). A molten stream is injected into a region of high velocity gas flow and fans out into a hollow cone shape, atomisation occurring at the circumferential periphery of the cone. The break-up of liquid metal at the periphery of the cone involves ligament formation under the shearing action of the gas medium. These ligaments then break up into particles of approximately spherical shape of 10-50μm diameter before solidifying. As a result of the 10^4°C per second cooling rates achieved in gas atomisation, aluminium alloy powders have predominantly dendritic solidification structures, with secondary dendrite arm spacings from 2 to 5μm (63).

Most aluminium alloys are atomised in air and are either irregular or spherical in shape, depending on the oxygen partial pressure of the atomising gas (64). A high oxygen partial pressure causes an irregular shaped particle, due to the relatively thick surface oxide layer which reduces the surface tension of molten droplets, whereas inert gas atomisation produces spherical powders which are smooth and oxide deficient. The oxide film in air atomised powder may also be hydrated if the atomising gas contains moisture.

(ii) Mechanical Alloying.

The MA process is a high energy process, developed by the International Nickel Co., and is an improved version of SAP processing (59). Metal powders making up the desired alloy composition are subjected to repetitive welding and fracturing, resulting in an intimate mixture of the alloy constituents. These powders are then consolidated by extrusion and forging to the desired product form. An organic additive is used during the process which reacts to form oxide and carbide dispersoids, to control grain size and contribute to alloy strength. Elemental powders may be ball milled into complete solid solution, with oxides

and carbides being evenly distributed.

The high energy milling occurring in this process enables many strengthening mechanisms to be used, such as fine grain size strengthening, oxide and carbide dispersion strengthening and fine precipitation strengthening.

The first stage in the production sequence for PM aluminium alloys (65) is cold compaction, which partially breaks up the surface oxide layer. The amount of compaction is important, as interconnected porosity is required for effective degassing, which is normally conducted after cold compaction. 75% theoretical density has been found to satisfy this condition (64).

The 'green' compact is then encapsulated in an aluminium canister and degassed at elevated temperatures in a vacuum. Degassing of aluminium alloy compacts is usually a necessary feature in the production sequence , as a 100% dense heat-treatable PM part can only be produced when all H_2O, H_2 and other volatile and gaseous contaminants have been removed from the bulk powder. Insufficient degassing would cause blister formation in a product when hot consolidated or heat-treated (66).

In practice, the hydrogen content of aluminium alloy powder compacts can be reduced to about 1ppm after degassing, and the oxygen content is reduced from about 0.6wt.% to 0.3wt.%. The hydrated oxide film, 5-10nm thick, is reduced to an amorphous Al_2O_3 continuous film, about 4nm thick. Degassed PM 7XXX series alloys have been shown to contain crystalline MgO particles in the Al_2O_3 film, as shown in figure 6 (64). At the elevated degassing temperature, H_2O reacts with the aluminium and magnesium in these alloys, to form additional Al_2O_3 and MgO.

After degassing, the billets are usually hot pressed to 100% density in a vacuum. In PM 7XXX series alloys, material flow breaks up the dehydrated surface oxide film into Al_2O_3 fragments, Al_2O_3/MgO clusters and MgO crystallites, as shown in figure 6. However, hot consolidation does not move these particles away from prior particle boundaries, and so incomplete powder particle bonding results.

The PM billet is then scalped, that is, the aluminium canister is machined from the billet surface. The hot pressed billets are then hot worked using conventional techniques such as

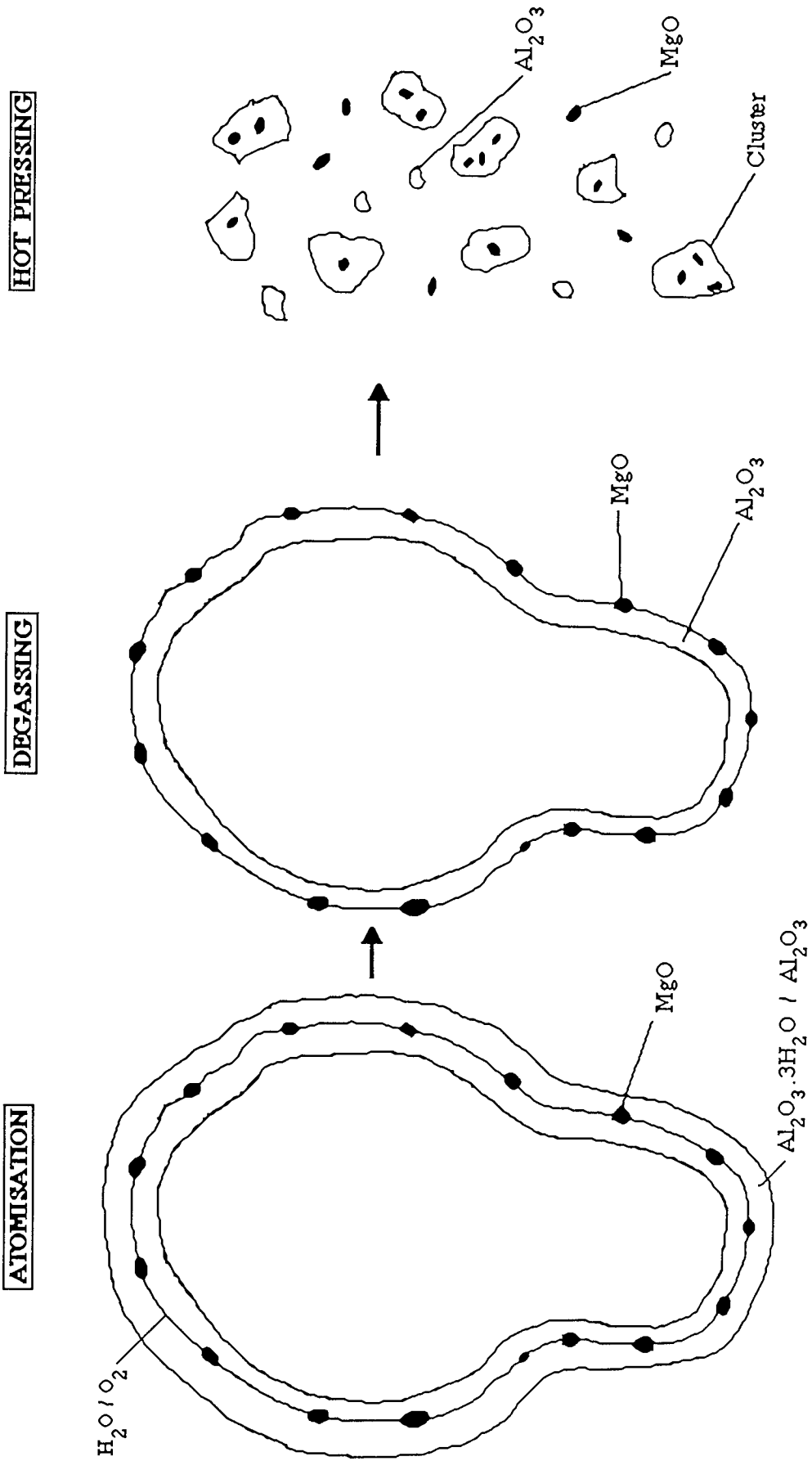

Figure 6: Powder surfaces after atomisation, degassing and hot pressing (from ref.58).

forging, extrusion or rolling. This stage is where these wrought PM alloys differ from the PM products that many people are familiar with, ie. compacted and sintered. The oxide skin generally negates isostatic pressing, because it has to be broken up by shear deformation to achieve acceptable levels of ductility and other mechanical properties. Thus heavy deformation must be applied to break up the oxide skin at prior particle boundaries, elongate powder particles in the direction of material flow and string-out the oxides. Sufficient hot work distributes the oxide particles uniformly, and prior particle boundaries are unrecognisable (64).

The extrusion process has been the most widely used technique for PM aluminium alloy hot working to date (67). The shear stresses intrinsic to extrusion cause extensive shearing and flow of particles, particularly at high extrusion ratios. Also, continuous break-up and rewelding of particles takes place. Forging has also been confirmed as a key fabrication process in the development of high strength PM aluminium alloy components (68).

The grain size in PM aluminium alloys is dependent upon the oxide distribution. As the amount of deformation increases, the spacing between oxide stringers decreases and so does the grain size, as the oxide particles pin grain boundaries. With sufficient deformation to disperse the oxides, grain sizes can reach a minimum of around 1.5μm (64).

These consolidation practices were originally developed for 7XXX series PM alloys, and are now also being used for 2XXX series PM alloys.

The wrought PM billet is then solution heat treated and aged, using practices comparable to those used for IM alloys. The classic ageing response of an increase to peak strength followed by a decrease in strength is also observed in PM aluminium alloys, but at reduced time and temperature when compared to IM alloys of similar composition. This is due to the improvements in homogeneity due to the RS route and the increased surface area of subgrain and grain boundaries in PM alloys, so increasing the number of precipitation sites. This increased surface area of subgrain and grain boundaries leads to an increase in precipitation on these boundaries, with a corresponding reduction in intragranular precipitation. Subgrain and grain boundary precipitation is not as effective as intragranular precipitation in strengthening. The maximum attainable strength is therefore reduced by using a PM route rather than an IM route for an identical composition (69). PM processing of 2XXX and

7XXX series alloys yields highly recrystallisation-resistant products, due to grain boundary pinning, so the fine grain size is retained.

2.4.2. DEVELOPMENT OF PM ALUMINIUM ALLOY TECHNOLOGY

Aluminium powders were first investigated for use in wrought components in the 1940's. Sintered aluminium products (SAP) used alumina dispersions to improve the high temperature strength of parts consolidated from milled aluminium powder.

Most research on PM aluminium alloys to date (58, 61) has been aimed at modifications to the conventional IM2XXX and 7XXX series alloys, taking advantage of the smaller grain size and more uniform distribution of dispersoids available by this route. However, some new chemistries have been developed, one being Al-Fe-X alloys which produce thermally stable dispersoids at high temperatures. PM aluminium-lithium alloys are also of interest, as the powder route can eliminate the toughness problems associated with these alloys.

Since the mid-1970's, PM aluminium alloy development has been proceeding in three main areas (62):

(i) High strength, fatigue and corrosion resistant alloys.

(ii) Low density alloys with improved modulus of elasticity.

(iii) Elevated temperature alloys with useful engineering properties upto temperatures of 345°C.

With all three of these areas of development, the use of fast cooling rates has allowed higher alloy contents to be used, with greater precipitation hardening volume fractions and so improved strength.

(i) High strength, fatigue and corrosion resistant alloy development.

The cost of producing PM aluminium alloys is 1.5 to 2.5 times higher than their IM counterparts (68). In order to justify this expense, the alloys have been designed to have increased strengths with comparable corrosion resistance.

PM alloys can be strengthened by a combination of solid solution strengthening, grain refinement, precipitation hardening and dispersion hardening. Since rapid solidification leads to the formation of fine grained, supersaturated solid solutions, these alloys would be expected to be strong.

The corrosion performance of PM aluminium alloys is also better than that of their IM counterparts (70). IM alloys formed by rolling, extrusion or forging often exhibit well defined directionally oriented grains that result in reduced resistance to exfoliation corrosion and stress corrosion cracking (SCC) in short transverse directions, although recently developed heat treatment procedures have eased this problem. The fine, equiaxed grain structures in PM alloys increase resistance to SCC and exfoliation, in both 2XXX and 7XXX series alloys.

The first commercial PM aluminium alloys for airframe applications were 7XXX series alloys with alloying additions that are insoluble in solid aluminium, such as cobalt. Alloys 7090 and 7091 were the first generation of high strength PM aluminium alloys, which were developed in the 1960's and 70's and are now well established (62). These are Al-Zn-Mg-Cu-Co alloys similar in composition to the IM alloy 7175. The addition of cobalt (0.4wt.% in alloy 7091, 1.5wt.% in 7090) forms Al_9Co_2 particles which are finely dispersed and refine the grain size. Along with Al_2O_3, MgO and $MgAl_2O_4$ particles from prior particle boundaries, these cobalt-containing dipersoid particles have been shown to increase the strength of these alloys (58). However, the general corrosion and SCC resistance of these first generation PM alloys is probably the most important advantage over IM 7XXX series alloys.

The major deficiencies in these alloys are in fracture toughness and fatigue crack propagation resistance, as a result of efforts to maximise strength. Second generation PM aluminum alloys were therefore developed to improve on these areas. The first of these, an Alcoa alloy designated CW67, is an Al-Zn-Mg-Cu alloy containing small amounts of zirconium and nickel to form dispersoids that control recrystallisation. Produced in the same manner as alloys 7090 and 7091, it has shown enhanced combinations of strength, fracture toughness, SCC resistance and fatigue crack propagation resistance when compared to current IM and PM alloys (65, 68).

As well as the high strength 7XXX series alloys, some PM development has been focused on the more damage tolerant 2XXX series alloys (61, 65, 66, 69). The main alloy modification to these alloys has been to adjust the amount of dispersoid forming elements

present in the PM product, to form more thermally stable dispersoids and take advantage of the naturally occurring oxide dispersoids present (61). This results in an increase in room and elevated temperature strength, while maintaining toughness levels. Only minor modifications have been made to take advantage of the PM route to retain higher percentages of strengthening elements in solid solution, because of the high mobility of copper and magnesium at processing temperatures.

A PM alloy based on the 2124 IM alloy composition with increased manganese and zirconium additions has been shown to have increased strength and toughness properties (69). Another PM 2XXX series alloy, a Kaiser alloy designated PM63, has been shown to have increased minimum strength levels, 30% higher than a corresponding IM alloy (66). The PM material under investigation is a variation of the IM 2014 composition, with additions of zirconium to form dispersoids (65). The alloy, an Alcoa alloy designated CZ20, is a fatigue and corrosion resistant alloy developed for aircraft wheel applications, with mechanical properties superior to IM 2014.

(ii) Low density, high modulus alloy development.

Section 2.3. has already established the weight savings that can result from the use of aluminium-lithium alloys, with reductions of density by up to 15% and corresponding increases of modulus up to 10%. However, problems encountered with melting and casting of aluminium-lithium alloys and deficiencies in short transverse mechanical properties such as ductility and fracture toughness have slowed down their progress (38).

The beneficial properties of aluminium-lithium alloys can be further improved by PM approaches (58, 71). The PM approach gets rid of the problems of direct chill casting, and refinement of the microstructure reduces compositional segregation. Al-Li-Cu-Mg alloys, with 3-4wt.% lithium, have been developed with density reductions in the range of 12-14%.

(iii) High temperature alloy development.

Conventional IM aluminium alloys start to lose their strength above 150°C, because strengthening precipitates coarsen rapidly and lose coherency. However, PM offers a means of dispersing intermetallic phases that resist coarsening and provide strength up to 345°C (62). These improved high temperature aluminium alloys have been developed to compete with titanium alloys for thermal stability and elevated temperature strength in aircraft

structural applications.

High temperature PM aluminium alloys are based on the Al-Fe-Ce, Al-Fe-Mo, Al-Fe-Ni and Al-Fe-V systems (71).These 10-15wt% rare earth and transition element additions are made due to their extremely low solubility and diffusion rate. RS retains them in solid solution and subsequent heat treatment precipitates a very thermally stable dispersion of intermetallic particles. This dispersion strengthening would not be possible to the same extent in IM alloys.

Semi-commercial high temperature PM aluminium alloys, such as the Alcoa alloy CU78 (Al, 8.3%Fe, 4%Ce), totally outclass IM alloys such as 2024, 2219 and 2618 (65). Alloy CU78 also has excellent creep properties.

However, major limitations to these alloys exist. Alloy CU78 is very difficult to fabricate into components, due to its improved high temperature properties. The pressures necessary to consolidate and extrude or roll the product into a suitable form are very high. Also, the high volume fraction of fine dispersoids, 20vol% and over, can adversely affect ductility and toughness.

3. FATIGUE AND FAILURE OF METALLIC MATERIALS

The failure of structural and machine elements are commonly split into two categories, ductile and brittle fracture. These two processes can be further split up into two categories, crack initiation and crack propagation. Ductile fracture is characterised by plastic deformation before and during crack propagation, and so occurs when the elastic limit of the metal has been exceeded. The fracture surfaces show some plastic deformation, characterised by dimples caused by the formation of voids. Brittle fractures show no gross deformation and very little microdeformation. A fast rate of crack propagation is usual, along well-defined crystallographic planes or defects such as grain boundaries. Either brittle or ductile fracture, or both, can occur in the failure of most metallic materials, depending on temperature, strain rate, stress conditions, heat treatment and the impurity elements present.

The theoretical cohesive strength of a solid can be calculated from certain material properties (72). However, engineering materials typically have fracture stresses that are 10 to 1000 times lower than the theoretical value. It is therefore concluded that defects, such as cracks, are responsible for this drop in fracture stress.

Conventional design criteria are based on the flow stress, usually the yield stress or 0.2% proof stress. The design stress is then the calculated flow stress divided by some safety factor. A typical safety factor is 1.5 for wrought steel in applications such as pressure vessels or boilers. These design criteria are adequate for many engineering structures, but they do not recognise the possibility of the presence of cracks, due to high concentrations of stress. There have been many instances of structural failure at stresses well below the design stress, due to material defects or cracks (73). Because of this drawback in the use of conventional design criteria, fracture mechanics has become more popular in the design of high strength materials due to its ability to predict the effect of stress concentrating defects in a structure.

3.1. FRACTURE MECHANICS

The aim of fracture mechanics is to calculate whether or not a defect of a given size will propagate in catastrophic manner under service loading, and so determine how safe the

structure is with respect to failure by fracture. Using fracture mechanics it should be possible to calculate the critical crack size at the expected service load, and how long it takes for a crack to grow to this size.

The property that measures resistance to fast fracture is the fracture toughness of the material, which is measured by loading to fracture testpieces which contain sharp cracks of known lengths. Under elastic conditions, this property is described by the critical stress intensity factor K_c. This term is used for high strength materials, but in lower strength alloys used in conventional engineering structures fracture is often associated with local plasticity, so invalidating elastic analysis. In this case, the critical crack opening displacement, δ_c, is often used as a parameter for measuring fracture toughness, and more recently the J Integral has been used for a materials having appreciable plasticity.

3.1.1. LINEAR ELASTIC FRACTURE MECHANICS

The use of linear elastic fracture mechanics is now being applied to many design problems to give a fracture safe structure containing a given defect size. It involves the study of stresses and strains at the tips of sharp cracks or defects in elastic bodies, and relates them to the applied loading.

There are three types of relative movements of two crack surfaces which represent the local deformation at a crack front, as shown in figure 7. These are the opening mode (mode I), the sliding mode (mode II) and the tearing mode (mode III) (74). Each of these modes represents a basic type of stress-field at the crack tip, but the superposition of the three modes describes the general case of cracking. However, mode I is the most important situation and this is the usual mode for fracture toughness tests. Mode I cracking will therefore be concentrated on.

The theory behind fracture mechanics emanates from the work of A.A.Griffith in 1920 (75), who tried to explain the discrepancy between the observed fracture strength of brittle solids and the theoretical cohesive strength. While it cannot be applied directly to metals, Griffith's ideas have had great influence on the thinking about the fracture of metals. He considered the situation of a through thickness sharp crack of length 2a in an infinite plate, as illustrated in Figure 8a. The plate is subjected to a tensile stress, σ, applied at infinity. If

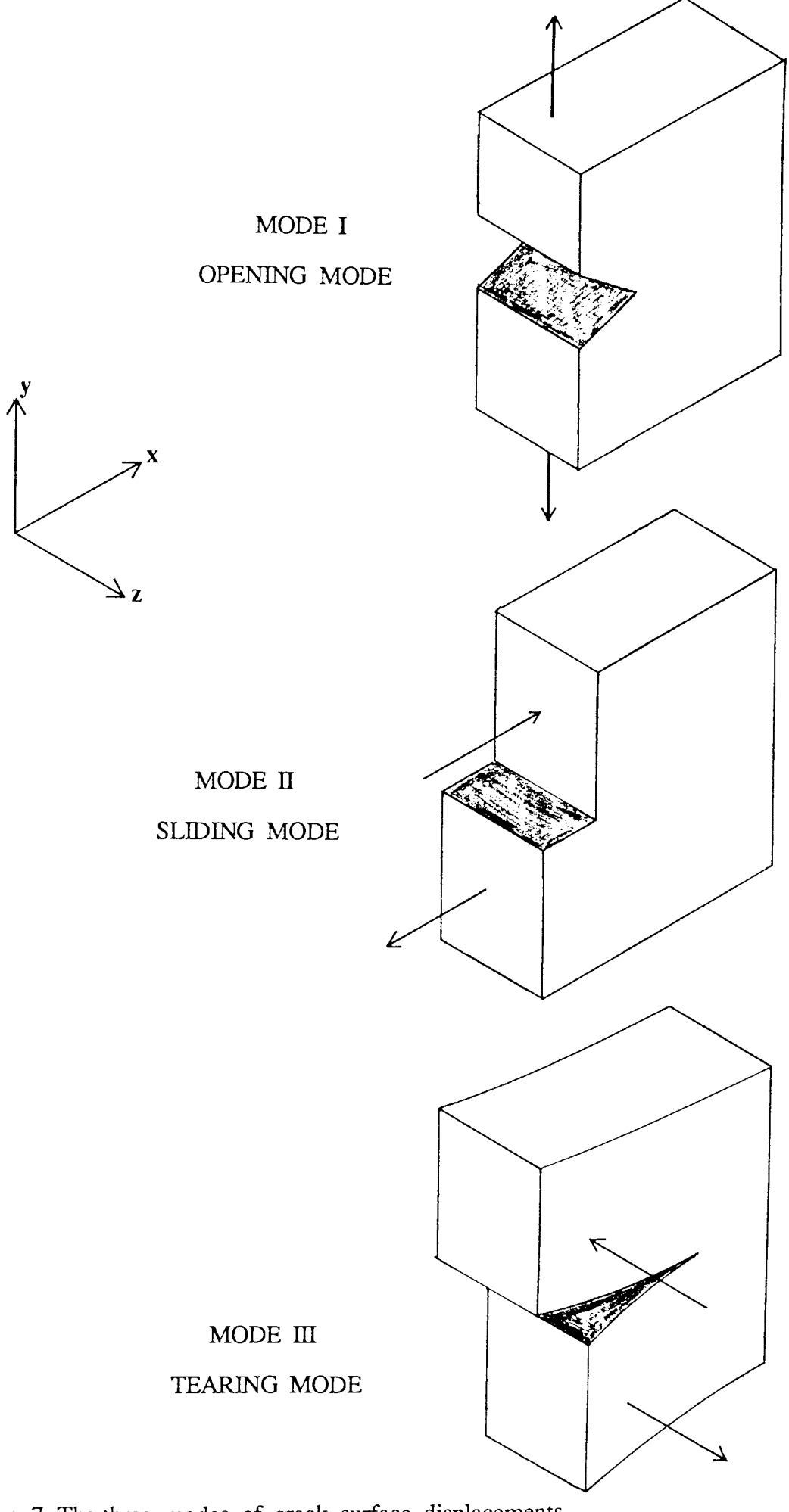

Figure 7: The three modes of crack surface displacements.

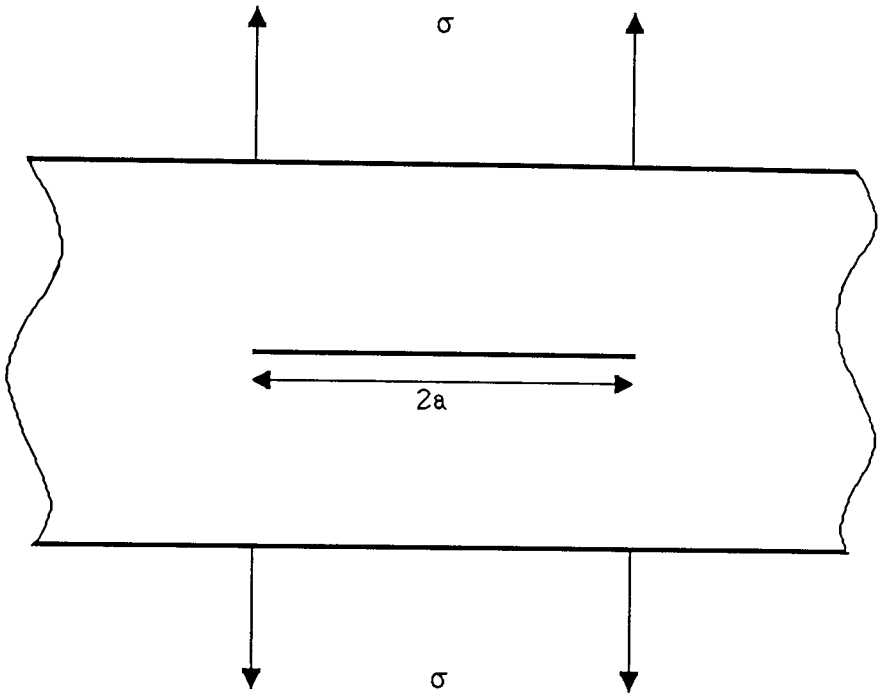

(a) Crack in an infinite plate.

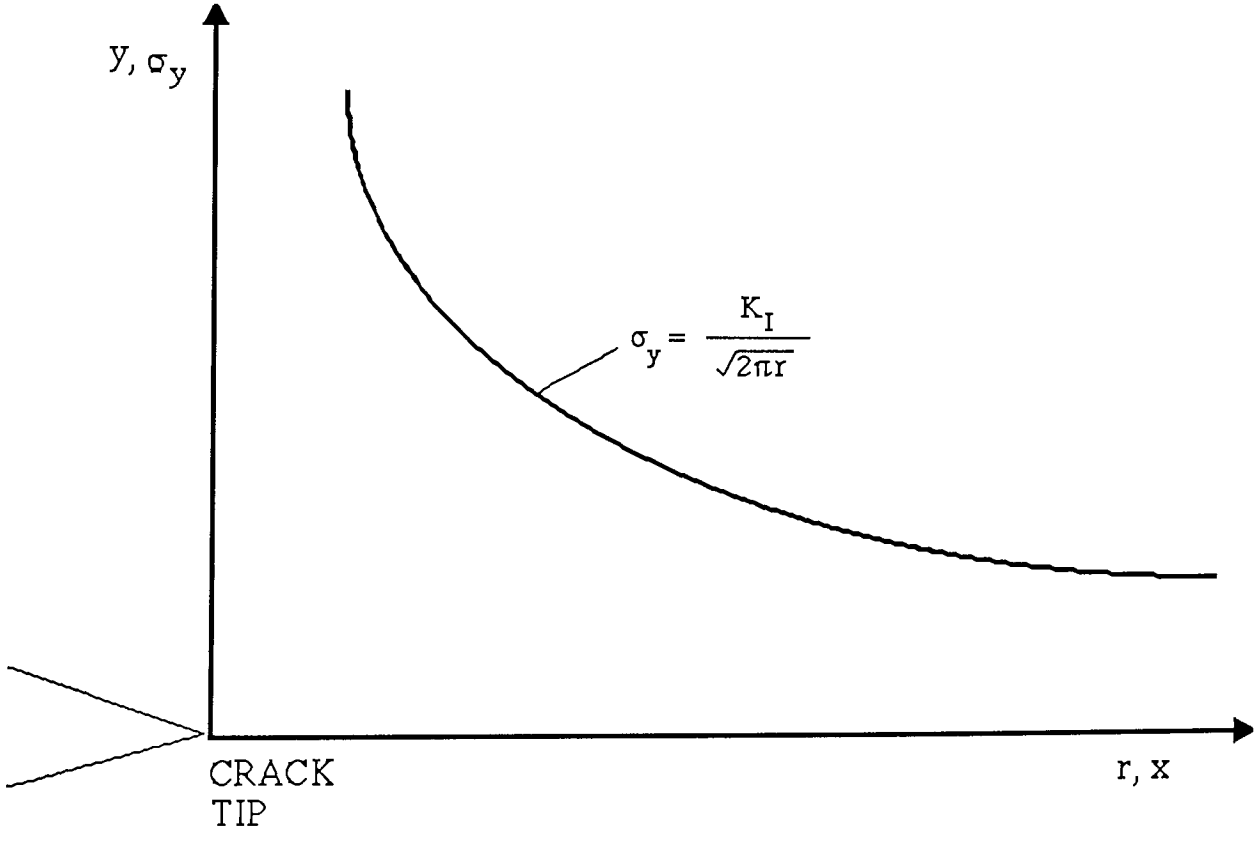

(b) Elastic stress field at the crack tip.

Figure 8: Irwin model for crack tip stress field evaluation.

the crack produces a stress concentration of sufficient magnitude, the theoretical cohesive strength is reached at the crack tip, even at a nominal stress well below this theoretical value.

Griffith stated that "a crack will propagate when the decrease in elastic strain energy is at least equal to the energy required to create the new crack surface". This statement is based on the fact that when the crack spreads in a brittle manner it produces an increased surface area of the sides of the crack. This requires energy to overcome the cohesive force of the atoms (i.e., an increase in surface energy). The source of this increased surface energy is the elastic strain energy which is released as the crack spreads. This criterion has been used to determine the magnitude of the tensile stress required to just cause a crack of a certain size to propagate as a brittle fracture.

The remainder of Griffith's paper dealt with various aspects of the strength of brittle solids. An energy balance, assuming linear elastic behaviour, gives the fracture stress, σ_f:

$$\sigma_f = \left(\frac{2\,E.\,\gamma_s}{\pi(1-\upsilon^2)a}\right)^{1/2} \qquad \ldots.(3.1.)$$

where E = Young's modulus, υ = Poissons ratio and $2\gamma_s$ = work of fracture (in this case, γ_s = surface energy). This equation is for plane strain conditions, that is, the plate thickness is large compared to the crack length. Because E, υ and γ are material properties it can be seen that crack extension occurs when $\sigma_f\sqrt{a}$ reaches a critical value. The expression therefore provides a relationship between fracture stress and crack length as long as the other properties are known.

However, this relationship is for very brittle materials, and so it does not apply to metals. Modifications have to be made to take account of the occurence of plastic flow at the crack tip before the onset of crack extension. Orowan (76) modified the Griffith equation by including γ_p to express the plastic work required to extend the crack wall:

$$\sigma_f = \left(\frac{2E\,(\gamma_s + \gamma_p)}{\pi\,(1-\upsilon^2)a}\right)^{1/2} \qquad \ldots.(3.2.)$$

for plane strain conditions.

A similar approach by Irwin (77, 78) was based on fracture occurring at a fracture stress corresponding to a critical value of the crack extension force, G_c:

$$\sigma_f = \left(\frac{E.G_{IC}}{\pi\,(1-\upsilon^2)a}\right)^{1/2} \qquad \ldots.(3.3.)$$

where G_{IC} is the plane strain (mode I) fracture toughness of the material. In metals, G_{IC} is a measure of the amount of plastic work which must be done before the crack extends. It can be related to the other measure of plane strain fracture toughness, K_{IC}, by:

$$G_{IC} = \frac{(K_{IC})^2\,(1-\upsilon^2)}{E} \qquad \ldots.(3.4.)$$

In a plane-stress situation (thin sheet), the $(1 - \upsilon^2)$ factor is missing in equations 3.1., 3.2., 3.3. and 3.4., and the materials toughness is then written as K_c or G_c. While the crack extension force, G, has a more direct physical significance to the fracture process, the stress intensity factor, K, is preferred in working with fracture mechanics because it is more amenable to analytical determination. There is a fuller explanation of K_C and K_{IC}, the critical values of K, later in this section.

Irwin (77) calculated the stress field in the vicinity of crack tips subjected to deformation for the same situation (figure 8a). He noted that the local stresses near a crack depend on the product of the tensile stress and the square root of the half flaw length, a. This relationship was called the stress intensity factor, K. For this situation, the value of K is given by:

$$K = \sigma\,\sqrt{\pi a} \qquad \ldots.(3.5.)$$

However, this expression is for an infinite body. For a plate of finite size, the general form of the stress intensity factor is given by:

$$K = f(a/W) * \sigma\sqrt{\pi a} = Y * \sigma\sqrt{\pi a} \qquad \text{....(3.6.)}$$

where Y is a function of specimen and crack geometry, a is crack length, W is specimen width and σ is nominal stress. For a given geometry, Y depends on the ratio a/W, and is usually an algebraic, trigonometric or polynomial function chosen to make the surface forces zero. A plot of Y versus a/W is called a K-calibration curve (79, 80).

The stress intensity factor is a convenient way of describing the stress distribution around a flaw. On the cracking plane ahead of the crack tip and close to the tip the local tensile stress, σ_L, has a distribution given by:

$$\sigma_L = \frac{K_I}{\sqrt{2\pi r}} \qquad \text{....(3.7.)}$$

where r is the distance ahead of the crack tip and K_I is the stress intensity factor for mode I cracking. This distribution of stress ahead of the crack is illustrated in figure 8b.

Equation 3.7. is an elastic solution, which does not prohibit the stresses becoming infinite at the crack tip. In reality, such high stress magnitudes do not occur. The material in this region undergoes plastic deformation, creating a plastic zone surrounding the crack tip. However, as long as the stress field is dominated by the stress intensity (that is, the plastic zone size, r_y, at the crack tip is small relative to local geometry) the principles of LEFM can still be applied, but this is obviously a limitation to its use.

The crack tip plastic zone size can be estimated by looking at the plane stress situation and setting y equal to the yield strength, σ_{ys}:

$$r_y = \frac{1}{2\pi}\left(\frac{K}{\sigma_{ys}}\right)^2 \qquad \text{....(3.8.)}$$

Figure 9 shows a more exact stress distribution at the crack tip. In order to take up the load carried by the elastic material in the region $O < r < r_y$ the plastic zone must extend to a distance R, so that the area under stress- distance curve remains the same (81). Rice (82) has

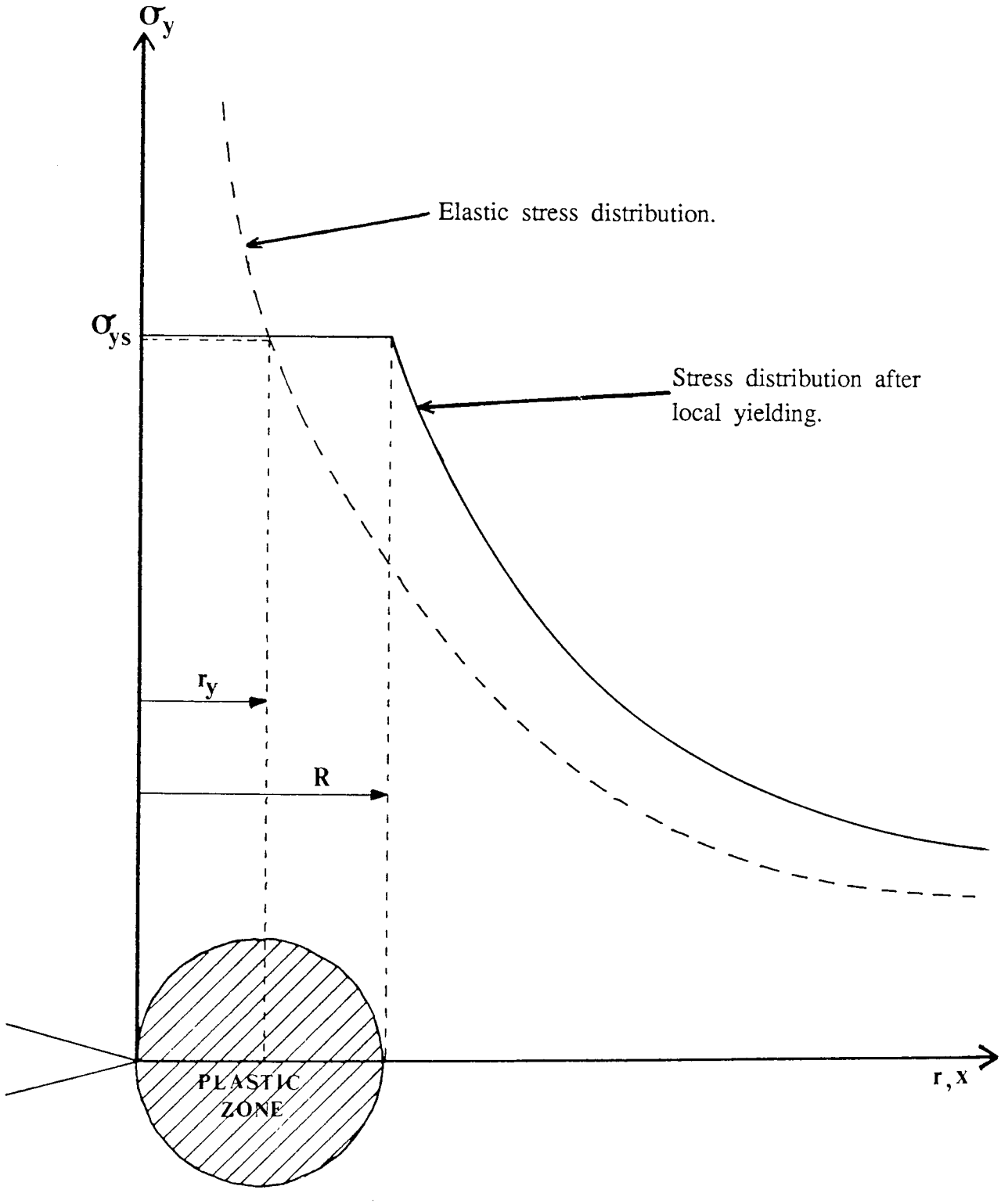

Figure 9: Stress distribution in the crack tip region.

suggested that this distance, R, is approximately equal to $2r_y$.

Under plane strain conditions the tensile stress for plastic yielding is increased, due to plastic constraint. This means that the plastic zone size is smaller, by a factor estimated to be $2\sqrt{2}$:

$$r_y = \frac{1}{5.6\pi}\left(\frac{K}{\sigma_{ys}}\right)^2 \qquad \text{....(3.9.)}$$

Unstable fracture occurs when the stress intensity factor at the crack tip, K, reaches a critical value, K_c, which is the fracture toughness of the material. It is dependent upon materials, temperature, strain rate, environment and thickness of specimen. For mode I deformation and plane strain conditions, the critical stress intensity factor is designated K_{IC}. It represents the ability of a material to withstand a given stress intensity at the crack tip and resist crack extension, and is a material property called the plane strain fracture toughness (83). The fracture toughness measured under plane strain conditions is obtained under maximum constraint, using thick test specimens rather than thin ones. The minimum thickness to achieve plane strain conditions and valid K_{IC} measurements is:

$$B = 2.5\left(\frac{K_{IC}}{0.2\%P.S.}\right)^2 \qquad \text{....(3.10.)}$$

where K_{IC} is an estimate and 0.2%P.S. is the 0.2% proof stress.

3.1.2. YIELDING FRACTURE MECHANICS

LEFM principles can only be used in situations where crack tip plasticity is small relative to the specimen size. In some cases this condition is impractical, for instance with structural steels where a minimum thickness requirement would be 0.3m, and so other toughness parameters have to be used.

In situations of extensive plasticity, the most used toughness parameter is the crack opening displacement (COD), δ, developed by A.A.Wells (84). It is the opening of a crack

at a position corresponding to the original crack tip. A specific value of COD characterises the onset of crack extension. A critical value, δ_c, can be measured in a testpiece which has undergone extensive yielding, and this value can then be used to calculate the toughness of a much larger body. Wells showed that the COD can be related to LEFM parameters up to general yield (85).

Another method, the J-integral method, relies on the determination of an energy term (J) which expresses the change in potential energy when a crack is extended by an amount da (86). The objective of J_{IC} testing is to determine the value of J at initiation of crack growth, by testing a series of specimens with slightly different crack lengths. This critical value of the J Integral is a material property in the same way that K_{IC} is for a linear elastic body.

3.2. FATIGUE FAILURE

It has long been recognised that a metal subjected to a repetitive or fluctuating (dynamic) stress will fail at a stress lower than that required to cause failure on a single application of load. These are called fatigue failures. They have become progressively more prevalent as technology has developed a greater amount of equipment, such as road transport, aircraft, turbines, etc. subject to repeated loading and vibration. Fatigue causes over 80% of the operating failures of machine elements. It is a particularly deceiving failure mechanism, as it progresses unseen and without any obvious warning.

Fatigue crack initiation usually occurs at a point of stress concentration, such as a sharp corner or notch, or at a metallurgical stress concentration like an inclusion. This crack then propagates slowly into the material, roughly perpendicular to the stress axis, as a sharp, narrow fissure. The progress of the fracture is usually indicated by a series of ripples or 'beachmarks' on a microscopic scale, which are in the form of concentric arcs progressing from the point of crack initiation. On a macroscopic scale the fatigue surface is characterised by the absence of gross plastic deformation. This continues until the remaining unbroken ligament cannot support the applied load and so undergoes a simple tensile fracture.

Figure 10 illustrates the general types of fluctuating stresses that can cause fatigue. Figure 10a and 10b are constant amplitude stress cycles of sinusoidal waveform, one a completely reversed cycle (10a) and the other a repeated cycle of stress (10b). Figure 10c is a variable amplitude stress cycle, which could be typical of the waveform in an aircraft component subjected to periodic, unpredictable loads. This section concentrates on constant amplitude fatigue work.

In order to guard against premature failure of a design by fatigue, it is necessary to characterise the fatigue resistance of the constructional material being used. The stress and strain distribution in the design, environmental conditions, surface conditions, etc. should all be taken into account. This requires investigation on both an atomic scale (structural aspects) and on a larger scale (engineering aspects) of the three stages of fatigue.

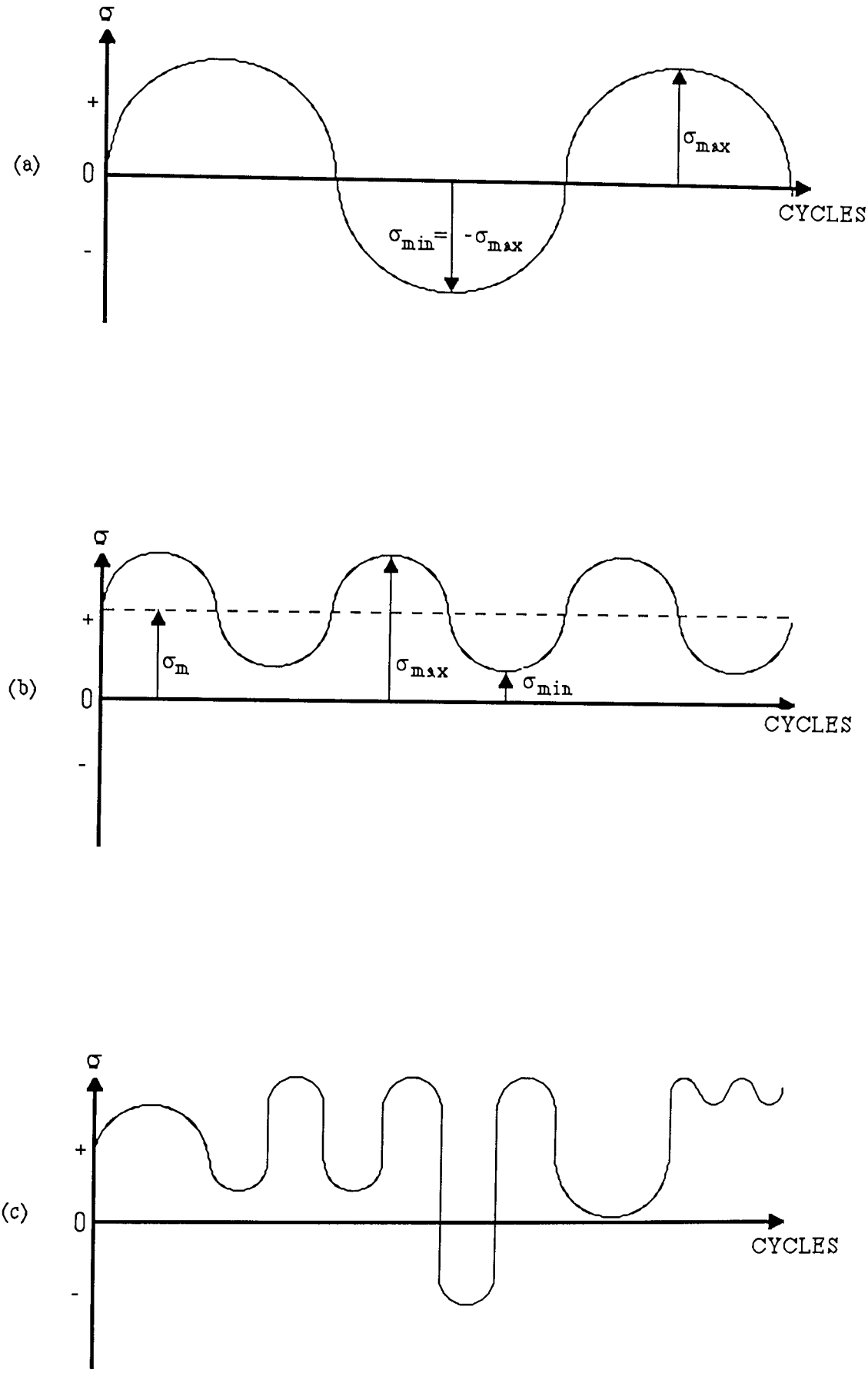

Figure 10: Typical fatigue stress cycles.

3.2.1. STRUCTURAL ASPECTS OF FATIGUE

A multi-stage model for fatigue failure has been established by several researchers (87, 88), dividing the fatigue process into the following stages:

(i) Crack initiation - persistant slip bands develop from cyclic plastic deformation and slip band intrusion and extrusion.

(ii) Slip band crack growth - growth of the initial crack on planes of high shear stress, commonly termed stage I crack growth.

(iii) Crack growth on planes of high tensile stress - growth of the crack perpendicular to the maximum tensile stress, termed stage II crack growth.

(iv) Ultimate failure - final fast fracture at a critical crack size, at which the remaining cross-section cannot support the applied load.

Fatigue cracks are usually initiated at a free surface, although in brittle materials they initiate around inclusions or precipitates. The metal deforms under cyclic strain by slip on specific planes. This plastic deformation occurs locally on a microscale due to stress concentrations, which may be scratches, sharp changes in cross-section, pits, inclusions, embrittled grain boundaries, etc. However, even when the surfaces are flaw free and no stress concentrators are present a fatigue crack can form if the stress amplitude is high enough. In this case, long range dislocation motion takes place leading to slip steps, and so roughening, of the surface (fatigue damage).

Several models have been proposed to explain the initiation of fatigue cracks in this way (89, 90, 91). These describe a mechanism of repeated slip, forming slip band intrusions and extrusions. This mechanism has been supported by experimental observations (89, 91). Slip occurs in grains oriented such that planes of easy slip are in the direction of the maximum applied shear stress. The Cottrell and Hull mechanism (90) is illustrated in figure 11. The number of slip bands, and their thickness, increases with number of cycles. As the slip bands develop further, they become 'persistant slip bands' (PSB). Also extrusion stops, while intrusion continues. The tip of the intrusion becomes a very active dislocation source, and grows by the movement of dislocations away from it. Microcracks are then formed from the PSB due to further slip band intrusion. This is called Stage I crack growth (87), and

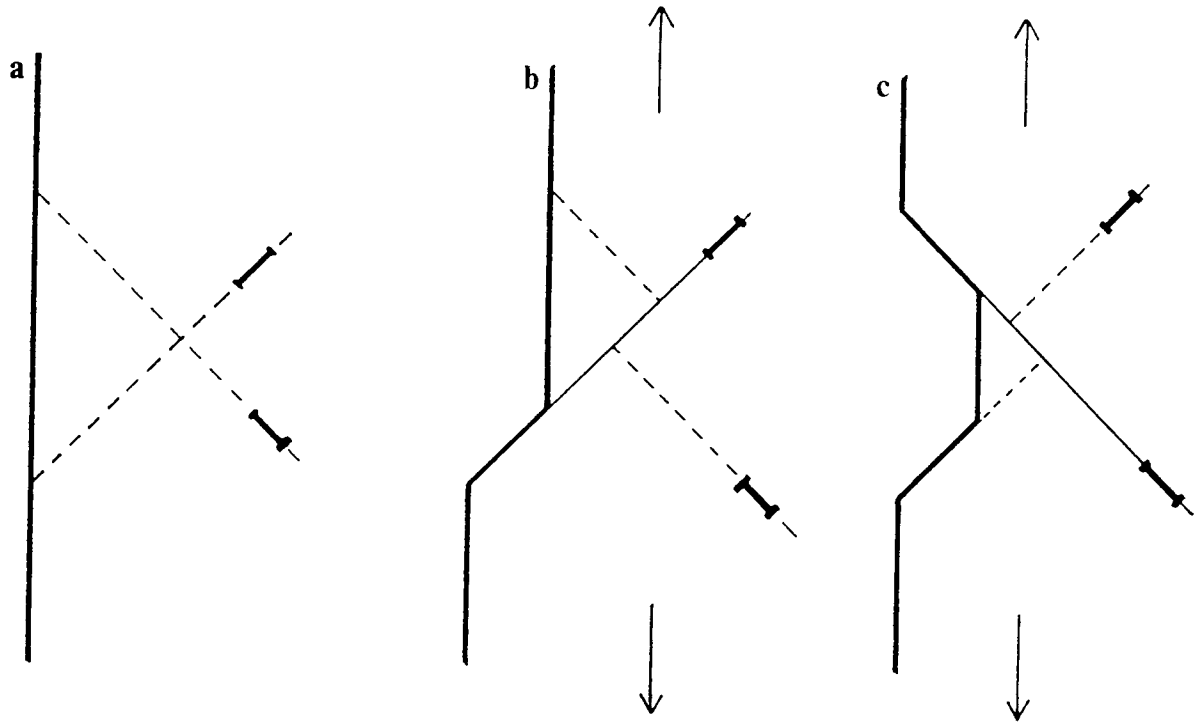

FORWARD CYCLE

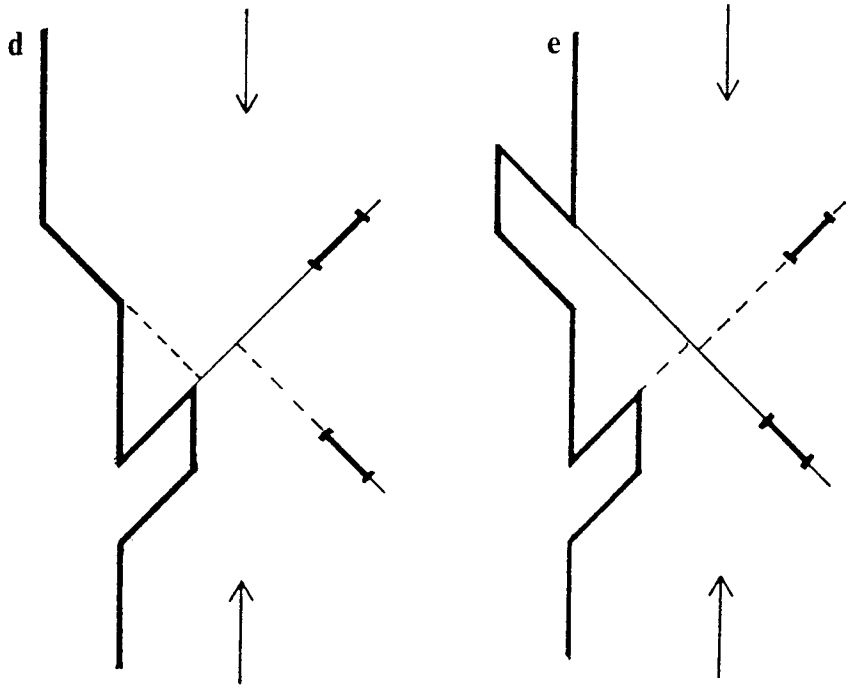

REVERSE CYCLE

Figure 11: Cottrell-Hull model for the formation of slip band inrusions and extrusions.

along with initiation it takes up over 80% of the fatigue life in high cycle fatigue. Although it is difficult to define the start of stage I crack growth, the formation of PSB are generally agreed to signify this, as fatigue damage is then irreversible and intrusion continues while extrusion has ceased. However, in practice crack initiation and stage I crack growth are treated as one.

Initiation and Stage I crack growth life can be increased by a smoother surface condition, so reducing the number of stress concentrations. A smaller grain size and unembrittled grain boundaries are also of benefit. Stage 1 involves many hundreds of individual slip band cracks that propagate along the active slip planes and eventually link up to form a single dominant crack. At this point slip becomes more difficult and mechanisms dominated by tensile stress are favoured. The fracture then follows a path macroscopically normal to the tensile stress - this is termed Stage II crack growth. In this stage, the crack advances a finite distance in each loading cycle (92), producing a striation on the fracture surface to record this distance that the crack front moves. These striations are in the form of parallel ridges separated by plateaus, with a slightly curved front perpendicular to the direction of crack growth. The striation spacings vary with stress intensity amplitude, increasing with increasing stress at the crack tip. The formation of striations can be affected by inclusions, especially at high crack propagation rates.

Most fatigue crack propagation theories involve the alternate blunting and resharpening of the crack tip, as shown in figure 12, (93). At the start of a loading cycle the crack tip is sharp. On application of a tensile load the crack advances and simultaneously becomes blunter, and the crack tip plastic zone expands. It is during this loading stage that the new fracture surface is created by the plastic shearing process. Upon reversal of the load the slip direction in the end zone is reversed and the extended material at the tip is crushed together, exerting a back stress which causes a striation on the fracture surface. The crack is also resharpened, and is ready to advance and be blunted in the next cycle. This continues until the crack becomes long enough to cause final fracture. A number of modified models have been formulated. A shear slipping model is one of these (94), where slip occurs on a number of parallel planes. A series of fine slip steps appear on the fracture surface, and a

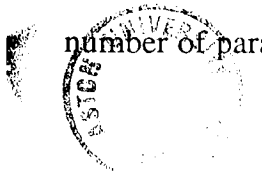

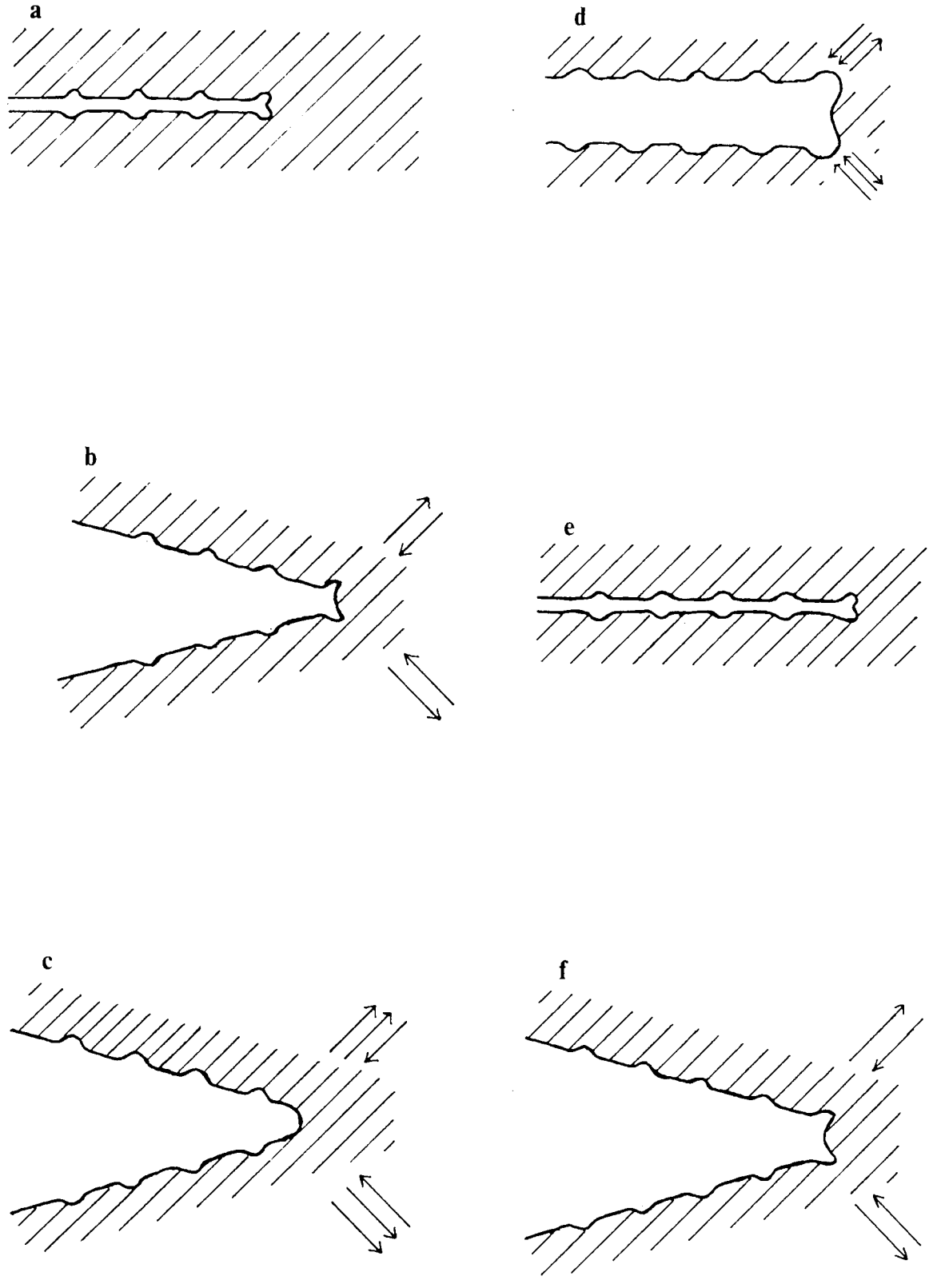

Figure 12: Crack propagation mechanisms in Stage II.

large step, or striation, is produced during each stress cycle. Just before fast fracture there is a mixed-type failure mode, sometimes termed stage III crack growth. Some static fracture occurs, due to the higher stress intensity factor, by microvoid coalescence in ductile materials and by microcleavage or intergranular mechanisms in brittle materials. The three stages of crack growth are illustrated in figure 13.

3.2.2. ENGINEERING ASPECTS OF FATIGUE

For the engineer to design successfully against fatigue failure he needs to estimate crack initiation life and fatigue crack propagation rate. The fatigue life of a specimen depends on the value of the cyclic stress applied during the test. To assess this it is usual to test a number of specimens at various stress levels, and measure the life of each specimen as the number of cycles required to cause failure. The normal method of representing engineering fatigue data is by means of S-N diagrams, representing the dependence of stress on number of cycles to failure.

The two basic types of S-N curves are shown in figure 14. One has a well defined stress limit below which failure does not occur. This stress, S_1, is called the fatigue limit. The other curve is typical of most aluminium alloys, where there is no fatigue limit. The relationship between the nominal stress, S, and the number of cycles, N, can be in terms of the number of cycles to failure, N_f, or the number of cycles to initiation, N_i.

However, for successful fatigue design the mechanisms in different stages of fatigue have to be investigated to predict the behaviour of a crack under different conditions.

In engineering terms, the initiation of a crack corresponds to a crack length of 0.1-0.25 mm (95). In the case of commercial aluminium alloys, a crack depth of at least 0.127mm signifies the end of stage I crack growth (96). In high cycle fatigue (HCF) almost the entire life of the specimen is spent in forming this engineering crack, only around 10% of the fatigue life is spent in stage II growth, and so N_f is also considered to represent N_i. However, in low cycle fatigue (LCF) the propagation of a crack represents a significant part of the life of a component. Manson (97) suggested a correlation between N_i and N_f for this case:

$$N_i = N_f - 4.0(N_f)^{0.6} \qquad \text{....(3.11.)}$$

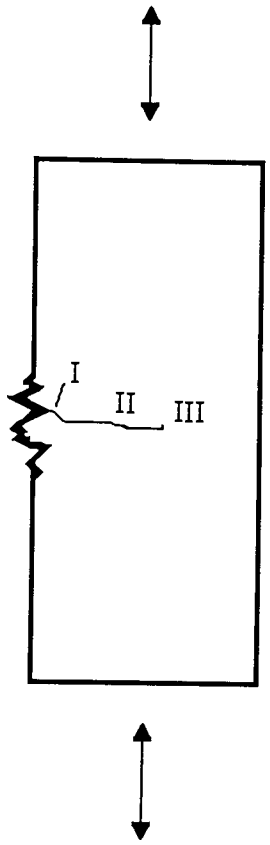

Figure 13: The three stages of crack growth.

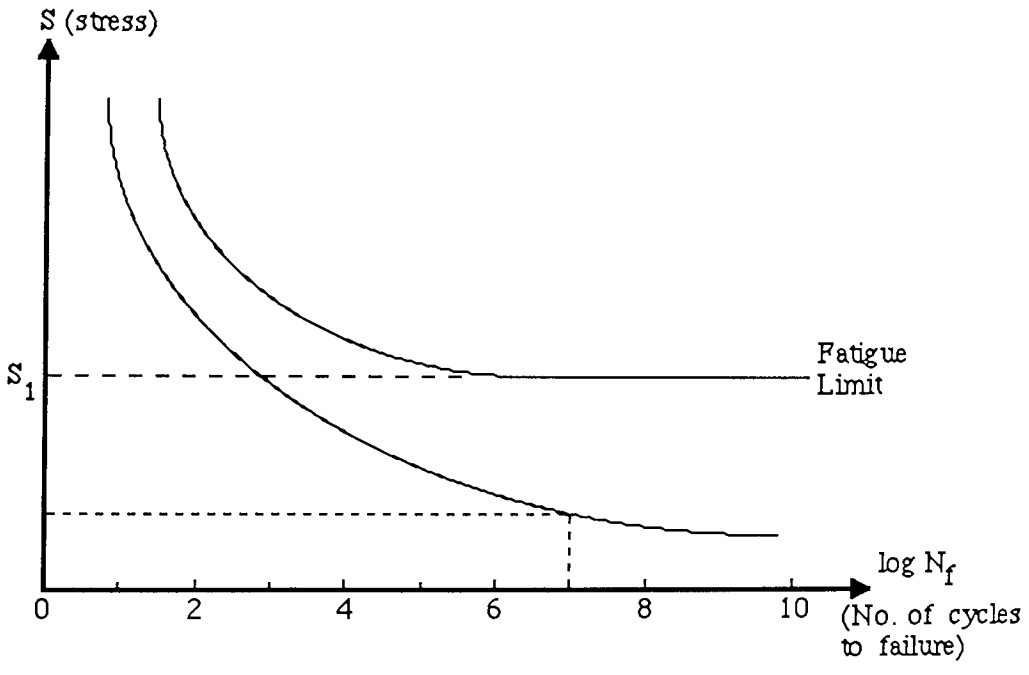

Figure 14: Typical S-N curves.

Most fatigue crack propagation tests are conducted by subjecting a fatigue cracked specimen to constant stress amplitude. The crack length, a, is measured simultaneously with number of cycles, N, and the data is presented as in figure 15, which also shows the effect of the magnitude of the cyclic stress.

The three curves in figure 15 can be reduced to a single curve by representing the data in terms of da/dN versus ΔK, where da/dN is the crack growth rate per cycle of loading and ΔK is the cyclic stress intensity factor. da/dN is calculated from the data in figure 15. ΔK is the stress intensity difference due to the maximum and minimum values of stress at the crack tip, and is calculated consecutively with da/dN at corresponding values of crack length.

$$\Delta K = Y (\sigma_{max} - \sigma_{min}) \sqrt{\pi a} \qquad \text{....(3.12.)}$$

where $Y = f(a/W)$, a = crack length, W = specimen width, σ_{max} = maximum applied stress and σ_{min} = minimum applied stress.

Numerous laws have been proposed, but the most popular law governing fatigue crack propagation is the Paris Law (98).

$$\frac{da}{dN} = A(\Delta K)^n \qquad \text{....(3.13.)}$$

where A and n are experimental constants. The most commonly used presentation is a log-log plot. Figure 16 shows that the fatigue crack propagation behaviour can be divided into three regions, which relate to stages I, II and III crack growth referred to in section 3.2.1.

Region I exhibits a fatigue threshold cyclic stress intensity factor, ΔK_{th} , below which there is no crack growth. Region II can be represented by the Paris equation (eqn 3.12). Region III is a high crack growth rate region where the maximum stress intensity approaches the critical stress intensity for static failure, K_c, and so some static-type fracture also occurs.

The range of each region in fatigue crack growth depends upon the material and the

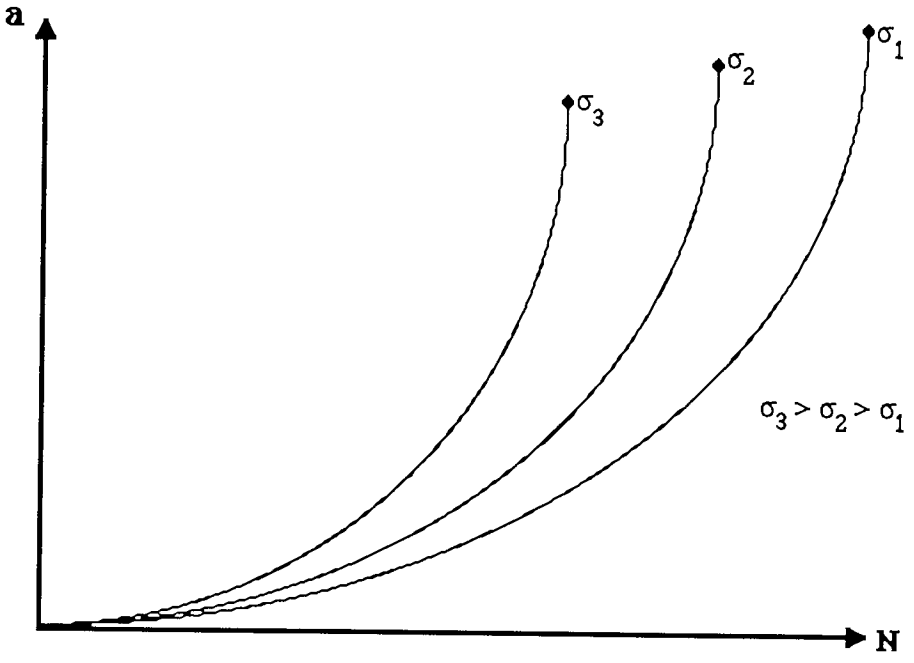

Figure 15: Fatigue crack growth rate representation - a versus N.

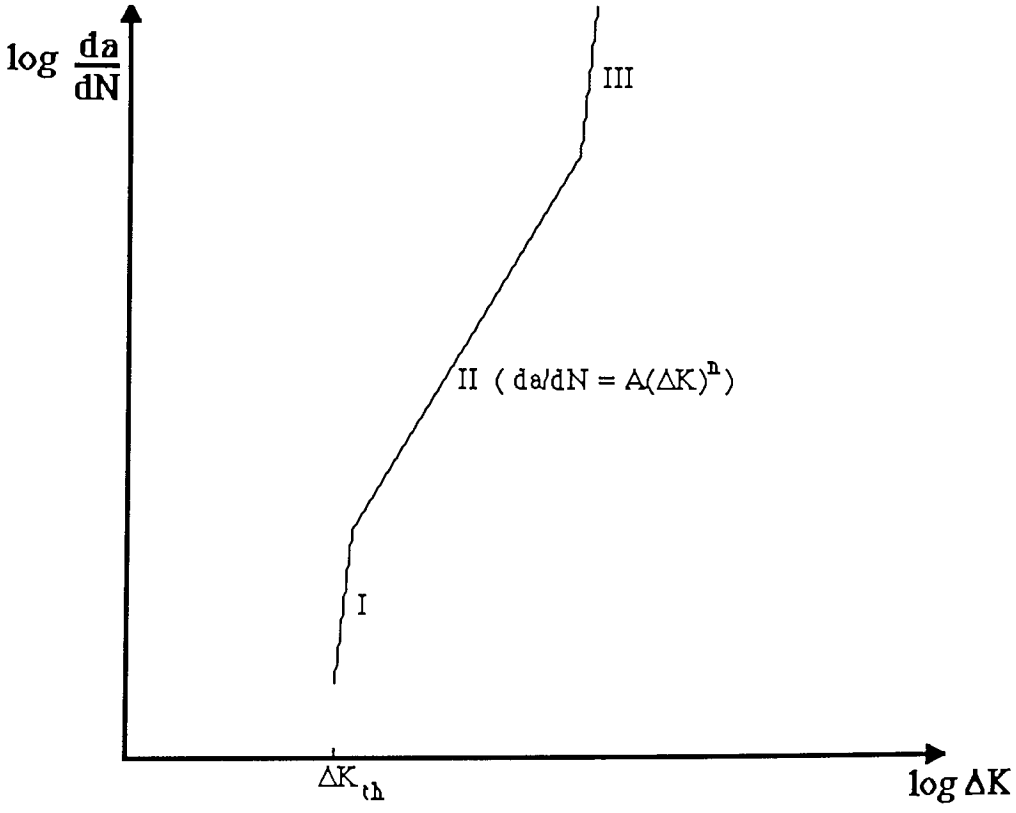

Figure 16: Fatigue crack growth rate representation - da/dN versus ΔK.

magnitude of the stress. Fatigue crack propagation rates increase with increasing mean stress and constant stress range. The threshold stress intensity range, ΔK_{th} , is decreased markedly with increasing mean stress.

It should be noted that a large safety factor needs to be applied when predicting growth rates using the Paris Law, due to the many uncontrollable variables which affect fatigue crack growth.

3.2.3 THE EFFECT OF NOTCHES ON FATIGUE

The previous section dealt with fatigue from smooth specimens, but in practice notches and other geometric stress-raisers are hard to avoid. The effect of a geometric discontinuity in a loaded structural component is to intensify the magnitude of the nominal stress in the vicinity of the discontinuity. Fatigue is therefore a notch sensitive mechanism, not only affecting initiation but also propagation to an extent. Specimens containing notches are therefore tested to study the effect of stress raisers on fatigue.

Notch effects on initiation can be quantified in two ways, by stress concentration methods (i) or fracture mechanics methods (ii). Both of these methods characterise the stress and strain field at the notch root, and relate this to the nominal stress applied to the specimen.

(i) The degree of concentration of stress and strain caused by a notch is measured by the elastic stress concentration factor, K_t, which is the ratio of the maximum local stress, σ_{max}, at a notch to the nominal stress,

$$K_t = \frac{\sigma_{max}}{\sigma_{nom}} \qquad \ldots.(3.14.)$$

The fatigue life of a notched component could then be calculated by multiplying the stress scale of the S-N curve by K_t, to give $K_t.\Delta S$ v. N_i, or $K_t.S_{max}$ v. N_i curves. However, the calculation of K_t assumes a completely elastic stress-strain response in the local stress at the notch root and does not take into account any cyclic plastic behaviour at the tip. For this reason, the effective stress concentration factor in fatigue, K_f, was developed, and defined

as:

$$K_f = \frac{\text{Fatigue strength of unnotched specimens}}{\text{Fatigue strength of notched specimens}} \qquad \ldots.(3.15.)$$

So by comparing the S-N curves of notched and unnotched specimens the effect of notches on fatigue strength can be determined, in the form of $K_f.\Delta S$ v. N_i or $K_f.S_{max}$ v. N_i curves.

Neuber (99) proposed the following relationship:

$$K_f = (K_\sigma . K_\varepsilon)^{1/2} \qquad \ldots.(3.16.)$$

where $$K_\sigma = \frac{\text{local stress range, } \Delta\sigma}{\text{nominal stress range, } \Delta S}$$

$$K_\varepsilon = \frac{\text{local strain range, } \Delta\varepsilon}{\text{nominal strain range, } \Delta e}$$

On the assumption that as long as the local strain amplitude at a notch root is equal to the strain amplitude of a smooth specimen then the fatigue lives will be the same, the approximate life of initiation of cracks can be predicted from the local strain amplitude, $\Delta\varepsilon$. (100). However, K_f has to be determined experimentally for each notch type, material, type of loading and stress level, so extensive experimentation is required.

(ii) The fracture mechanics approach to initiation from notches overcomes many of the problems found with the stress concentration approach, and was first analysed by Bilby and Heald (101). They related N_i to a critical value of the summation of plastic displacement, ϕ_c, on a single plane:

$$N_i = \frac{2\gamma.G}{\pi\,(\Delta K)^2} \qquad \ldots.(3.17.)$$

where γ = plastic work done per unit area of fracture = $\phi_c.\sigma_y$

(ϕ_c= critical cumulative displacement, σ_y= yield stress)

G = elastic shear modulus, ΔK = stress intensity factor range

Rearranging this expression, assuming ϕ_c, σ_y and G to be constant:

$$N_i = C(\Delta K)^{-2} \quad \text{....(3.18.)}$$

Jack and Price (102) suggested that in practice slip occurs randomly on several planes rather than one, and so ϕ_c should be obtained from the sum of the squares of the individual displacements. This changes the relationship to:

$$N_i = C(\Delta K)^{-4} \quad \text{....(3.19.)}$$

For a blunt notch, the effective stress intensity range, ΔK_{eff}, replaces ΔK in the expression (103), where:

$$\Delta K_{eff} = \Delta K[\rho_o/\rho]^{1/2} \quad \text{....(3.20.)}$$

where ρ_o = critical value of notch root radius below which the notch can be treated as a crack

ρ = root radius of the notch.

ΔK = calculated stress intensity range of a crack of the same depth as the notch.

This changes the relationship to:

$$N_i = C(\Delta K.[\rho_o/\rho]^{1/2})^{-4} \quad \text{....(3.21.)}$$

This relationship has been shown to give a very good correlation of experimental results for both steel (102) and aluminium alloys (104).

Another parameter that has been used to describe the behaviour of fatigue crack initiation at notch tips in aluminium alloys is $\Delta K/(\rho)^{1/2}$ (104). However, even if these parameters have had some success, a stress intensity factor should not be associated with the tip of a blunt notch, as the K-calibration for cracks emanating from them falls to zero at the notch

tip. A function has therefore been developed to deal with this problem (105). Assuming a slip band at the notch tip to be equivalent to a short, sharp crack, a modified version of Jergeus' equation (106) for the K-calibration in the notch stress field was developed:

$$Y_n = Y_L.\left[\frac{a_o.\tanh(2(1+a_o/\rho)^{1/2}.(C+C_B)/(a_o.\rho)^{1/2}) + (C+C_B)}{(a_o + C)}\right]^{1/2} \quad ....(3.22.)$$

where Y_n is the modification of the standard K-calibration factor, Y_L.
C_B is a material parameter. The grain size or mean free path is the effective short crack length, equivalent to the slip band at the notch tip.
C is the crack length.

Using equation 3.6., the effective stress intensity, K_n, can be calculated. The effective stress intensity range, ΔK_n, is thus another parameter to describe the behaviour of fatigue crack initiation at notch tips.

Fatigue crack growth is affected by notches up to a critical crack length, C_o. Cracks greater than this length comply with previously mentioned fatigue crack growth laws, and the notch can be treated as a crack. However, crack growth rate in short cracks is affected, due to the influence of the notch stress field. The value of C_o varies considerably according to the investigator (100). The estimation of C_o usually involves some function of notch depth and/or root radius. Estimations of C_o of this type vary from $0.13\sqrt{a_o\rho}$ (107) to $0.5\sqrt{a_o\rho}$ (106).

With crack lengths less than this critical value, equivalent crack lengths are used to account for the contribution of a notch. Relationships have been developed to calculate the equivalent crack length of a notch (106, 107) or to obtain the stress intensity factor in the notch stress field (105). Equation 3.22. is used to find the contribution of the notch to the crack length, so that a K-calibration factor can be calculated.

3.2.4. FATIGUE OF ALUMINIUM ALLOY SYSTEMS.

All of the structural and engineering aspects of fatigue mentioned in this section can be applied to the fatigue response of aluminium alloys. Fatigue cracks have been shown to

initiate at coarse slip lines in both 2XXX series (108) and 7XXX series (109) alloys. However, fatigue crack initiation has also been shown to be affected by intermetallic particles and inclusions (96), cracks initiating at cracks in surface inclusions or at inclusion-matrix interfaces. The process of fatigue crack growth in high strength aluminium alloys has been described as a combination of three micromechanisms (110): micro-void coalescence, plastic blunting of the crack tip and cleavage of environmentally embrittled material. At higher crack propagation rates, intermetallic particles again have an effect, by inducing small amounts of ductile fracture (111). It can therefore be seen that inclusions and intermetallic particles play a major role in fatigue processes in aluminium alloys at times (4).

Aluminium-lithium alloys have good resistance to high cycle fatigue and low ΔK fatigue crack growth, for several reasons (4). Firstly, the δ' precipitate promotes planar slip and reduces cross slip. Also, extensive crack deflection processes induced by the δ' precipitates improve crack growth behaviour. Secondly, all models of crack growth indicate that resistance to fatigue crack growth should increase with increasing modulus. However, it has been shown with these alloys that their low fracture toughness increases the fatigue crack growth rates at high stress intensity ranges. This is because crack growth behaviour in the high ΔK region is controlled by the same microstructural features that control toughness. The alloys show a low resistance to fatigue crack initiation, due to the high stress intensities at grain boundaries, caused by PFZ's, pronounced textures and the shearing of coherent precipitates, leading to planar slip. Thus, the factors that improve fatigue crack growth resistance have a detrimental effect on fatigue crack initiation.

Work on the fatigue crack growth behaviour of Al-Li-Cu-Mg alloys has shown superior properties to conventional 2XXX series alloys (112, 113). As well as the previously mentioned reasons for lower fatigue crack growth rates in these alloys, a pronounced crystallographic texture has been shown to improve crack growth behaviour, although anisotropy of crack growth properties is apparent. To a lesser extent, the fatigue behaviour of Al-Li-Cu, Al-Li-Mg and AL-Li-Mn alloys have been shown to be good when compared to conventional alloys (114, 115).

The fatigue properties of filamentary reinforced metals are generally found to be superior to their monolithic counterparts. Under fatigue loading, the stress in the matrix of a

composite is lower than that which would occur in the unreinforced matrix, since the fibres carry a more than proportional share of the load. Therefore, the initiation of cracks can be expected to be delayed and their subsequent propagation rate is likely to be much reduced, Also, the interfaces may act to deflect or stopcracks by opening up to produce a void. The effect of reinforcement on fatigue life should therefore be quite significant.

Composite fatigue failures have been found to originate at stress concentrations, usually located at the filament-matrix interface. A failure sequence has been reported (116) as follows:

1. Failure is initiated at pre-existing filament breaks or at filament breaks formed on initial application of load.
2. The stress concentrations in the matrix resulting from cracked filaments increase in intensity with time as a result of matrix strain hardening.
3. Eventually these stress concentrations become intense enough to initiate cracks at an adjacent filament-matrix interface.
4. These cracks propagate along the filament-matrix interface until a weak point is found in the filament. The filament breaks and the process is continued. Composite failure takes place when the crack exceeds the critical length established by reinforcement content, matrix properties and specimen dimensions.

Several modes of failure have been identified by observations of fatigue damage on fracture surfaces (117). Specific areas have been described where the fibres and matrix fail in combinations of either fatigue or tension. Fibre breakage, debonding, delamination and matrix cracking have all been shown to contribute to final fracture in a variety of ways (118). These types of damage increase until the crack propagates catastrophically.

The difference in failure mechanism in tension and fatigue are an important factor in composite design, as the current practice of optimising tensile strength does not necessarily result in optimum fatigue strength. Fatigue resistant composites require fibres with high strength and modulus in a matrix of lower modulus and a small yield stress to UTS ratio, with a low fibre-matrix interface strength (117). In Saffil-reinforced aluminium alloys, fatigue properties have been mixed to date. Using an LM25 matrix alloy, which is essentially an aluminium-silicon alloy, fatigue properties have been poor (23), due to fibre

cracking and a strong fibre-matrix bond which encourages fatigue cracks to propagate into the matrix material. However, Saffil reinforcement has been shown to increase the fatigue limit of an Al-Si-Cu-Mg-Ni piston alloy (30), possibly due to the fact that the fibre-matrix bond was noted to be weak. In general, if reinforcement of an alloy increases the monotonic tensile strength then the fatigue strength is also increased (31).

Aluminium powder metallurgy (PM) alloys have been shown to have superior fatigue strength as compared to their ingot metallurgy (IM) counterparts (119, 120), in the case of both smooth and notched specimens. This is attributed to the superior fatigue crack initiation resistance of PM alloys. This improvement is due to the fine homogenous grain structure, which inhibits the initiation of cracks by constraining the slip band length. Crack initiation sites are also reduced due to the lack of defects in the form of brittle constituent particles, which are suppressed by the high solidification rates during powder formation. However, at low to moderate levels of ΔK, aluminium PM alloys only have comparable, or even inferior, fatigue crack growth resistance to IM alloys. The superiority of PM alloys is restricted to high ΔK's. This is due to the fact that in PM alloys the plastic zone size is larger than the grain size so that grain boundaries restrict slip reversibility (119). Efforts have been made to improve the crack growth resistance of these materials by modification of the grain structure through recrystallisation (121). Fatigue crack growth rate roughly follows a grain size dependence, decreasing with increasing grain size. Recrystallisation to intermediate or coarse grain sizes has been shown to increase the resistance to fatigue crack growth in PM 2XXX series alloys and their threshold stress intensity for crack growth, K_{th}, to increase. At the same time, there is no reduction in fatigue crack initiation resistance associated with this treatment, as might be expected with an increase in grain size. Anisotropy in fatigue properties increases with increasing local deformation, due to the enhancement of longitudinal fatigue properties (122). The greater resistance to crack initiation that leads to this is because of a smaller subgrain size and uniform precipitation which promotes more homogenous slip.

Fatigue properties of the Alcoa developed alloy CZ20 are promising (65). The fatigue strength is superior to 2014, and its better fracture toughness indicates that high ΔK crack growth rates would be slower.

4. CORROSION FATIGUE

The simultaneous action of cyclic stress and corrosive attack is known as corrosion fatigue. The presence of the corrosive environment often greatly reduces the fatigue strength of metals and alloys, even though the loss of metal by corrosion may be negligible.

The reduction of fatigue resistance can be defined in terms of the damage ratio, that is the corrosion fatigue strength divided by the air fatigue strength. For aluminium alloys in a salt water environment, this ratio is typically around 0.4 (123). However, even water vapour in the atmosphere reduces the fatigue strength of aluminium alloys, and so almost all fatigue testing on these alloys are, in effect, conducted under corrosion fatigue conditions.

Materials which show a definite fatigue limit when tested in air show no indication of a fatigue limit when the test is carried out in a corrosive environment, as shown in figure 17. At high stresses and short endurance, the corrosion fatigue and air fatigue curves are practically identical and microscopical observations suggest that the failures are identical. But at lower stresses the combination of any corrosive environment and fluctuating stress results in reduced fatigue stress and the disappearance of the fatigue limit (124). Also, the effect of a corrosive environment on fatigue strength is most severe when it is applied where oxygen has free access to the metal surface. So if an aqueous corrodent is sprayed or dripped onto the metal surface the subsequent fatigue strength is lower than if the specimen were immersed completely (125). The corrosive effect can be further accentuated by rapid movement of the corroding medium over the surface of the metal, washing away any protecting layers that may form, as in a salt spray test.

The main effect of corrosion on its own is to produce sharp pits, which act as notches. So with the joint action of corrosion and fatigue a multiplicity of slip band cracks can form, developing at lower stresses than in air tests and all on slightly different planes, resulting in a lower fatigue strength. A corrosion fatigue fracture surface shows the same characteristics as normal fatigue fractures, but they are sometimes discoloured by corrosion products or severely damaged by superficial corrosion.

Corrosion fatigue data are usually presented in the same manner as air fatigue data (126). For fatigue life studies S-N curves are still used to establish a corrosion fatigue limit. The

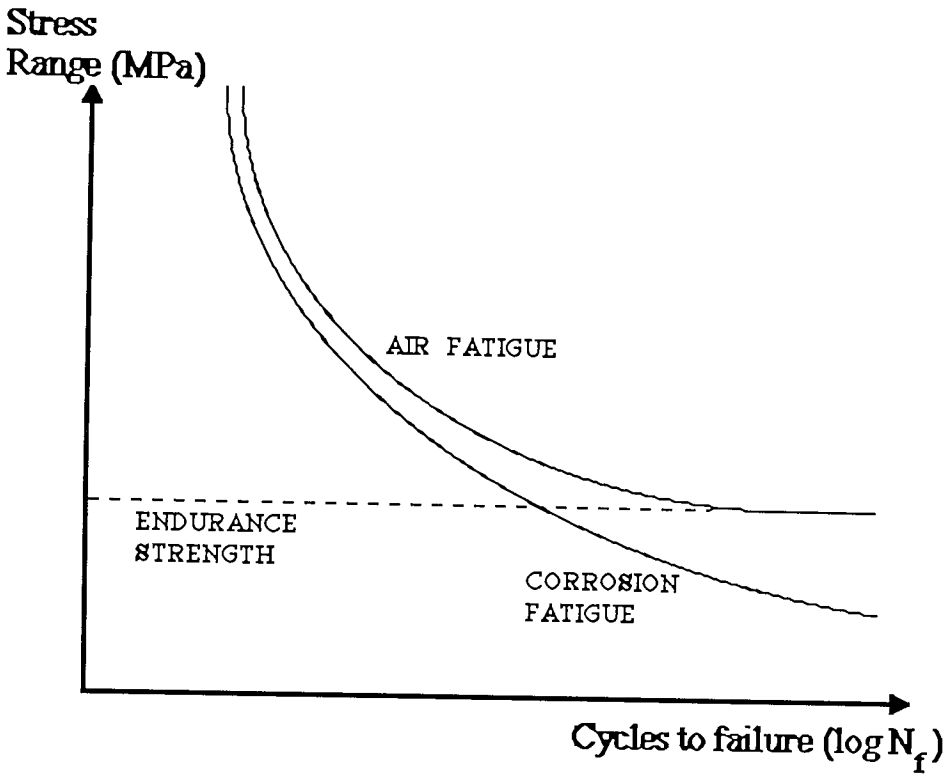

Figure 17: Typical air fatigue and corrosion fatigue curves.

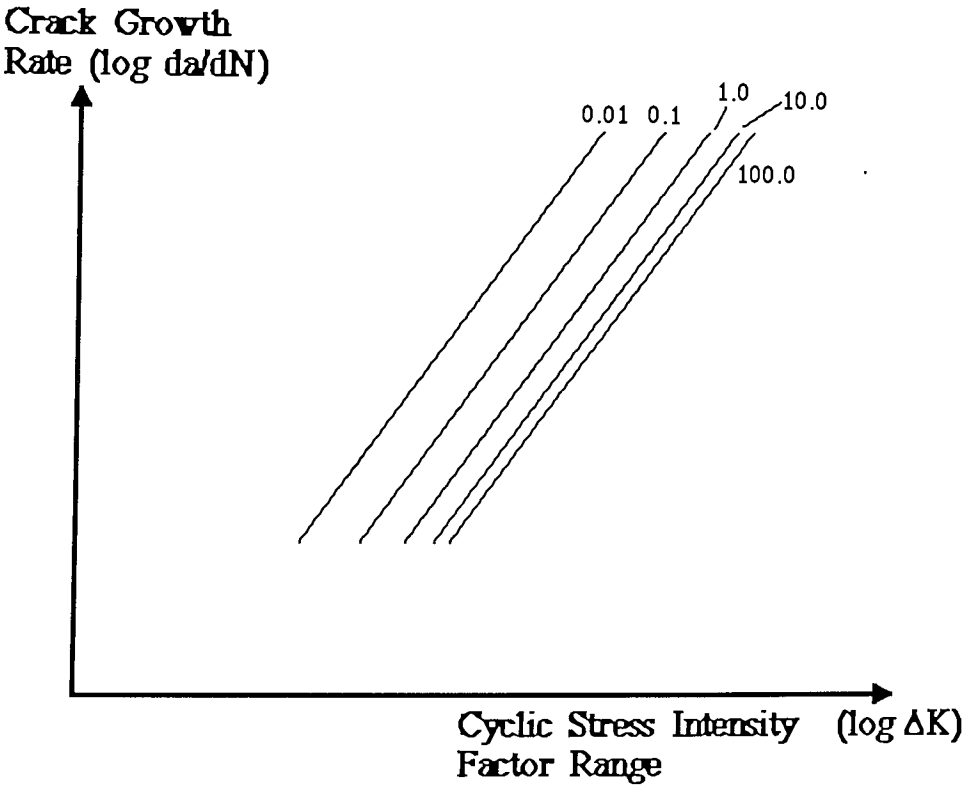

Figure 18: Typical fatigue crack growth rates as a function of stress intensity range ($MN.m^{-3/2}$) and frequency (Hz).

simplest fatigue tests of this type use rotating beam specimens. Air fatigue and corrosion fatigue tests can be carried out on the same apparatus, with provisions made to subject the specimen to a corrosive environment by spraying or dripping a solution onto the specimen, creating a mist in an enclosure about the specimen, or immersing the specimen in a solution. For corrosion fatigue crack growth studies, the same fracture mechanics principles can be applied. Compact tension (CT), centre-cracked tension (CCT) or single edge notch (SEN) specimens are commonly used. There are many types of aqueous solutions used to simulate marine environments, including fresh natural seawater, synthetic seawater and sodium chloride solutions. The relative severity of these solutions in corrosion fatigue have been studied (126, 127).

In air fatigue tests, the stress cycle frequency has little or no influence on fatigue resistance over the range of 10 to 200 Hz. However, in corrosion fatigue there is a definite dependence on testing speed (128). Since corrosive attack is a time-dependent phenomenon, the higher the testing frequency then the less the damage due to corrosion, as shown in figure 18. The influence of cyclic frequency is more pronounced with a more aggressive environment (129). It has been shown that at low frequencies the rate of damage is roughly proportional to the frequency (124). At higher frequencies the rate of damage becomes more frequency independent. For corrosion fatigue below the threshold stress intensity for stress corrosion cracking, K_{ISCC}, the magnitude of the frequency effect depends upon the particular environment-material system and on the cyclic stress intensity frequency (124), and can be represented by:

$$\frac{da}{dN} = D(t) \,.\, (\Delta K)^2 \qquad \ldots(4.1.)$$

In air, D(t) is a constant within the frequency range of 10 to 200 Hz, and so approximates to the Paris equation.

Corrosion fatigue crack growth rates can increase further when K_{ISCC} is exceeded, due to the effect of stress corrosion cracking (130). Corrosion fatigue crack growth can therefore be divided into two broad categories, firstly true corrosion fatigue where $K_{max} < K_{ISCC}$ and

secondly stress corrosion assisted corrosion fatigue where $K_{max} > K_{ISCC}$.

There are a number of methods available for preventing corrosion fatigue (131). Altering the design of a component to reduce the stress on it may eliminate the problem. Alternatively, shot peening or nitriding the surface of the component to induce compressive stresses may keep notches from opening up and giving access to the corrosive medium. Corrosion inhibitors have also been shown to be effective in reducing or eliminating the effects of corrosion fatigue in aircraft components (132). Resistance to corrosion fatigue can be improved by using coatings such as zinc or cadmium on steel and aluminium on Alclad aluminium alloys, although these coatings may cause a reduction in fatigue strength in air. In some cases, cathodic protection using sacrificial anodes is suitable for improving the corrosion fatigue strength of metals.

4.1. MECHANISMS OF CORROSION FATIGUE

4.1.1. GASEOUS CORROSION FATIGUE MECHANISMS

In some cases, fatigue tests in air at room temperature are influenced by corrosion fatigue (133). In practice, fatigue crack initiation rarely occurs without an oxidising atmosphere being present, since initiation processes are relatively slow and oxide forms on newly generated surfaces in microseconds even in a relatively high vacuum. Fatigue tests carried out in vacuum or inert gases produce different results to those carried out in laboratory air, giving an appreciable improvement in fatigue lives. It has been stated (134) that this is due to the combined effects of oxygen and water vapour, although in the case of aluminium alloys water vapour is the main cause, resulting in hydrogen embrittlement. The detrimental effect is due to surface contamination, making slip irreversible and so the development of persistant slip bands occurs sooner. Others (135) have suggested a mechanism based on the dissociation of water vapour to assist crack nucleation. The first process, by inhibiting slip reversal on its initial plane, promotes crack growth by an intrusion process. The second process, by absorption of hydrogen ions into the metal lattice, promotes brittle behaviour by reducing the surface energy of the material. Atomic hydrogen is transported by dislocations into slip bands which accelerates their link-up.

A gaseous environment has the greatest effect early in the crack growth process, having little or no effect at high crack growth rates. The main influence of the environment on crack growth is to supply active atoms to the crack tip. Subsequent interaction with the crack tip allows the degradation mechanism to take place. Of the two explanations proposed (136), the process of corrosive attack of the crack tip is favoured over that of the prevention of rewelding of crack surfaces by the formation of oxide layers. Since the atmospheric effect decreases with increasing stress intensity a crack rewelding process is not a satisfactory explanation, since the higher stresses involved should intensify a rewelding effect. But in the same way that it interferes with slip processes in fatigue crack initiation, surface oxidation makes slip irreversible and accelerates crack growth.

4.1.2. AQUEOUS CORROSION FATIGUE MECHANISMS.

Most service components, for example aircraft, operate in a wet condition, and sometimes in salt-laden atmospheres. In this case, corrosion fatigue is an electrochemical process. Virtually all corrosive environments affect crack initiation processes, with a highly localised corrosion process rather than a general one.

Various mechanisms have been suggested for corrosion fatigue crack initiation in aqueous environments. None of these mechanisms adequately explains crack initiation in general, as it is a function of both the material and the environment, but initiation is usually at surface discontinuities associated with slip bands. The most acceptable mechanism theories can be categorised as follows (129, 133):

(i) Early investigators favoured the theory of stress concentration at the base of pits created by the corrosive medium, as large cracks have been found to originate at large hemispherical pits at the metal surface. Although pit formation is responsible for a reduction in fatigue life, corrosion fatigue has also been shown to occur in environments where pitting does not occur.

(ii) It was later suggested that failure is caused by distorted metal acting as an anode with undistorted metal acting as a cathode. Very fine cracks advance as a result of a combination of electrochemical attack at the plastically deformed areas of metal and a mechanical action.

(iii) A mechanism by which environmental adsorption reduces the surface energy of the metal, increasing the propagation of microcracks, has been shown to apply to some aluminium alloys. Cathodically produced hydrogen diffuses faster by a dislocation transport process and so collects at interfaces within the structure, causing hydrogen embrittlement and resulting in early crack nucleation.

(iv) In a reaction where the corrosion product forms a barrier in the undisturbed state, fatigue deformation might act as a corrosion accelerator by breaking up the corrosion products. Oxide films are cathodic to the exposed metal because of the restraint they place on the diffusion of metal ions into solution. So a break in the oxide film provides an anode of exposed metal surrounded by a large cathode of oxide-covered surface, producing electrochemical attack at these ruptures in a normally protective film. However, corrosion fatigue crack initiation has been observed where film rupture does not occur.

(v) The production of slip bands by fatigue deformation also exposes fresh metal surface, and so many anodic sites are produced where attack could be concentrated. Corrosion fatigue crack initiation would therefore occur by persistant slip bands being preferentially attacked, leading to stress intensification and subsequent early propagation. Corrosion increases the density of persistant slip bands, due to the unlocking of dislocations at preferentially attacked slip band steps increasing plastic deformation at the surface, and so numerous crack initiation sites are produced.

The effects of an aqueous environment on fatigue crack growth are similar to the previously described gaseous environmental effects. Once the embrittling elements in the liquid are brought to the surface, the same mechanisms apply. The only difference is the additional electrochemical role of the crack tip, with polarizing effects having a great influence (137). In aqueous corrosion fatigue crack growth the reactants present in the liquid environment must be supplied to the crack tip region, where it reacts with newly cracked material produced by fatigue processes. Anodic dissolution of material at the crack tip is responsible for the environmental contribution to corrosion fatigue crack growth. If the corrosion reaction produces a deleterious chemical species, for instance the hydrogen ions

that are produced by cathodic reaction in aqueous solutions in cracks in aluminium alloys (138), it can be adsorbed at the metal surface and diffuse to ahead of the crack tip to cause localised damage, for example hydrogen embrittlement.

Corrosion fatigue cracks usually initiate and grow in a transgranular fashion, similar to fatigue crack processes in air. But increased corrosive attack can change the initiation or growth process to intergranular or a mixture of transgranular and intergranular cracking, which can be associated with a greatly decreased fatigue resistance (126). There is an indication that there is a relationship between stress corrosion cracking of an alloy and corrosion fatigue, depending upon the time available for hydrogen to diffuse (133). At high crack growth rates hydrogen cannot diffuse to grain boundaries and so it interacts with growing transgranular cracks instead. A transition from transgranular to mixed or intergranular crack growth in corrosion fatigue usually takes place with decreased ΔK or cyclic frequency, or increased environmental attack.

Corrosion fatigue crack growth has been categorized into three types of behaviour, as illustrated in figure 19, showing the interactions of pure fatigue, environmental enhancement of fatigue crack growth and stress corrosion cracking (SCC) (129). Type A shows the combined interaction of cyclic and corrosive crack growth mechanisms, and is typical of the effect of water on aluminium alloy fatigue response. Type B shows no environmental effect below the threshold stress intensity factor for stress corrosion cracking, K_{ISCC}, but a combination of cyclic and stress corrosion crack growth above this threshold. Type C is a mixture of types A and B, and is typical of most alloy - environment systems. The response is similar to type A below K_{ISCC} and a combination of cyclic, corrosive and stress corrosion crack growth mechanisms above the threshold.

4.2. CORROSION FATIGUE IN ALUMINIUM ALLOY SYSTEMS.

Aluminium alloys have relatively low corrosion fatigue strengths, under half the fatigue strength in air. Pitting is a problem with many alloys, particularly 2XXX and 7XXX series alloys, providing stress raisers and promoting early fatigue failure. The corrosion fatigue resistance of high strength aluminium alloys is poor in most salt solutions, due to

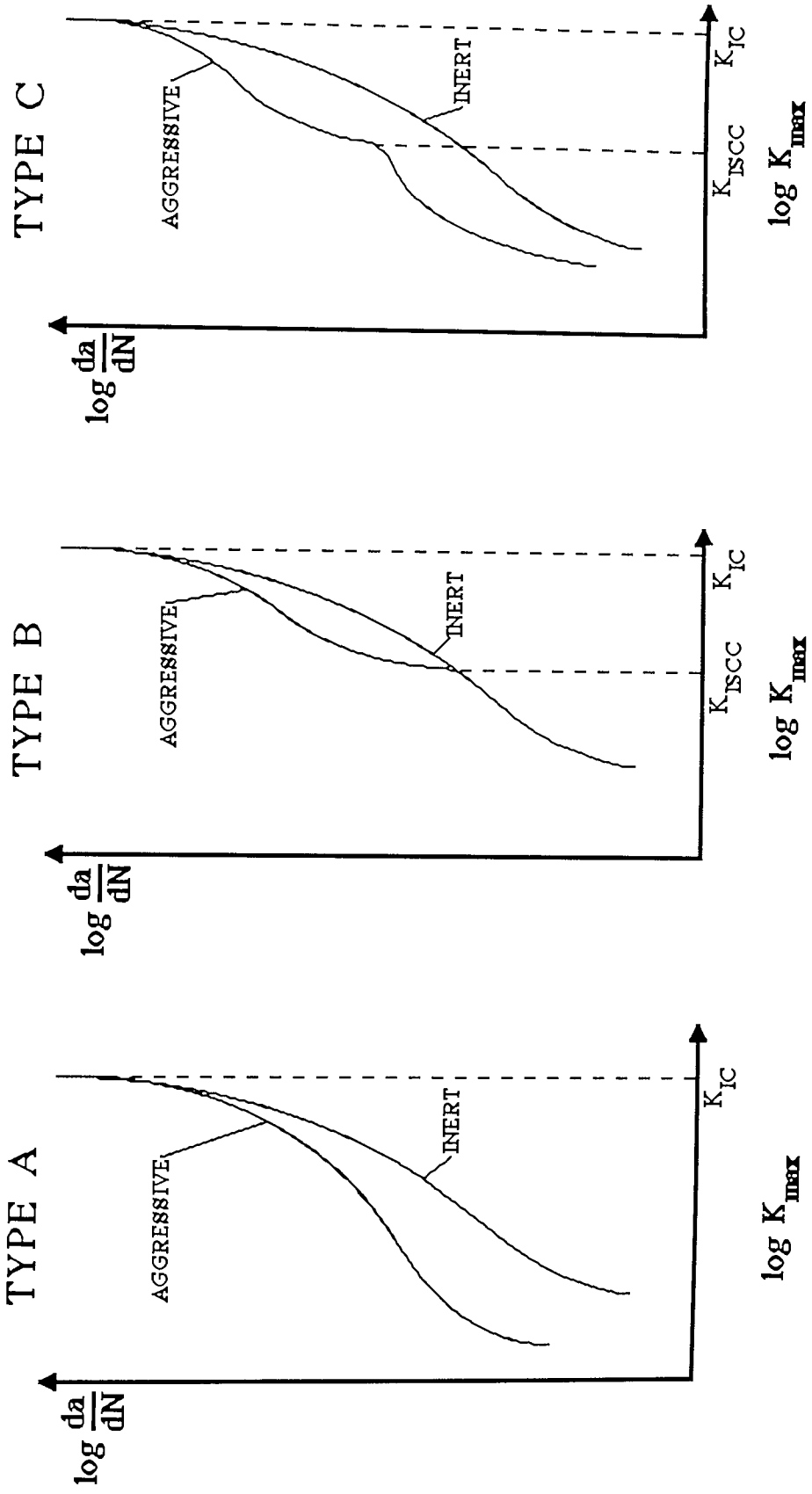

Figure 19: Types of corrosion fatigue crack growth behaviour.

preferential dissolution at the tips of growing cracks and preferential adsorption of the damaging ionic species (139). Other work on these alloys indicates that localised hydrogen embrittlement may be responsible for their poor corrosion fatigue resistance (133). The effect of the addition of halide ions to the liquid environment (water) on the rate of fatigue crack growth of aluminium alloys has been investigated (140). The corrosion fatigue failures are characteristically transgranular, as opposed to intergranular stress corrosion cracking failures.

A comprehensive review of corrosion fatigue data for aluminium alloys has been made (141). In general, 2XXX series alloys have been found to be less sensitive to corrosion fatigue cracking than 7XXX series alloys, and an increased copper content in these alloys increases corrosion fatigue resistance. In 7XXX series alloys, hydrogen adsorption has been found to promote the formation of brittle striations on transcrystalline facets in stage II crack growth (142), along with some intercrystalline failure due to anodic grain boundary precipitation (143). Both 2XXX and 7XXX series alloys have to be heat treated to high strength levels, which reduces their corrosion resistance.

The nature of the precipitates in these high strength aluminium alloys is important, influencing the fatigue life in corrosive environments (54). In aluminium-lithium alloys the coherent shearable precipitates cause dislocation movement to be concentrated, with planar bands of intense slip (45) which are more sensitive to localised corrosion. Aluminium-lithium alloys are therefore more sensitive to corrosion fatigue than conventional alloys, with their semi-coherent precipitates (4). These conventional alloys are subjected to prolonged ageing times to improve their resistance to corrosion fatigue, which makes the precipitates semi-coherent, or incoherent and nonshearable. This promotes dislocation looping and so the slip becomes more diffuse. However, if the ageing time is too long the strength of the alloy is markedly reduced, due to the incoherent particles, so that the corrosion fatigue strength will be reduced even if there is negligible corrosive effect. Prolonged ageing times are harmful to the corrosion fatigue resistance of aluminium-lithium alloys, due to the formation of the anodic δ phase. Underaged and peak aged condition Al-Li-Cu-Mn alloys have been found to have crack growth rates an order of magnitude lower than overaged ones (144). They are relatively insensitive to ambient moisture, but crack growth rates in salt

solutions are 2-3 times higher than in air (144). All of the published data for corrosion fatigue of aluminium-lithium alloys have so far been for Al-Cu-Li or Al-Cu-Li-Mn alloys (144, 141) and only limited data is available for Al-Li-Cu-Mg alloys (112). However, corrosion and Stress Corrosion Cracking data has been published (145, 146) which indicates that corrosion fatigue properties would be superior to conventional alloys. Stress corrosion cracking resistance is higher in 8090 than 7XXX series alloys, and approaches that of 2014. The corrosion resistance has been improved by overageing Al-Li-Cu-Mg alloys, the deleterious effects of overageing being minimised by the presence of copper and magnesium suppressing the $\delta' \rightarrow \delta$ transformation.

The corrosion fatigue properties of metal matrix composites seem to depend upon the individual fibre-matrix system. The effect of water vapour on the fatigue properties of aluminium-boron composites can be up to 20 times worse than the effect on aluminium alloys (147), due to the fracture sensitivity of boron filaments to water vapour rather than any matrix-filament interface effect. On the other hand, the fatigue strengths of graphite-aluminium and SiC-aluminium composites have been found to be less sensitive to sea water exposure than aluminium alloys (148, 149). No corrosion fatigue data is available for Saffil-reinforced composites. However, they do not suffer from galvanic corrosion in the presence of water as graphite-aluminium composites do and their inherent chemical inertness suggests that corrosion fatigue resistance should be relatively good (19).

The properties that are particularly improved by the powder metallurgy (PM) route are fatigue performance and stress corrosion resistance (150), suggesting that corrosion fatigue properties of alloys produced via this route would be superior to those manufactured via an ingot metallurgy (IM) route. This has been shown to be the case for PM 7XXX series alloys (150), although transverse properties have been shown to degrade to lower fatigue strengths than in the IM alloy (119). Corrosion fatigue data is not available for any PM 2XXX series alloys, but similar trends are expected. The Alcoa developed alloy CZ20 has been shown to have better fatigue properties than 2014 and similar stress corrosion resistance (65), indicating superior corrosion fatigue properties.

5. CRACK MEASUREMENT TECHNIQUES

For a detailed evaluation of material properties, an accurate measure of slow crack growth is necessary. It is also desirable that the method gives a continuous measurement of crack length and is independent of the test in its application.

There are several available methods for the measurement of crack growth during destructive testing (151). They include optical methods, compliance methods, ultrasonic methods, acoustic emission, Eddy-currents and electrical methods.

Probably the most popular methods are the electrical potential methods (152), as they offer themselves more readily to continuous assessment of crack length. These rely on the fact that the potential distribution in the vicinity of a crack changes with crack growth. Electrical current application is usually symmetrical about the crack plane. Across this, suitably sited probes measure the changing potential associated with crack growth. Two variations of the method are available, namely the A.C. and D.C. techniques. The D.C. (direct current) potential drop method has been used for this project, due to the lower costs and higher stabilty involved, so it will be considered further.

5.1. D.C. POTENTIAL DROP METHOD (153)

Here, a constant D.C. current is passed through the specimen and the change in resistance of the specimen as the crack grows is detected by measuring the change in potential across the open mouth of the starter notch. These measurements of electrical potential are then related to crack lengths or, rather, crack areas, by pre-established calibration curves (152, 154, 155). The choice of calibration can be theoretical (152,155) or experimental (154). These calibration curves are a complex function of specimen geometry, probe position, electrical current and material. Ideally, both should be produced. Due to the fact that there are so many variables involved in theoretical calibrations, and that specimen thickness and notch effect is not taken into account in them, the establishment of an experimental calibration using actual size specimens is essential.

The optimum position for attachment of current leads and potential probes in single edge notched (SEN) bend and compact tension (CTS) test pieces are shown in figure 20. For

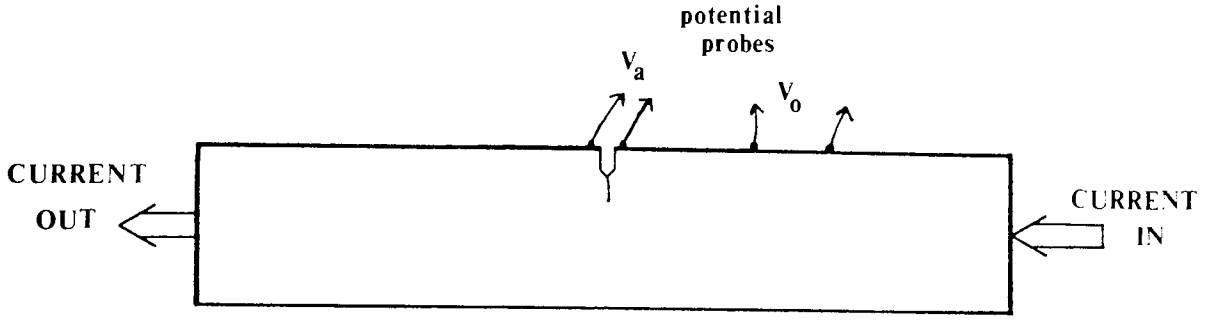

(a) SEN

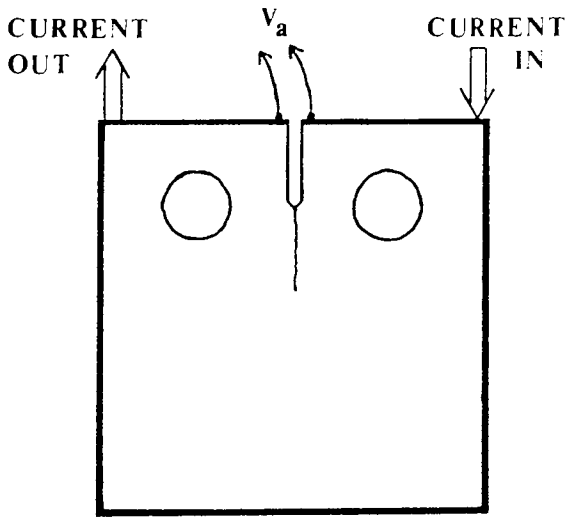

(b) CTS

Figure 20: Optimum positions for current leads and potential measuring probes.

SEN specimens the optimum position for current input is at the specimen ends. The best position for the potential measurement probes is on the top face of the specimen, across the open mouth of the notch. Increased sensitivity is obtained by steepening the potential gradient at the crack plane by placing current leads closer, but the sensitivity to probe position is also increased and non-uniform current flow would result.

The current used depends upon the material under investigation. Aluminium alloys have a higher conductivity than steels, and so need higher current inputs to achieve the same probe potential difference. For the optimum conditions of sensitivity to crack growth and no specimen heating effects a current of 30 to 50 amperes has been shown to be suitable for aluminium alloys (100).

5.1.1. CALIBRATION

In the calibration, potential readings correspond to average crack length values, as the measured potential is characteristic of crack area rather than crack length.

An experimental calibration curve is usually established for the subsequent tests. This is obtained by plotting the measured potential across the crack (V_a) against the crack length (a) using the results of several specimens cracked to different lengths. An alternative method of displaying the results is to plot $V_a/V_o.W$ versus a/W, where V_o is the potential drop per unit length over an uncracked area of the specimen and W is the specimen width. This is a non-dimensional record, allowing calibrations of wider application, for example with different materials and specimen sizes provided that all dimensions are changed in proportion including the location of the current and potential leads.

Theoretical calibrations are based on solutions to Laplace's equation for specific boundary conditions of a given testpiece geometry. From this, Johnson (152) developed a solution to the electrical potential distribution for a sheet of uniform width containing a central, infinitely thin slit.

$$\frac{V_a}{V_0} = \frac{\cosh^{-1}\left(\dfrac{\cosh(\pi y/W)}{\cos(a/W)}\right)}{\cosh^{-1}\left(\dfrac{\cosh(\pi y/W)}{\cos(a_o/W)}\right)} \qquad \ldots.(5.1.)$$

where V = potential difference between two points on the specimen centre line spaced a distance y on either wide of the slit.

a_o = initial half crack length.

a = half-crack length

W = specimen width

A better agreement with experimental data was found by modifying this relationship to apply to an elliptical starting flaw rather than a razor slit (154).

A more detailed two-dimensional solution was developed by Gilbey and Pearson (155), for a sheet of width W containing an edge crack of length a in the X-Y plane (see figure 21). The current input and output points are S and T respectively and the potential drop probes are at points Q and R.

Two specific current flow conditions were considered. For a situation where the current input and output positions are widely spaced the solution approximates to uniform current flow. In this case, the potential across the crack is:

$$V = \mathrm{Im}\left(K_1 . \cos^{-1}\left(\frac{\cos(\pi z/2W)}{\cos(\pi a/2W)}\right)\right) \qquad \ldots.(5.2.)$$

where $z = x + iy$

$$K_1 = \frac{V_o \,.\, 2W}{\pi}$$

(Im = 'imaginary part of')

If the distance between current input and output ($d_1 + d_2$ in figure 22) is small enough,

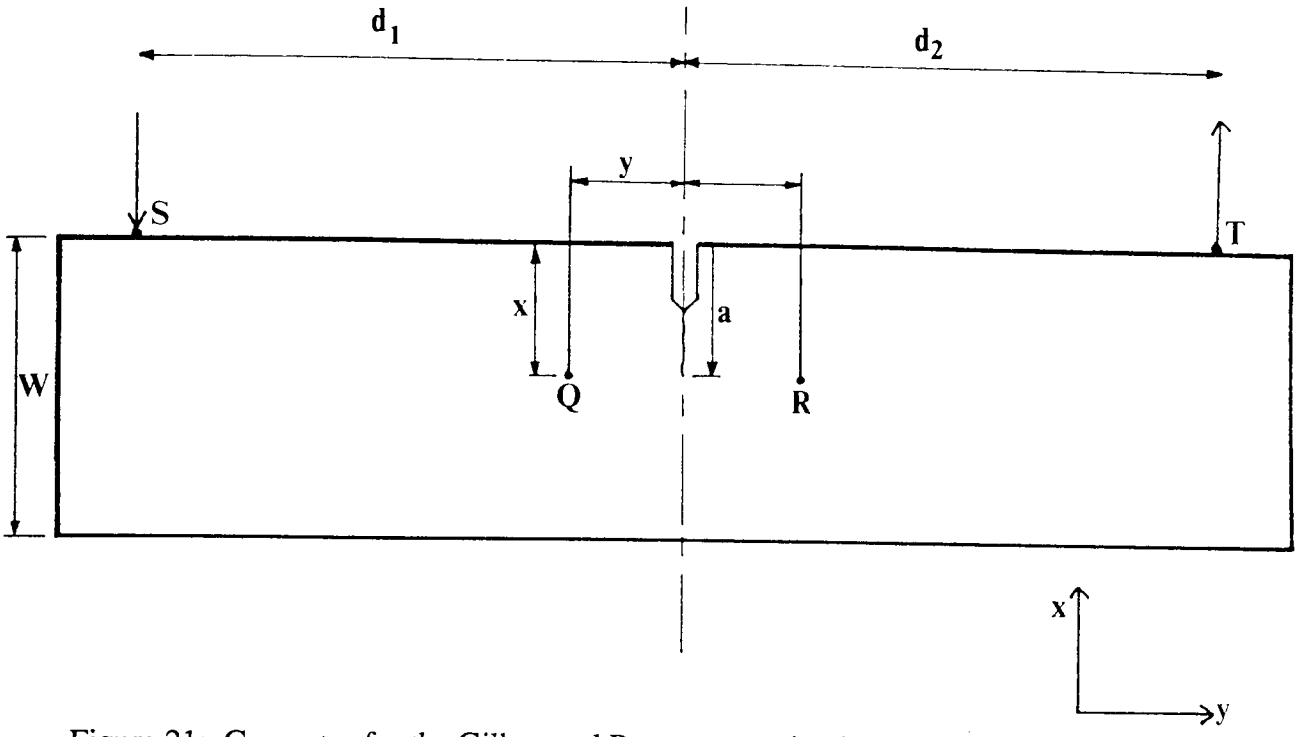

Figure 21: Geometry for the Gilbey and Pearson equation in relation to the specimen.

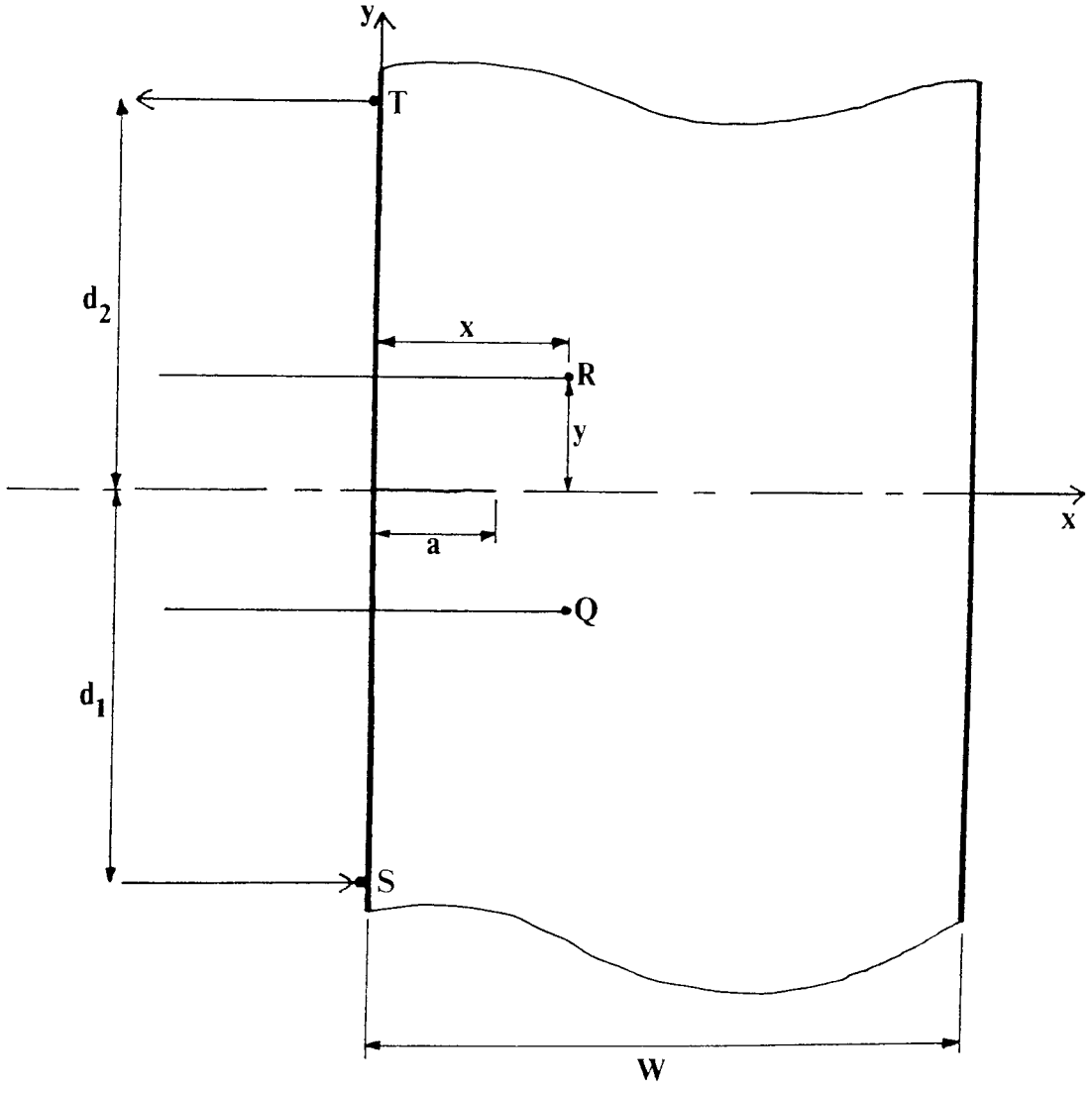

Figure 22: Geometry for the Gilbey and Pearson equation.

non-uniform current flow occurs (ie point application of current).

In this case,

$$V = \mathrm{Re}\left(K_2 \cdot \ln\frac{(\varepsilon + ic)}{(\varepsilon - ic)}\right) \qquad \text{....(5.3.)}$$

where $\varepsilon = (\sec^2(\pi z/2W) \cdot \cos^2(\pi a/2W) - 1)^{1/2}$

$$c = (1 - \cos^2(\pi a/2W) \cdot \mathrm{sech}^2(\pi d/2W))^{1/2}$$

$$K_2 = \frac{V_o \cdot W}{\pi}$$

(Re = 'real part of')

This solution approaches that for uniform current flow as d_1 and d_2 increase.

The Gilbey and Pearson theoretical calibration can be simplified by limiting the potential measurements to the front face only (i.e. x = O). In this case, the solution can be simplified to:

$$a = \frac{2W}{\pi} \cdot \cos^{-1}\left(\frac{1 - B_1^2}{B_2 - B_1 B_3}\right)^{1/2} \qquad \text{....(5.4.)}$$

where $B_1 = \dfrac{(e^{V_a} / 2K_2) - 1}{(e^{V_a} / 2K_2) + 1}$

$$B_2 = \mathrm{sech}^2\left(\frac{\pi y}{2W}\right)$$

$$B_3 = \mathrm{sech}^2\left(\frac{\pi d}{2W}\right)$$

The solution can be further simplified to:

$$a = \frac{2W}{\pi} \cos^{-1}\left(\frac{\cosh(\pi y/2W)}{\cosh(\pi V_a/4V_0W)}\right) \qquad \text{....(5.5.)}$$

As before, the Gilbey and Pearson theoretical calibrations can be used to plot non-dimensional calibration curves of the form V_a/V_oW versus a/W. In this way, calibrations independent of material and current but dependent upon the potential measurement points and current input and output positions are produced.

However, these theoretical calibrations have several limitations.

1. Solutions for only the simplest geometries are available, and it is more usual to carry out calibration tests for the more complex ones.
2. These theoretical calibrations consider cracks to emerge as thin slits from the plane surface of a specimen, whereas most testpiece designs incorporate starter notches to locate and accelerate crack initiation. In this case, the calibration only applies to long crack lengths, where the influence of the notch is negligible. (The electrical potential distribution is considered to be analogous with the stress distribution).
3. The calibration only refers to an average crack length and does not take into account the variations of crackfront shape or multiple cracking.
4. Resistivity changes are brought about by plasticity at the notch tip, leading to uncertainty in initiation and early fatigue crack growth. However, this effect has been considered to be negligible.
5. There is some uncertainty in stress corrosion and corrosion fatigue studies over the possible interference with electro-chemical conditions adjacent to the crack tip. However, it has been claimed that the P.D. technique has been proven successful in a salt water environment (156).

These limitations apply mainly to short crack growth situations, and the electrical potential technique can be successfully used for long crack length measurement where notch effects are negligible, using an experimental calibration backed up by a theoretical one.

6. EXPERIMENTAL PROCEDURE

6.1. MATERIALS

The conventional high strength aluminium alloy that was of interest in this investigation was 2014-T6, supplied as 40mm thick bar. The alloy 2014 is one of the 2XXX series of high strength aluminium alloys, equivalent to the British Standard aerospace alloy L168 (formerly BS L65). The chemical composition of the alloy investigated, along with the compositional limits, is shown in table 2. All material was examined in the T6 temper, which is itemised in table 3. The typical mechanical properties of 2014-T6 are shown in table 4.

The aluminium-lithium alloy investigated was 8090-T6. This alloy was previously given the draft specification DTD YYYA, corresponding to the RAE experimental alloy F92. The chemical composition of the material received, along with the compositional limits, is shown in table 5. The material was supplied as 25mm thick plate in the T8 condition. Details of the T8 heat treatment are itemised in table 6. However, a further heat treatment was given to obtain the T6 condition, shown in table 7.This was because the stretching treatment given in the T8 condition would be impracticable for the uses of the sponsoring company, Dunlop Aviation Ltd., and so only a solution treatment and artificial ageing treatment was given. Typical mechanical properties for 8090-T8 is shown in Table 8. Properties for 8090-T6 were not available in plate form.

The metal matrix composite material was supplied by ICI Mond Ltd., in the form of fibre-reinforced aluminium alloy discs of dimensions shown in figure 23. The fibre reinforcement was in the form of preformed discs of RF grade Saffil fibre. These preforms were infiltrated with liquid aluminium alloy to form the composite material, and supplied in this form (21, 22). 20% and 30% fibre volume fractions of Saffil were investigated, with alloy 6061 being used as the matrix material. The chemical composition of alloy 6061 is shown in table 9. These composite materials were given a heat treatment conforming to 6061-T6, shown in table 10. Typical mechanical properties for 6061-T6 are shown in table 11, but typical mechanical properties for the composite were not available.

The powder metallurgical aluminium alloy under investigation was an Alcoa wrought PM alloy, the developmental alloy CZ20. This is a PM variation of the IM alloy 2014, supplied as a forged billet, 75mm thick. The chemical composition of the alloy investigated, along with the nominal composition, is shown in table 12. CZ20 was investigated in the T6 condition, which is itemised in table 13. Unfortunately, the full heat treatment details could not be released by Alcoa. Typical mechanical properties for CZ20-T6 are shown in table 14.

Element	Percentage (by Weight)		
	Min	Max	Actual
Copper	3.9	5.00	4.18
Silicon	0.5	0.90	0.78
Manganese	0.4	1.20	0.78
Magnesium	0.2	0.80	0.47
Iron	---	0.50	0.43
Chromium	---	0.10	0.06
Nickel	---	0.10	---
Zinc	---	0.25	0.06
Titanium	---	0.15	0.03
Ti + Zr	---	0.20	0.03
Others: each	---	0.05	---
Others: total	---	0.15	---
Aluminium	---	Rem	Rem

Table 2: Chemical composition of BS L168.

Solution	Treatment	505 ± 5°C	for 4hrs
Water	Quench	< 40°C	
Artificial	Ageing	175 ± 5°C	for 12hrs
Air	Cool		

Table 3: T6 heat treatment for BS L168.

	0.2% PS (MPa)	UTS (MPa)	Elongation (%)	K_{IC} ($MN.m^{-3/2}$)	E (GPa)
Minimum	440	490	7	---	---
Typical	465	500	10	30	71

Table 4: Mechanical properties of BS L168 (2014-T6).

Element	Percentage (by Weight)		
	Min	Max	Actual
Lithium	2.2	2.7	2.50
Copper	1.0	1.6	1.19
Magnesium	0.6	1.3	0.68
Iron	---	0.30	0.11
Silicon	---	0.20	0.04
Chromium	---	0.10	---
Manganese	---	0.10	---
Zinc	---	0.25	---
Titanium	---	0.10	0.028
Zirconium	0.04	0.16	0.10
Sodium	---	0.002	< 0.001
Aluminium	---	Rem	Rem

Table 5: Chemical composition of 8090.

Solution Treatment	525 ± 5°C for 1hr.
Water Quench	≤ 40°C
Cold Stretch	2.5%
Artificial Ageing	190°C for 1hr.
Air Cool	

Table 6: T8 heat treatment for 8090.

Solution Treatment	525 ± 5°C for 1hr
Water Quench	< 40°C
Artificial Ageing	190°C for 24hrs
Air Cool	

Table 7: T6 heat treatment for 8090.

Orientation		0.2% PS (MPa)	UTS (MPa)	Elongation (%)	K_{IC} ($MN.m^{-3/2}$)	E (GPa)
Longitudinal	Minimum	410	460	5	30	---
	Typical	450	495	6	37	79
L. Transverse	Minimum	390	450	5	25	---
	Typical	420	480	7	33	79
S. Transverse	Minimum	365	420	2.5	18	---
	Typical	365	435	2	16	---

Table 8: Mechanical properties of 8090-T8.

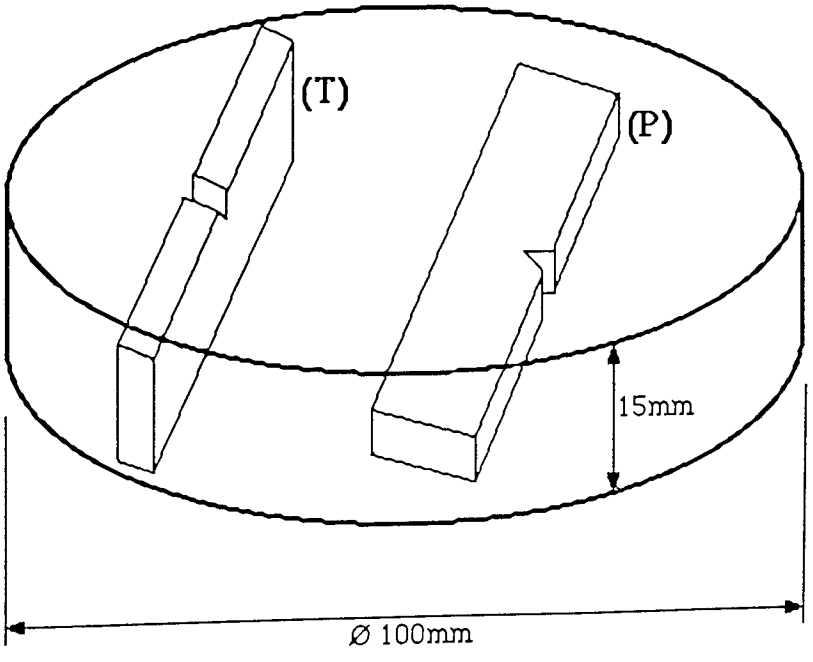

Figure 23: Saffil-reinforced aluminium alloy discs.

Element	Percentage (By Weight)		
	Min	Max	Actual
Magnesium	0.80	1.20	1.0
Silicon	0.40	0.80	0.6
Copper	0.15	0.40	0.2
Iron	---	0.70	---
Manganese	---	0.15	---
Chromium	0.04	0.35	0.25
Zinc	---	0.25	---
Titanium	---	0.15	---
Others: Each	---	0.05	---
Others: Total	---	0.15	---
Aluminium	---	Rem	Rem

Table 9: Chemical composition of 6061.

Solution Treatment	530 ± 5°C for 95mins
Water Quench	< 40°C
Artificial Ageing	160 ± 5°C for 18hrs
Air Cool	

Table 10: T6 heat treatment for 6061.

	0.2% PS (MPa)	UTS (MPa)	Elongation (%)	E (GPa)
Minimum	240	280	8	---
Typical	280	310	13	71

Table 11: Mechanical properties of 6061-T6.

Element	Weight Percentage	
	Typical	Actual
Copper	4.5	4.67
Silicon	1.0	1.10
Manganese	1.0	1.04
Magnesium	0.5	0.42
Iron	---	0.02
Titanium	---	< 0.01
Zinc	---	0.02
Zirconium	0.4	0.52

Table 12: Chemical composition of CZ20.

Solution Treatment	
Water Quench	< 40°C
Artificial Ageing	
Air Cool	

Table 13: T6 heat treatment for CZ20.

	0.2% PS (MPa)	UTS (MPa)	Elongation (%)	K_{IC} ($MN.m^{-3/2}$)
Tangential	392	472	13.3	29.6
Axial	387	462	10.5	---
Radial	381	461	13.5	28.3

Table 14: Typical mechanical properties of CZ20-T6.

6.2. SPECIMEN AND TEST DESIGN

Specimen orientation relative to the grain flow of the material is explained in figures 24 and 25. A two-letter code describes the orientation, the first letter indicating the specimen axis and the second letter the direction of crack growth. This coding system can be applied to plate (figure 24) or forgings (figure 25). 2014-T6 was investigated in the L-S orientation, 8090-T6 was studied in the L-S, L-T and T-L orientations and CZ20-T6 in the C-L and C-R orientations. Specimen orientation in Saffil-reinforced 6061-T6 is described in terms of whether the crack growth direction is in the plane of the composite disc (P) or through its thickness (T), as shown in figure 23.

In all cases, specimen dimensions were chosen to satisfy the conditions for plane strain under cyclic loading. For plane strain conditions to apply, the crack tip plastic zone size, r_y, has to be less than 2% of the specimen thickness, B. The cyclic plastic zone size, r_y^c, is a quarter of the monotonic plastic zone size, r_y, and so equation 3.9. can be adapted to take this into account. If the specimen thickness has to be more than 50 times larger than the plastic zone size, then:

$$B > \frac{50}{4 \times 5.6\pi} \left(\frac{K_{IC}}{\sigma_{ys}}\right)^2 \qquad \ldots.(6.1.)$$

for plane strain conditions to apply. For 2014-T6, 8090-T6 and CZ20-T6 a thickness of at least 5mm is required, and at least 3mm for Saffil-reinforced 6061-T6.

For all fatigue and corrosion fatigue work a sinusoidal waveform was used. Air fatigue testing was conducted in laboratory air, at a frequency of 20Hz. Corrosion fatigue testing was conducted in a salt water (3.5% NaCl) solution, at a frequency of 10Hz. All testing was conducted at ambient temperature.

6.2.1. FATIGUE LIFE

For fatigue and corrosion fatigue life (cycles to specimen failure) testing of 2014-T6 and 8090-T6, rotating beam specimens were used, as shown in figure 26. These specimens were tested about a zero mean stress, so that R=-1.0 (R is the ratio of minimum to maximum

stress in the fatigue cycle). The stress concentration factor, K_t, for this specimen was calculated to be 1.02 (157). The specimens were designed so that for every 2lb of weight hung on the load pan a stress of 1tsi was exerted on the specimen. The specimens were labelled as R65XX for 2014-T6 and R92XX for 8090-T6, XX being the individual specimen number.

6.2.2. FATIGUE CRACK INITIATION

For the fatigue and corrosion fatigue crack initiation testing of 2014-T6 and 8090-T6, pure (4-point) bend specimens were used, as shown in figure 27a. These specimens were tested with an R-ratio of 0.45. The depths and root radii of all notches were checked using a Nikon Shadowgraph, Model 5a. The notch root radii were calculated by assuming the notch root to be part of a circle. Then,

$$\rho = \frac{a^2 + b^2}{2bm} \qquad \ldots.(6.2.)$$

where ρ is the notch root radius, m is the magnification of the image, and a and b are shown in figure 28. All of the specimens were polished with a 1μm abrasive pad to minimise the effect of any surface roughness.

The stress required for initiation was quantified by both stress concentration methods and fracture mechanics methods. The stress concentration factor, K_t, for these specimens was calculated to be 1.49 (157). The fibre stress range, Δs, at the root of the notch was calculated using:

$$\Delta s = \frac{9.\Delta P.W}{2B(W - a)^2} \qquad \ldots.(6.3.)$$

where ΔP = load range.

a = notch depth.

For the case of pure bending the solution of Tada (158) was used to calculate the stress

intensity at crack initiation. From equation 3.6.,

$$K_I = \sigma\sqrt{(\pi a)} \cdot f(a/W)$$

where K_I = stress intensity factor in mode I cracking.

$$\sigma = \text{bending stress} = \frac{6M}{BW}$$

M = bending moment in the specimen.

The K-calibration, f(a/W), is given as:

$$f(a/W) = \left(\frac{2W}{\pi a}\tan\frac{\pi a}{2W}\right)^{1/2} \times \frac{0.923 + 0.199(1 - \sin(\pi a/2W))^4}{\cos(\pi a/2W)} \qquad \ldots.(6.4.)$$

A modified version of this K-calibration factor, to measure the effective stress intensity at the root of the notch, was calculated using equation 3.22.

In engineering terms, crack initiation in commercial aluminium alloys has been shown to correspond to a crack length of 0.127mm (96). The presence of a crack of this length was therefore used as the definition of crack initiation. This crack depth was related to a change in potential difference, using the experimental electrical potential calibration, so that crack initiation could be defined as a deviation from the steady potential across the notch on the chart recorder.

The specimens were labelled as 65XX for 2014-T6, 92XX for 8090-T6 (L-S), 93XX for 8090-T6 (L-T) and 94XX for 8090-T6 (T-L). XX was the individual specimen number.

6.2.3. FATIGUE CRACK PROPAGATION

For the fatigue and corrosion fatigue crack propagation testing of 2014-T6 and 8090-T6, the same specimens were used as those for crack initiation testing of these materials. All specimens had a sharp notch machined in the bottom of the smooth notch, to direct the propagating crack, as shown in figure 27b. In addition, side-grooves were machined on the 8090-T6 specimens which were longitudinally orientated with crack growth in the short transverse direction (L-S specimens), as shown in figure 27c. This was done to stop the

crack deviation found in un-side-grooved specimens of this type, which will be explained more fully in a later section. 5% side-grooves were found to be sufficient. The specimens were tested in three-point bending for crack propagation work, with R values of 0.1 and 0.45. The ratio of 0.1 was chosen so that the minimum stress in the fatigue cycle was as close to zero as possible. The R ratio of 0.45 was recommended as being the closest constant amplitude fatigue cycle to a real life aircraft stress waveform.

For the case of three-point bending with a span to width ratio of 4:1, the solution of Walker and May (79) was used to calculate the stress intensity during crack propagation. The K-calibration, f(a/W), is given as:

$$f(a/W) = 1.93(a/W)^{1/2} - 3.07(a/W)^{3/2} + 14.53(a/W)^{5/2} - 25.11(a/W)^{7/2} + 25.80(a/W)^{9/2} \quad \ldots.(6.5.)$$

$$\text{where } K_I = \frac{f(a/W) \times 6M}{B.W^{3/2}}$$

The load ranges used in fatigue and corrosion fatigue testing were calculated from this solution. It was not possible to measure the fatigue crack growth rates for the whole range of stress intensity factor ranges, ΔK, with one specimen. Therefore, load ranges were chosen to give an overlapping selection of stress intensity ranges in different specimens. A constant load range, ΔP, was applied for each test.

For the fatigue and corrosion fatigue testing of CZ20-T6 and 2014-T6 (again, for comparison of propagation data from both specimen designs), three-point bend specimens were used, as shown in figure 29. The Walker and May solution was again used to calculate the stress intensity during crack propagation. R values of 0.1 and 0.45 were used.

For the fatigue crack propagation testing of Saffil-reinforced 6061-T6, the specimen dimensions in figure 30 were used. The specimens were once more tested in three-point bending, the Walker and May K-calibration being used. R values of 0.1 and 0.45 were used.

All fatigue and corrosion fatigue crack propagation data was taken outside the notch

affected area of the specimens. The critical crack length, C_o, under which the fatigue crack propagation rate is affected, was calculated as $0.5\sqrt{(a_o\rho)}$ (106). This critical crack length was under 0.5mm for all of the sharp notched specimens. However, a critical crack length of 3.5mm was calculated for the smooth notched specimens that had been used for crack initiation testing. Accordingly, no propagation data was used under this notch-affected crack depth.

The same labels were used for 2014-T6 and 8090-T6 smooth notched specimens (65XX for 2014-T6, 92XX for 8090-T6 (L-S), 93XX for 8090-T6 (L-T) and 94XX for 8090-T6 (T-L)). Labels for the sharp notched specimens were CXX for 2014-T6, AXX for CZ20-T6 (C-L), RXX for CZ20-T6 (C-R), 20XX for 20% Saffil-reinforced 6061-T6 and 30XX for 30% Saffil-reinforced 6061-T6.

A seven-point polynomial method was used to calculate the fatigue crack growth rate (da/dN) from the values of a and N, a modified version of the reduction technique recommended in ASTM E647 (159). A computer program developed to produce values of da/dN and ΔK from inputted values of V_a and N (along with specimen dimensions, load range and an expression which converts readings of V_a to a (the experimental calibration)) is listed in Appendix 1.

6.2.4. OTHER MECHANICAL TESTING

The Saffil-reinforced composite materials are only recently developed, and so basic mechanical properties had to be evaluated. No.14 Hounsfield tensile specimens, shown in figure 31, were machined from spare material to investigate these tensile properties. Tensile tests were also conducted on 2014-T6, 8090-T8, 8090-T6 and CZ20-T6 as a material quality control check.

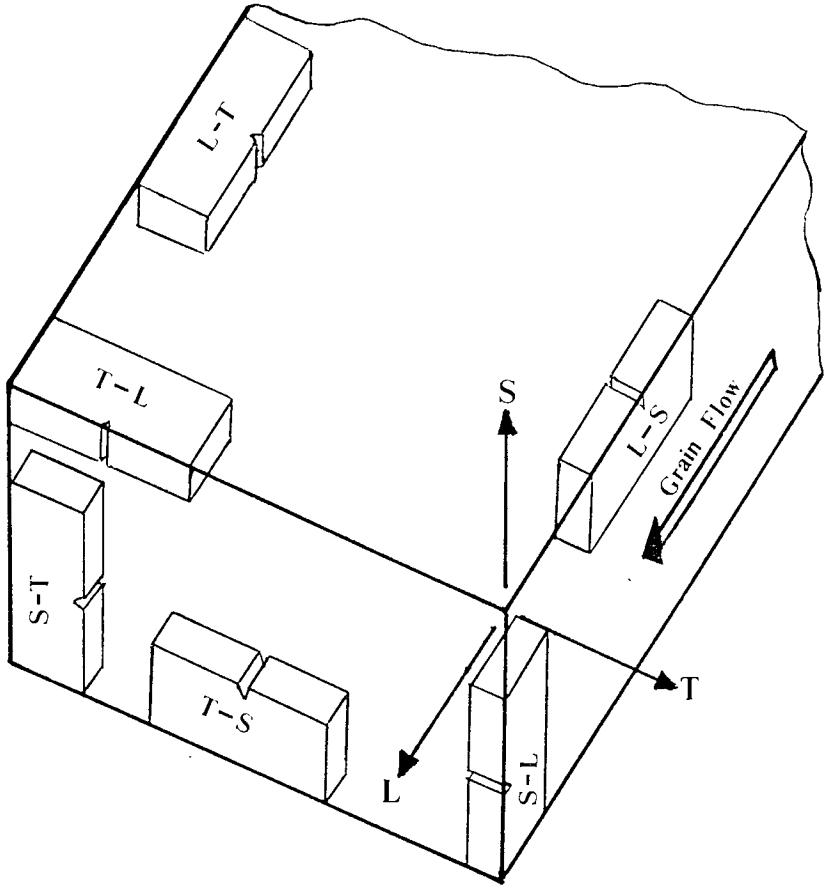

Figure 24: Specimen orientation relative to grain flow for plate.

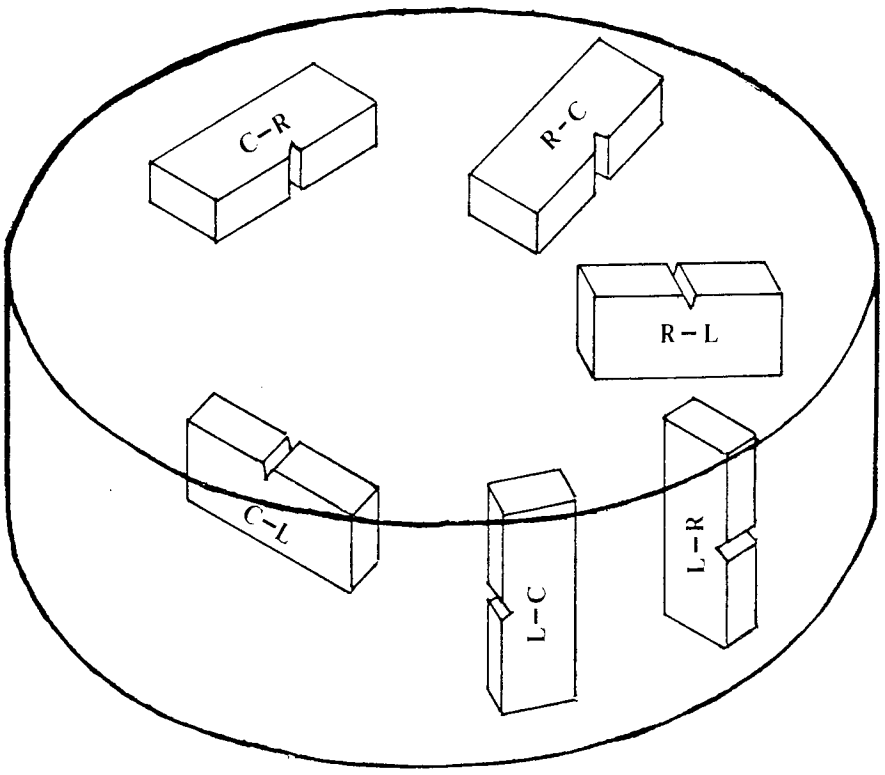

Figure 25: Specimen orientation relative to grain flow for forgings.

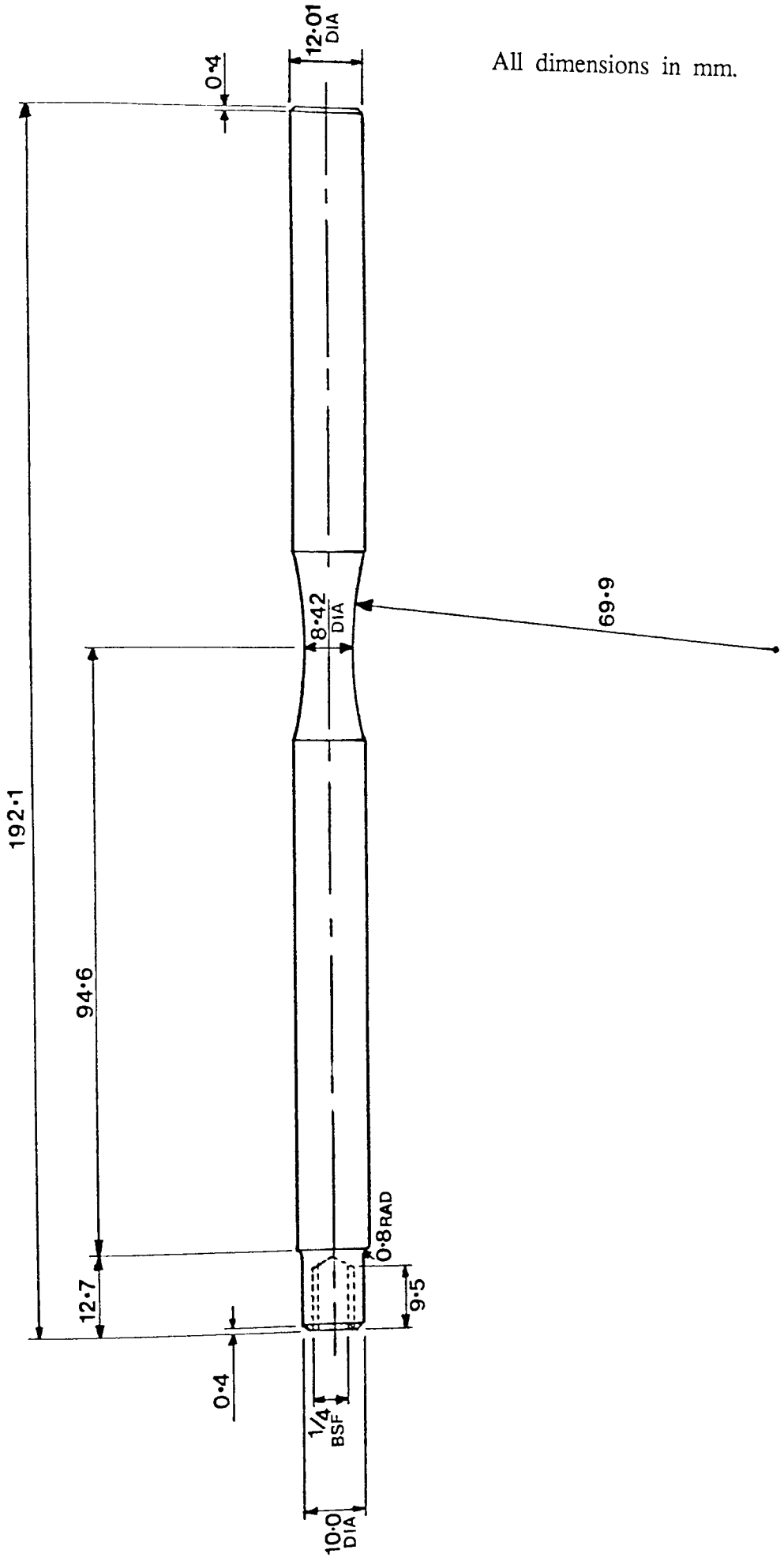

Figure 26: Rotating beam specimen dimensions.

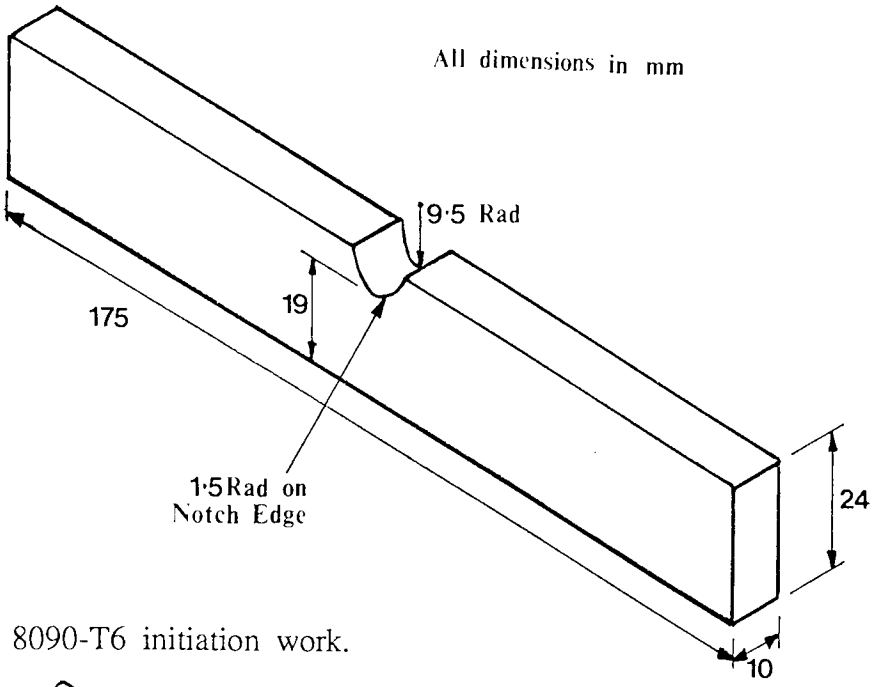

(a): 2014-T6 and 8090-T6 initiation work.

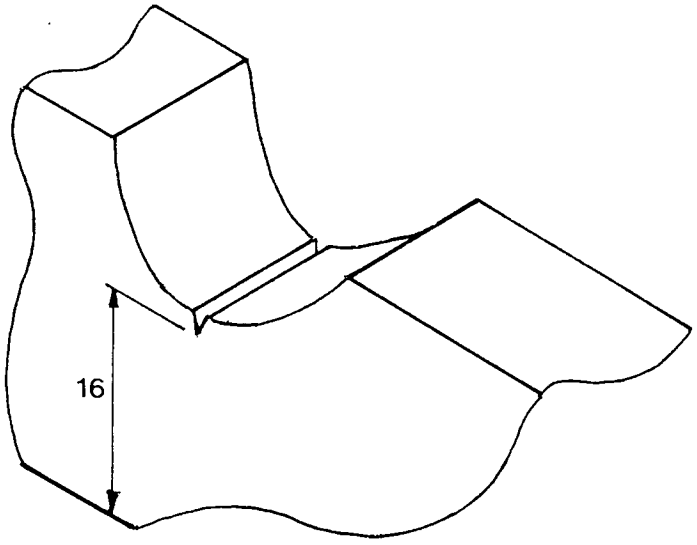

(b): Sharp notch for 2014-T6 and 8090-T6 propagation work.

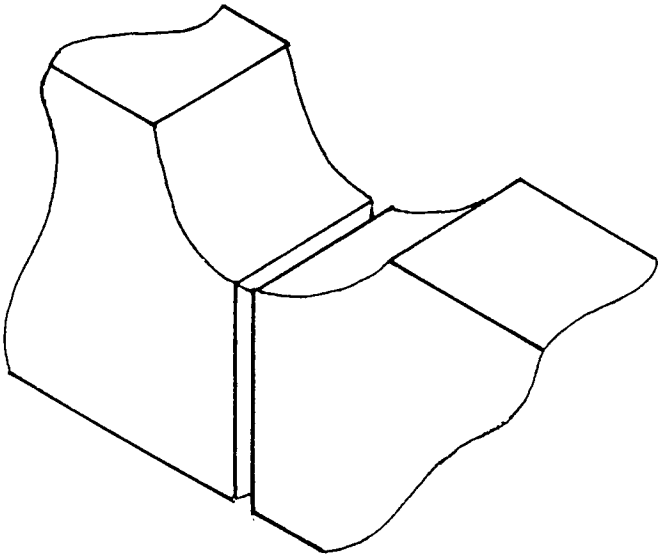

(c): Sharp notched and side-grooved 8090-T6(L-S) specimens.

Figure 27: 2014-T6 and 8090-T6 smooth notched specimen dimensions.

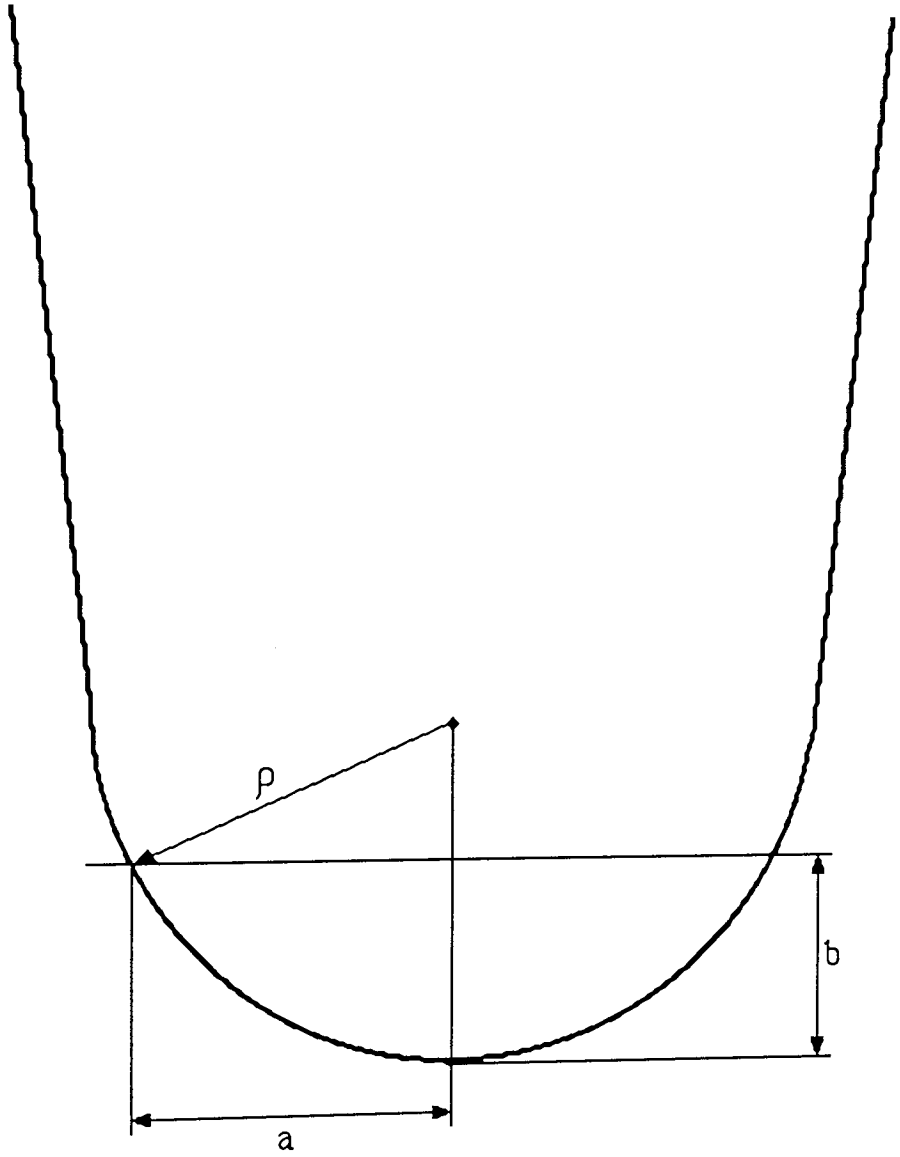

Figure 28: Measurement of notch root radius.

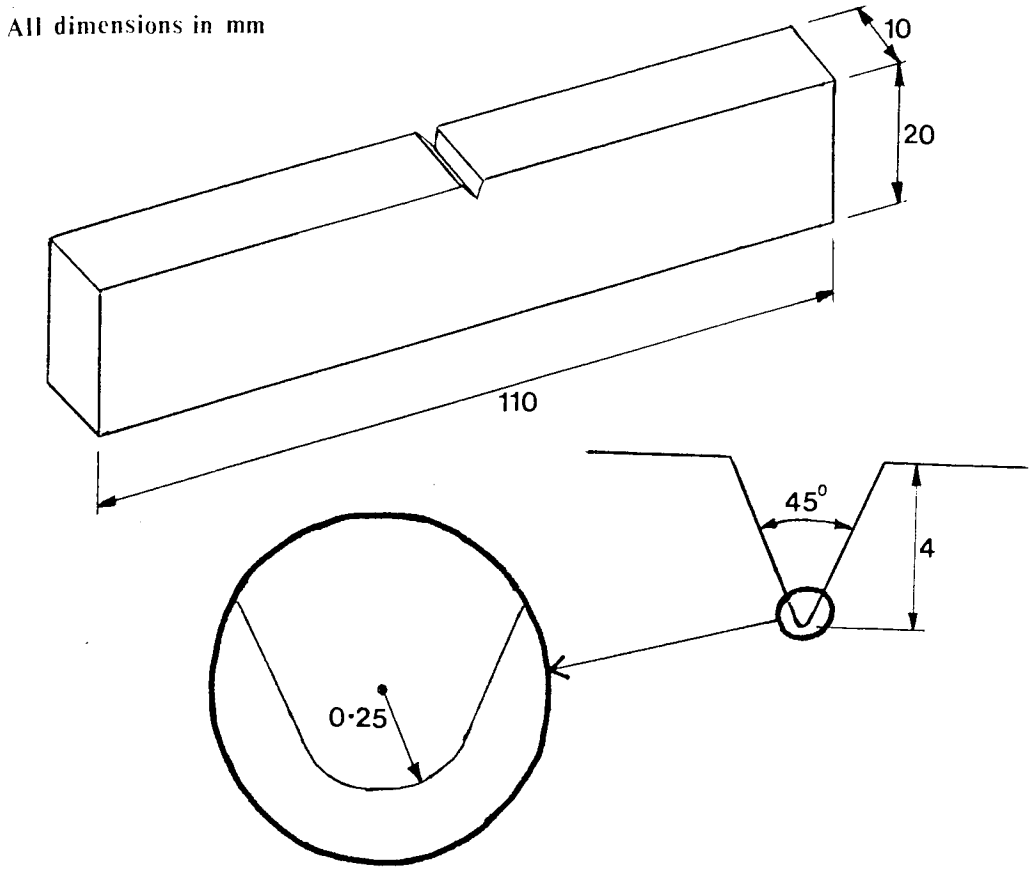

Figure 29: CZ20-T6 and 2014-T6 sharp notched specimen dimensions.

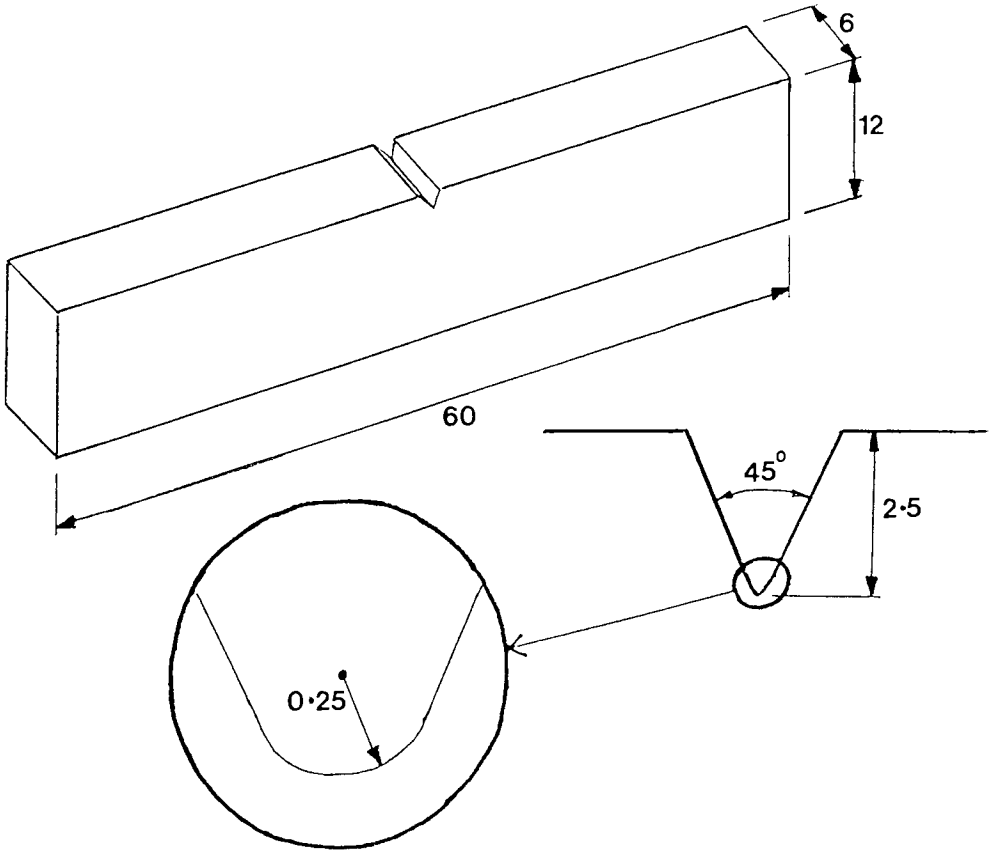

Figure 30: Saffil-reinforced 6061-T6 specimen dimensions.

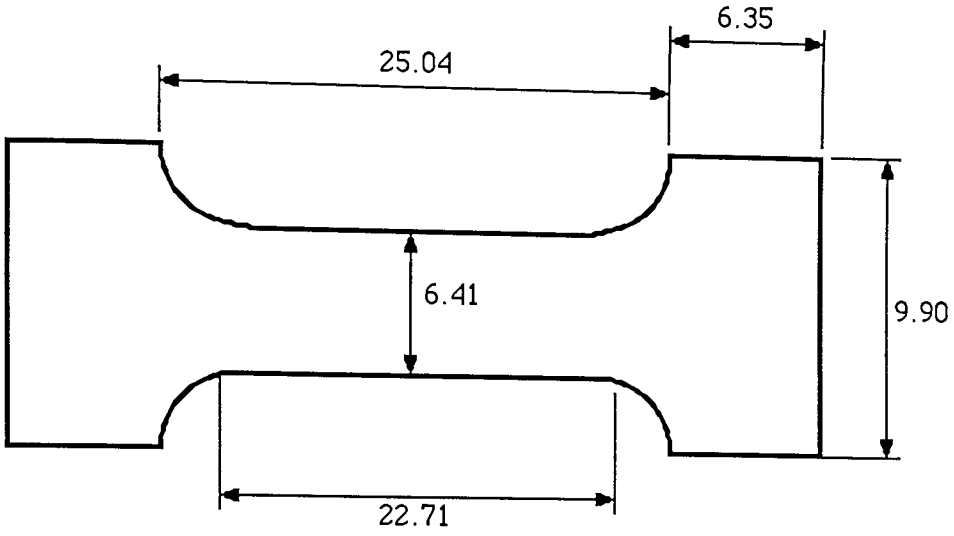

Figure 31: No. 14 Hounsfield tensile specimen dimensions.

6.3. EQUIPMENT

6.3.1. TESTING EQUIPMENT

All fatigue and corrosion fatigue life testing on 2014-T6 and 8090-T6 was carried out on an Avery 7304 dynamic fatigue testing machine. The machine is motor driven, the rotating specimens acting as a loaded beam, as shown in figure 32. The rotation of the specimens, at 50Hz, leads to an alternating stress of sinusoidal waveform being applied, with a zero mean stress and the maximum stress in tension equalling the minimum stress in compression (R=-1.0). For corrosion fatigue life testing a weeping wick arrangement was used, as shown in figure 33, and schematically in figure 34. A bulk 3.5% NaCl solution supplies a felt wick, which drips solution onto the notched part of the specimen. The rotational speed of the specimens, 3000rpm or 50Hz, also causes a salt mist in the corrosion chamber.

All fatigue and corrosion fatigue crack initiation and propagation testing on 2014-T6, 8090-T6 and CZ20-T6 was carried out on a Servotest 177-F8 50kN electrohydraulic fatigue machine, as shown in figure 35. Fatigue crack propagation testing on Saffil-reinforced 6061-T6 was carried out on an ESH 50kN electrohydraulic machine, shown in figure 36. These machines make use of an electrohydraulic control system. They are regulated by a load cell or a stroke transducer, which controls a servo valve governing the oil flow. In both cases, the fatigue machine was switched on for at least 30 minutes before the start of a test. This was necessary to ensure complete thermal and electrical stabilisation of the electrical and electronic systems.

For corrosion fatigue crack initiation and propagation testing, a corrosion tank was fitted to the Servotest fatigue machine, as shown in figure 37, and schematically in figure 38. Specimens were totally immersed in a 3.5% NaCl solution.

Tensile testing of Saffil-reinforced 6061-T6 was carried out on a 50 tonne capacity Instron testing machine. A crosshead speed of 0.05 cm/min was chosen to give a slow enough strain rate.

6.3.2. CRACK MONITORING EQUIPMENT

For fatigue and corrosion fatigue crack initiation and propagation testing, fatigue crack length was measured using the electrical potential method.

Figures 39 and 40 show the probe locations and circuit diagram for the electrical potential method. The constant current supply necessary for this method was supplied by a Farnell Power Supply. For the 2014-T6, 8090-T6 and CZ20-T6 specimens a current of 30A was chosen so as to obtain maximum sensitivity and minimal heating in the specimen. For Saffil-reinforced 6061-T6 a current of 8A was chosen, for the same reasons. A lower current was chosen in this case because the specimens were smaller and the material has a higher resistivity, which increases sensitivity and heating effects. The current was introduced into the specimen from its two ends by toolmakers clamps covered with 1mm thick annealed electrical purity copper. The specimen was electrically insulated from the test machine before testing.

The electrical potential was measured by 0.193mm diameter nichrome probe wires, spot-welded at either side of the notch opening for maximum sensitivity. The potential drop between these probe wires was backed off by a DC voltage calibration unit, and then fed into a Tekman 200 chart recorder. For maximum sensitivity in measuring crack growth a full scale deflection of 50μV was used on the chart recorder.

Current was allowed to pass through the specimen for at least 30 minutes before the fatigue test began, to allow time for the chart recorder and specimen temperature to stabilise. During fatigue testing the back-off voltage and chart speed were adjusted as crack length increased, in order to produce a satisfactory record of voltage against time.

Experimental calibration of the electrical potential method was by measurement of the equivalent crack length and potential increment at fracture of several specimens. Equivalent crack length was calculated by taking an average of five measurements of fatigue crack length across a broken specimen, using a travelling microscope. The potential increment is the change in potential drop between the uncracked specimen and the fractured specimen. The experimental calibration could then be represented either as a graph of crack length, a, versus potential increment, ΔV, or in a non-dimensional form. Equation 5.5. suggests that a/W would be a function of V/V_0W. Therefore, the non-dimensional experimental calibration

would be in the form of a/W versus V_a/V_oW, where a is the total crack length (notch depth plus crack length) and V_a is the corresponding potential across the probe wires. The potential V_o was measured by placing probe wires across an unnotched section of the specimen, 10mm apart, and measuring the potential difference per millimetre of specimen length.

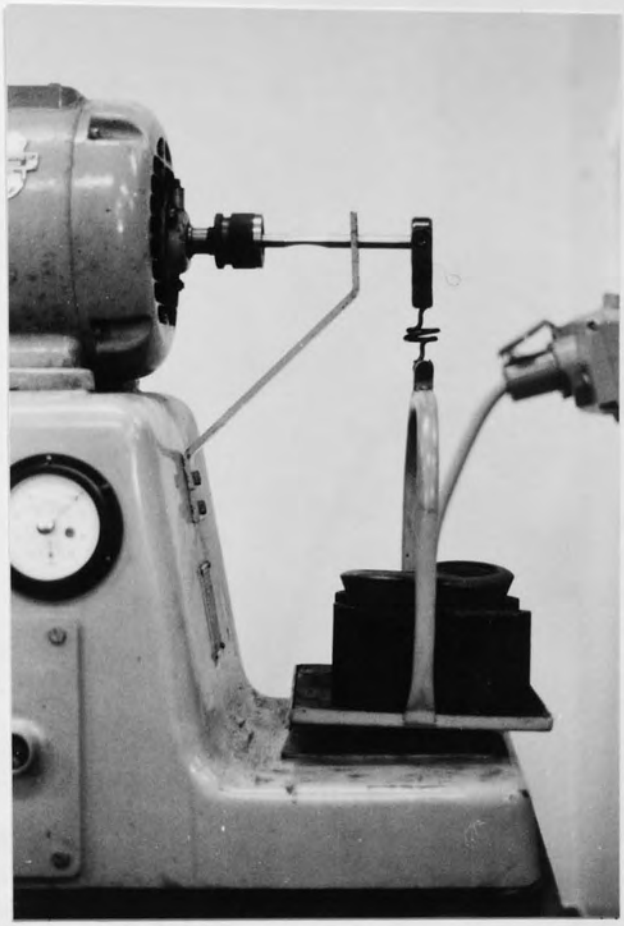

Figure 32: Avery 7304 dynamic fatigue testing machine.

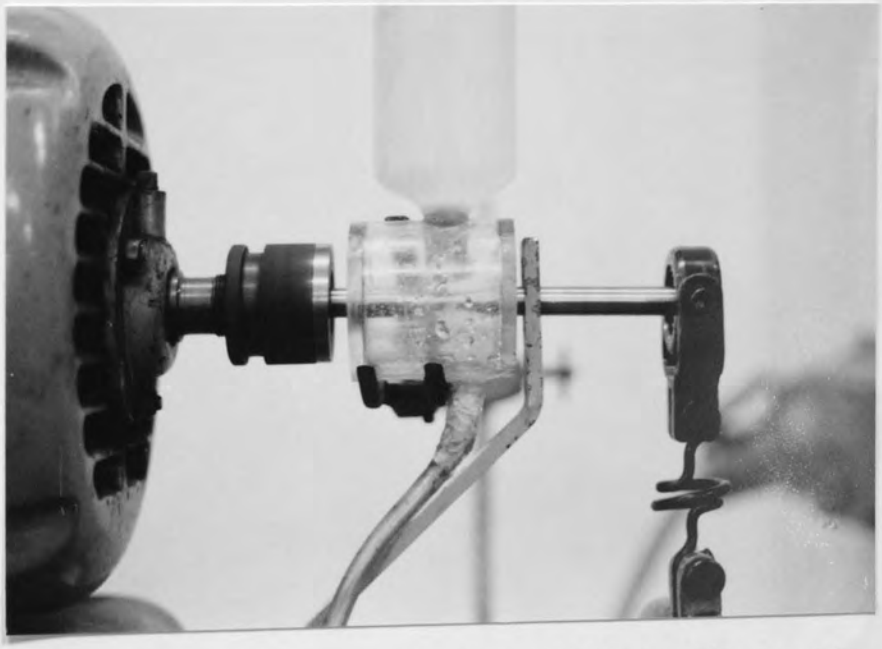

Figure 33: Corrosion fatigue set-up on the Avery fatigue testing machine.

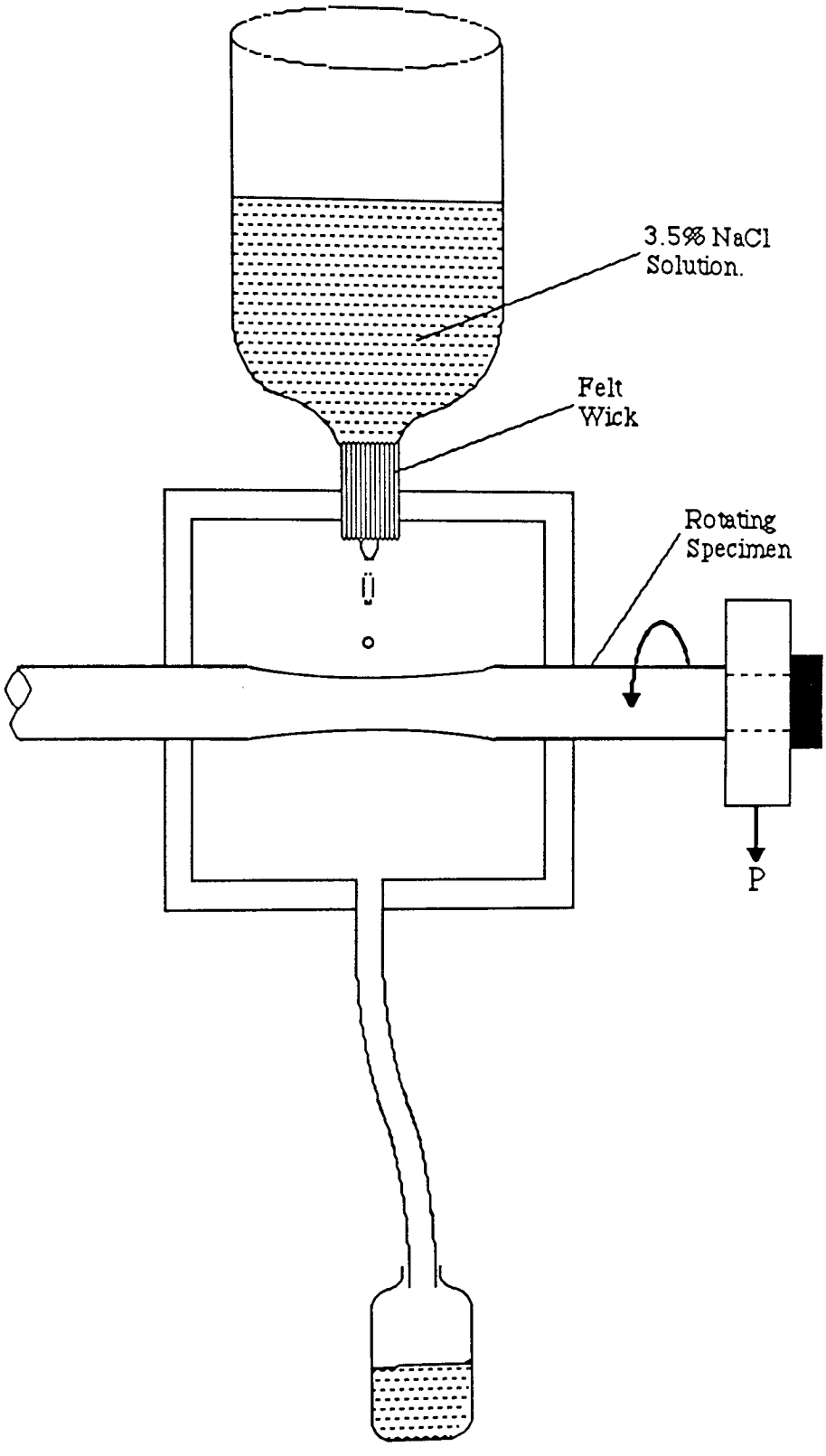

Figure 34: Corrosion fatigue set-up on the Avery fatigue testing machine.

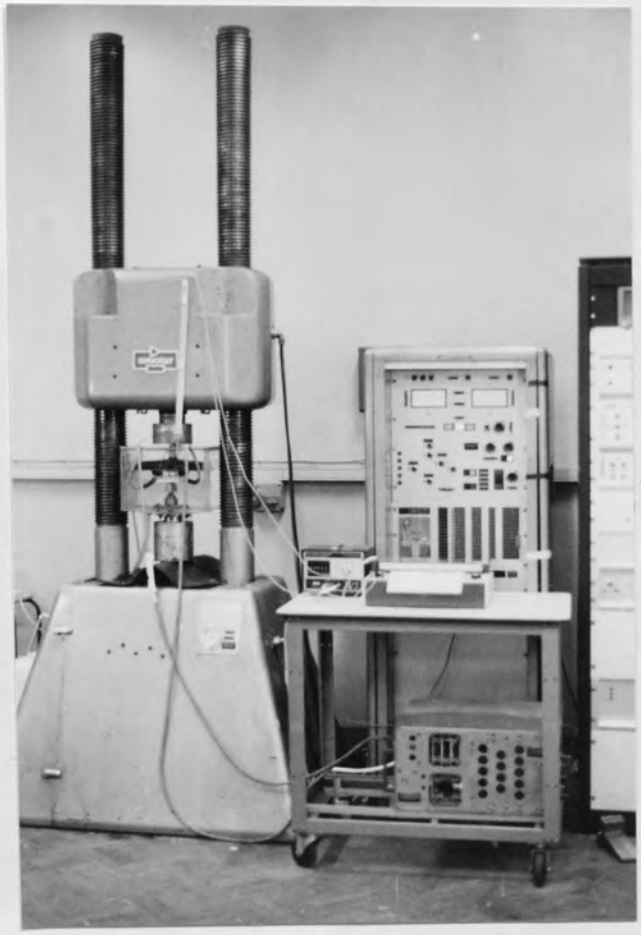

Figure 35: Servotest 177-F8 50kN electrohydraulic fatigue testing machine.

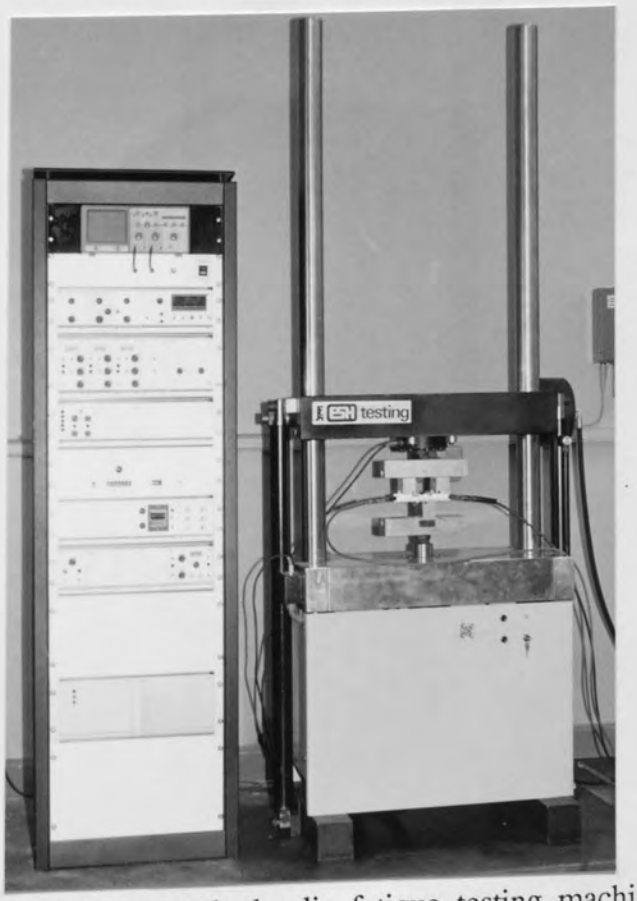

Figure 36: ESH 50kN electrohydraulic fatigue testing machine.

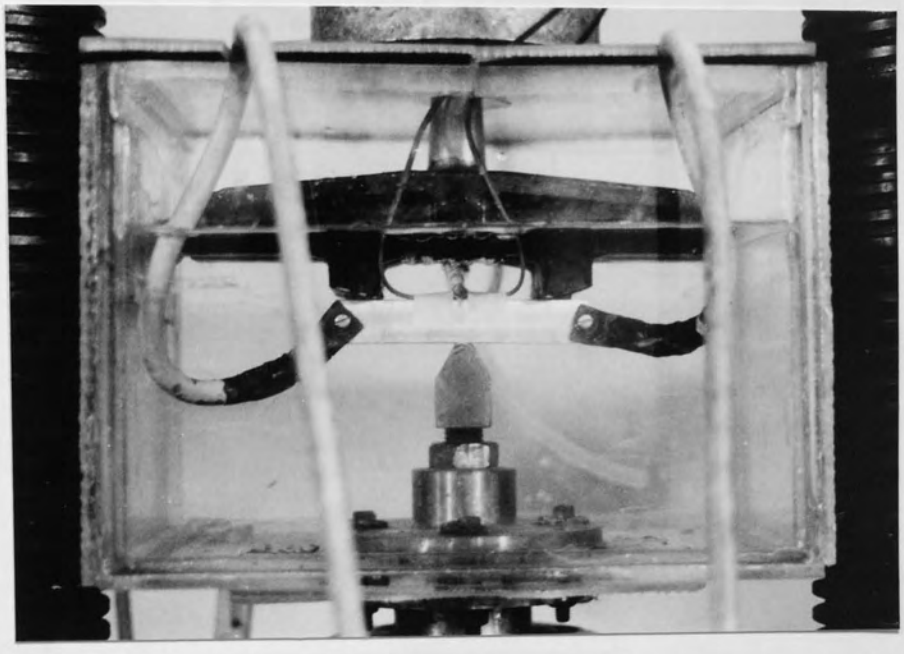

Figure 37: Corrosion fatigue set-up on the Servotest fatigue testing machine.

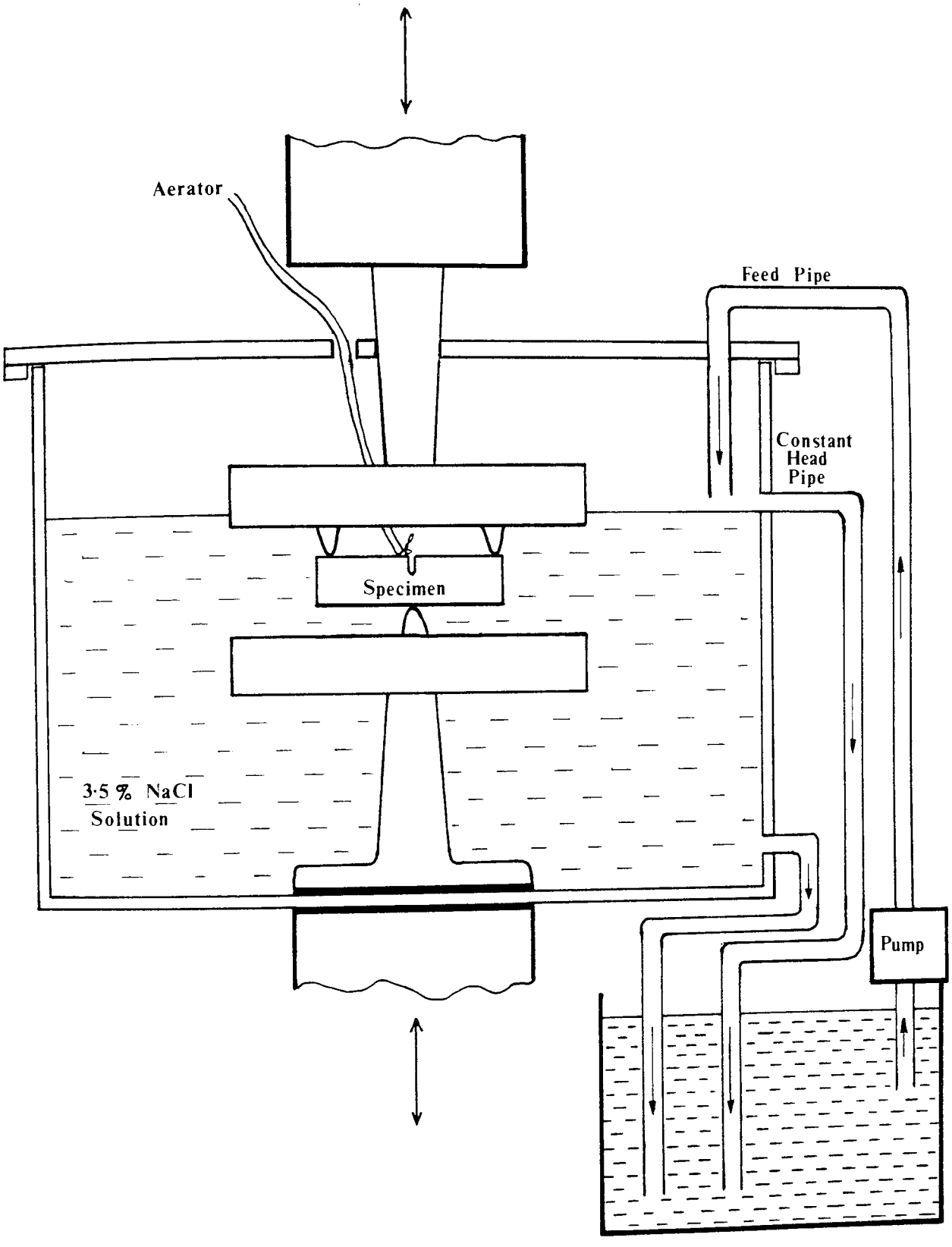

Figure 38: Corrosion fatigue set-up on the Servotest fatigue testing machine.

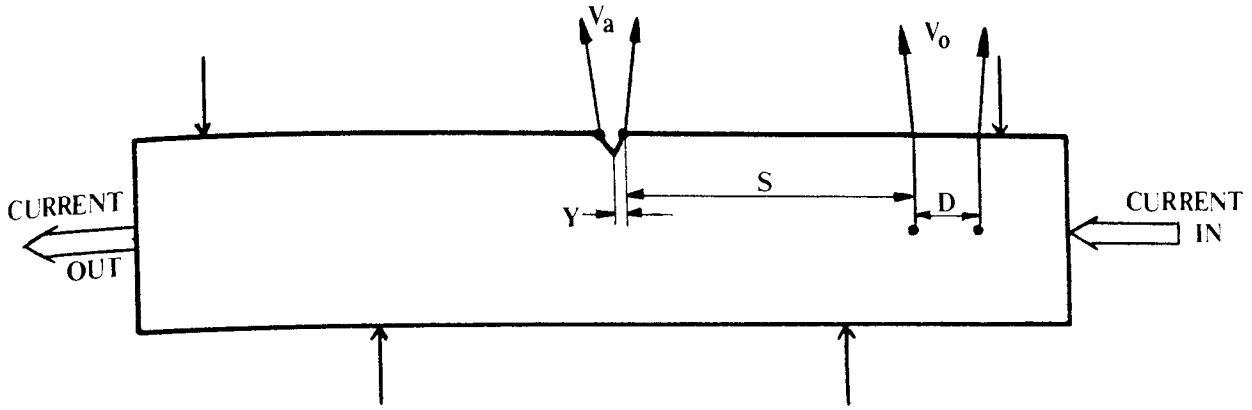

Figure 39: Probe location for the electrical potential method.

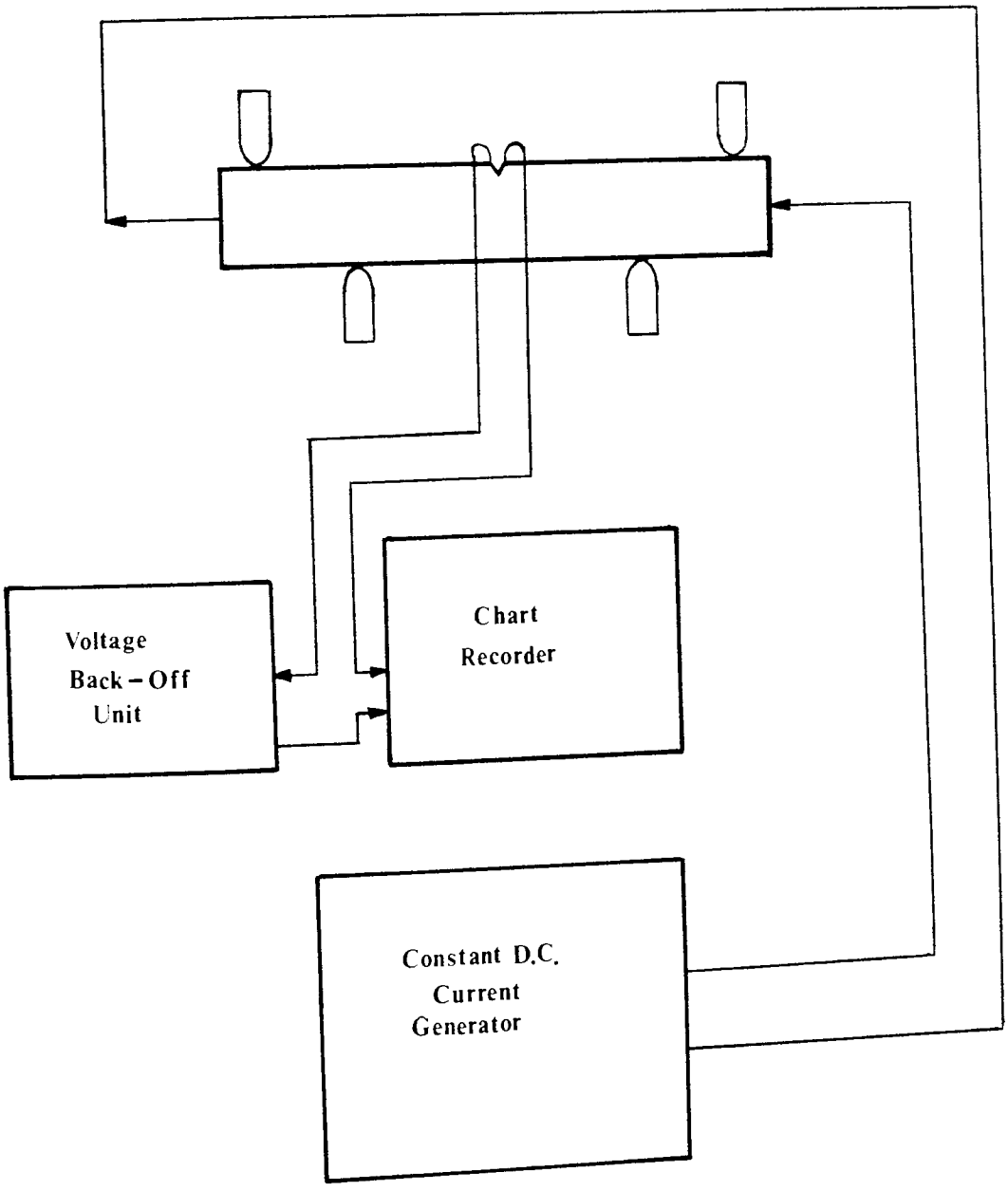

Figure 40: Electrical potential difference system.

6.4. METALLOGRAPHY

Specimens were taken from all of the alloys for metallographic examination. All orientations were prepared and examined, by polishing to a 1μm diamond polish and etching in Kellers reagent (1 vol% HF, 1.5 vol% HCl, 2.5 vol% HNO_3, 95 vol% H_2O). Examination was by optical metallography, with some electron microscopy of the Saffil-reinforced 6061-T6.

Fracture surfaces were examined by both optical metallography and scanning electron microscopy. Optical micrographs of broken specimens were produced to aid in crack length measurement, while electron microscopy was used for more detailed examination, where the features of the crack initiation sites and the fracture surfaces from the slow crack growth region to the final fast fracture region were examined.

7. RESULTS

7.1. ELECTRICAL POTENTIAL CALIBRATION

The results of the experimental electrical potential calibration are shown in figure 41, where the curves are presented as V_a/V_0W versus a_0+c/W (V_a is the change in potential drop with crack growth, V_0 is the potential drop per unit length of uncracked specimen, W is the specimen width, a_0 is the notch depth and c is the crack depth at which the change in potential was measured). This is the non-dimensional form of the electrical potential calibration. V_0 was taken for each specimen. c was measured as an average crack depth, by measuring the crack length at five positions along the crack front and taking the arithmetic mean. This was done because the crack fronts were found to be uneven, as shown in later figures. The calibration therefore only measures crack lengths that represent equivalent through thickness crack lengths.

A two-point polynomial was found to give the most representative fit to the points in figure 41. The curves were therefore expressed as:

$$\frac{a_0 + c}{W} = A + B\left(\frac{V_a}{V_0W}\right) + C\left(\frac{V_a}{V_0W}\right)^2 \qquad \ldots.(7.1.)$$

The constants A, B and C in this expression are presented in table 15 for each material and orientation.

The average value of V_0 for each material and orientation is shown in table 16. The measured V_0 for the 8090-T6 specimens varied with orientation, due to the individual differences in specimen dimensions. No difference in V_0 was noticed between CZ20-T6 C-L and C-R specimen orientations. However, there was a difference in measured V_0 between the 20% and 30% Saffil-reinforced 6061-T6 specimens, as expected. For comparison, the theoretical electrical potential calibrations are also presented in figure 41. These were calculated using equation 5.5., V_0 being calculated from values for electrical conductivity for each material. Theoretical electrical conductivity and V_0 for each material is shown in table

16, with the experimental value for V_0. No values for the electrical conductivity of Saffil-reinforced composites or CZ20-T6 could be supplied, so the experimental values for V_0 were used in the theoretical calibration for these materials. The values for electrical conductivity for Saffil-reinforced 6061-T6 and CZ20-T6 in table 16 are also experimental values.

The theoretical calibration curve agrees fairly well with the experimental calibration curve for sharp notched specimens (figures 41b, 41f, 41g, 41h and 41i). However, no such ageement exists with the blunt notched specimens(figures 41a, 41c, 41d and 41e), because the theoretical solution is based on the assumption of the existence of a sharp crack. For this reason, the experimental calibration curve was used for the calculation of propagation data.

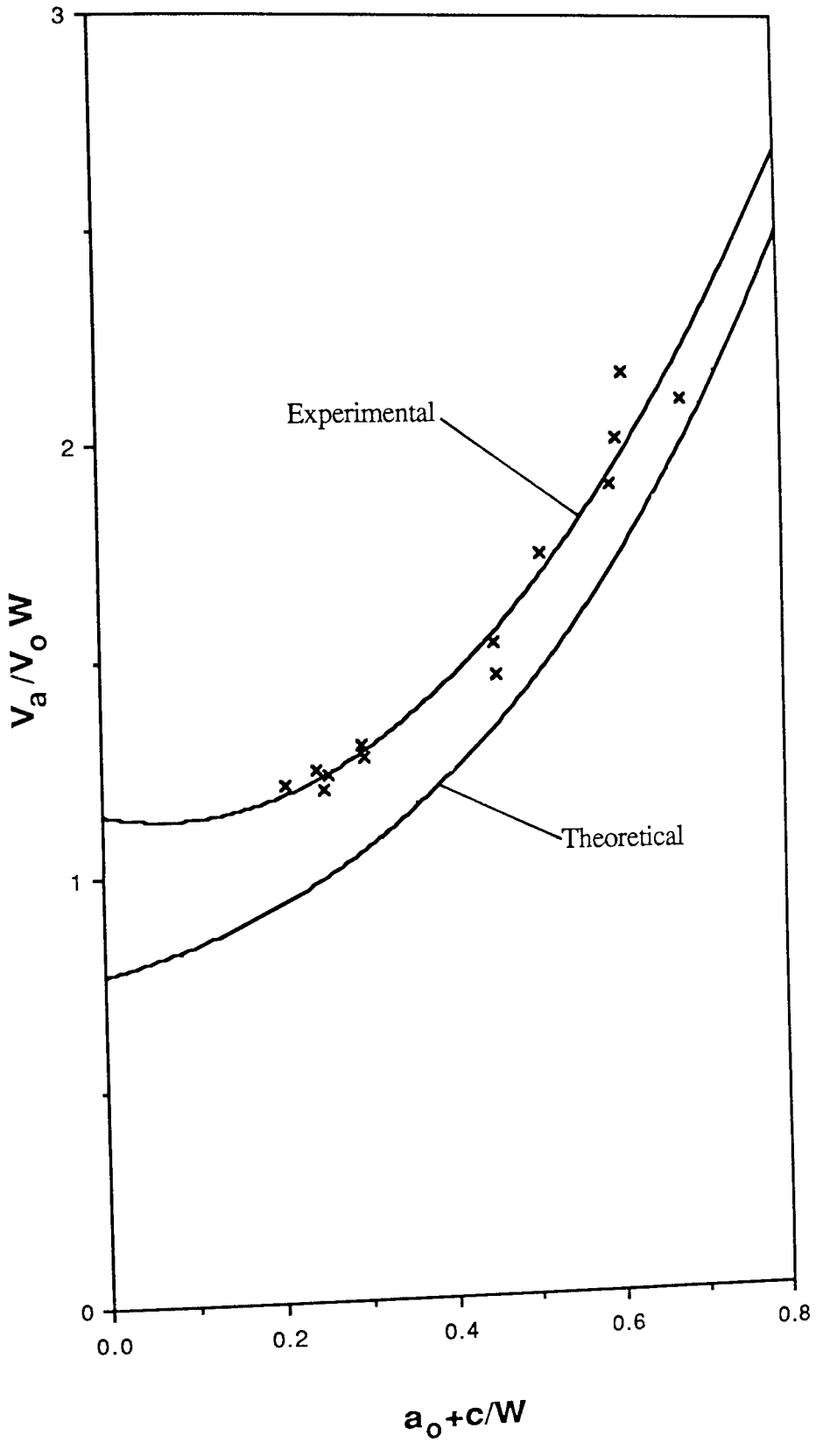

Figure 41a: Electrical potential calibration for the smooth notched 2014-T6 specimens.

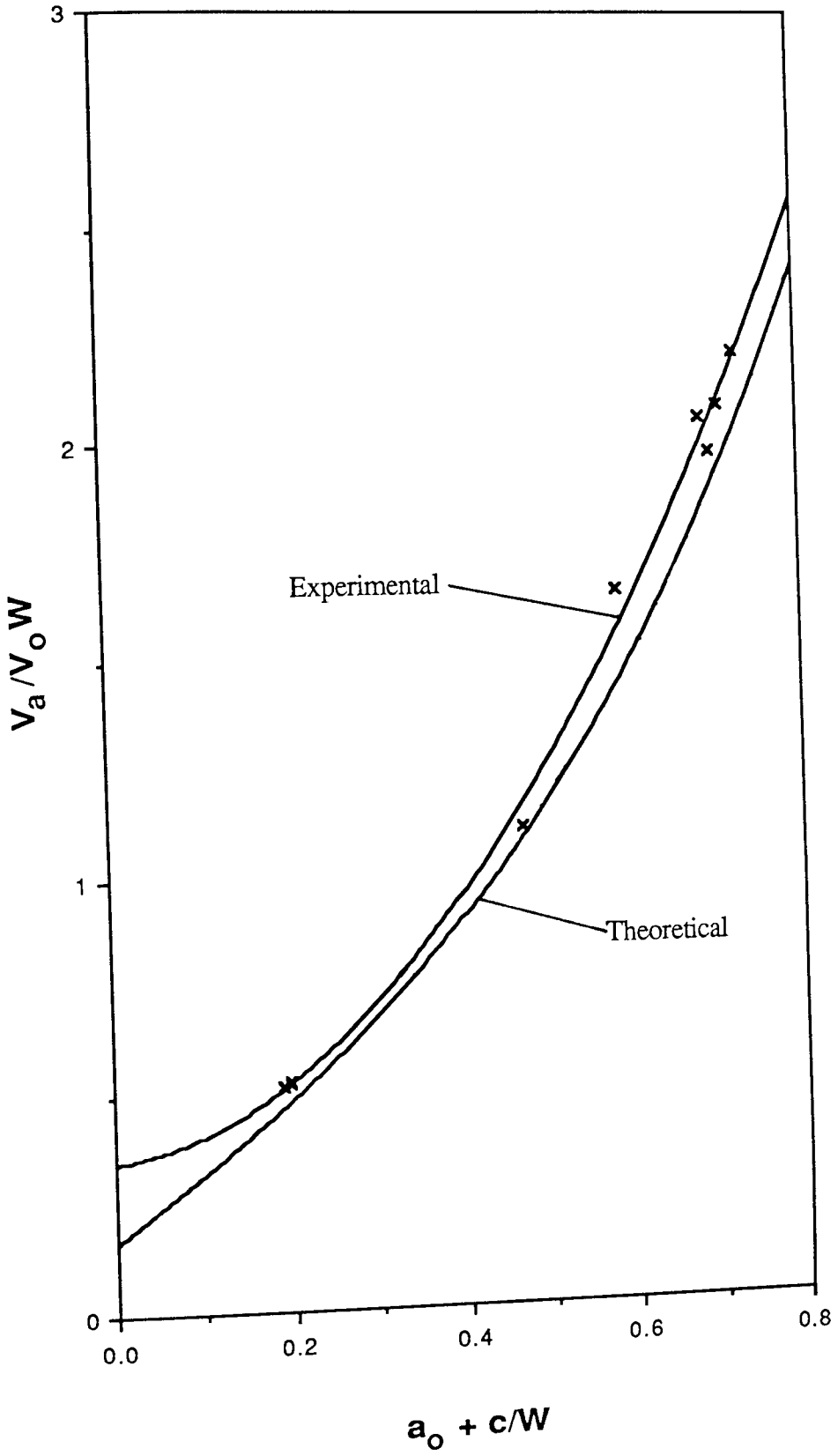

Figure 41b: Electrical potential calibration for the sharp notched 2014-T6 specimens.

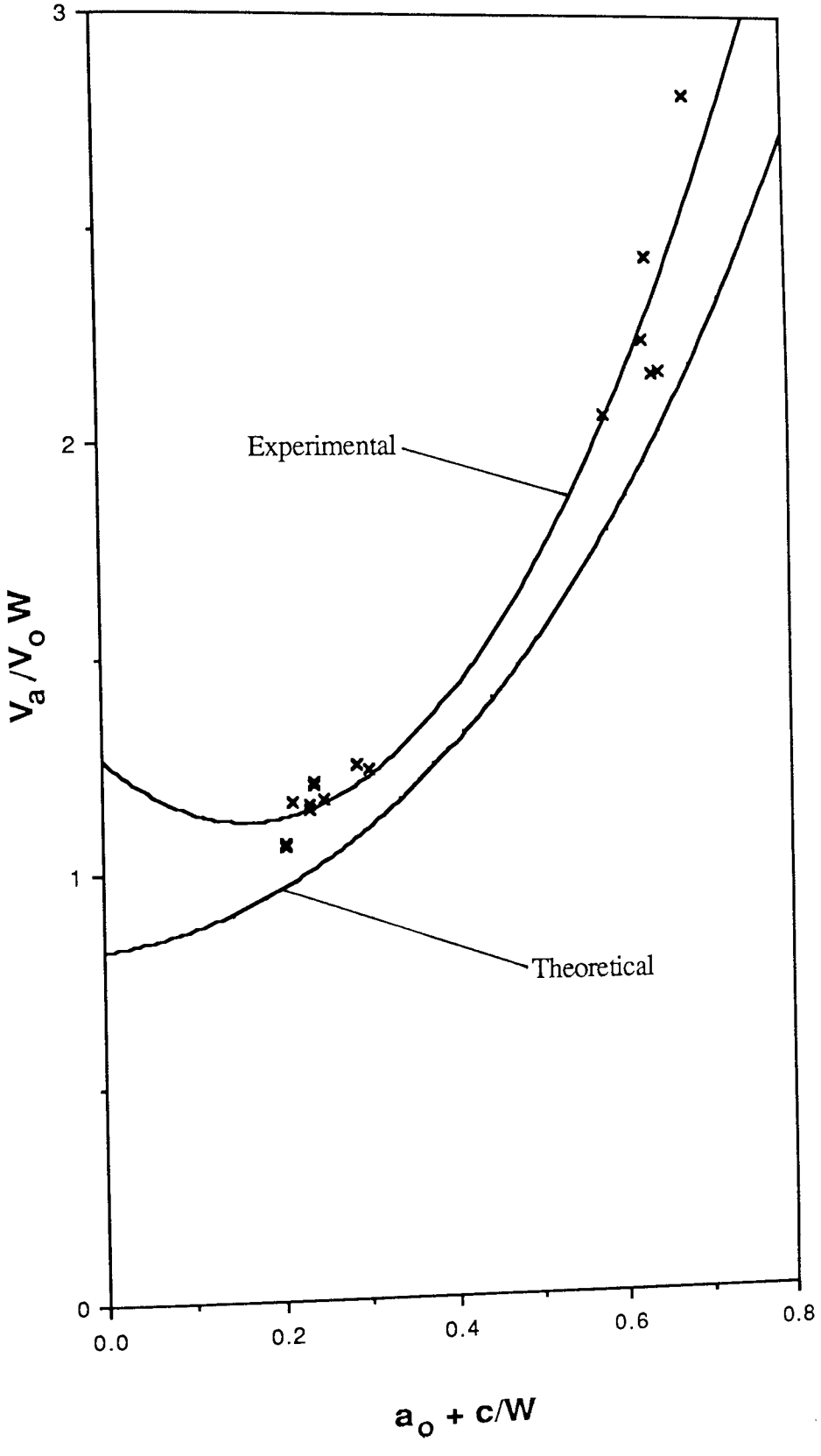

Figure 41c: Electrical potential calibration for the 8090-T6 (L-S) specimens.

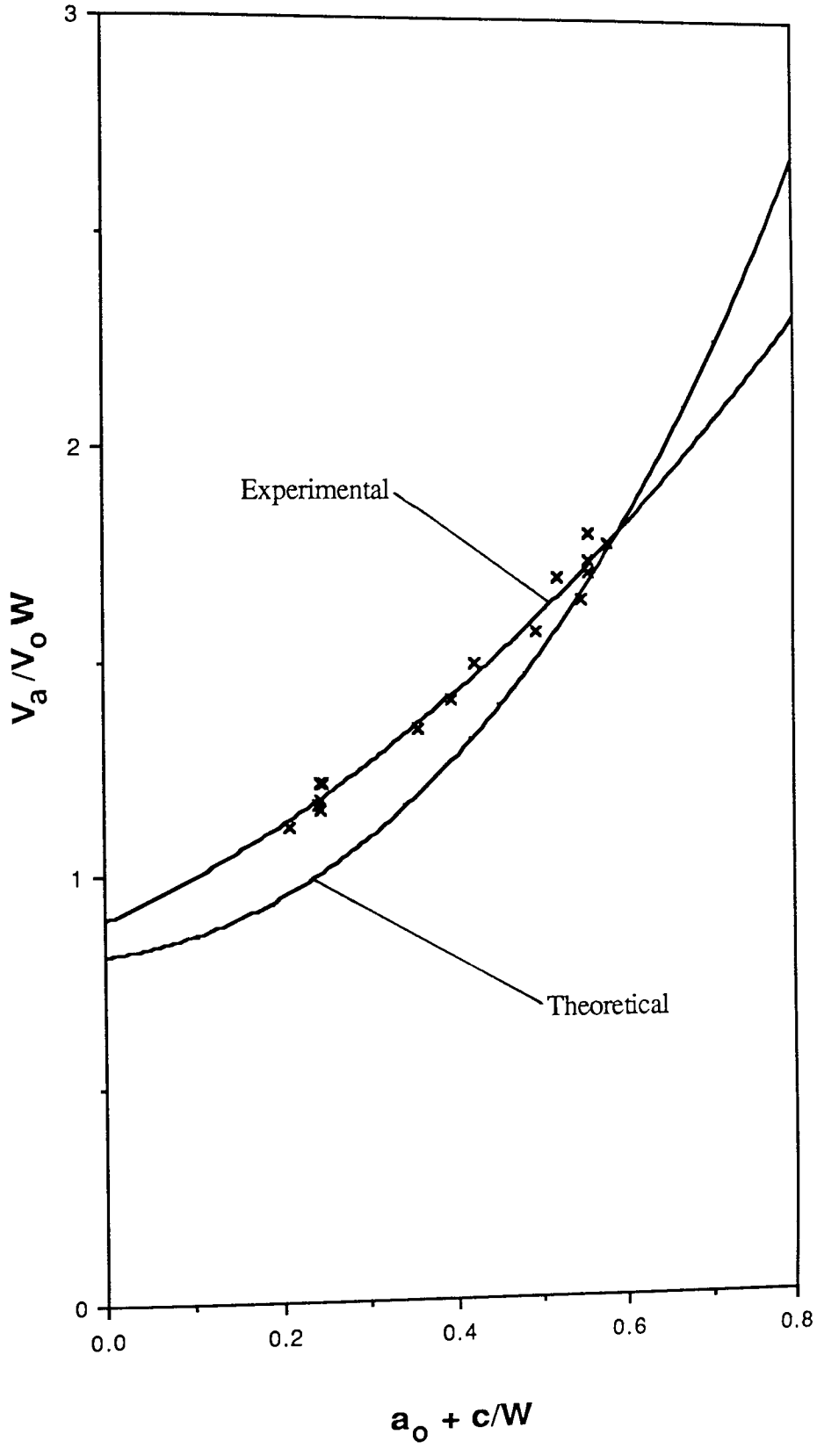

Figure 41d: Electrical potential calibration for the 8090-T6 (L-T) specimens.

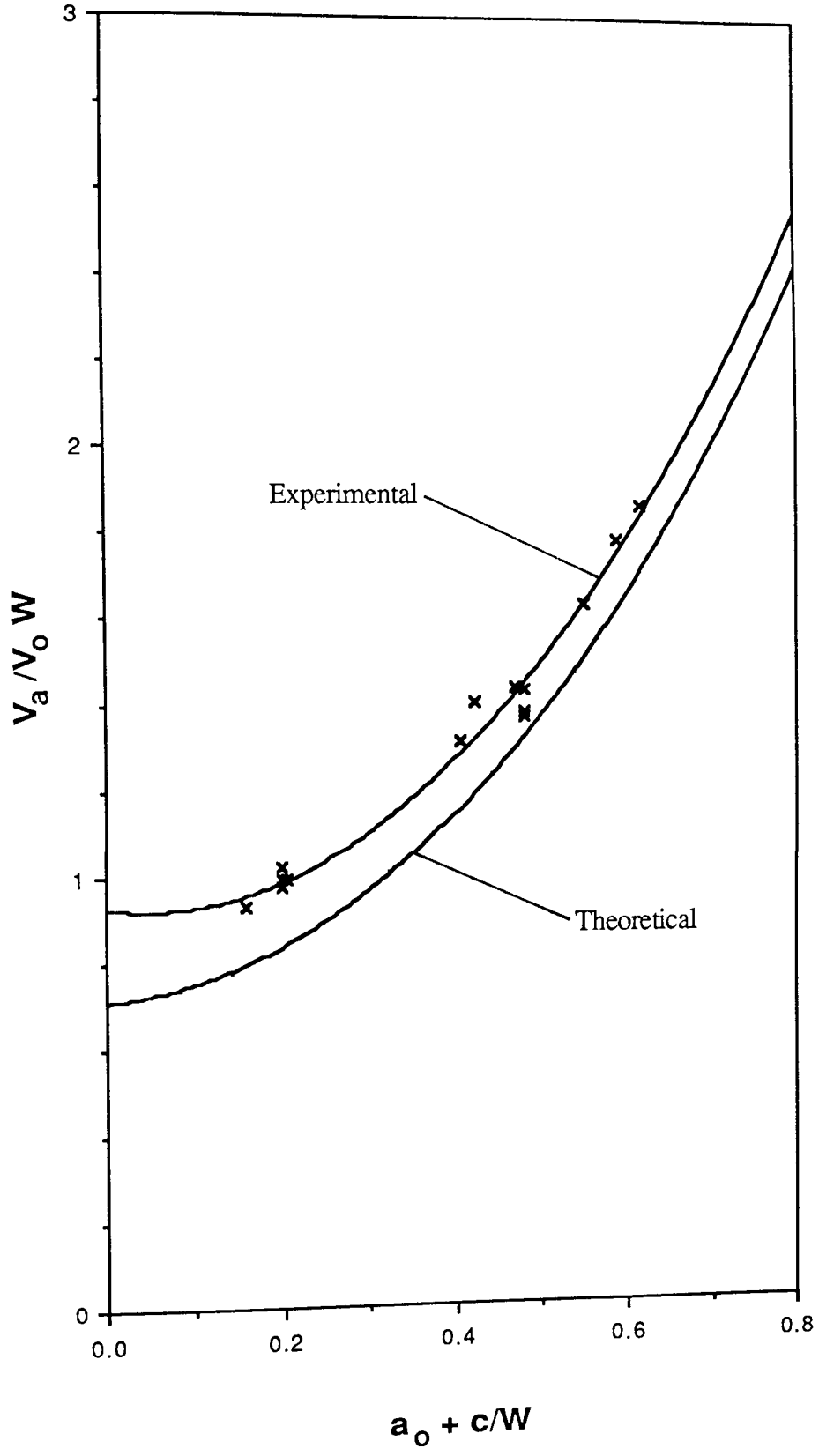

Figure 41e: Electrical potential calibration for the 8090-T6 (T-L) specimens.

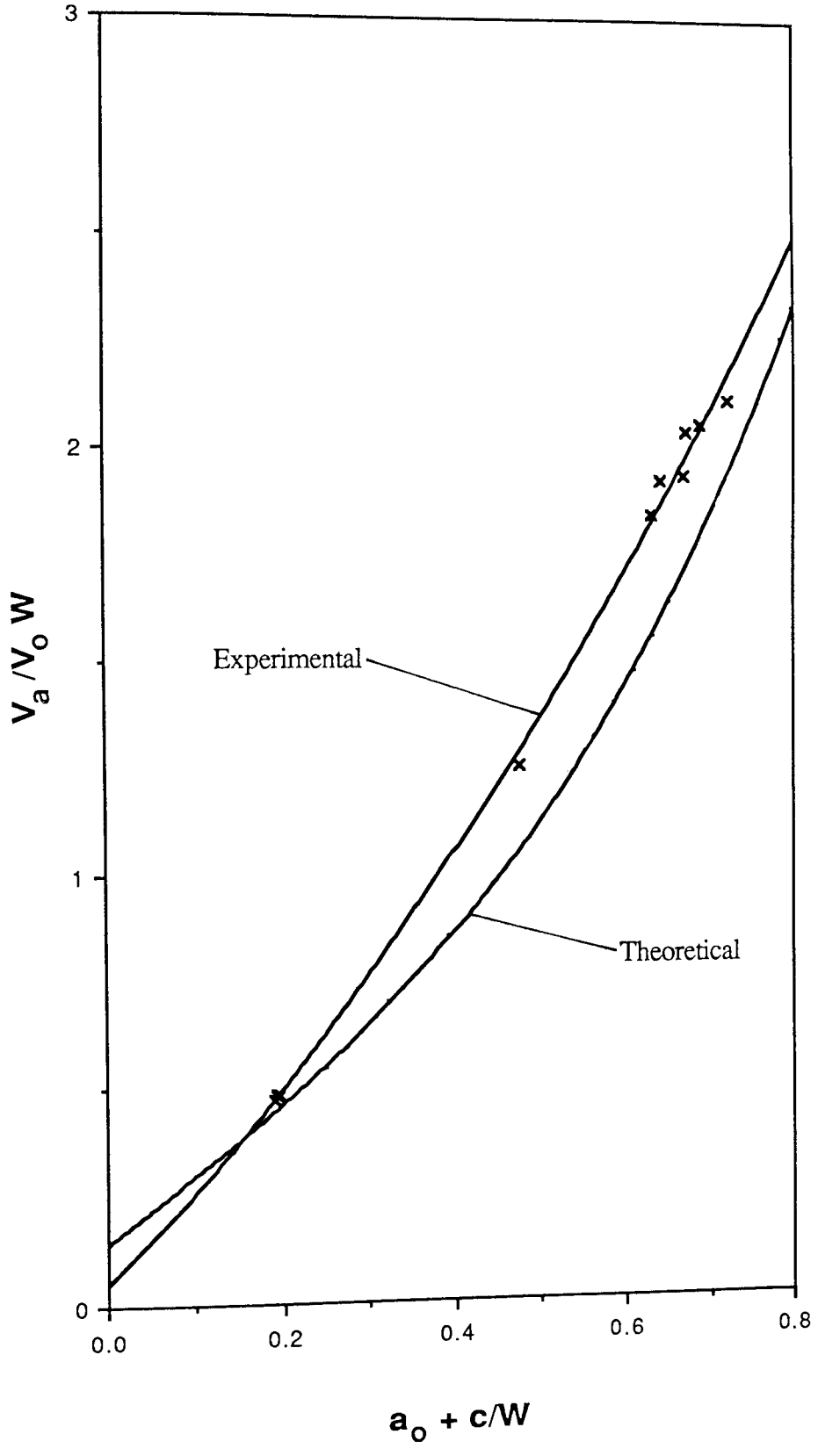

Figure 41f: Electrical potential calibration for the CZ20-T6 (C-L) specimens.

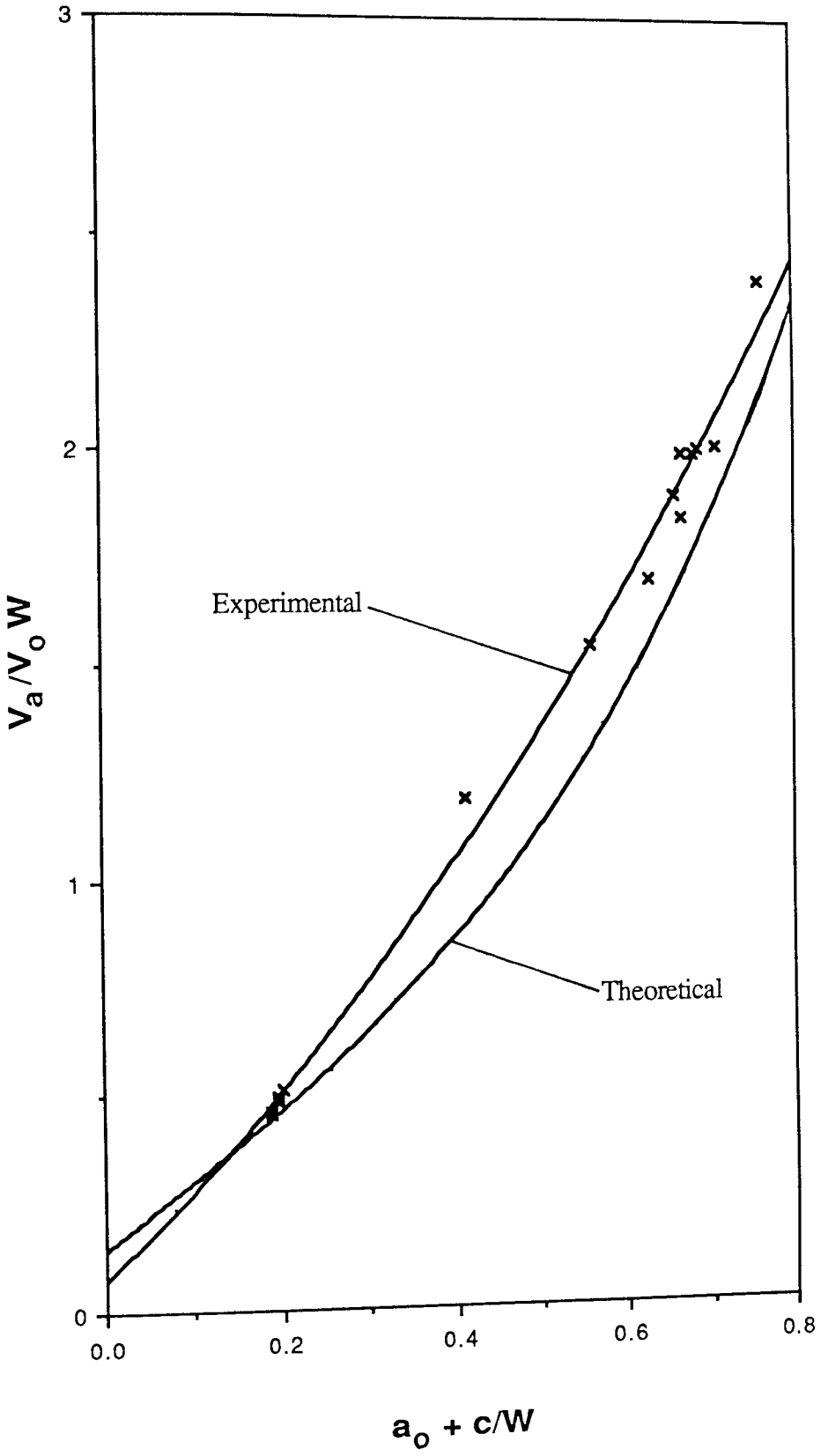

Figure 41g: Electrical potential calibration for the CZ20-T6 (C-R) specimens.

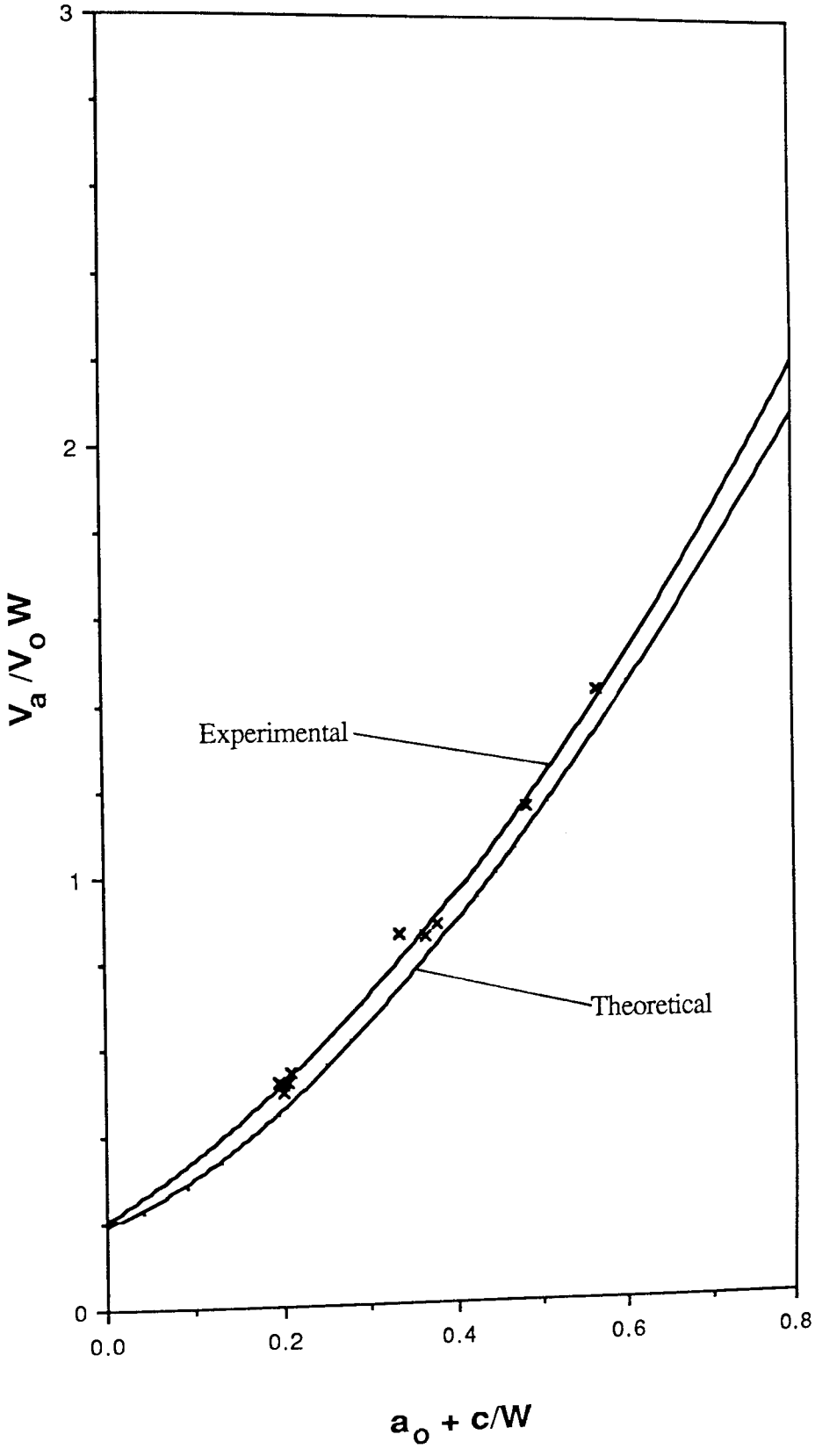

Figure 41h: Electrical potential calibration for the 20% Saffil-reinforced 6061-T6 specimens.

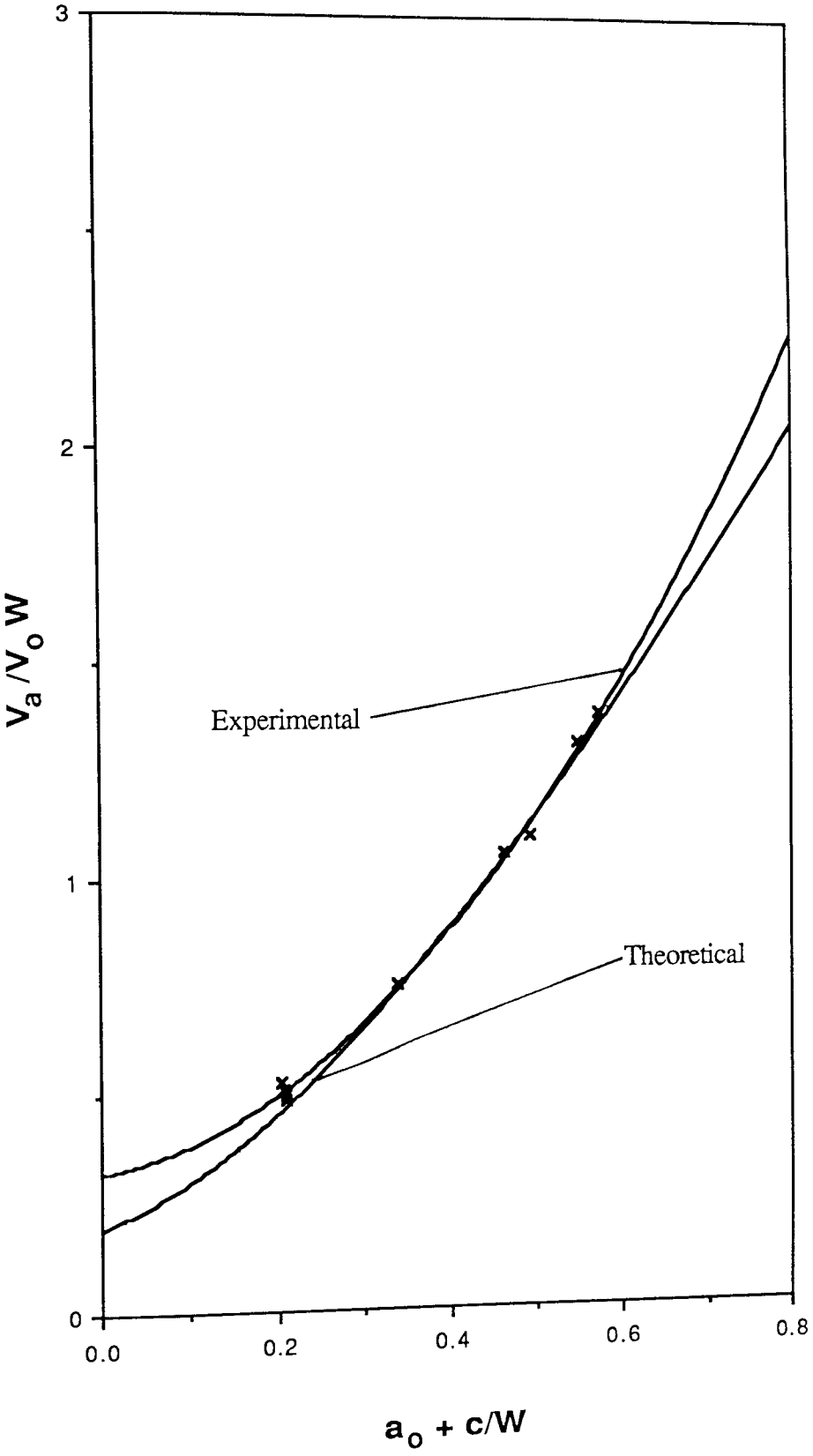

Figure 41i: Electrical potential calibration for the 30% Saffil-reinforced 6061-T6 specimens.

Specimen	A	B	C
65XX	1.146	-0.418	2.933
CXX	0.351	0.259	3.141
92XX	1.264	1.775	5.400
93XX	0.894	0.895	1.090
94XX	0.927	0.279	2.884
AXX	0.051	1.971	1.352
RXX	0.075	1.899	1.320
20XX	0.203	1.252	1.563
30XX	0.323	0.372	2.571

Table 15: Constants A, B and C for the two-point polynomial fit of experimental electrical potential calibration.

Material	Expt. Vo. (μV/mm)	Theoretical Vo (μV/mm)	Elect. Cond. ($\Omega^{-1}.m^{-1}$)
8090-T6(L-S)	10.75	10.75	11.63×10^6
(L-T)	10.98	10.76	11.63×10^6
(T-L)	11.54	11.50	11.63×10^6
2014-T6(L-S) (smooth notch)	5.67	5.38	23.26×10^6
2014-T6(L-S) (Sharp notch)	6.74	6.51	23.26×10^6
CZ20-T6(C-L)	6.42	---	23.05×10^6
CZ20-T6(C-R)	6.26	---	23.63×10^6
20% Saffil/ 6061-T6	7.45	---	14.91×10^6
30% Saffil/ 6061-T6	7.78	---	14.28×10^6

Table 16: Measured and theoretical values for V_0 and electrical conductivity.

7.2. FATIGUE TESTING

7.2.1. FATIGUE LIFE TESTING

Results of the work on the rotating beam specimens (R=-1.0) are presented in table 17a to 17d. Each 2lb in weight applied corresponds to 1tsi in peak stress (=15.444MPa). N_f is the number of cycles to failure of the specimen. Results are presented for fatigue life, in air and salt water, for 2014-T6 and 8090-T6. The data is graphically presented in the form of S-N curves (peak stress versus cycles to failure) in figure 42. In general, the fatigue life of 2014-T6 exceeded that of 8090-T6 at all stresses except close to the fatigue limit in both air and salt water.

7.2.2. FATIGUE CRACK INITIATION TESTING

Specimen dimensions of the smooth notched specimens, shown in figure 27a, used to investigate fatigue and corrosion fatigue crack initiation of 2014-T6 and 8090-T6 are listed in tables 18a to 18d. The experimental results are shown in tables 19a to 19h. Both stress concentration methods and fracture mechanics methods were used to quantify the stress required to initiate a crack. The R value was kept constant at 0.45, with the load range, ΔP, being varied. Δs was calculated using equation 6.3., and was multiplied by the stress concentration factor, 1.49, to find the notched stress range. ΔK_n is the effective stress intensity factor range, calculated using equations 3.6., 6.4. and 3.22. C_B, the grain size in the direction of crack growth, was used to calculate this. N_i is the number of cycles to initiation of a crack of length 0.12-0.13mm.

Fatigue crack initiation results are graphically presented in figures 43 and 44, for both fatigue and corrosion fatigue work. Figure 43 presents the results in the form of S-N curves, with $K_t.\Delta s$ plotted against N_i. Data for all 2014-T6 and 8090-T6 specimens are presented in figure 43a and results are separated out for 2014-T6, 8090-T6(L-S), 8090-T6(L-T) and 8090-T6(T-L) in figures 43b, 43c, 43d and 43e respectively. Figure 44 presents the results in the form of N_i versus ΔK_n, which can be represented in the form:

$$N_i = B(\Delta K_n)^n \qquad \text{....(7.2.)}$$

The values of B and n obtained from the best fit for the specimens are given in table 20. Again, the data for all 2014-T6 and 8090-T6 specimens are presented in figure 44a, with results being separated out in figures 44b, 44c, 44d and 44e.

As in the fatigue life testing, the fatigue crack initiation life of 2014-T6 exceeded that of 8090-T6 at high stresses, with similar fatigue lives close to the fatigue limit. This effect was not as pronounced in the salt water environment, where 8090-T6 was superior to 2014-T6 at stresses close to the fatigue limit.

7.2.3. FATIGUE CRACK PROPAGATION TESTING

The dimensions of the smooth notched specimens, shown in figures 27b and 27c, used to investigate fatigue and corrosion fatigue crack propagation of 2014-T6 and 8090-T6 are listed in tables 18a to 18d. Dimensions of the sharp notched specimens, shown in figures 29 and 30, used to investigate fatigue and corrosion fatigue crack growth of 2014-T6, CZ20-T6 and Saffil-reinforced 6061-T6 are listed in tables 21a to 21e.

The experimental results of fatigue crack propagation testing on all materials are shown in figures 45a to 45d, for R-values of 0.1 and 0.45 in air and a salt water environment. These results are separated into individual materials and orientations in figures 46a to 46h. The relationship between fatigue crack growth rate, da/dN, and the cyclic stress intensity range, ΔK, was described by the Paris Law (equation 3.13.):

$$\frac{da}{dN} = A(\Delta K)^n$$

The values of A and n obtained from a least squares regression analysis for each material, orientation, environment and R-value are shown in table 22.

In air the fatigue crack propagation resistance of 8090-T6 was superior to that of 2014-T6, markedly so at low levels of ΔK. At high levels of ΔK, fatigue crack growth rates were similar for both materials. In a salt water environment fatigue crack growth resistance was

more dependent upon the crack orientation of 8090-T6.

CZ20-T6, the PM variation of 2014-T6, showed similar fatigue crack propagation rates to 2014-T6 over the whole range of ΔK, in both air and salt water environments and at both R-values. The fatigue response of this PM alloy was a lot more predictable than 2014-T6, the propagation lines being fairly straight and similar for each specimen. There did not appear to be any effect of specimen orientation (C-L or C-R) on fatigue or corrosion fatigue crack propagation rates at low levels of ΔK. Fatigue crack growth rate was shown to slow down after a certain crack length in C-L specimens, producing the crack propagation curves shown in figure 47. The part of the curve where crack growth rates slowed down were ignored in figures 45 and 46, for reasons explained in a later section.

Fatigue crack growth resistance of Saffil-reinforced 6061-T6 was inferior to all of the other materials in this investigation. Although fatigue crack propagation resistance was equivalent to 2014-T6 at low levels of ΔK, it was inferior at higher levels. 30% Saffil composites showed slightly lower crack growth rates than 20% Saffil composites, over all ranges of ΔK, at both R-values. Also, fatigue crack propagation resistance was slightly higher in the through thickness direction (T orientation) than in the planar direction (P orientation), in both 20% and 30% Saffil-reinforced 6061-T6.

Specimen No.	Load (lb)	Stress (MPa)	Cycles (N)
R9207	24	185.4	11400000
R9211	27	208.5	510000
R9209	28.5	220.1	320000
R9204	30	231.7	81000
R9210	35	270.3	25000
R9206	38	293.5	9000

17a: 8090-T6 air data.

Specimen No.	Load (lb)	Stress (MPa)	Cycles (N)
R9207	9	69.5	1430000
R9212	11	85.0	750000
R9213	12	92.7	540000
R9202	15.5	119.7	260000
R9208	18.5	142.9	96000
R9203	22	169.9	87000
R9205	25	193.1	36000
R9201	28	216.2	24000

17b: 8090-T6 salt water data.

Specimen No.	Load (lb)	Stress (MPa)	Cycles (N)
R6507	19	146.7	10000000
R6511	25	193.1	11350000
R6502	27	208.5	3000000
R6509	29	224.0	450000
R6508	32	247.1	240000
R6514	35	270.3	150000
R6516	37	285.8	84000
R6513	40	308.9	48000

17c: 2014-T6 air data.

Specimen No.	Load (lb)	Stress (MPa)	Cycles (N)
R6505	12	92.7	1020000
R6510	15	115.8	640000
R6503	17	131.3	340000
R6512	22	169.9	145000
R6501	25	193.1	115000
R6515	28	216.2	50000

17d: 2014-T6 salt water data.

Table 17: Results of fatigue and corrosion fatigue life testing.

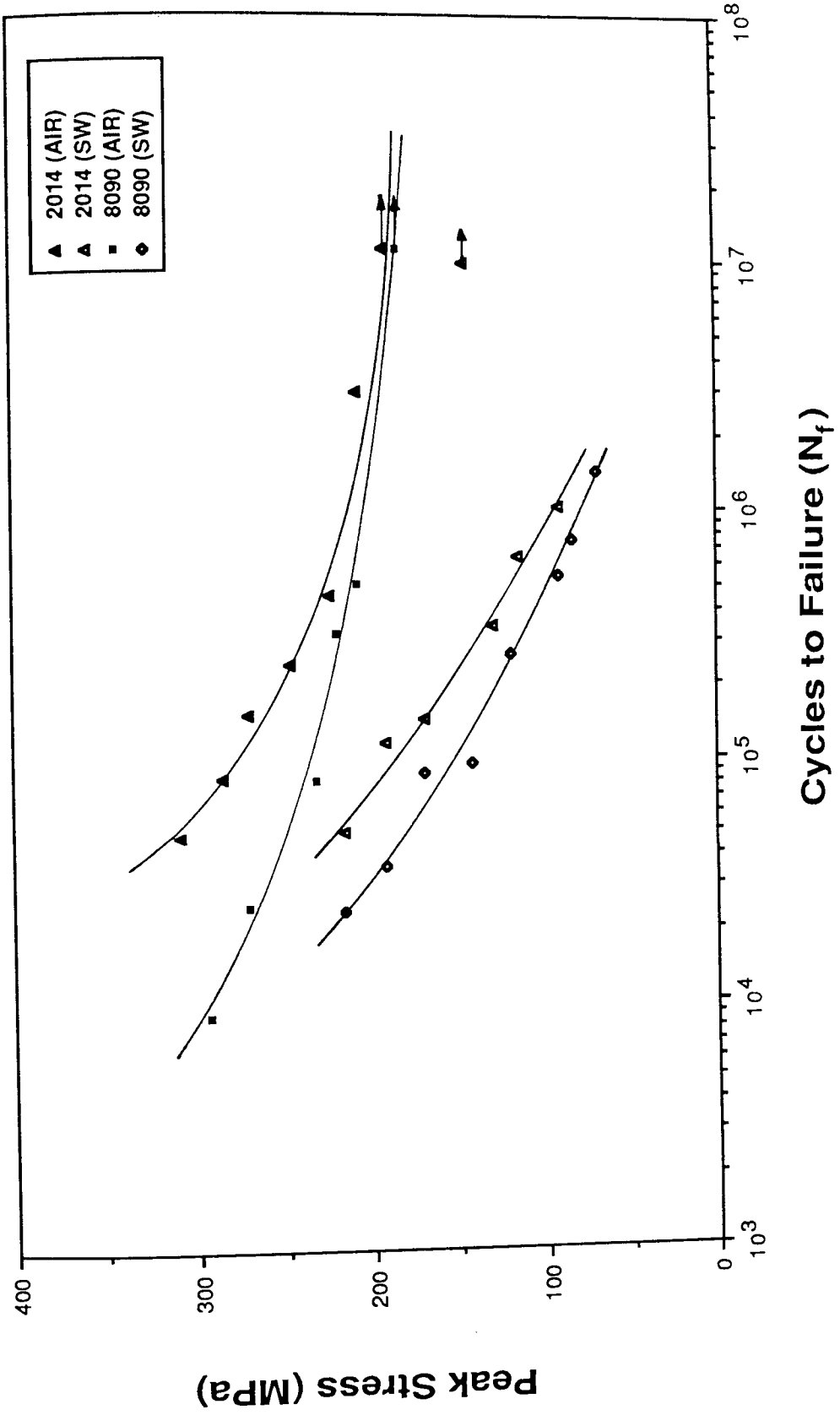

Figure 42: Rotating beam fatigue data (R=-1.0) for 2014-T6 and 8090-T6.

Specimen	W (mm)	B (mm)	Smooth notch depth (mm)	Root radius (mm)	Sharp notch depth (mm)
6501	24.03	10.01	5.02	9.88	----
6502	24.00	9.99	5.07	9.83	----
6503	24.00	9.98	5.00	9.73	----
6504	23.69	9.77	4.70	9.86	----
6505	23.82	10.01	4.95	9.77	----
6506	24.01	10.01	5.05	9.78	----
6507	24.01	10.01	5.00	9.90	1.25
6508	24.04	10.00	5.00	9.73	2.16
6509	24.01	9.99	5.00	9.74	1.24
6510	23.99	9.97	5.00	9.81	----
6511	24.03	9.98	5.00	9.90	0.90
6512	23.99	10.01	5.05	9.93	----
6513	24.02	9.99	5.05	9.85	----
6514	23.99	10.01	5.00	9.74	2.24
6515	24.02	10.03	4.98	9.74	----
6516	24.01	10.01	5.00	9.73	----
6517	24.01	10.01	5.00	9.73	----
6518	24.01	10.02	4.98	9.74	----
6519	24.01	10.04	4.99	9.91	1.10
6520	24.01	9.97	5.15	9.77	0.92

Table 18a: 2014-T6 smooth notched specimen dimensions.

Specimen	W (mm)	B (mm)	Smooth notch depth (mm)	Root radius (mm)	Sharp notch depth (mm)
9201	23.18	9.60	4.25	9.94	0.85
9202	23.94	10.07	4.90	9.90	2.33
9203	23.95	10.02	4.90	9.82	----
9204	23.78	9.66	4.80	9.93	2.08
9205	23.84	9.99	4.85	9.87	0.88
9206	24.04	10.03	5.00	9.81	0.74
9207	23.94	10.00	4.95	9.77	1.02
9208	23.84	10.04	4.85	9.79	0.76
9209	23.83	10.02	4.85	9.96	0.83
9210	23.85	10.02	4.85	9.96	----
9211	23.83	10.02	4.85	9.87	0.72
9212	23.98	10.03	4.98	9.74	----
9213	23.84	9.85	4.90	9.82	----
9214	23.94	10.06	4.95	9.77	----
9215	23.83	9.90	4.85	9.96	----
9216	22.75	9.56	3.85	9.83	----

Table 18b: 8090-T6 (L-S) specimen dimensions.

Specimen	W (mm)	B (mm)	Smooth notch depth (mm)	Root radius (mm)	Sharp notch depth (mm)
9301	23.99	10.04	4.99	9.84	0.89
9302	23.96	10.05	5.00	9.78	----
9303	23.96	10.05	5.00	9.91	0.80
9304	24.01	10.06	5.00	9.92	0.93
9305	23.97	10.08	5.10	9.88	1.38
9306	23.97	10.07	5.02	9.90	0.91
9307	23.99	10.08	5.05	9.73	0.74
9308	24.00	9.71	5.00	9.95	0.68
9309	23.97	10.03	5.05	9.86	0.82
9310	23.96	9.86	5.05	9.75	0.79
9311	24.00	9.64	----	9.82	0.86
9312	24.00	10.03	5.05	9.89	0.82
9313	24.02	10.04	5.00	9.77	0.75
9314	24.00	10.05	5.00	9.91	0.73
9315	23.98	10.04	5.01	9.85	0.86
9316	23.96	10.05	5.05	9.84	0.75
9317	23.98	10.07	4.98	9.77	0.67
9318	23.99	9.64	----	9.75	0.69

Table 18c: 8090-T6 (L-T) specimen dimensions.

Specimen	W (mm)	B (mm)	Smooth notch depth (mm)	Root radius (mm)	Sharp notch radius (mm)
9401	22.44	9.99	3.75	9.58	0.63
9402	22.44	10.00	3.57	9.56	0.80
9403	22.43	9.99	3.50	9.68	0.92
9404	22.42	10.02	3.50	9.68	0.84
9405	22.42	9.99	3.50	9.57	0.90
9406	22.44	10.02	3.55	9.80	----
9407	22.45	10.01	3.52	9.75	0.89
9408	22.44	10.00	3.50	9.68	0.92
9409	22.45	10.00	3.55	9.59	0.91
9410	22.43	10.02	3.55	9.59	1.01
9411	22.43	10.00	3.55	9.70	1.06
9412	22.46	10.00	3.53	9.75	0.88

Table 18d: 8090-T6 (T-L) specimen dimensions.

Specimen No.	ΔP (kN)	Kt.Δs (MPa)	ΔKn (MN.m$^{-3/2}$)	Ni (cycles)
6503	3.750	167.057	3.786	1035240
6504	4.000	178.191	4.038	241750
6506	4.500	200.465	4.542	45000
6501	4.500	200.465	4.542	115000
6513	5.000	222.739	5.046	60650
6512	5.500	245.013	5.552	30100
6505	6.000	267.287	6.056	17470
6517	6.000	267.287	6.056	28100
6518	6.500	289.561	6.560	23100
6510	7.500	334.109	7.570	14250
6502	8.500	378.657	8.580	7400

Table 19a: 2014-T6 fatigue crack initiation results.

Specimen No.	ΔP (kN)	Kt.Δs (MPa)	ΔKn (MN.m$^{-3/2}$)	Ni (cycles)
6516	1.750	77.960	1.768	182800
6511	2.000	89.096	2.014	79700
6515	2.500	111.369	2.530	53750
6519	3.000	133.641	3.034	33000
6514	3.500	155.918	3.536	25200
6520	4.000	178.192	4.040	15000
6509	4.000	178.192	4.040	23160
6507	4.500	200.465	4.544	31150
6508	5.000	222.742	5.046	13450

Table 19b: 2014-T6 corrosion fatigue crack initiation results.

Specimen No.	ΔP (kN)	Kt.Δs (MPa)	ΔKn (MN.m$^{-3/2}$)	Ni (cycles)
9216	4.00	177.564	4.033	351000
9212	4.25	188.662	4.286	246130
9215	4.50	199.760	4.538	124900
9204	5.00	221.956	5.042	50830
9213	5.25	233.053	5.294	56340
9214	5.50	244.151	5.546	42940
9206	5.75	255.249	5.798	26300
9202	6.00	266.347	6.050	15050
9203	6.50	288.542	6.554	10400

Table 19c: 8090-T6 (L-S) fatigue crack initiation results.

Specimen No.	ΔP (kN)	Kt.Δs (MPa)	ΔKn (MN.m$^{-3/2}$)	Ni (cycles)
9210	2.000	88.782	2.017	435060
9211	2.250	99.880	2.269	152880
9207	2.500	110.978	2.521	137180
9205	3.000	133.173	3.025	60000
9208	3.500	155.369	3.529	33850
9209	4.000	177.564	4.033	26550
9201	4.500	199.760	4.538	27860

Table 19d: 8090-T6 (L-S) corrosion fatigue crack initiation results.

Specimen No.	ΔP (kN)	Kt.Δs (MPa)	ΔKn (MN.m$^{-3/2}$)	Ni (cycles)
9307	3.250	145.363	3.291	3003500
9312	3.500	156.545	3.544	360500
9303	4.000	178.909	4.050	158200
9301	4.000	178.909	4.050	174700
9306	4.500	201.272	4.557	163000
9315	4.500	201.272	4.557	170300
9304	5.000	223.636	5.063	45900
9305	5.500	246.000	5.569	26000
9302	6.000	268.363	6.075	14000

Table 19e: 8090-T6 (L-T) fatigue crack initiation results.

Specimen No.	ΔP (kN)	Kt.Δs (MPa)	ΔKn (MN.m$^{-3/2}$)	Ni (cycles)
9317	1.500	67.091	1.519	778470
9313	2.000	89.454	2.025	213130
9308	2.500	111.818	2.531	59930
9309	3.000	134.182	3.038	43710
9314	3.500	156.545	3.544	30060
9310	4.000	178.909	4.050	19750
9316	4.500	201.272	4.557	13700

Table 19f: 8090-T6 (L-T) corrosion fatigue crack initiation results.

Specimen No.	ΔP (kN)	Kt.Δs (MPa)	ΔKn (MN.m$^{-3/2}$)	Ni (cycles)
9402	3.500	147.579	3.491	1401310
9401	4.000	168.662	3.989	243100
9404	4.500	189.745	4.488	90010
9403	5.000	210.827	4.987	52200
9407	5.500	231.910	5.485	45800
9406	6.000	252.993	5.984	13500

Table 19g: 8090-T6 (T-L) fatigue crack initiation results.

Specimen No.	ΔP (kN)	Kt.Δs (MPa)	ΔKn (MN.m$^{-3/2}$)	Ni (cycles)
9405	1.500	63.248	1.496	523060
9411	2.000	84.331	1.995	125470
9409	2.500	105.414	2.493	77560
9412	3.000	126.496	2.992	41290
9410	3.500	147.579	3.491	24910
9408	4.000	168.662	3.989	16520

Table 19h: 8090-T6 (T-L) corrosion fatigue crack initiation results.

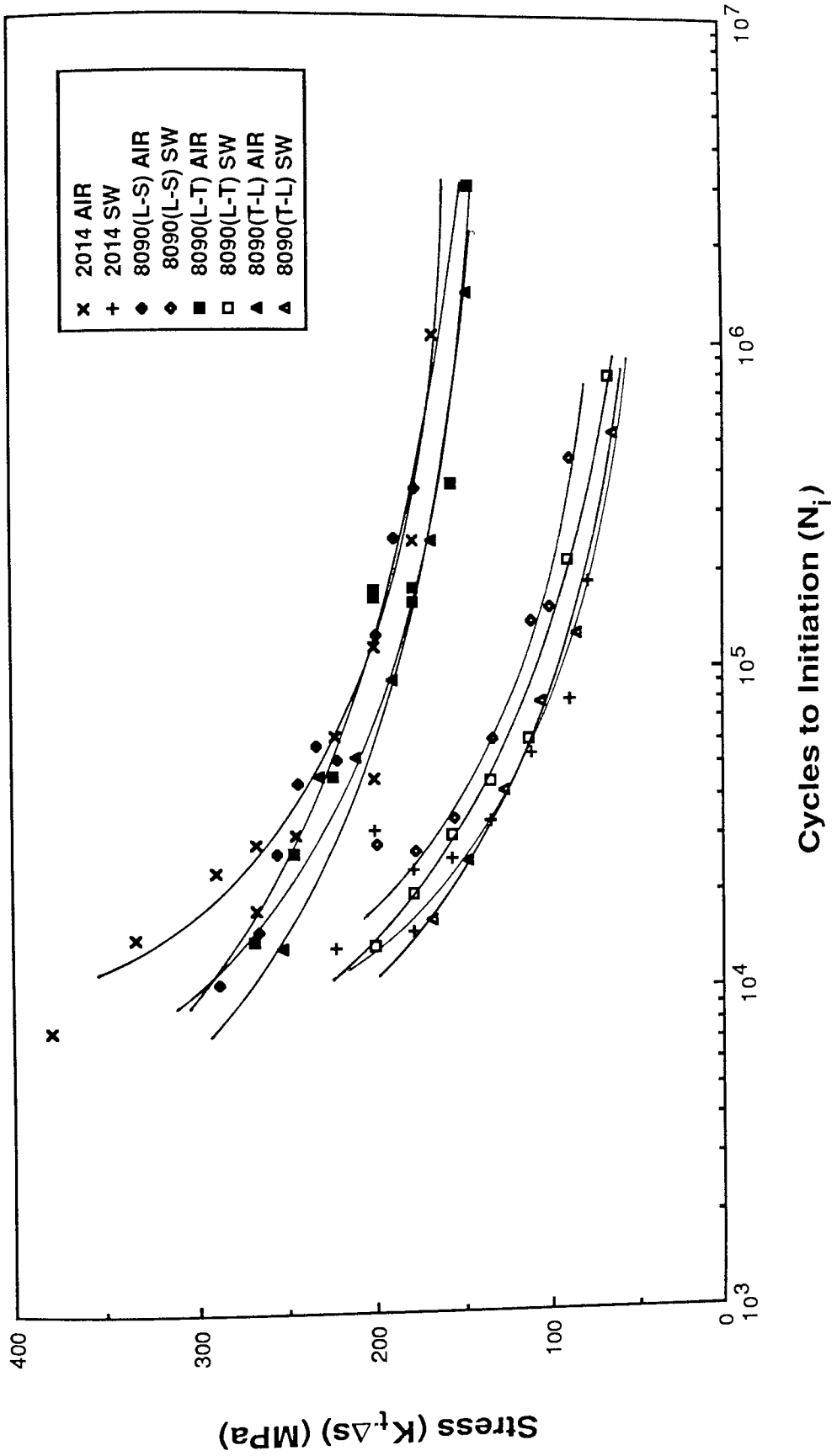

Figure 43a: Fatigue crack initiation results.

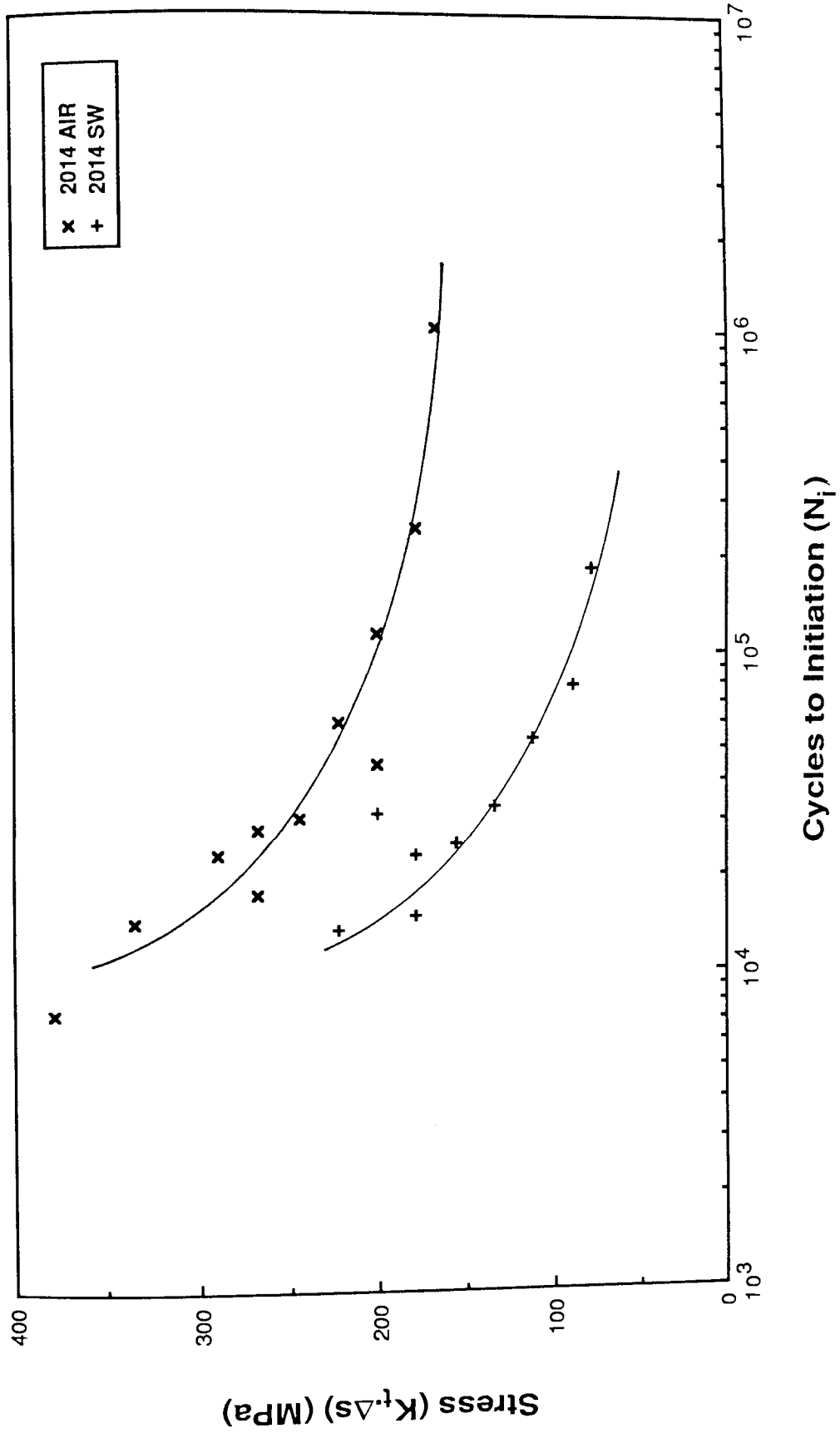

Figure 43b: 2014-T6 fatigue crack initiation results.

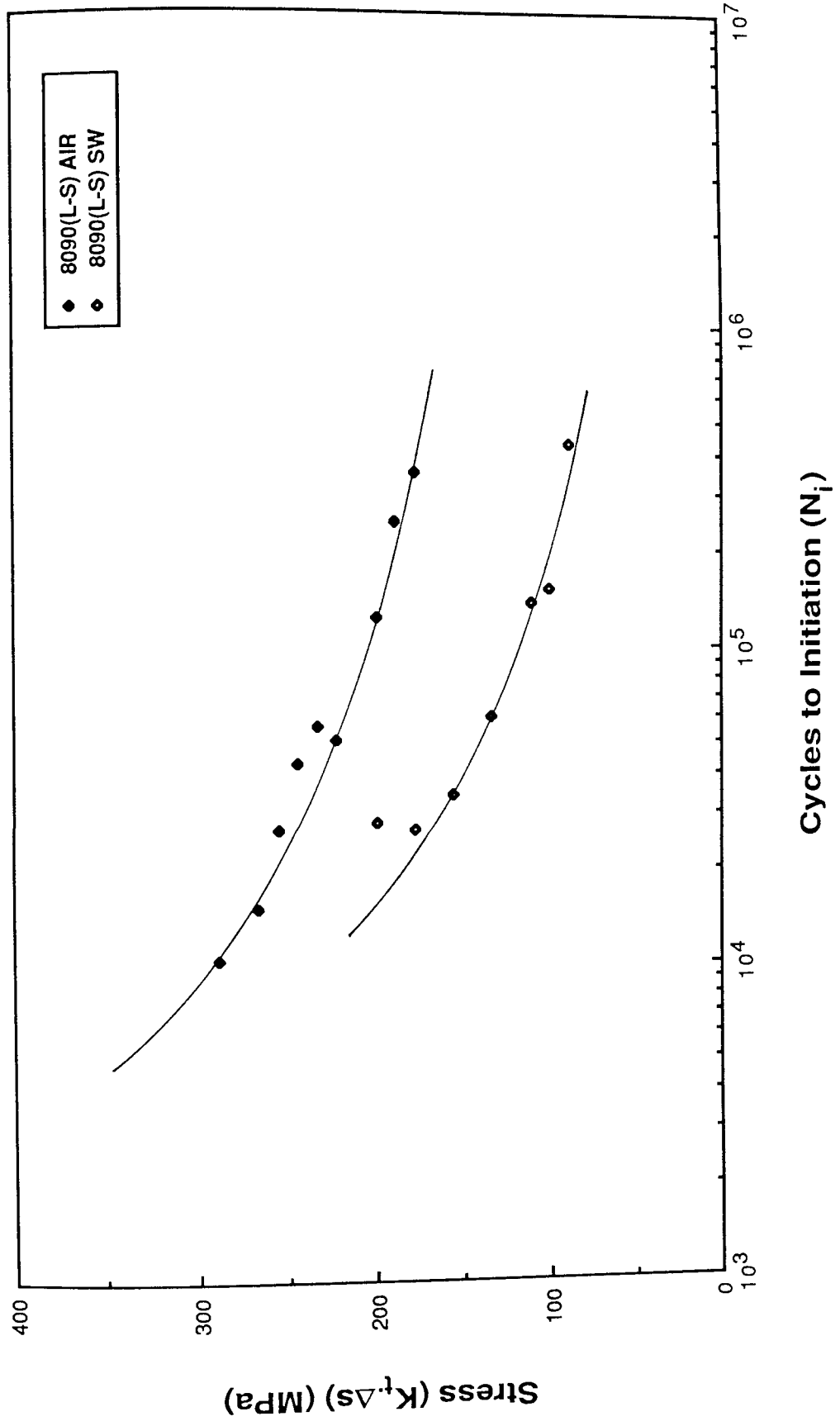

Figure 43c: 8090-T6 (L-S) fatigue crack initiation results.

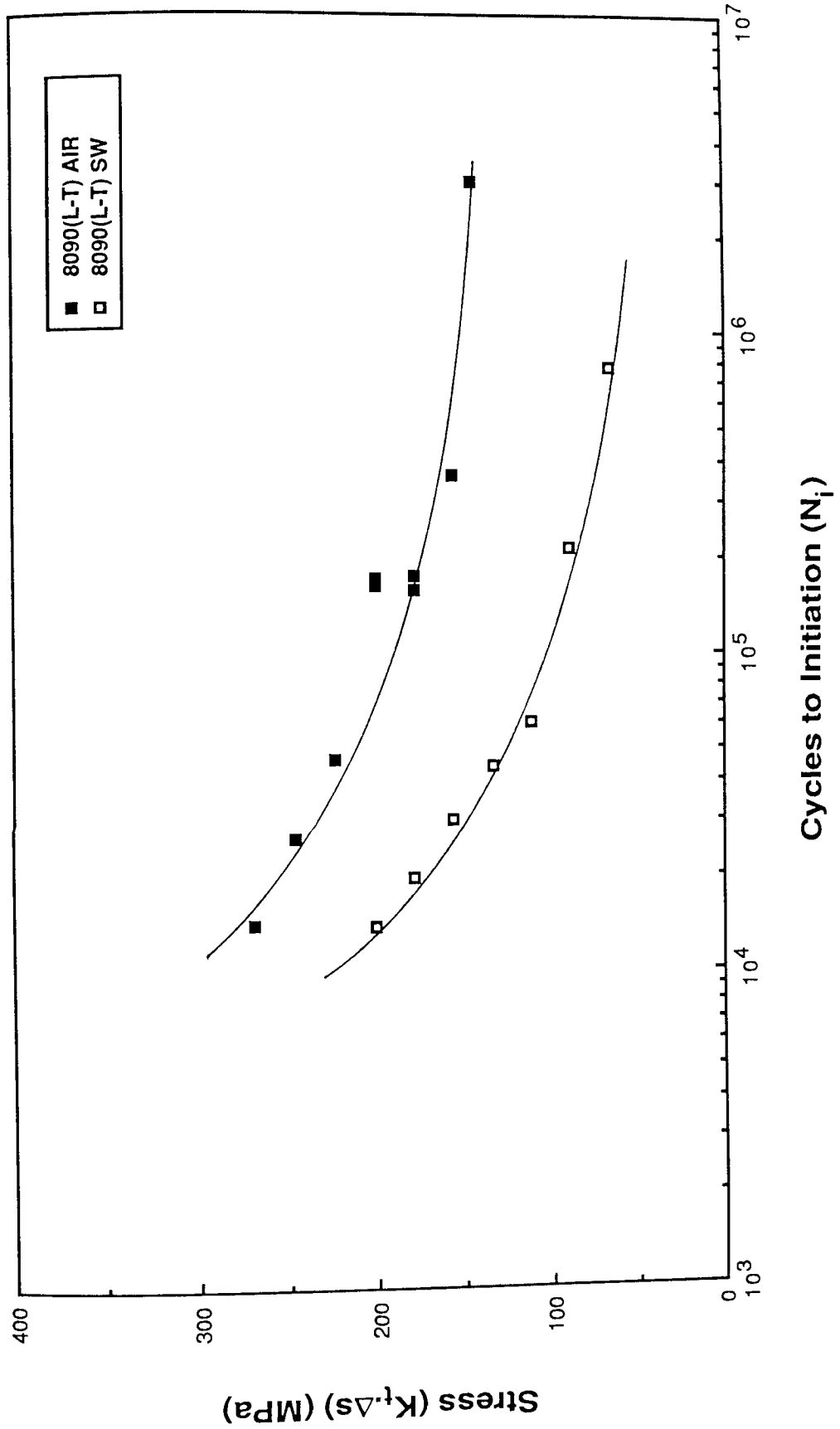

Figure 43d: 8090-T6 (L-T) fatigue crack initiation results.

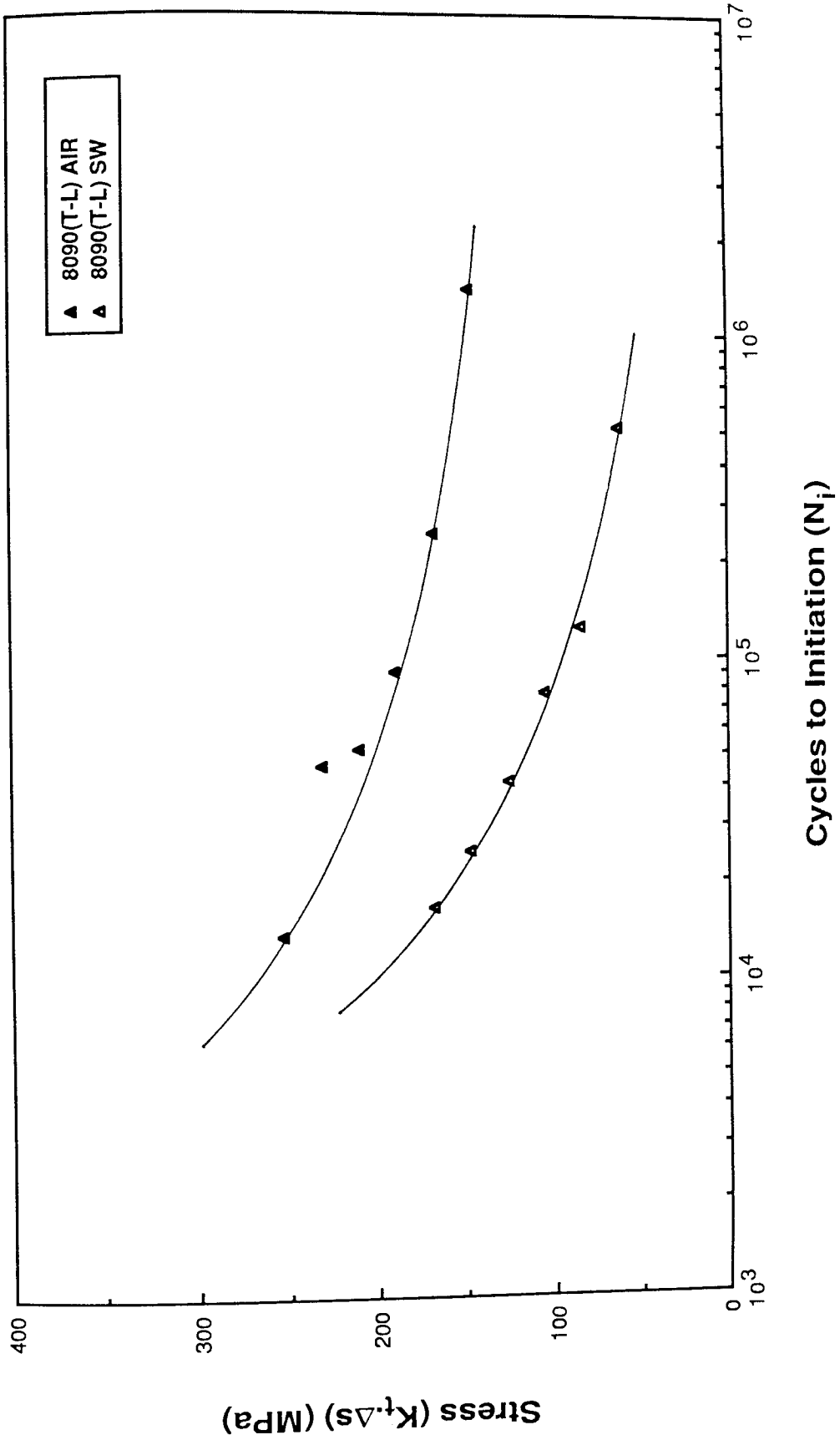

Figure 43e: 8090-T6 (T-L) fatigue crack initiation results.

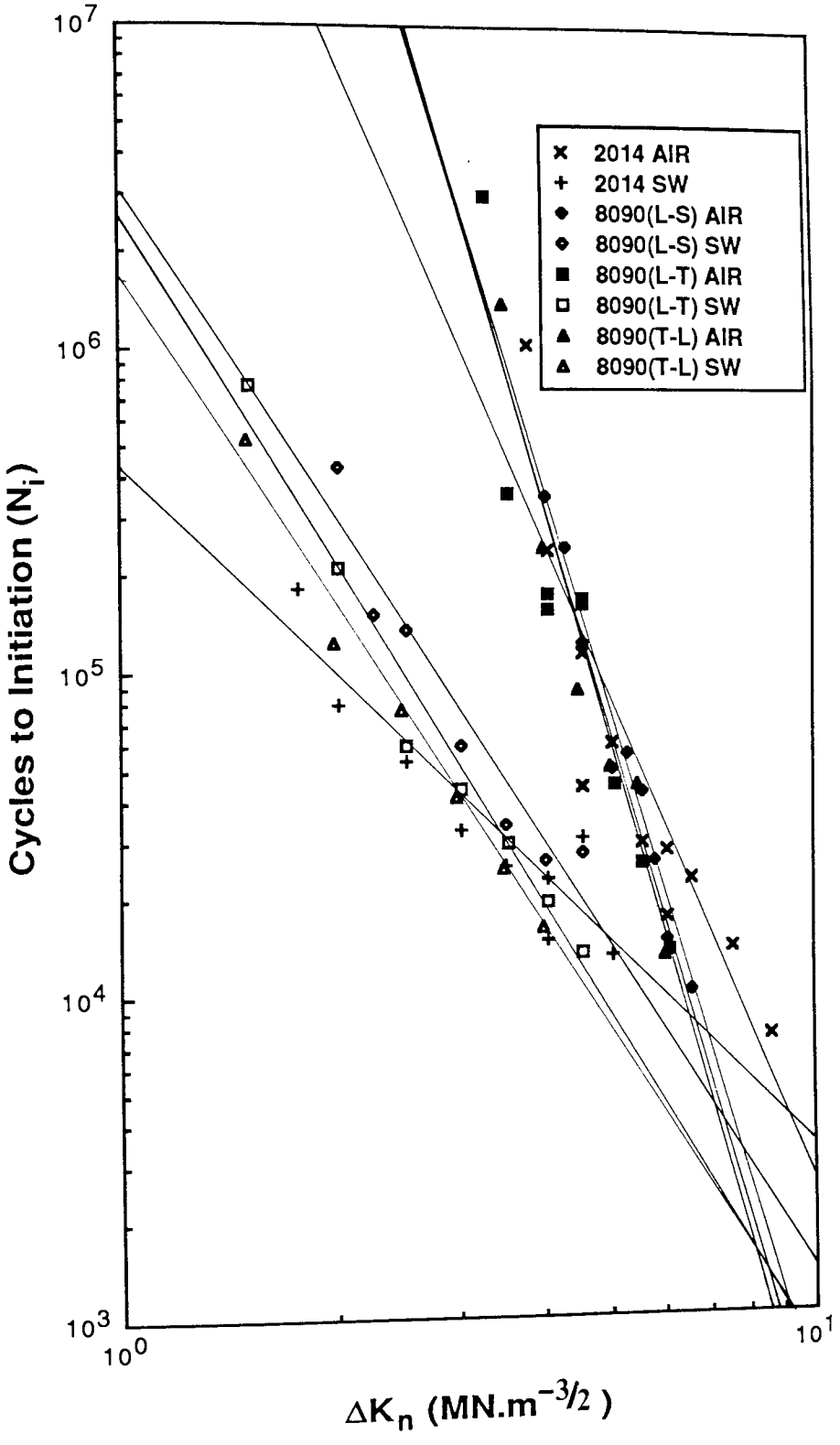

Figure 44a: Fatigue crack initiation results.

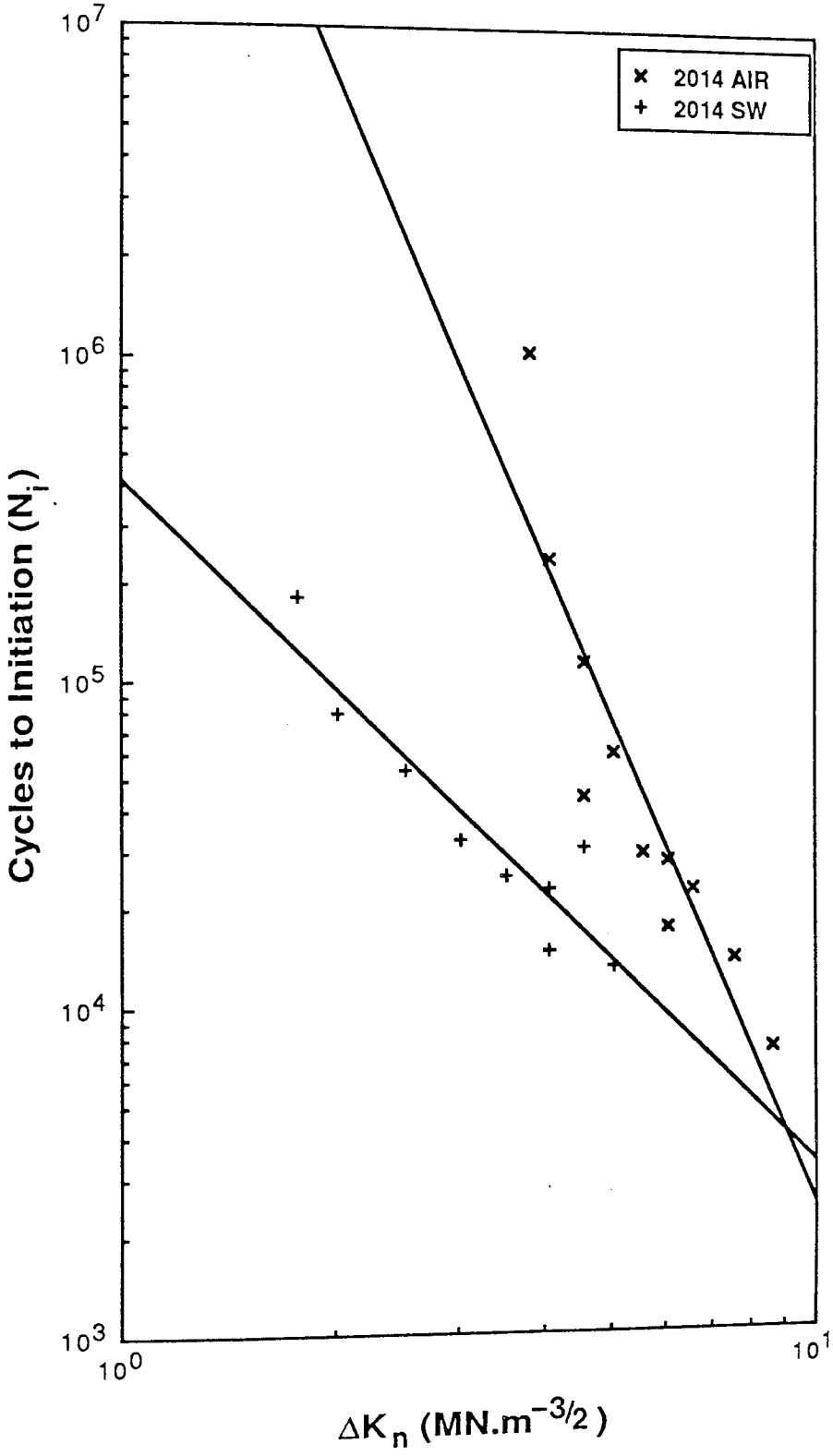

Figure 44b: 2014-T6 fatigue crack initiation results.

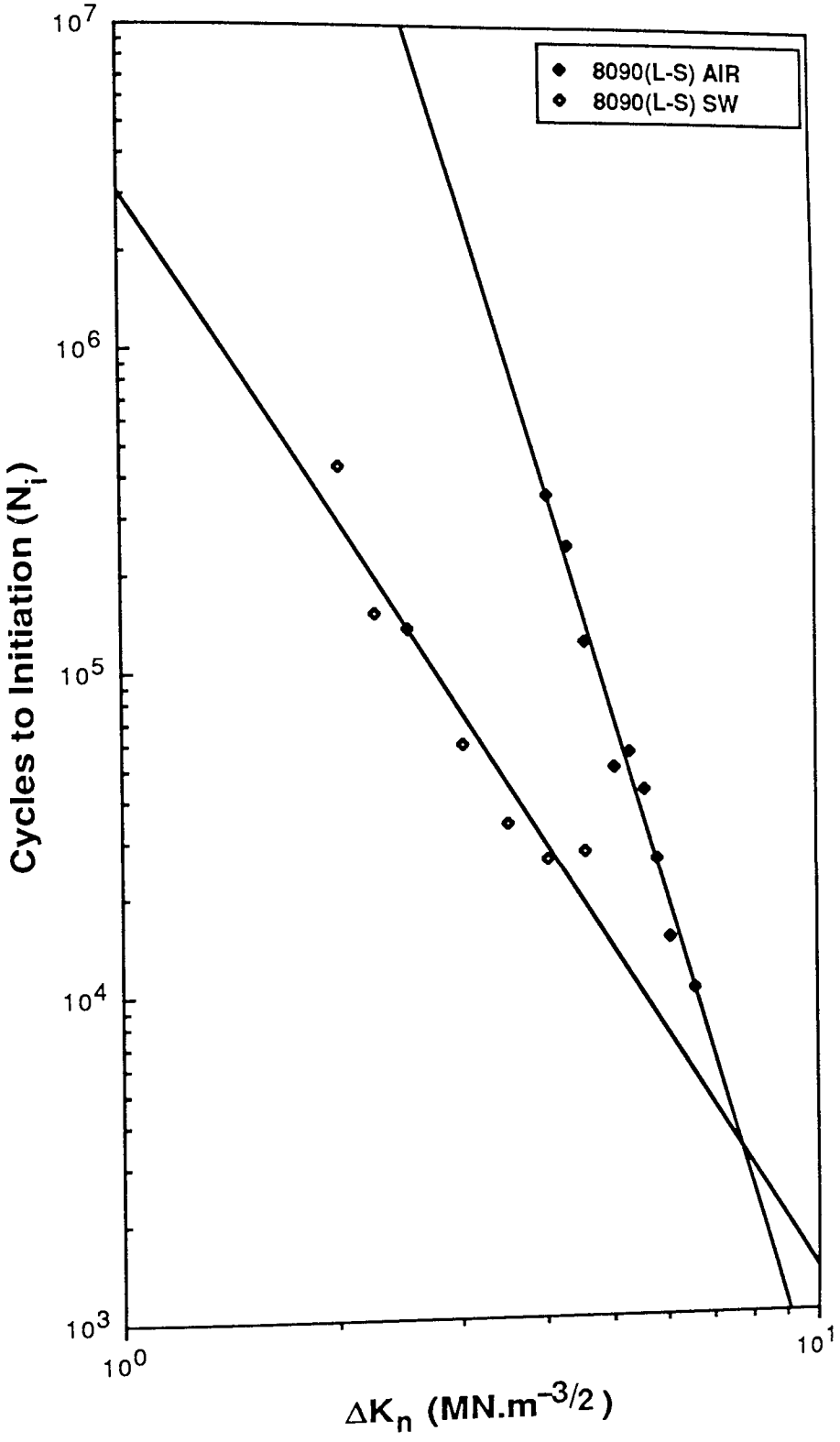

Figure 44c: 8090-T6 (L-S) fatigue crack initiation results.

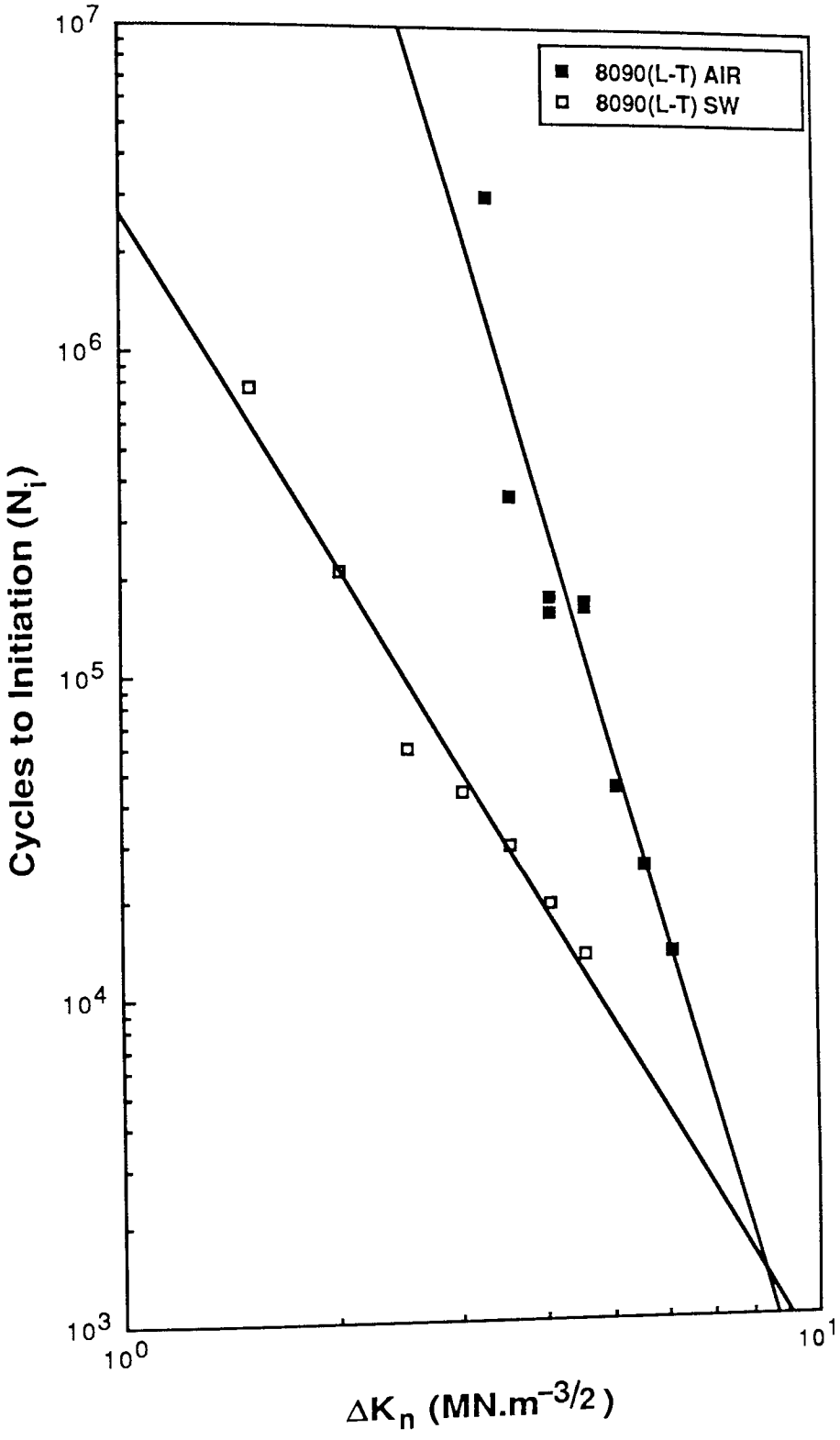

Figure 44d: 8090-T6 (L-T) fatigue crack initiation results.

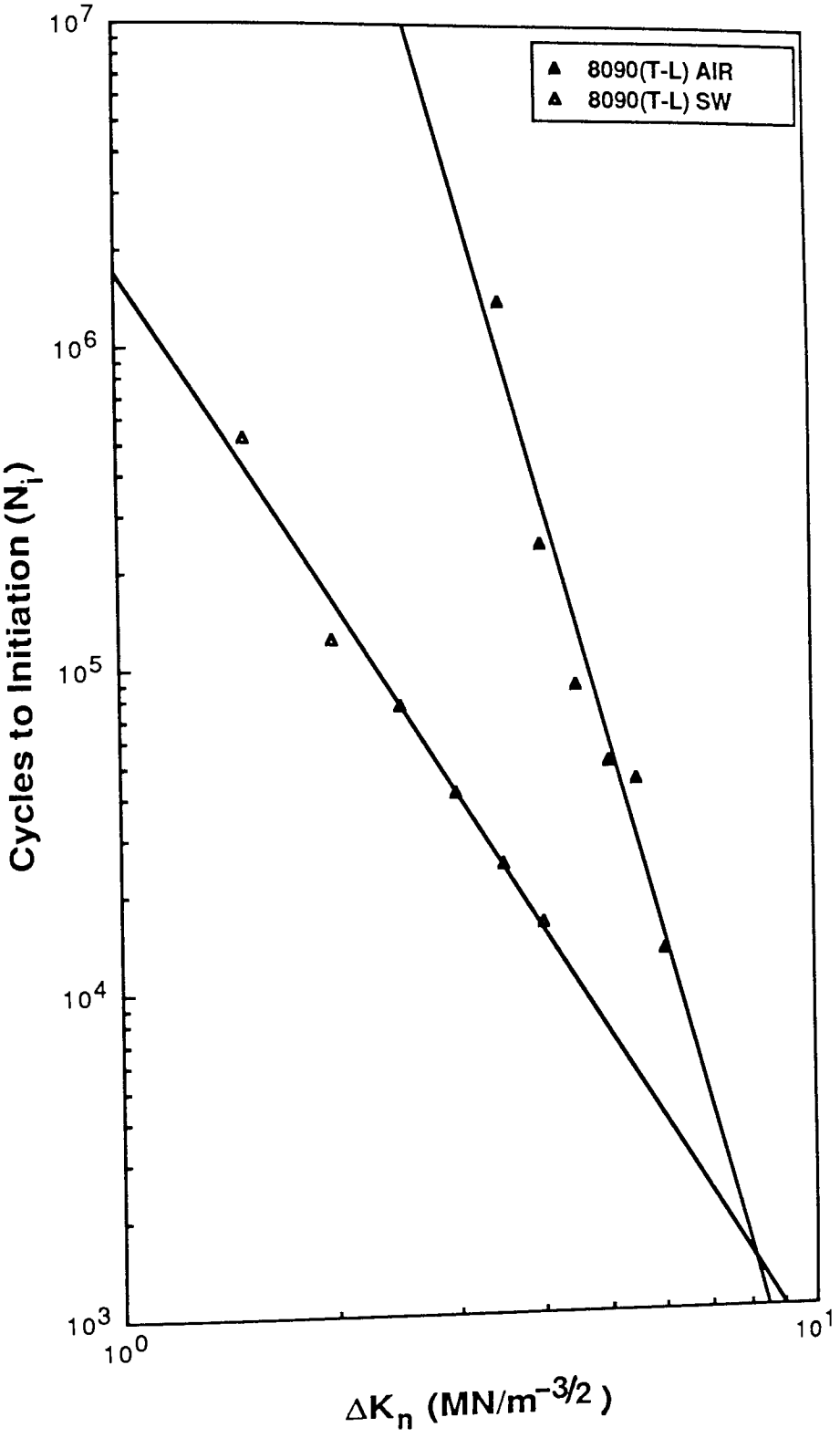

Figure 44e: 8090-T6 (T-L) fatigue crack initiation results.

		B	n
2014-T6	AIR	2.371×10^{8}	-4.997
	SALT WATER	4.176×10^{5}	-2.108
8090-T6(L-S)	AIR	8.086×10^{9}	-7.225
	SALT WATER	3.055×10^{6}	-3.358
8090-T6(L-T)	AIR	8.131×10^{9}	-7.381
	SALT WATER	2.652×10^{6}	-3.579
8090-T6(T-L)	AIR	1.484×10^{10}	-7.739
	SALT WATER	1.713×10^{6}	-3.398

Table 20: Constants B and n in the logarithmic fit of N_i versus ΔK_n.

Specimen	W (mm)	B (mm)	Notch depth (mm)
A01	20.02	10.13	3.83
A02	20.02	10.01	3.85
A04	20.02	10.13	3.80
A05	20.01	10.14	3.88
A07	20.02	10.14	3.70
A08	20.02	10.14	3.80
A10	20.01	10.14	3.66
A11	20.02	10.14	3.93
A13	20.02	10.13	3.80
A14	20.01	10.14	3.76
A16	20.02	10.14	3.78
A17	20.01	10.13	3.78
A19	20.02	10.13	3.83
A20	20.01	10.13	3.85
A22	19.99	10.14	----
A23	20.01	10.13	3.80

Table 21a: CZ20-T6 (C-L) specimen dimensions.

Specimen	W (mm)	B (mm)	Notch depth (mm)
R01	20.06	10.12	4.05
R02	19.98	10.12	3.75
R03	20.03	10.13	3.73
R04	20.03	10.13	3.88
R07	20.03	10.13	3.90
R08	20.03	10.13	3.74
R09	20.03	10.13	3.88
R10	20.02	10.13	3.90
R13	20.02	10.14	3.88
R14	20.02	10.13	3.85
R15	20.02	10.13	3.74
R16	20.02	10.13	3.74
R19	20.01	10.14	3.85
R20	20.01	10.14	3.78
R21	20.01	10.14	----
R22	20.02	10.14	3.75

Table 21b: CZ20-T6 (C-R) specimen dimensions.

Specimen	W (mm)	B (mm)	Notch depth (mm)
C01	19.93	9.69	3.83
C02	19.98	9.97	3.97
C03	19.97	9.98	3.96
C04	20.02	9.98	3.93
C05	20.01	10.01	3.95
C06	20.01	10.02	3.94
C07	20.01	10.00	3.80
C08	19.98	10.02	3.99
C09	20.00	10.00	3.88
C10	19.99	9.97	3.86

Table 21c: 2014-T6 sharp notched specimen dimensions.

Specimen	W (mm)	B (mm)	Notch depth (mm)
2001	12.02	6.03	2.36
2002	12.01	6.03	2.36
2003	12.02	6.04	----
2004	12.01	6.03	2.49
2005	11.99	6.04	2.42
2006	12.02	6.03	2.43
2007	12.02	6.02	2.48
2008	12.01	6.03	2.53
2009(T)	12.03	6.04	2.51
2010(T)	12.03	6.01	----

Table 21d: 20% Saffil/6061-T6 specimen dimensions.

Specimen	W (mm)	B (mm)	Notch depth (mm)
3001	11.99	6.02	2.52
3002	11.98	6.01	2.47
3003	12.01	6.03	2.50
3004	12.01	6.00	2.50
3005(T)	12.02	6.04	2.45

Table 21e: 30% Saffil/6061-T6 specimen dimensions.

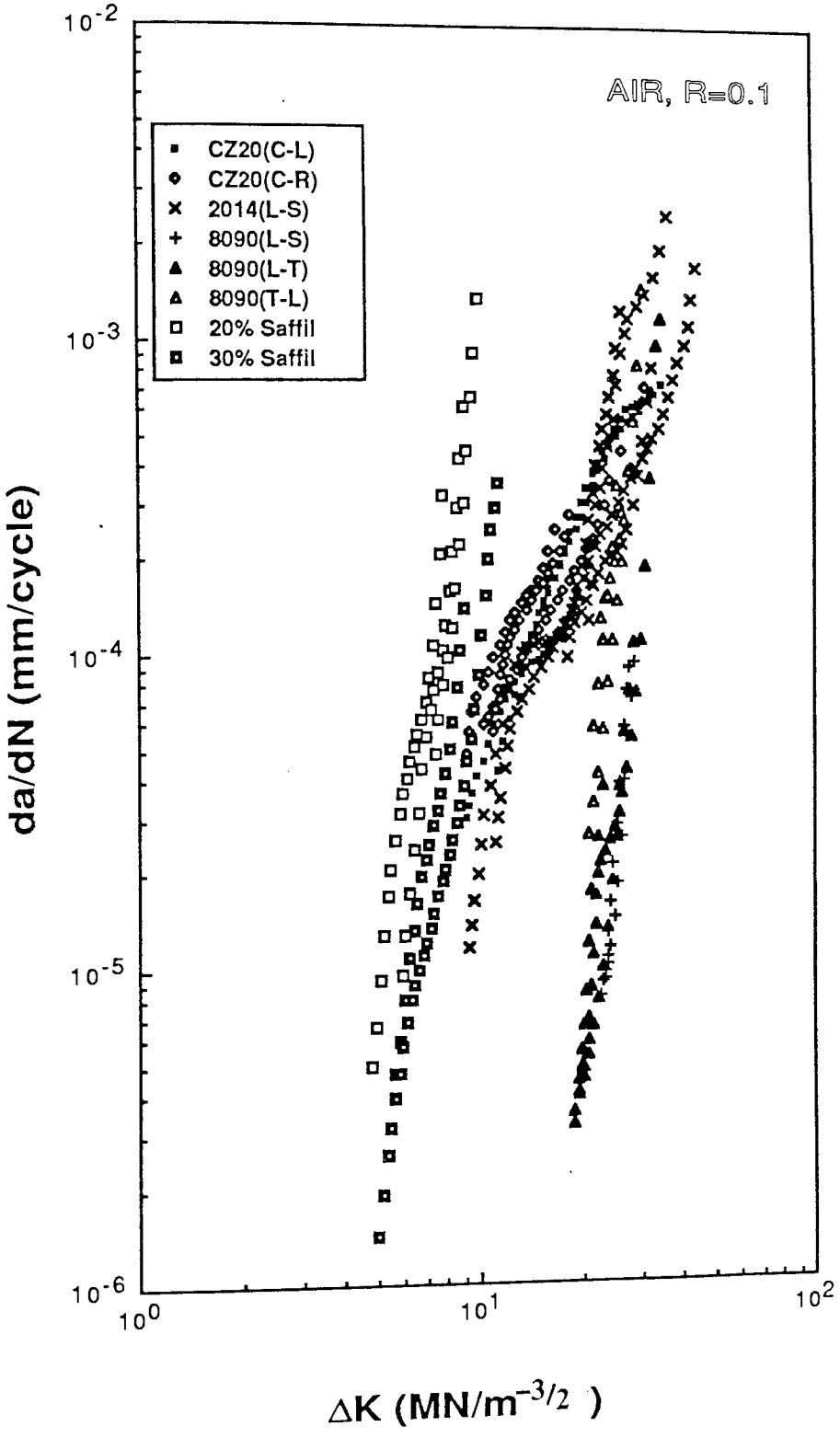

Figure 45a: Air, R=0.1 fatigue crack propagation data.

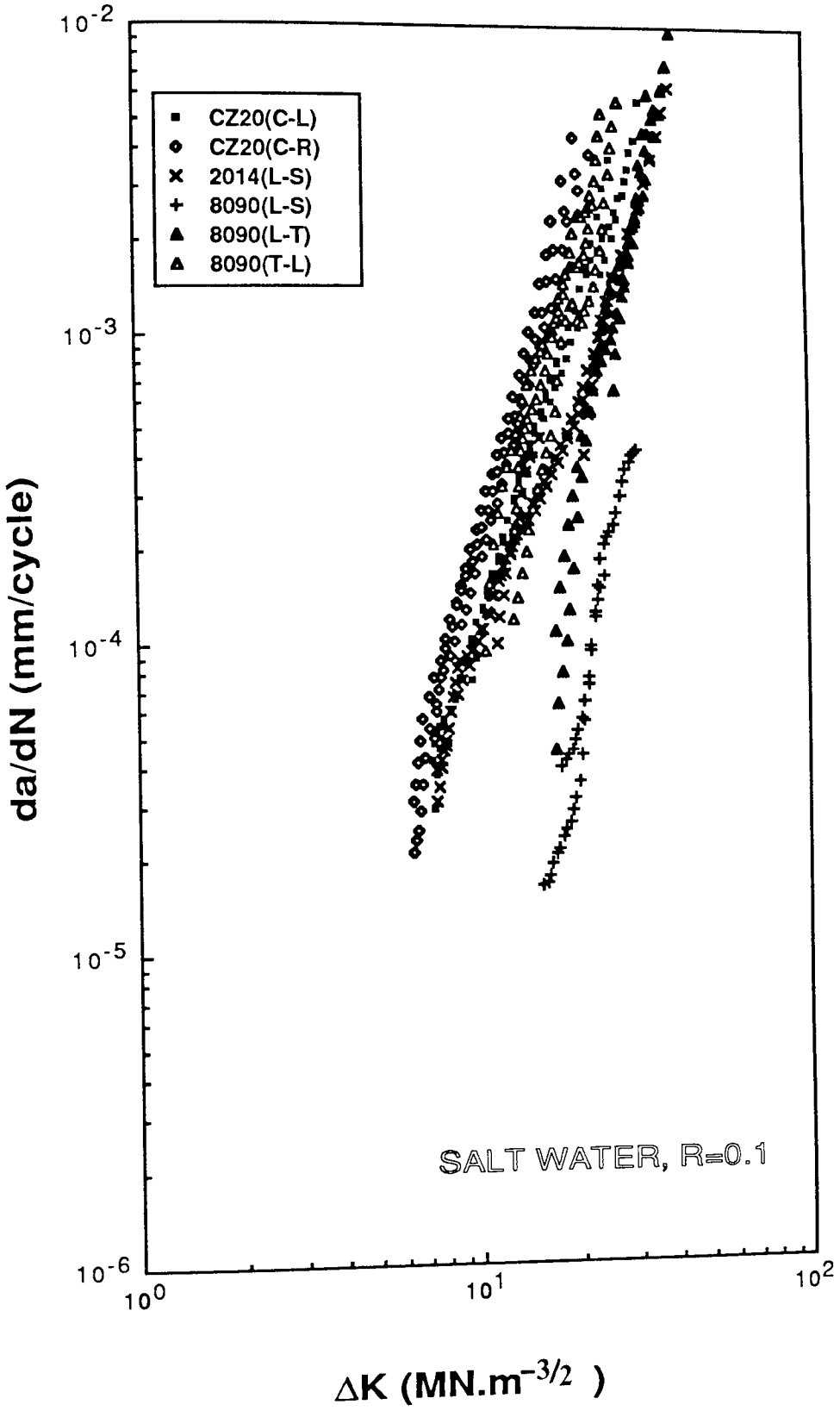

Figure 45b: Salt water, R=0.1 fatigue crack propagation data.

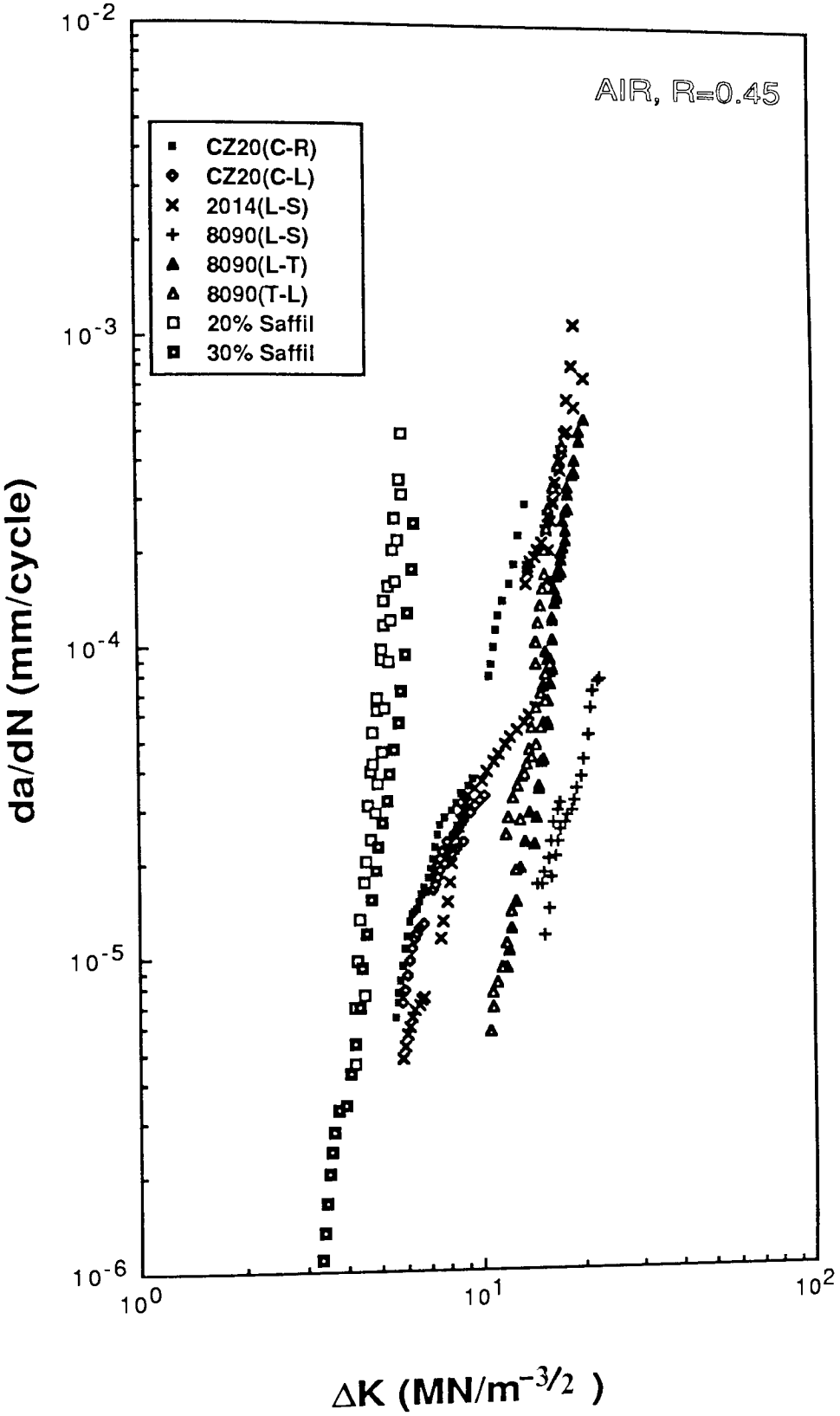

Figure 45c: Air, R=0.45 fatigue crack propagation data.

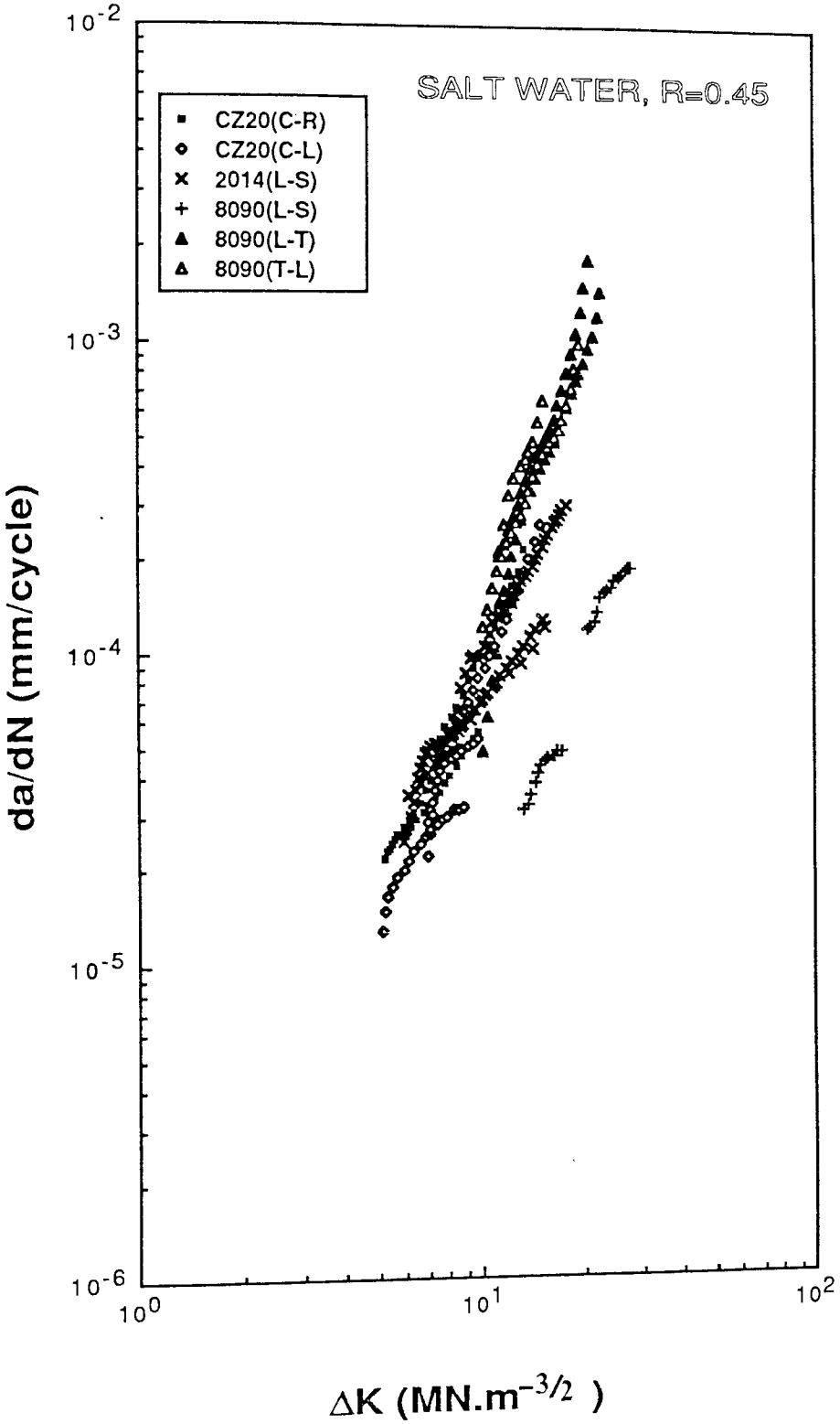

Figure 45d: Salt water, R=0.45 fatigue crack propagation data.

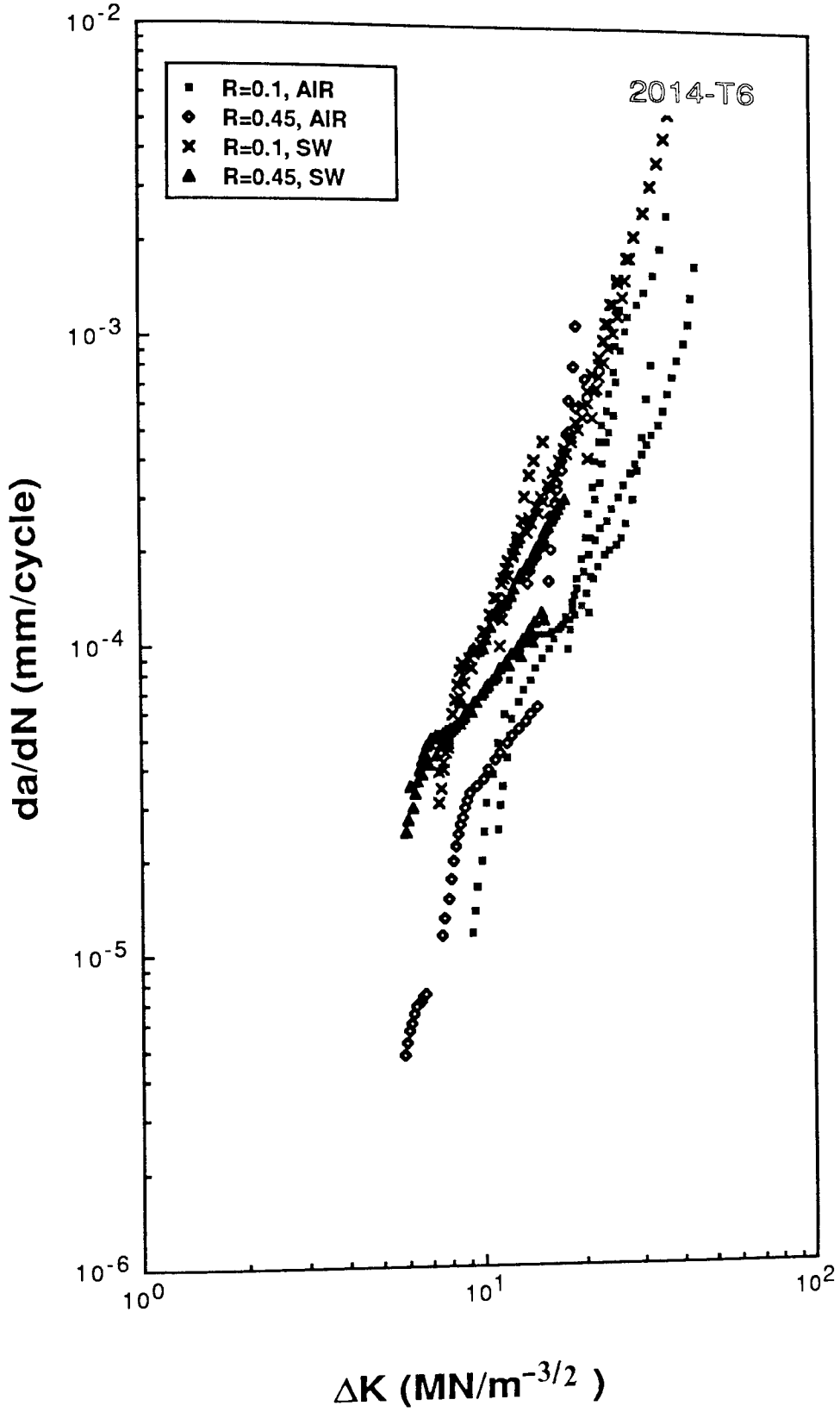

Figure 46a: 2014-T6 fatigue crack propagation data.

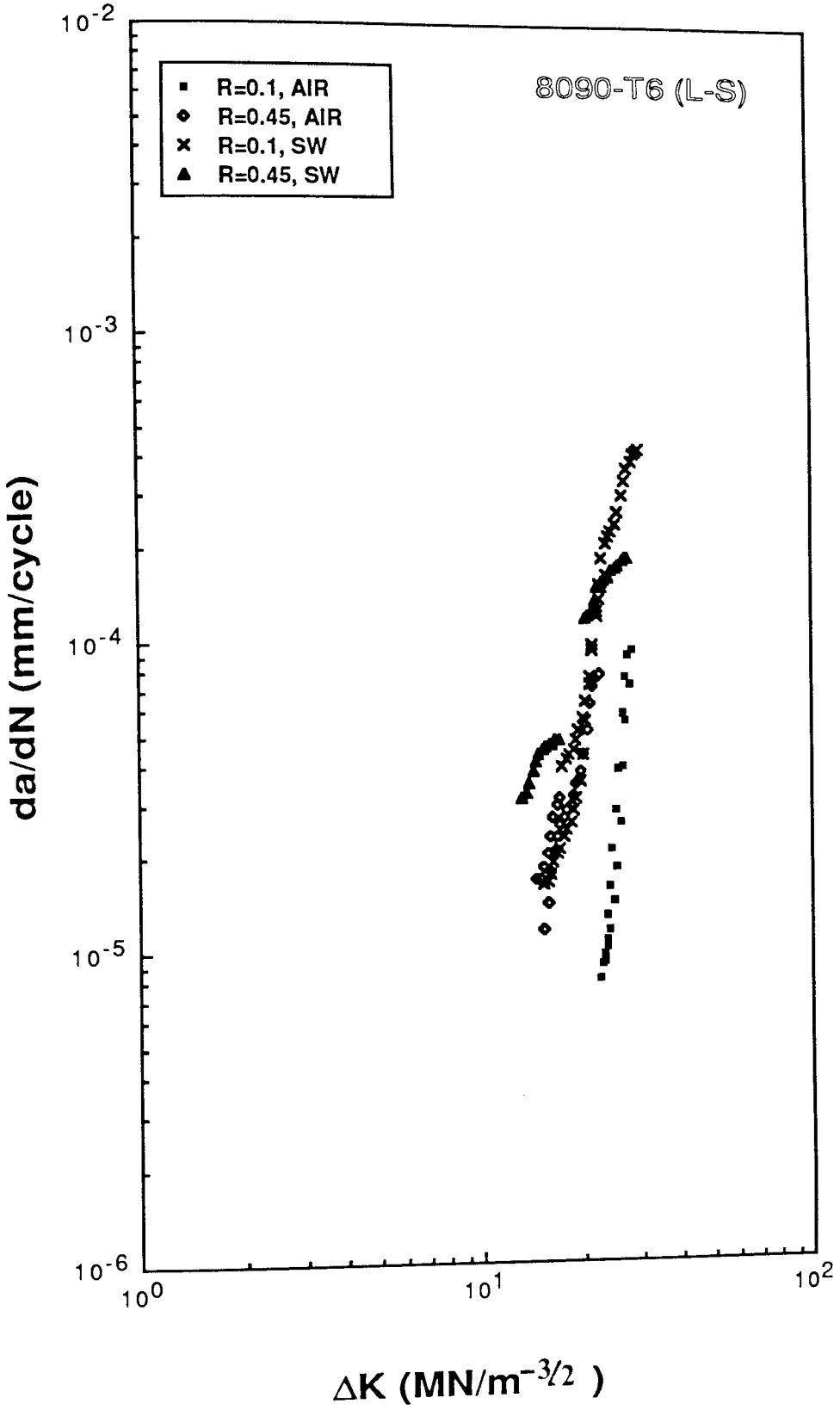

Figure 46b: 8090-T6 (L-S) fatigue crack propagation data.

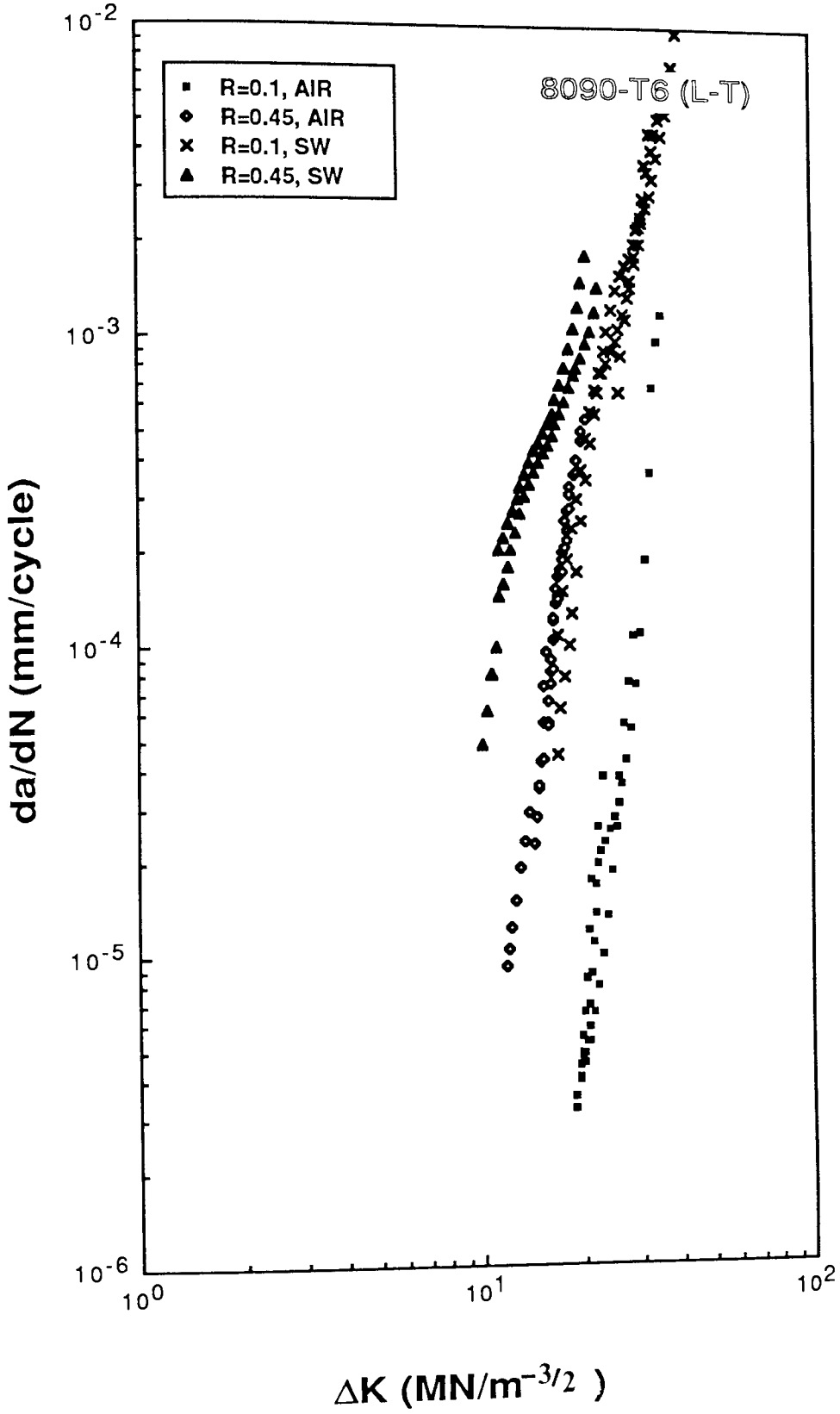

Figure 46c: 8090-T6 (L-T) fatigue crack propagation data.

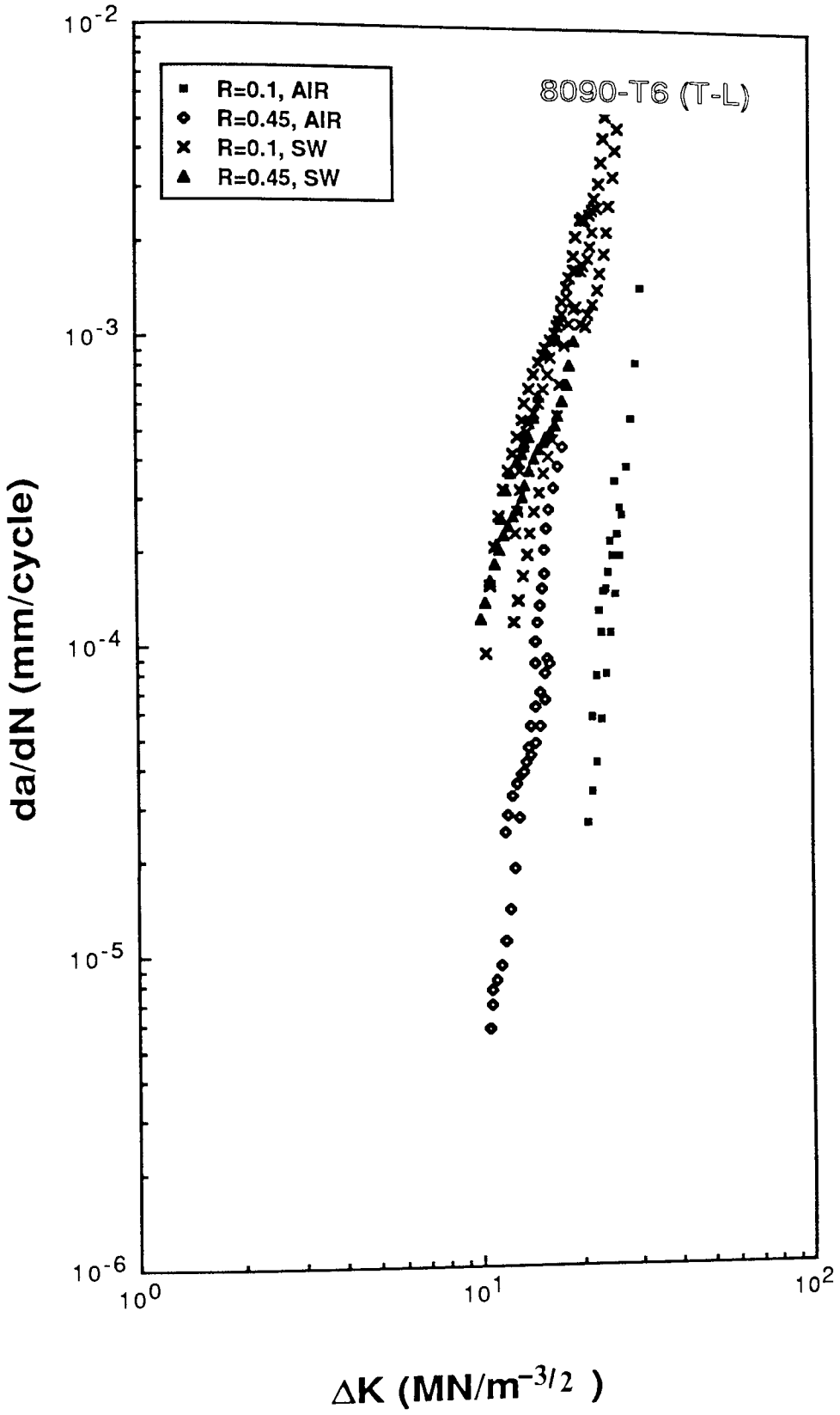

Figure 46d: 8090-T6 (T-L) fatigue crack propagation data.

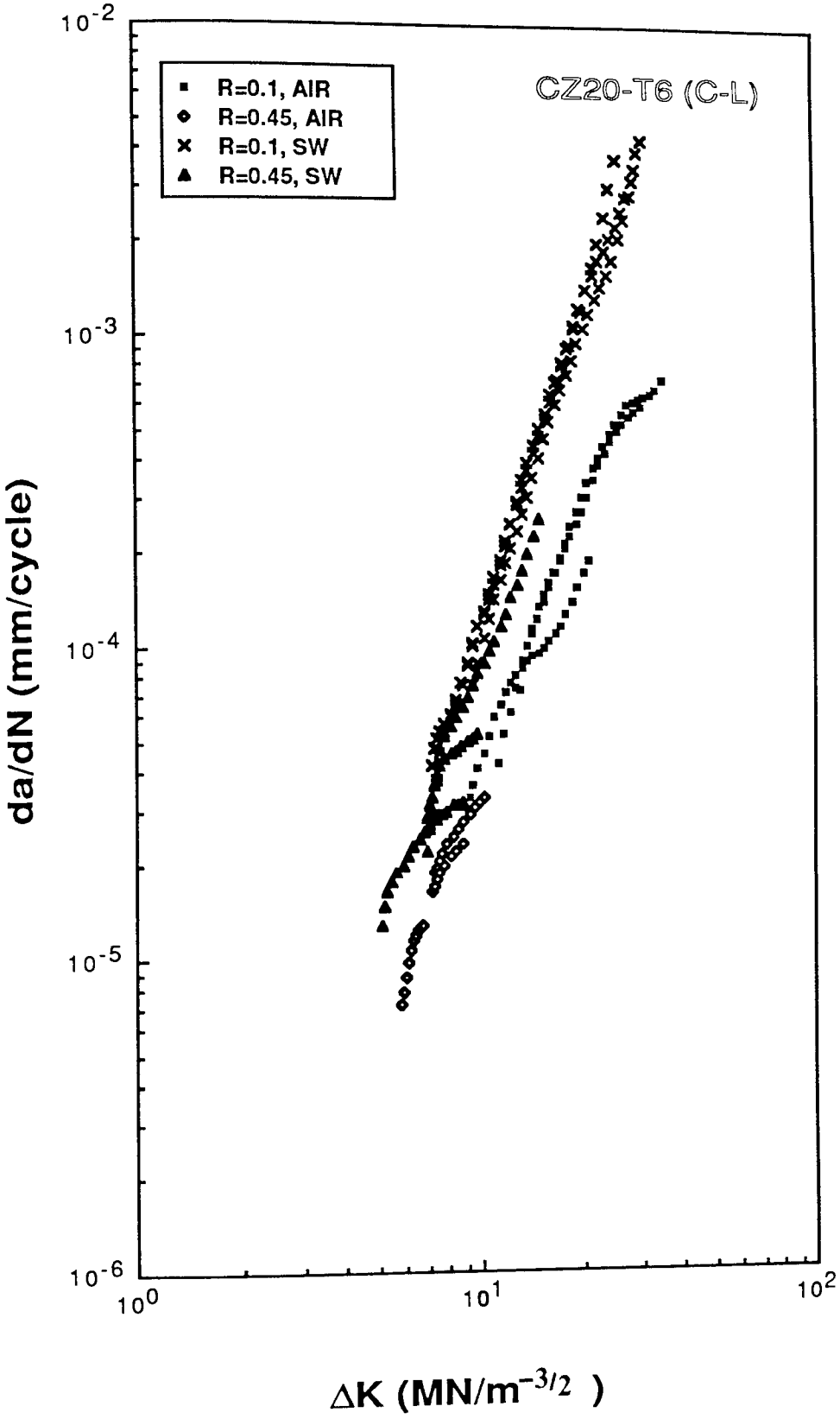

Figure 46e: CZ20-T6 (C-L) fatigue crack propagation data.

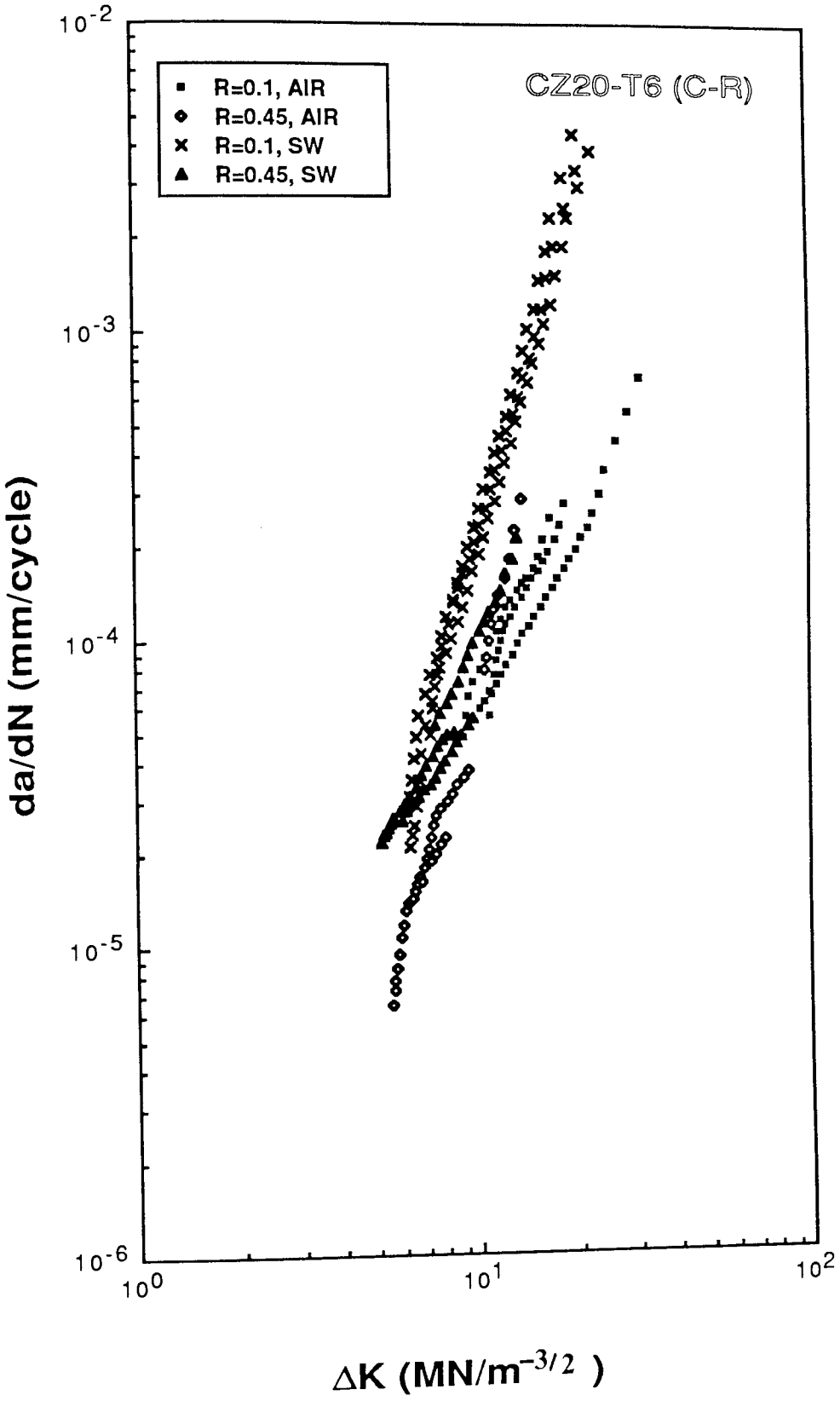

Figure 46f: CZ20-T6 (C-R) fatigue crack propagation data.

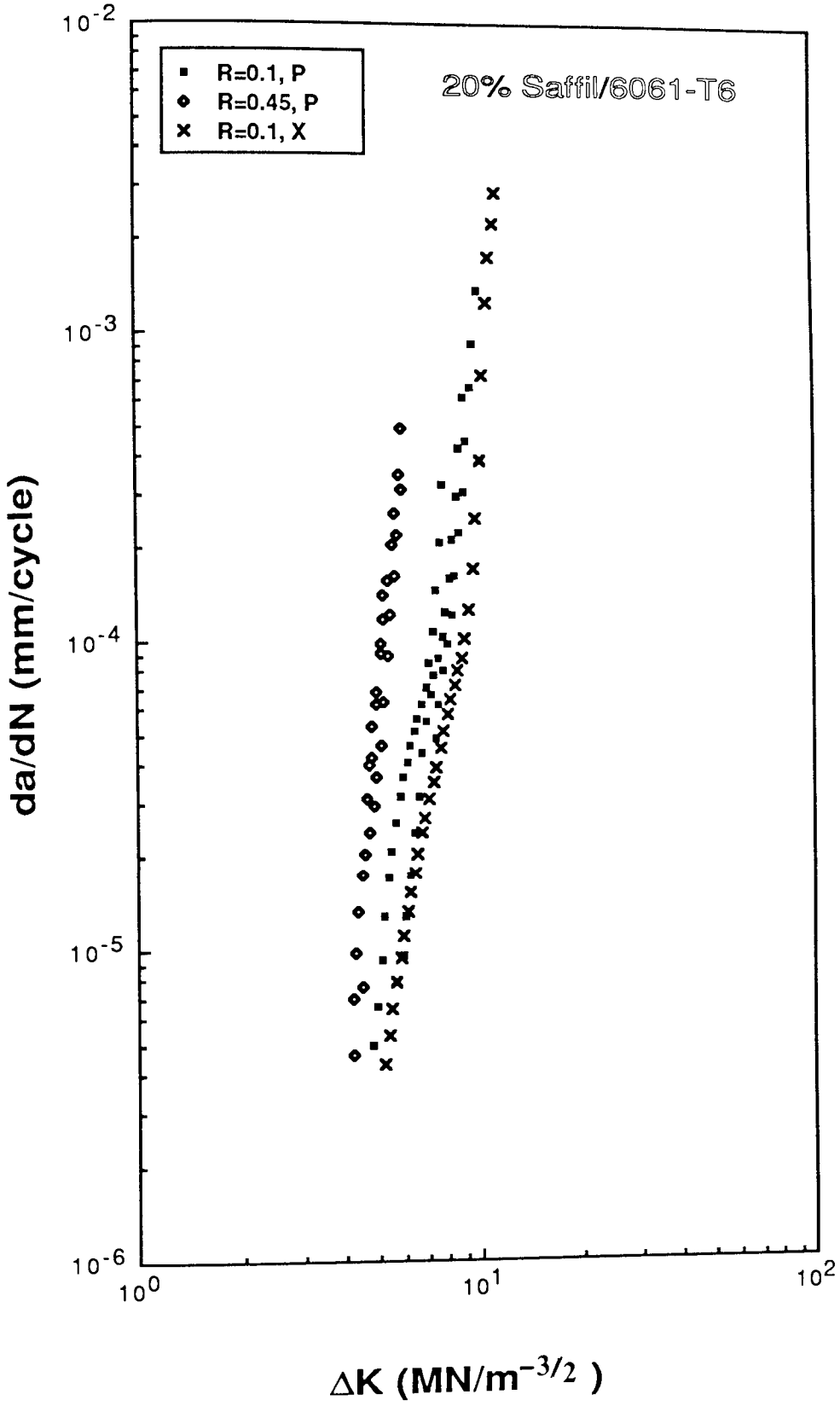

Figure 46g: 20% Saffil/6061-T6 fatigue crack propagation data.

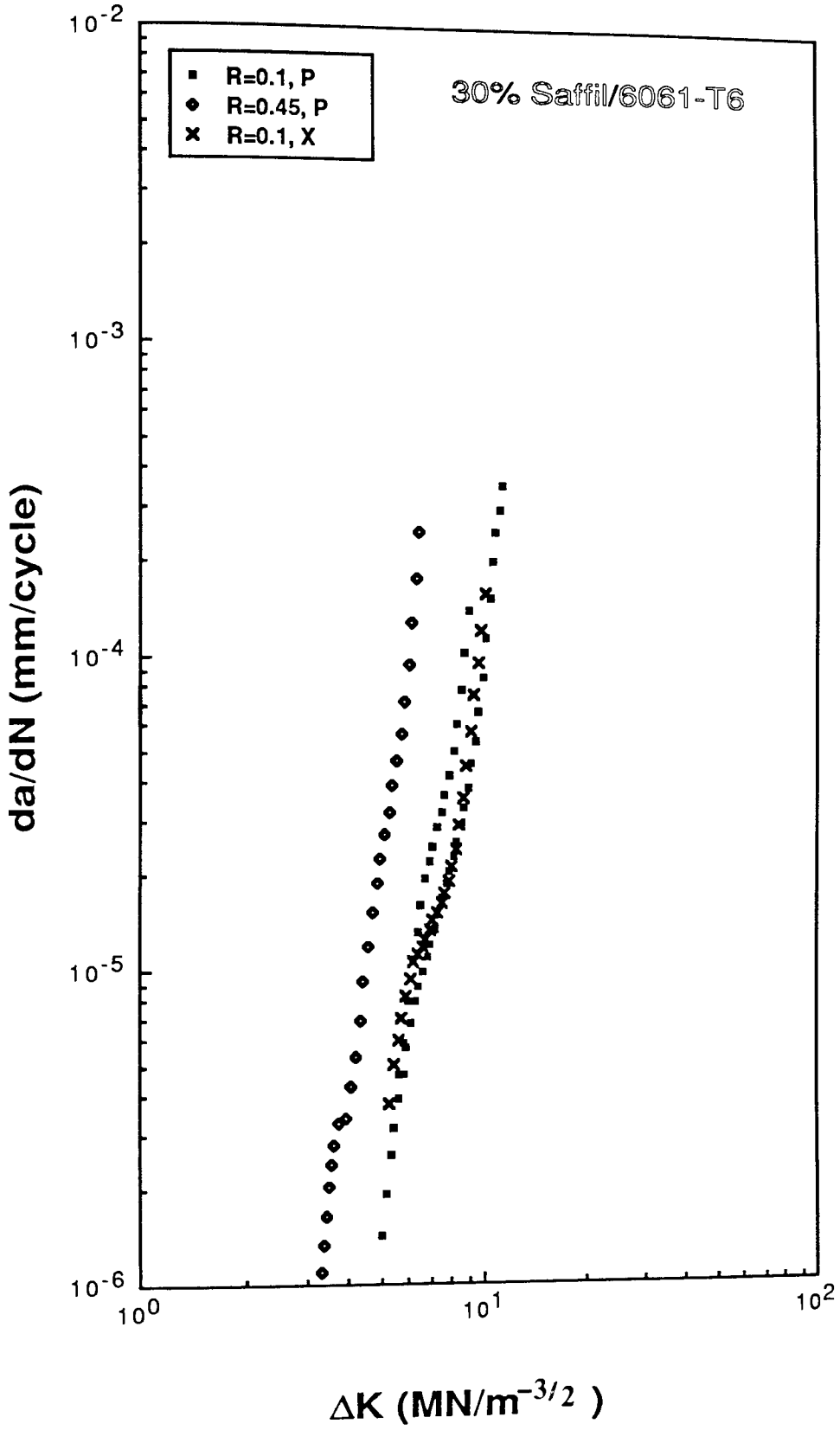

Figure 46h: 30% Saffil/6061-T6 fatigue crack propagation data.

Material	R-Value	AIR FATIGUE		CORROSION FATIGUE	
		A	n	A	n
2014-T6	0.1	4.3×10^{-8}	2.82	1.9×10^{-7}	2.75
	0.45	4.8×10^{-9}	3.94	1.0×10^{-6}	1.91
8090-T6(L-S)	0.1	4.1×10^{-21}	12.04	2.4×10^{-12}	5.69
	0.45	4.7×10^{-10}	3.86	2.5×10^{-8}	2.75
8090-T6(L-T)	0.1	2.1×10^{-17}	8.79	3.1×10^{-11}	5.36
	0.45	2.2×10^{-14}	7.99	3.1×10^{-8}	3.52
8090-T6(T-L)	0.1	2.1×10^{-17}	9.31	2.4×10^{-8}	3.73
	0.45	4.5×10^{-14}	7.98	3.0×10^{-7}	2.72
CZ20-T6(C-L)	0.1	1.3×10^{-7}	2.53	7.1×10^{-8}	3.26
	0.45	1.0×10^{-7}	2.61	1.8×10^{-7}	2.68
CZ20-T6(C-R)	0.1	9.6×10^{-7}	1.88	2.7×10^{-8}	3.91
	0.45	1.2×10^{-8}	3.78	4.1×10^{-7}	2.35
20% Saffil 6061-T6	0.1 (P)	2.0×10^{-10}	6.61		
	0.45 (P)	5.1×10^{-13}	11.63		
	0.1 (T)	2.1×10^{-11}	7.36		
30% Saffil 6061-T6	0.1 (P)	1.8×10^{-10}	5.86		
	0.45 (P)	1.1×10^{-10}	7.72		
	0.1 (T)	1.3×10^{-9}	4.88		

Table 22: Constants A and n in the logarithmic fit of da/dN versus ΔK.

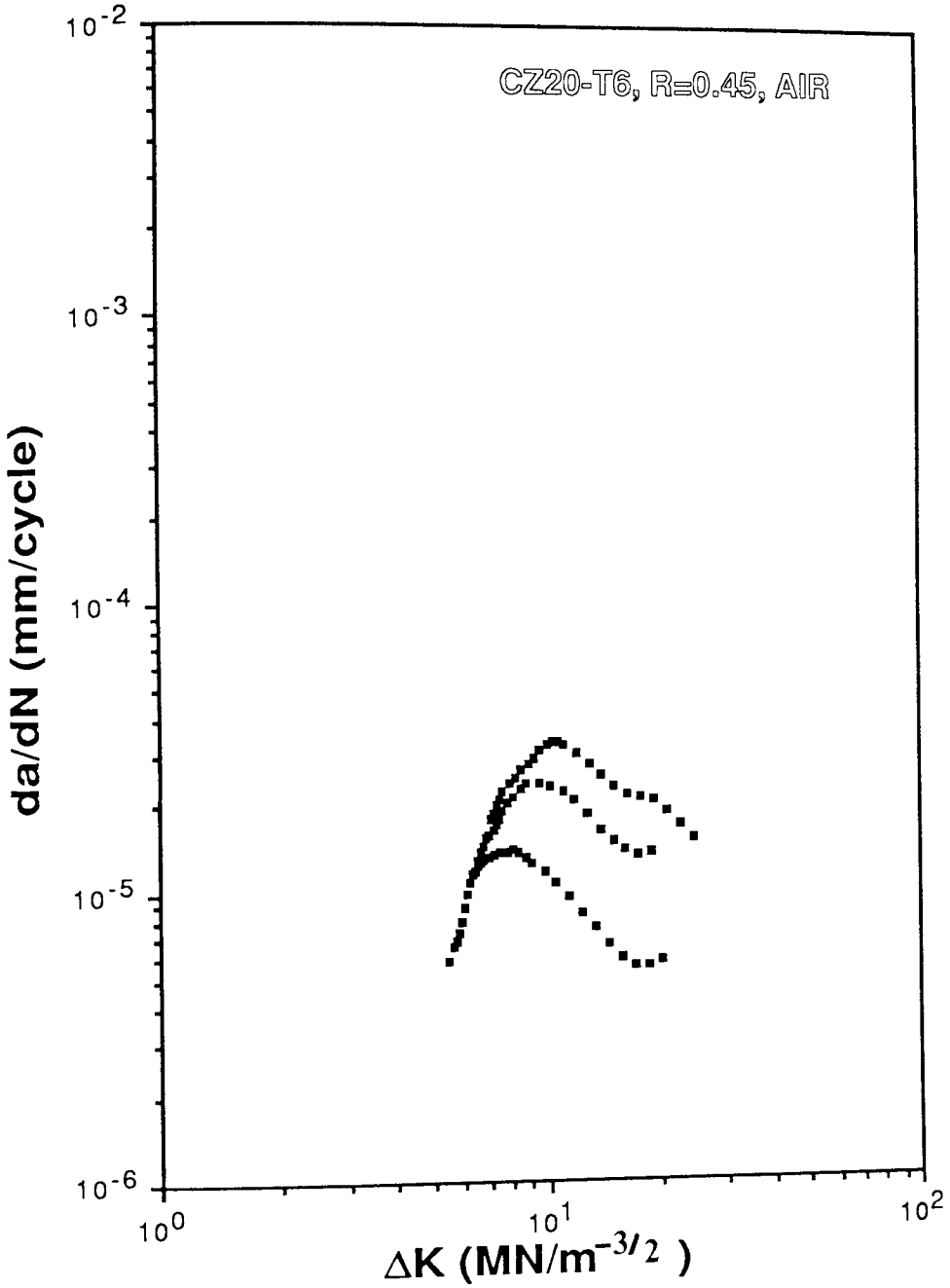

Figure 47: CZ20-T6 (C-L), R=0.45 air fatigue crack propagation data.

7.3. OTHER MECHANICAL TESTING

The results of the tensile testing are shown in tables 23 and 24. Tensile testing of 2014-T6, 8090-T6, 8090-T8 and CZ20-T6 was carried out at Dunlop Aviation Ltd. 8090-T8 showed typical tensile properties which were superior to the T6 condition, although ductility appeared unchanged. 8090-T6 showed inferior tensile properties when compared to 2014-T6. CZ20-T6 showed superior strength but inferior ductility when compared to typical tensile properties (table 14). However, strength levels in CZ20-T6 were still inferior to 2014-T6.

Tensile testing of Saffil-reinforced 6061-T6 was carried out at Aston University. Tensile properties are typical of Saffil composites, with greatly increased Young's Modulus but only slightly increased strength and a reduction in elongation to fracture when compared to properties of the unreinforced matrix alloy (table 11). Tensile properties were inferior to all of the other materials investigated. 30% Saffil-reinforced 6061-T6 showed superior properties to the 20% Saffil-reinforced material.

Material	Direction	0.2% PS (MPa)	UTS (MPa)	Elongation (%)
2014-T6	Longitudinal	481	526	10.0
8090-T8	Longitudinal	450	519	5.4
	Transverse	426	497	6.6
8090-T6	Longitudinal	345	442	6.0
	Transverse	369	458	6.5
CZ20-T6	Axial	395	468	7.0
	Tangential	420	492	12.5
	Radial	402	478	11.5

Table 23: Tensile properties of 2014-T6, 8090-T6, 8090-T6 and CZ20T6.

	0.2% PS (MPa)	UTS (MPa)	Elongation (%)	E (GPa)
20% Saffil/ 6061-T6	305	343	0.77	85.6
30% Saffil/ 6061-T6	328	358	0.73	99.9

Table 24: Tensile properties of Saffil-reinforced 6061-T6.

7.4. METALLOGRAPHY

Typical fracture surfaces for all fatigue specimens are shown in figures 48 to 53. Fracture surfaces of the rotating beam specimens are shown in figure 48, for 2014-T6 (figure 48a). and 8090-T6 (figure 48b). Crack growth directions are seen to be different with both materials. Typical fatigue fracture surfaces of the 2014-T6 specimens (smooth notched-65XX, sharp notched-CXX) are shown in figure 49, where crack fronts are seen to be slightly bowed. Typical 8090-T6 fatigue fracture surfaces are shown in figure 50, for L-S specimens (figure 50a) and L-T and T-L specimens (figure 50b). In both cases, crack fronts were irregular in shape. The coarseness of these 8090 fractures is highlighted in figure 51. Two 8090 (T-L) fatigue specimens are compared, the coarser of the two being typical of the material used in this investigation and the other being typical of present production material. A Saffil-reinforced 6061-T6 fatigue fracture surface is shown in figure 52, again showing a bowed crack front. Typical fatigue fracture surfaces of the CZ20-T6 specimens are shown in figure 53. CZ20-T6 (C-R) specimens (figure 53b) had a similar fracture appearance to 2014-T6 specimens , but (C-L) specimens fractured with some side-cracking (figure 53a).

Grain structures of the materials under investigation are shown in figures 54 to 73. The grain structure of the 2014-T6 material is shown in figure 54. The grains were basically equiaxed, with some elongation in the direction of working. An average grain size of 74μm was measured. The grain structure of 8090-T6 is shown in figure 55, at both low and high magnification. The structure shows partially or fully recrystallised grains within the original elongated grain structure, as shown in figure 56 at a higher magnification. The amount of recovery varied between grains, as shown in figure 57, from unrecrystallised to a pronounced subgrain structure to possibly fully recrystallised, equiaxed grains. The average size of these subgrains was measured to be 6μm in diameter. The 8090-T8 grain structure is shown in figure 58, with unrecrystallised, elongated grains. These elongated grains were much coarser in the centre of the rolled plate (figure 58a) than at the edge (figure 58b). The average grain thickness was measured to be 75μm in the centre to 6μm at the edge of the plate. The non-metallic material on the original grain boundaries could be seen much more clearly in the unetched condition, as shown in figure 59. This material was studied in the

SEM, as shown in figure 60, and was found to contain fluorine.

The grain structure of the CZ20-T6 forging is shown in figure 61. The very fine grains were equiaxed, with an average measured grain size of 2 to 3μm.

The structure of the Saffil-reinforced 6061-T6 material is shown in figure 62. The planar random distribution of fibres is shown at higher magnifications in figures 63, 64 and 65. Figure 63 shows the 20% Saffil/6061-T6 material in the plane of the disc, and at right angles to this plane (the through-thickness plane) in figure 64. Figure 65 shows the 30% Saffil/6061-T6 material in the through-thickness plane. Figures 64b and 65b are etched, showing the fine precipitation in the matrix. A lot of non-metallic inclusions were found in the structure, as shown in figure 66. Some of these inclusions were found to be very irregular in shape, as shown in figure 67, with sizes upto 0.5mm. The distribution of fibres within the structure varied, some areas having sparse reinforcement (figure 68a) and others having dense reinforcement (figure 68b). Some areas showed no reinforcement, as shown in figure 69. Some unreinforced areas appeared as though the original Saffil preform had cracked, as shown in figure 70. Electron micrographs of polished and etched Saffil/6061-T6 showed fibre diameters were mostly in the quoted range of 2-5μm, but some fibres were upto 15μm in diameter, as shown in figure 71. Fibre distribution in the un-infiltrated Saffil preform is shown in figure 72.

Fracture surfaces of the materials under investigation are shown in figures 73 to 102. 2014-T6 fatigue surfaces are shown in figure 73, at low (figure 73a) and high (figure 73b) levels of ΔK. Only limited evidence of striations (figure 74) could be seen, at low levels of ΔK. At high levels of ΔK the dimpling that occured was initiated from intermetallic particles of 1-2μm size (figure 75). The same dimpling occurred on fast fracture surfaces (figure 76).

Typical 8090-T6 fatigue surfaces are shown in figure 77, for L-S (figure 77a), L-T (figure 77b) and T-L (figure 77c) specimens. L-S fatigue fracture surfaces were a lot coarser than L-T or T-L surfaces. The preference of a crack to grow in a longitudinal direction in un-side-grooved L-S specimens is shown in figure 78. Optical microscopy showed these longitudinal cracks to follow the non-metallic particles along the elongated grain boundaries, as shown in figure 79. Optical and electron microscopy showed this longitudinal cracking to be a combination of delamination of longitudinal grain boundaries and transgranular shear,

as shown in figure 80. However, on close examination, figure 81, the grain boundary delamination was seen to be ductile, very shallow dimples being present on its surface. All 8090-T6 fatigue specimens showed regions of intergranular failure and transgranular shear, with selected areas of planar slip within the original elongated grains, as shown in figure 82. This planar slip occurred on more than one plane, as shown in figure 83. Only limited evidence of striations could be seen on 8090-T6 fatigue specimens, figure 84.

Typical fast fracture surfaces on the 8090-T6 fatigue specimens are shown in figure 85. A large amount of intergranular delamination can be seen. In L-T and T-L specimens this delamination produced fissures, as shown in figures 85b and 85c and figure 50. Along with this intergranular failure, transgranular failure, involving planar slip (figure 86), and ductile failure (figure 87) occurred.

Corrosion fatigue surfaces were similar to air fatigue fracture surfaces in 8090-T6. Any changes in mechanism were difficult to detect, due to the amount of corrosion product on the fracture surfaces. All of the same failure modes were detected, but in some cases slip planes showed 'stepping' on their surface, as shown in figure 88. There was also a small amount of corrosive attack of slip surfaces, as shown in figure 89. Corrosive attack on the smooth notches of corrosion fatigue specimens is shown in figure 90, showing increased pitting in 2014-T6 when compared to 8090-T6.

CZ20-T6 fatigue fracture surfaces were very similar in both C-L and C-R orientations, as shown in figure 91. Again, the fatigue fracture surfaces coarsened with increasing ΔK, as shown in figure 92. At higher magnification, figure 93, outlines of the grains could be seen. In C-L specimens some cracking occurred in the last areas of fatigue fracture, both on a large scale (figure 94a) and a microscale (figure 94b). As with the 2014-T6 fatigue specimens, fast fracture in the CZ20-T6 specimens consisted mainly of dimpling around particles. However, this dimpling was on a much finer scale in CZ20-T6 specimens, as shown in figure 95. Corrosion fatigue fracture surfaces were similar to air fatigue surfaces, but detailed examination was not possible due to the amount of corrosion product on these fracture surfaces.

Typical fatigue fracture surfaces for Saffil-reinforced 6061-T6 are shown in figure 96.

These were typical of both 20% and 30% Saffil material. Closer examination of these surfaces, figure 97, shows them to be different at low and high levels of ΔK. Fatigue fracture surfaces of Saffil/6061-T6 (T) specimens, figure 98, with crack growth in the through-thickness direction, were similar to Saffil/6061-T6 (P) specimens. The inclusions seen in polished specimens were also seen on fatigue fracture surfaces, as shown in figure 99. Fracture surfaces in Saffil/6061-T6 tensile specimens were identical to fast fracture in fatigue specimens, and were similar in both 20% and 30% Saffil material, as shown in figure 100. Close-up examination of these surfaces showed dimple formation around the fractured fibres, as shown in figure 101. Some evidence of fibre pull-out could be seen (figure 102).

(a)

(b)

Figure 48: Fracture surfaces for 2014-T6 (a) and 8090-T6 (b) rotating beam specimens.

(a)

(b)

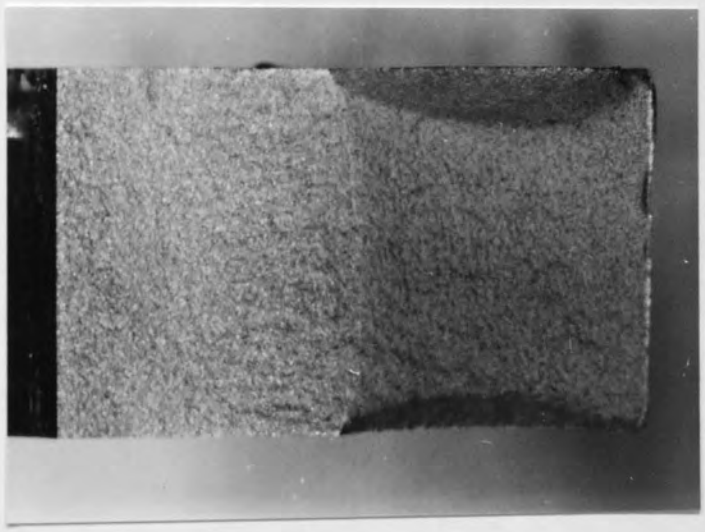

Figure 49: Typical fracture surfaces for 2014-T6 smooth notched (65XX) (a) and sharp notched (CXX) (b) specimens.

(a)

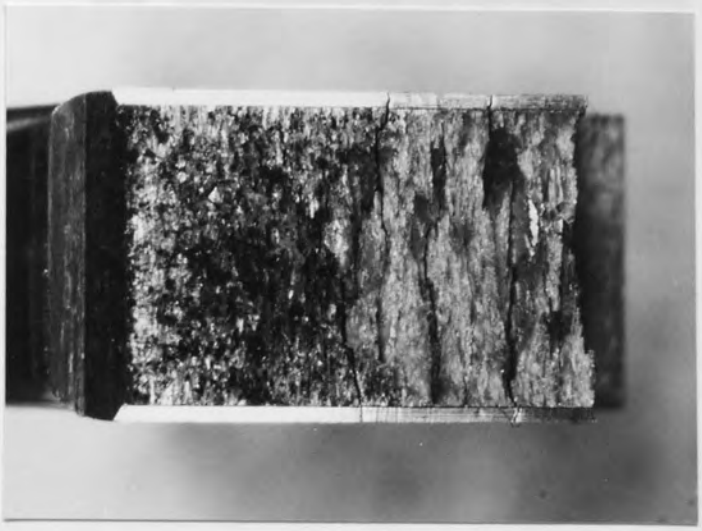

(b)

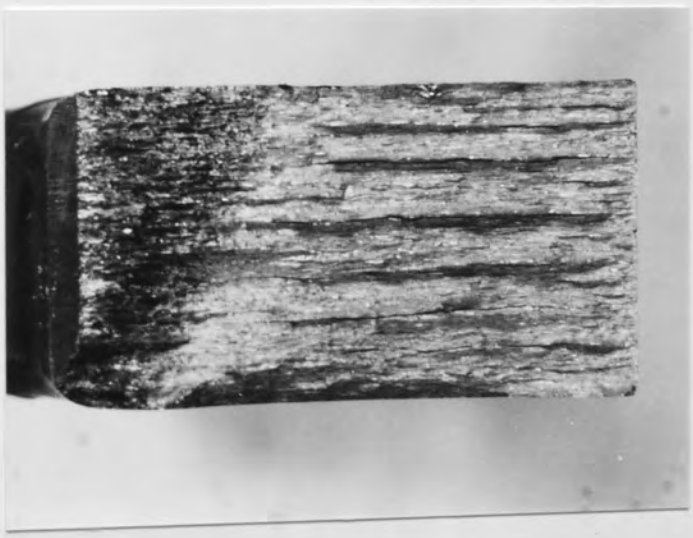

Figure 50: Typical fatigue fracture surfaces for 8090-T6 (L-S) (a) and (L-T) and (T-L) (b) specimens.

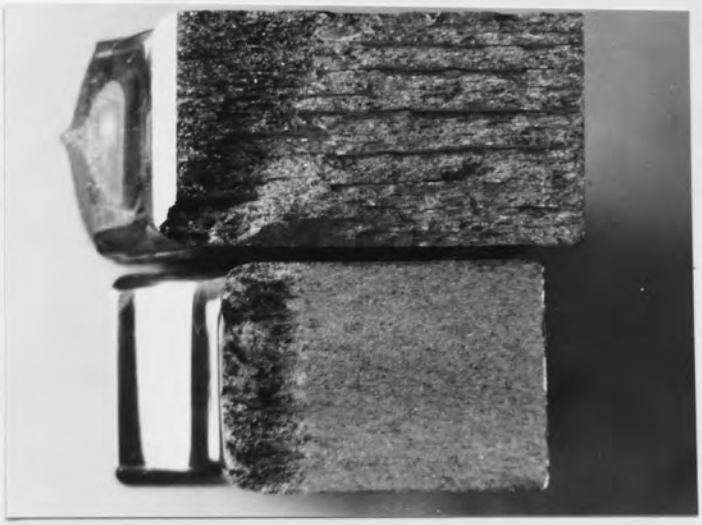

Figure 51: Comparison of the coarseness of fracture surfaces of material used in this investigation (top) and present production material (bottom).

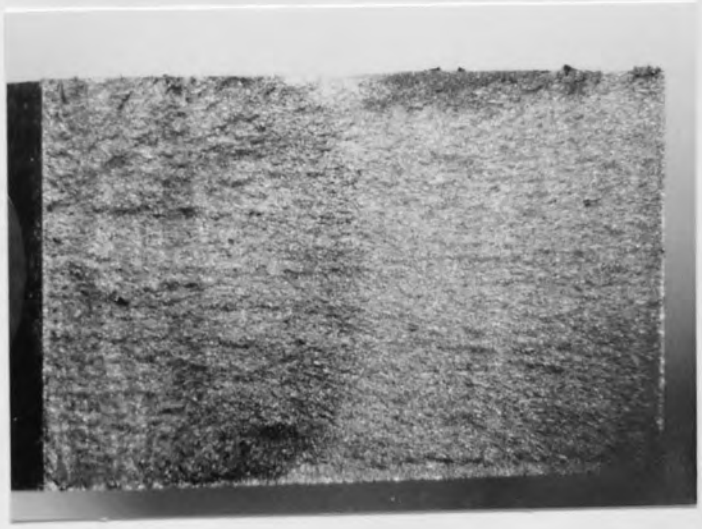

Figure 52: Typical fatigue fracture surface for Saffil-reinforced 6061-T6 specimens.

(a)

(b)

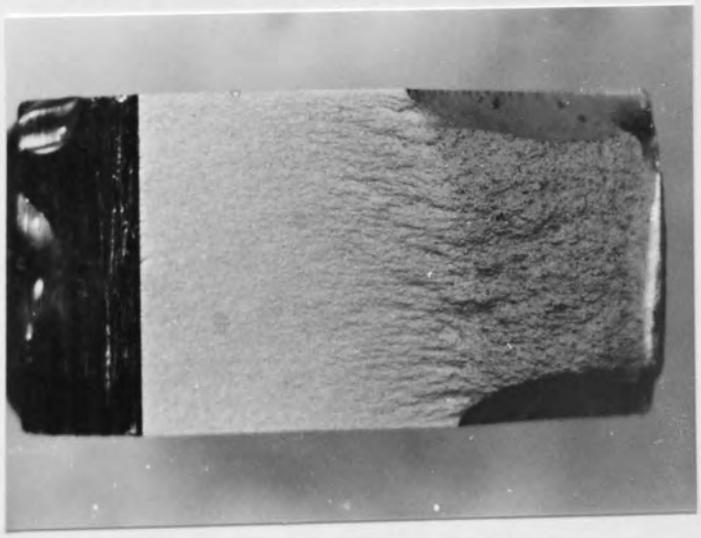

Figure 53: Typical fatigue fracture surfaces for CZ20-T6 (C-L) (a) and (C-R) (b) specimens.

Figure 54: Grain structure of 2014-T6 (x68).

(a)

(b)

Figure 55: Grain structure of 8090-T6 at x68 (a) and x340 (b).

Figure 56: 8090-T6 grain structure (x680).

Figure 57: Variance in the amount of recovery within the elongated grains in 8090-T6 (x340).

(a)

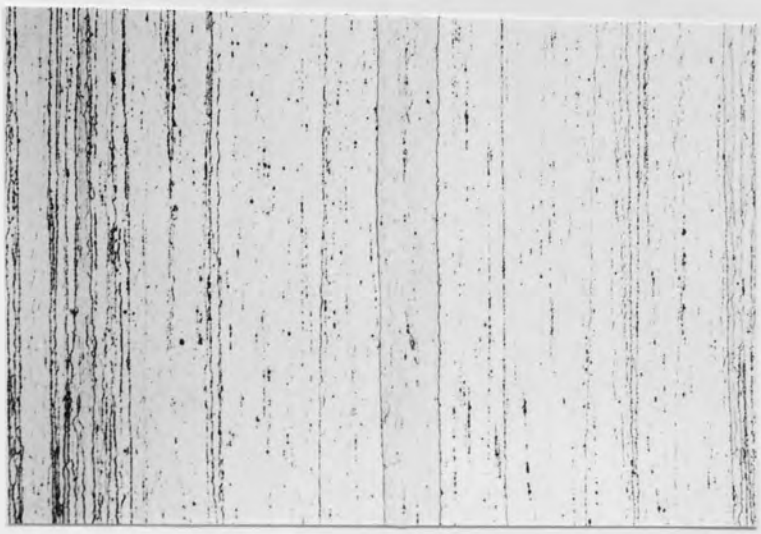

(b)

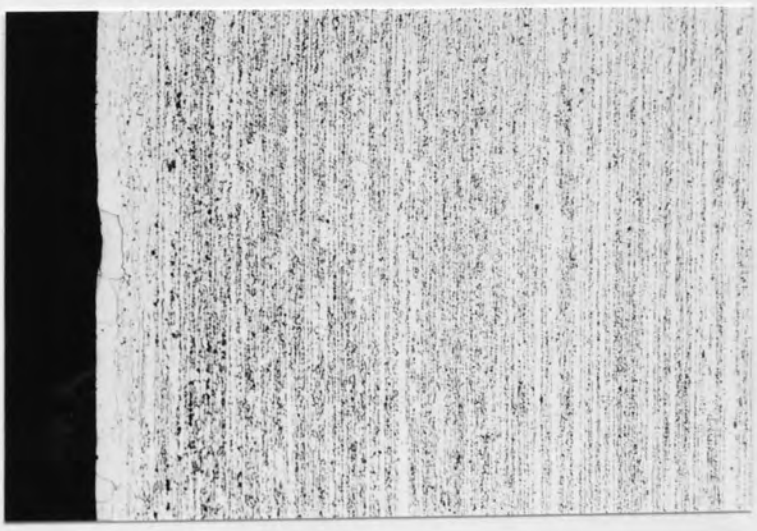

Figure 58: Grain structure of 8090-T8 at the centre (a) and edge (b) of the rolled plate. (x88).

(a)

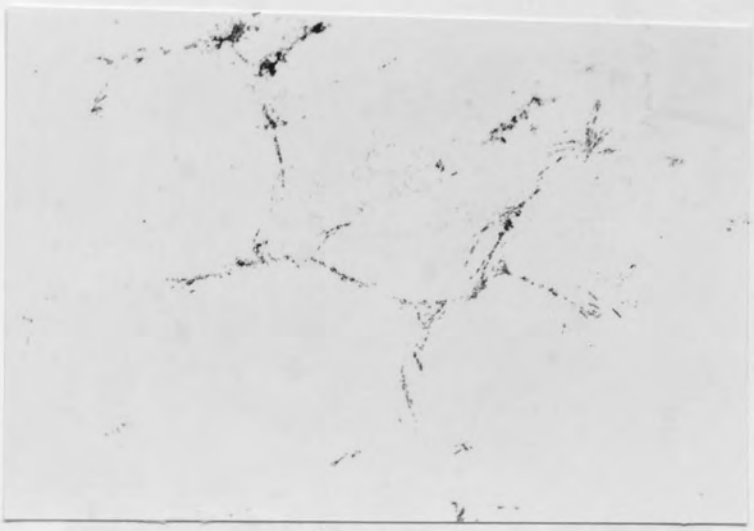

(b)

Figure 59: Unetched (a) and etched (b) views of grain structure and intergranular material (x136).

Figure 60: Intergranular precipitates in 8090.

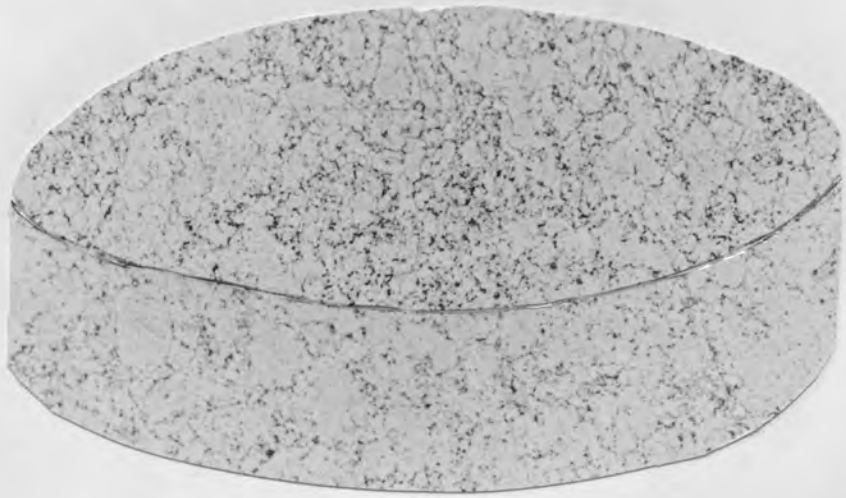

Figure 61: Grain structure of CZ20-T6 (x340).

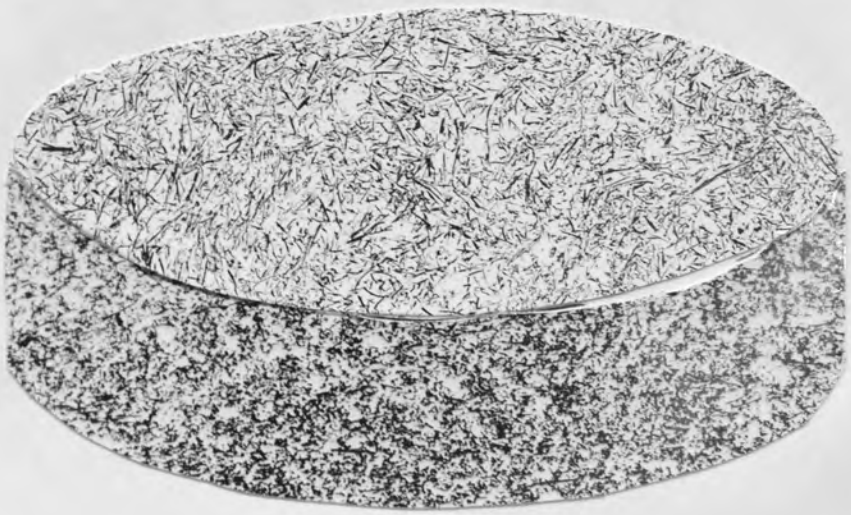

Figure 62: Structure of Saffil-reinforced 6061-T6 (x34).

(a)

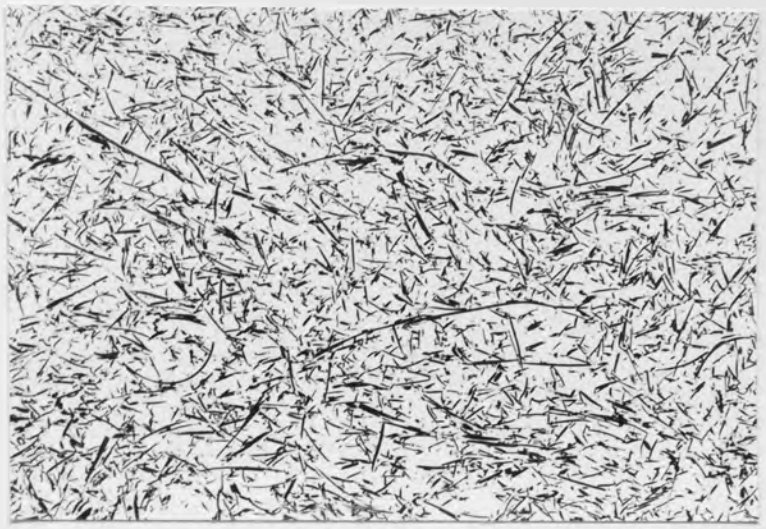

(b)

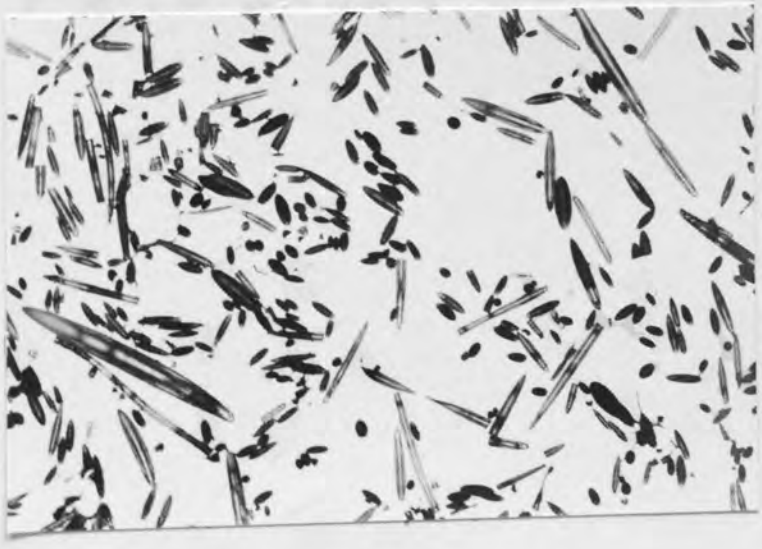

Figure 63: 20% Saffil/6061-T6 in-plane structure, x68 (a) and x340 (b).

(a)

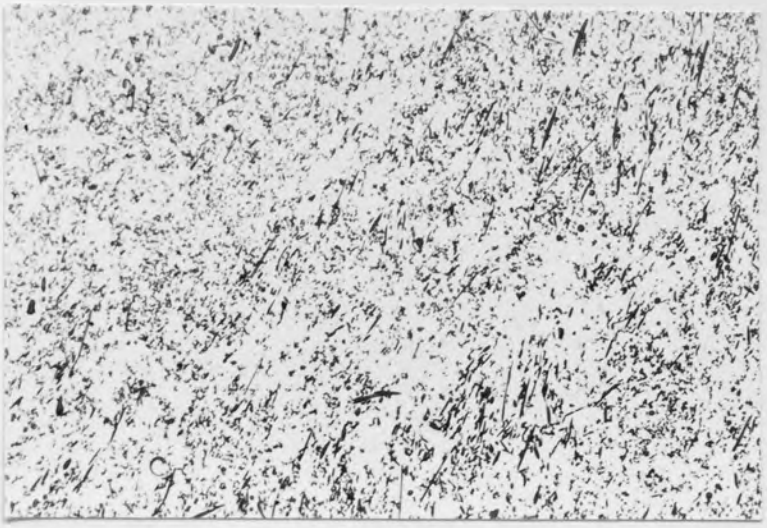

(b)

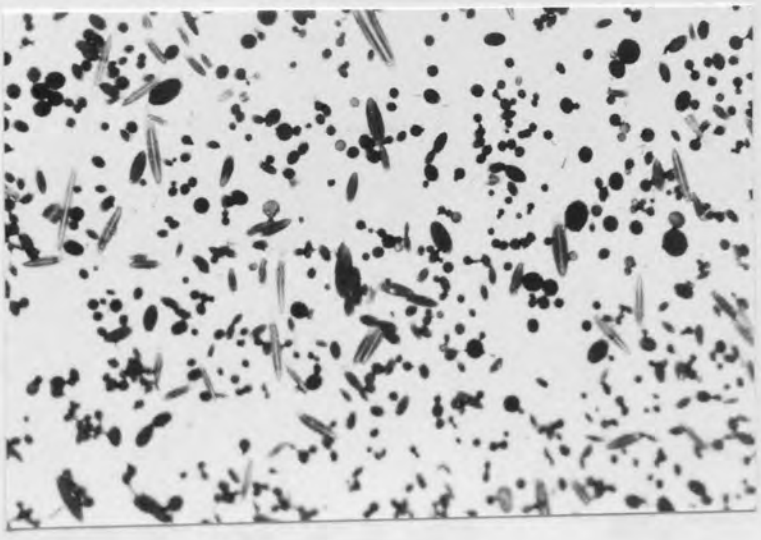

Figure 64: 20% Saffil/6061-T6 through-thickness plane structure, x68 (a) and x340 (b).

(a)

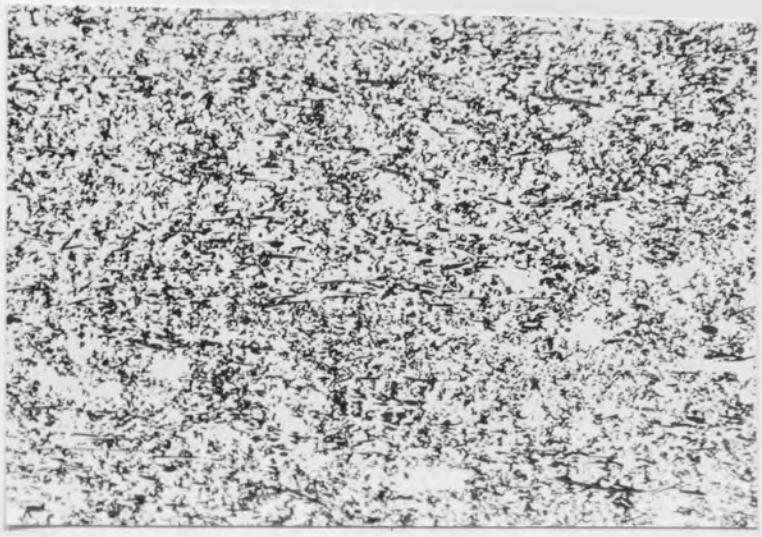

(b)

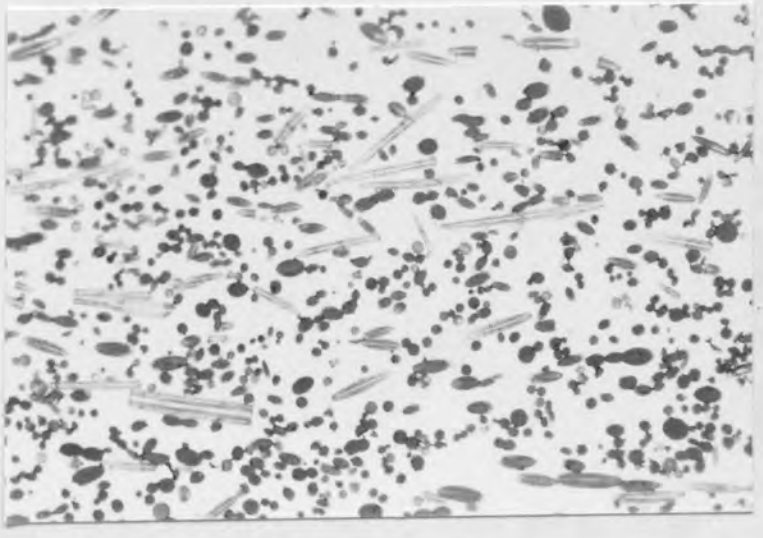

Figure 65: 30% Saffil/6061-T6 through-thickness plane structure, x68 (a) and x340 (b).

Figure 66: Distribution of non-metallic inclusions in the Saffil/6061-T6 structure (x34).

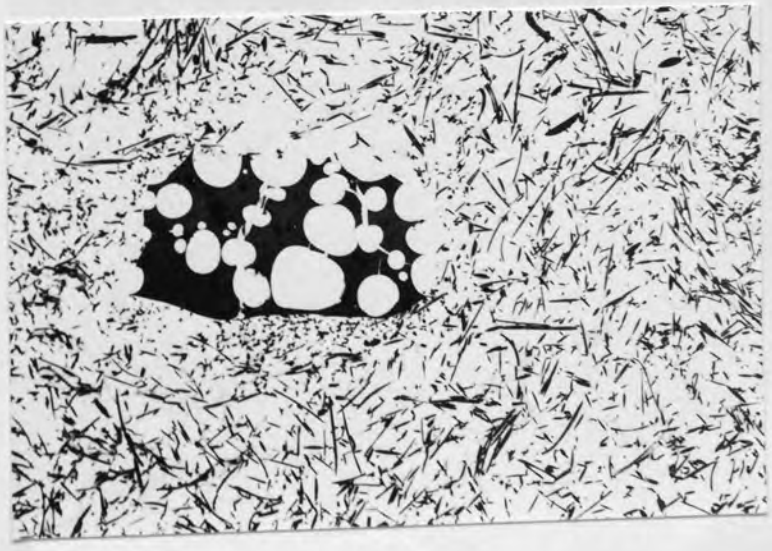

Figure 67: Non-metallic inclusion within the Saffil/6061-T6 structure (x134).

(a)

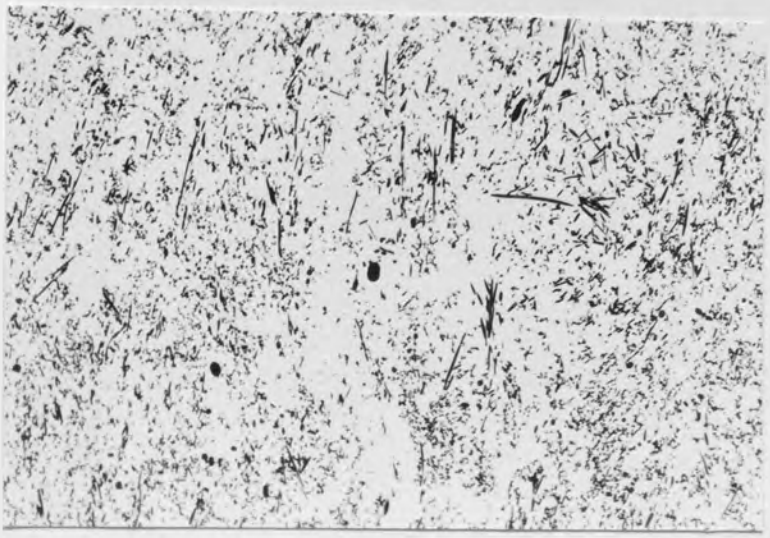

(b)

Figure 68: Variation in density of Saffil reinforcement (X68).

Figure 69: Unreinforced areas in Saffil/6061-T6 (x34).

Figure 70: Preform cracking (x34).

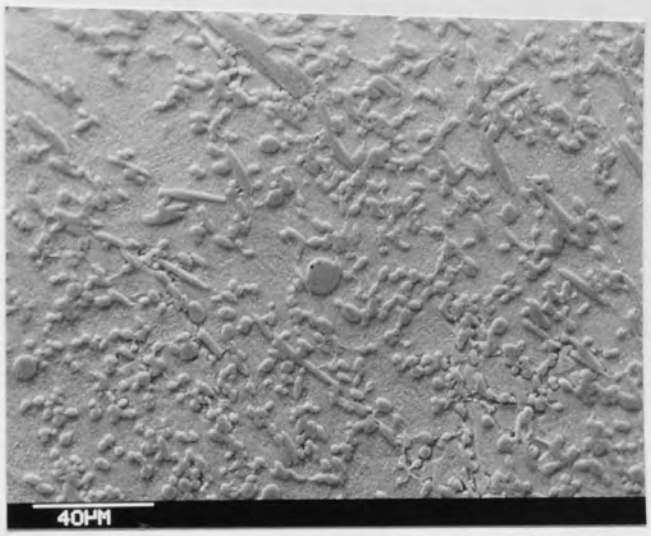

Figure 71: Saffil fibre diameter distribution.

Figure 72: Uninfiltrated Saffil fibres.

(a)

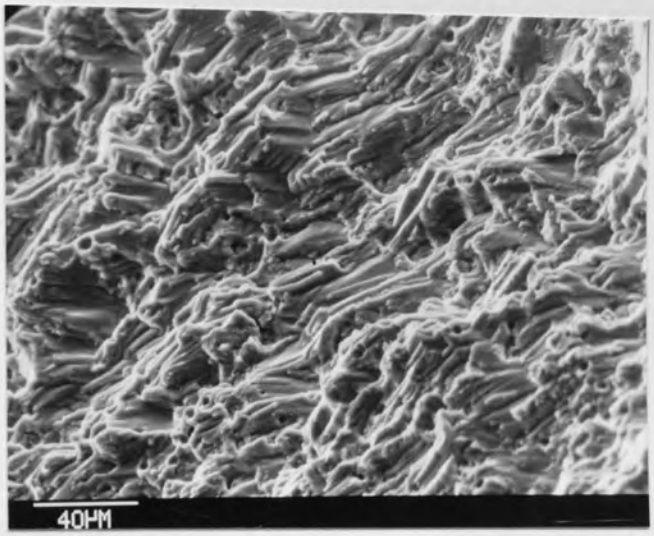

(b)

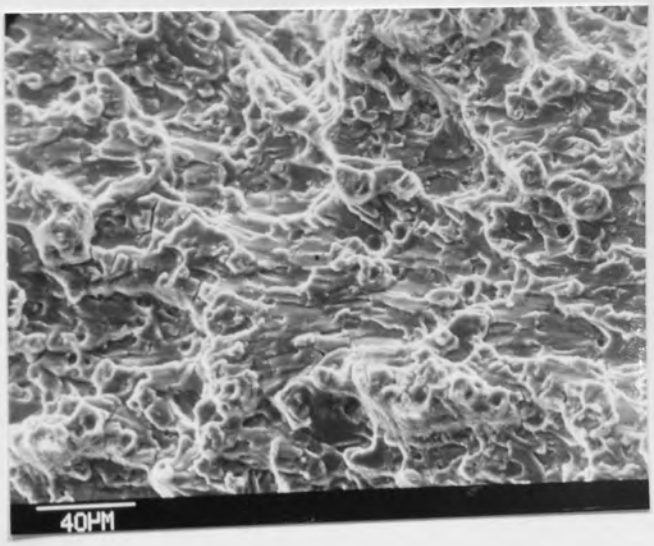

Figure 73: Fatigue fracture surfaces of 2014-T6 at low (a) and high (b) levels of ΔK.

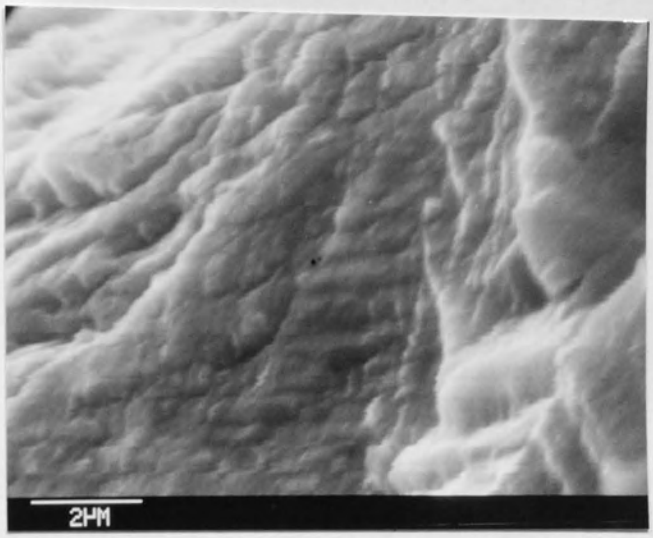

Figure 74: Striations in a 2014-T6 fatigue specimen.

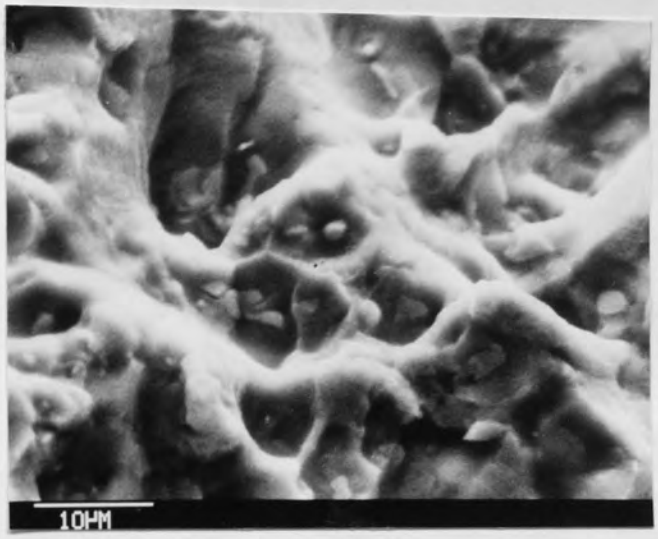

Figure 75: Dimpling in a 2014-T6 fatigue fracture surface.

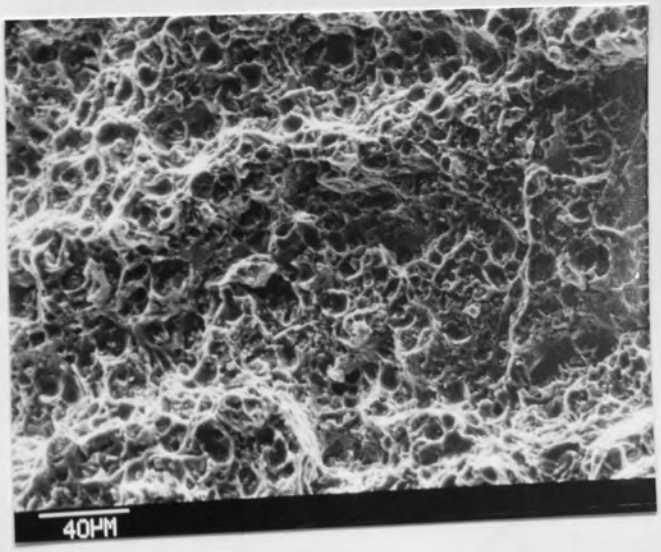

Figure 76: Dimpling in a 2014-T6 fast fracture surface.

(a)

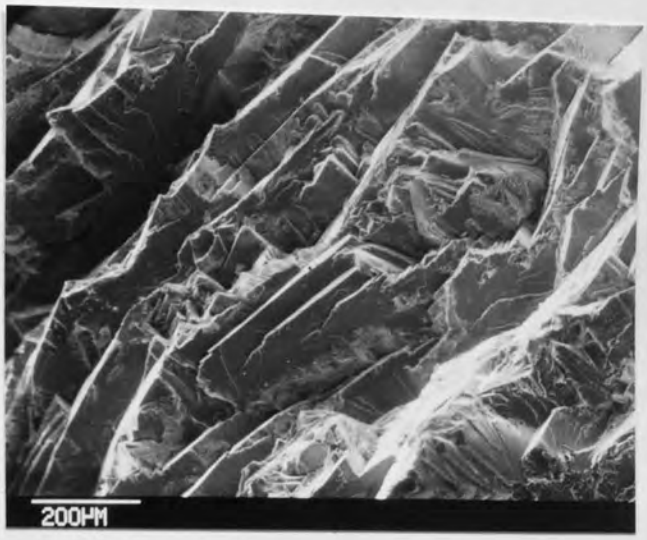

(b)

(c)

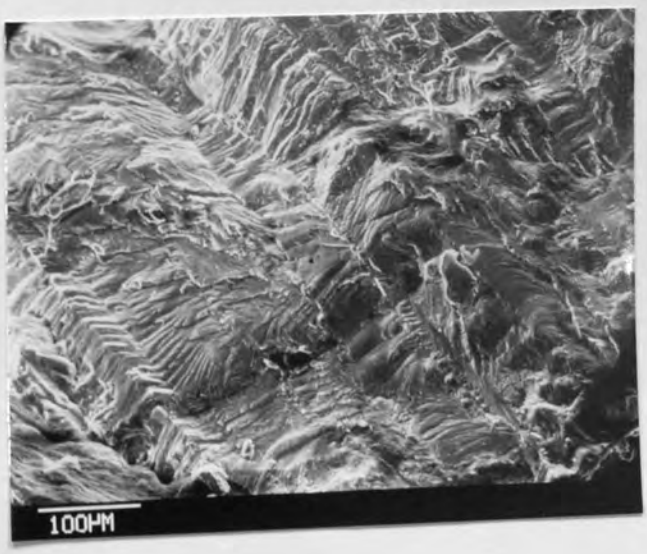

Figure 77: 8090-T6 fatigue fracture surfaces, in L-S (a), L-T (b) and T-L (c) orientations.

Figure 78: Longitudinal cracking in un-side-grooved 8090-T6 (L-S) specimens.

Figure 79: Crack path in un-side-grooved 8090-T6 (L-S) specimens.

(a)

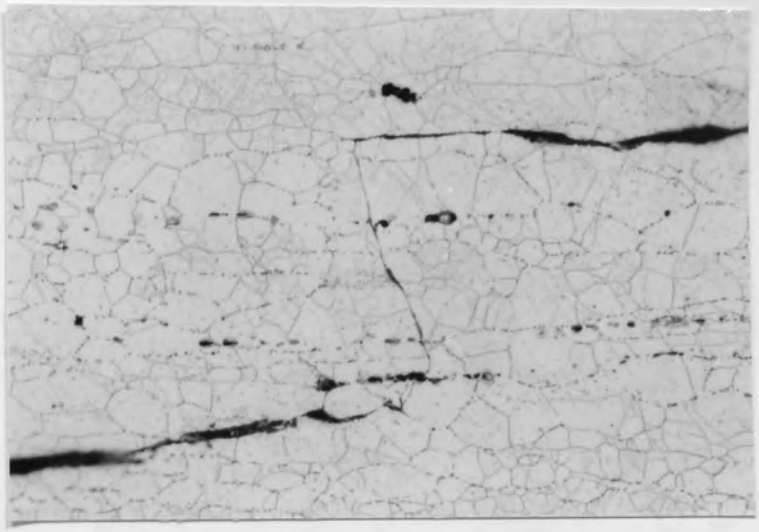

(b)

Figure 80: Optical (a) and electron (b) microscopy of delamination in un-side-grooved 8090-T6 (L-S) specimens.

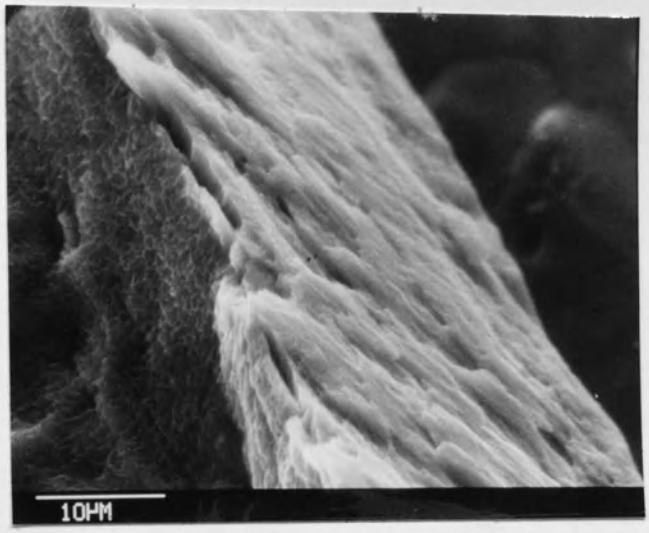

Figure 81: Dimpling on intergranular delaminations in 8090-T6 (L-S) specimens.

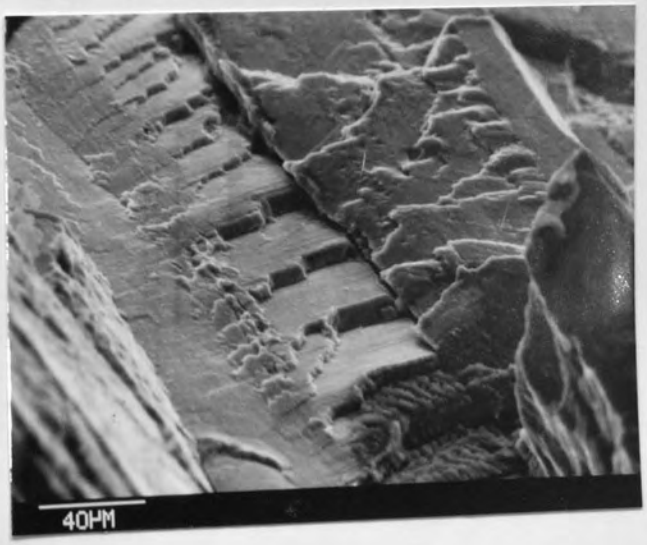

Figure 82: Planar slip in 8090-T6 fatigue specimens.

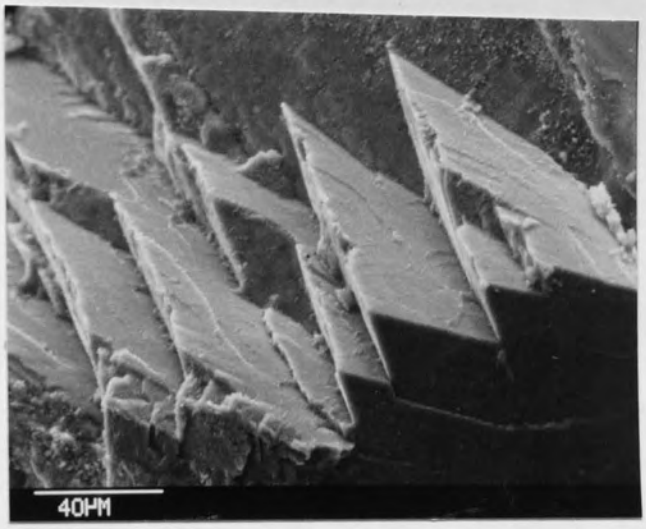

Figure 83: Planar slip on two planes in 8090-T6 fatigue specimens.

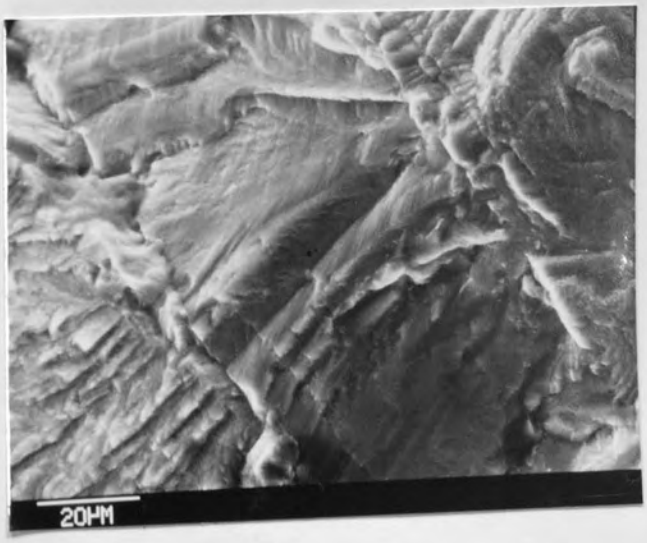

Figure 84: Striations on 8090-T6 fatigue specimens.

(a)

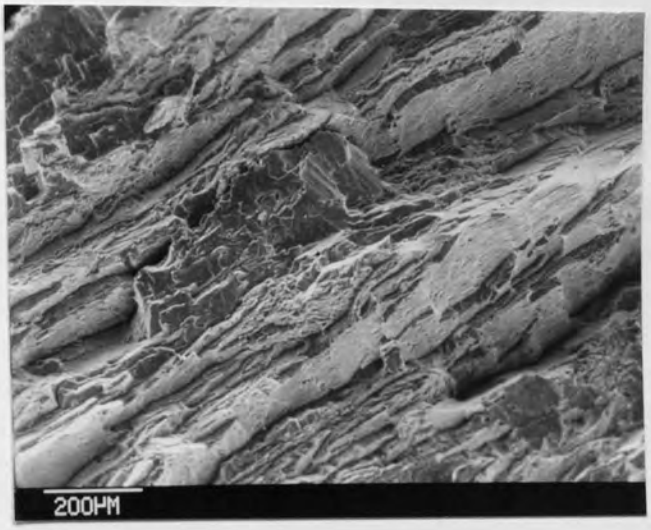

(b)

(c)

Figure 85: Fast fracture surfaces in 8090-T6 fatigue specimens.

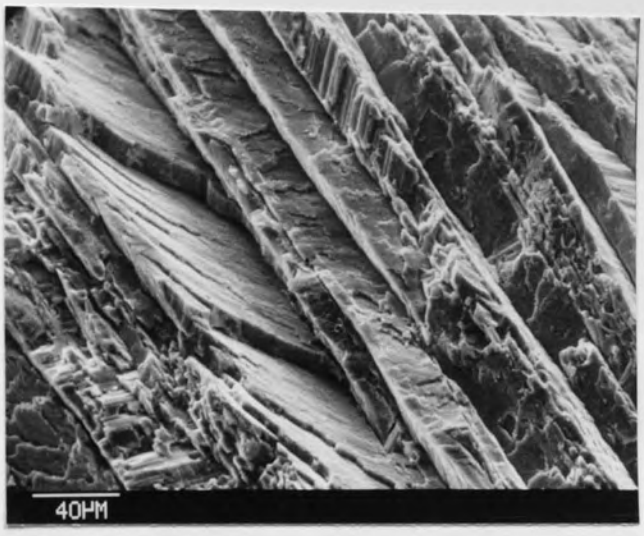

Figure 86: Transgranular failure on fast fracture surfaces of 8090-T6 fatigue specimens.

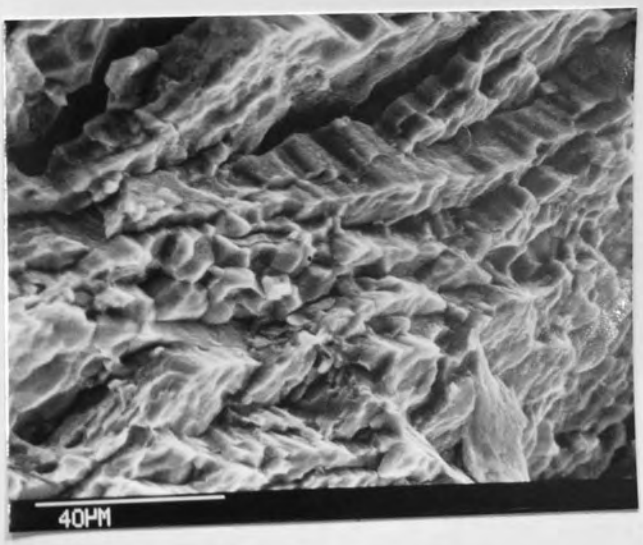

Figure 87: Ductile failure on fast fracture surfaces of 8090-T6 fatigue specimens.

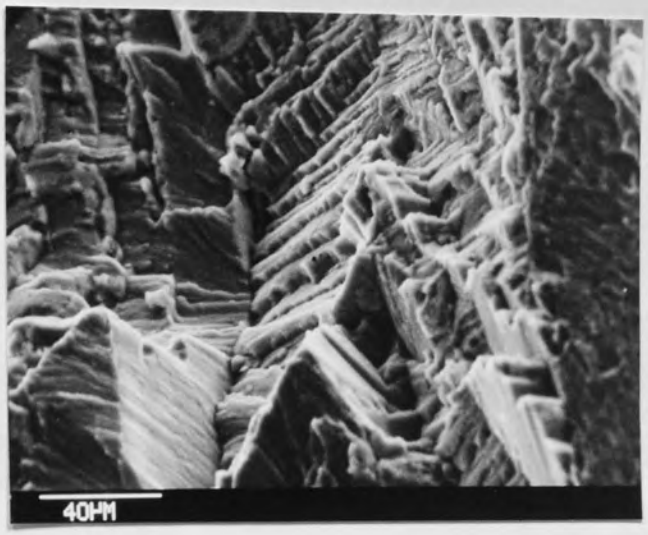

Figure 88: 'Stepping' of slip surfaces on 8090-T6 corrosion fatigue surfaces.

Figure 89: Corrosive attack of slip surfaces on 8090-T6 corrosion fatigue surfaces.

Figure 90: Corrosion pitting on 2014-T6 (left) and 8090-T6 (right) smooth notched corrosion fatigue specimens.

(a)

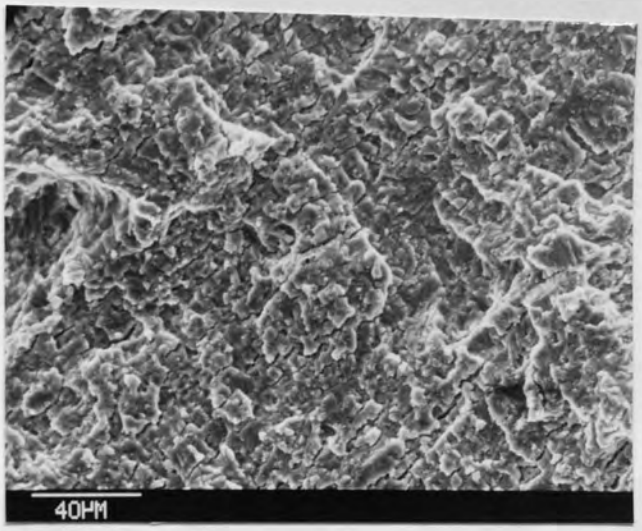

(b)

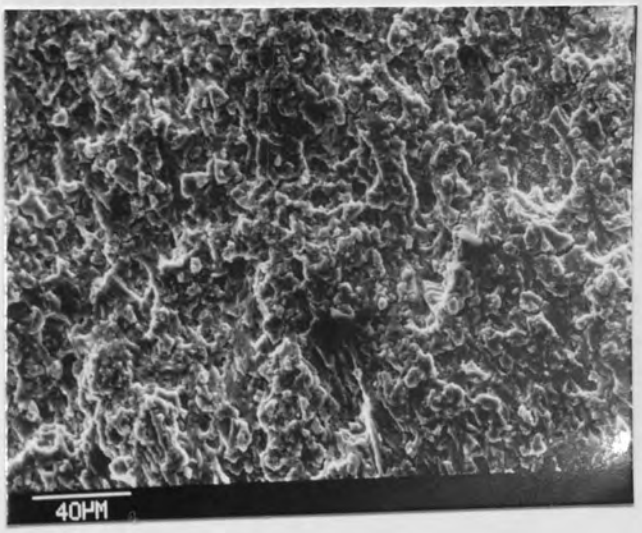

Figure 91: Typical fatigue fracture surfaces for CZ20-T6 (C-L) (a) and (C-R) (b) orientations.

(a)

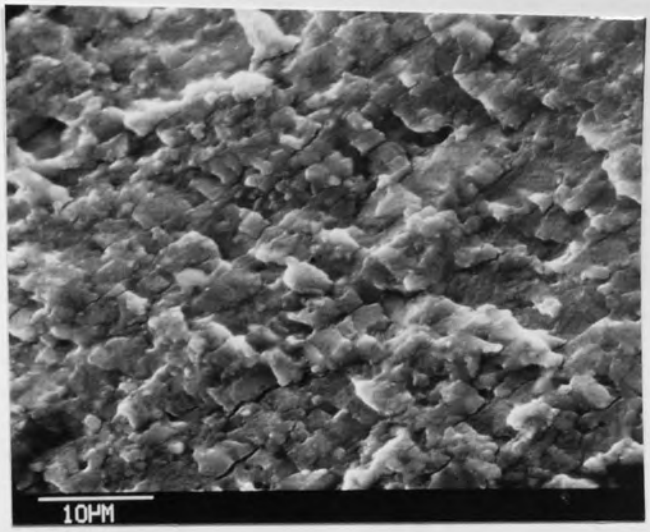

(b)

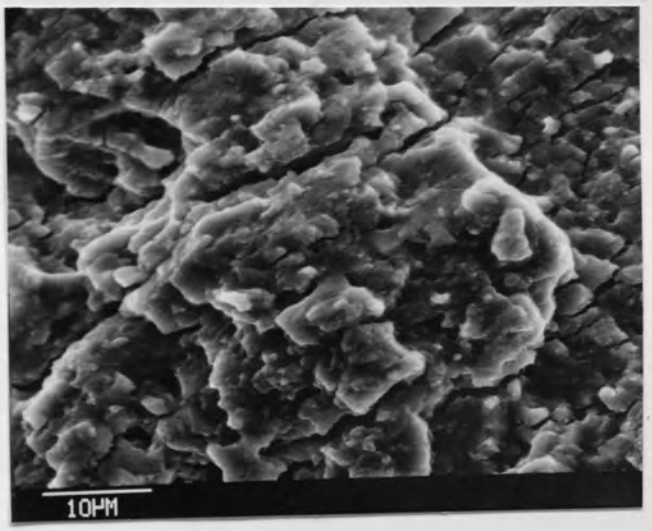

(c)

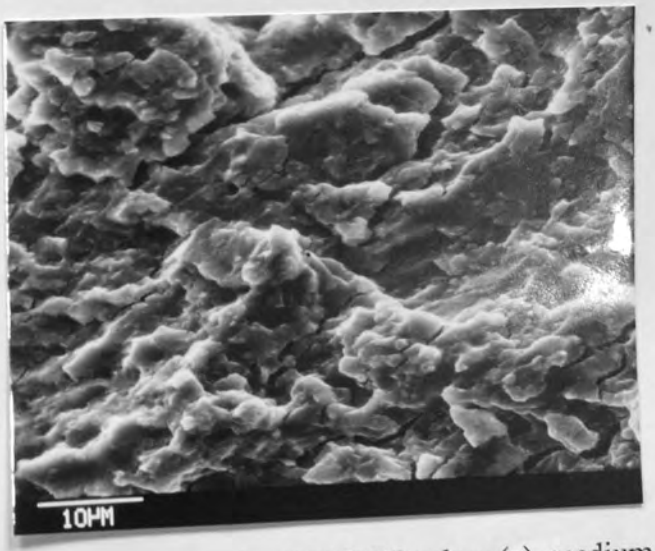

Figure 92: Fatigue fracture surfaces for CZ20-T6 at low (a), medium (b) and high (c) levels of ΔK.

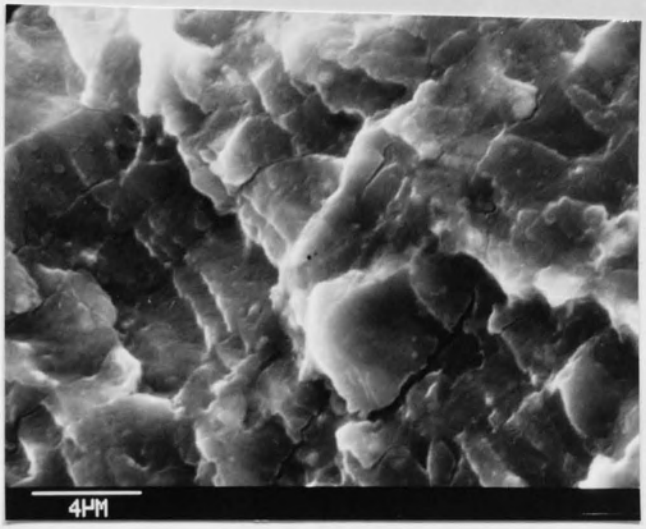

Figure 93: Fatigue fracture surface of CZ20-T6.

(a)

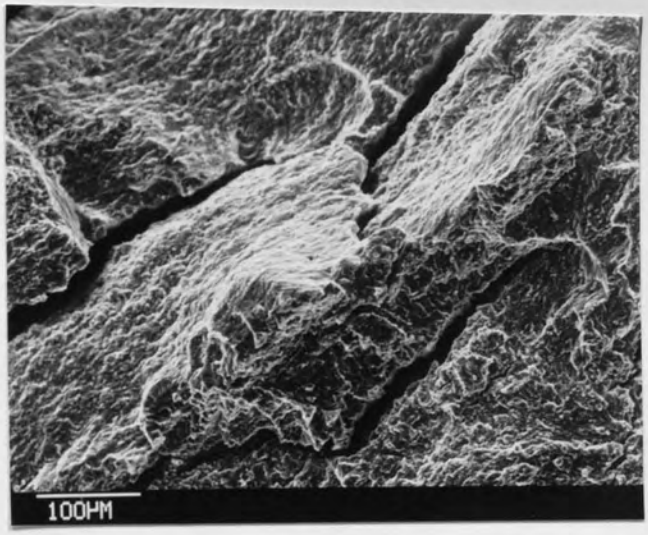

(b)

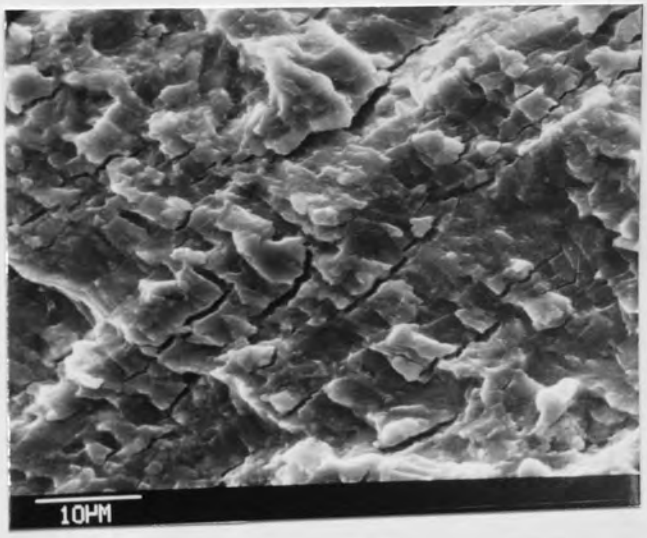

Figure 94: Cracking in CZ20-T6 (C-L) fatigue specimens.

(a)

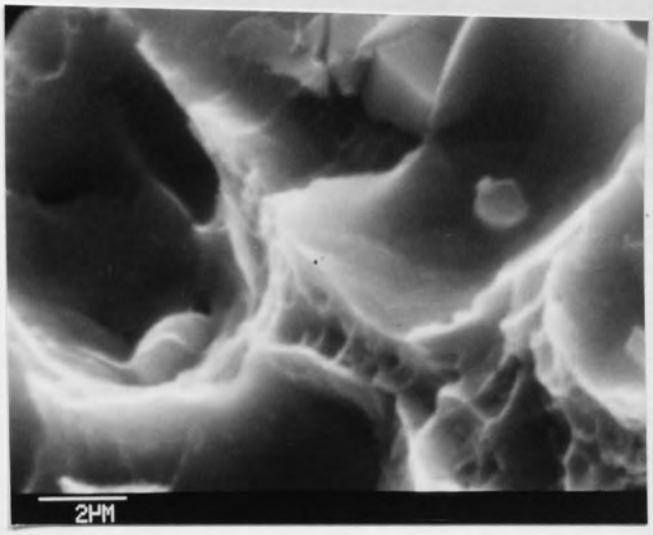

(b)

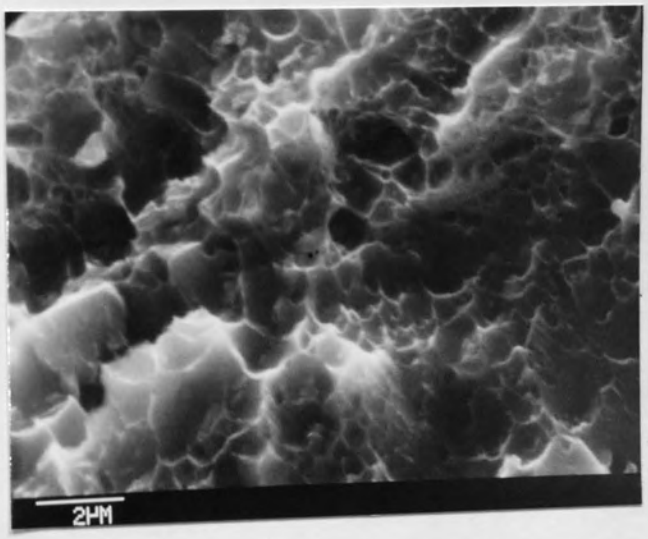

Figure 95: Dimpling in the fast fracture area of 2014-T6 (a) and CZ20-T6 (b) fatigue specimens.

(a)

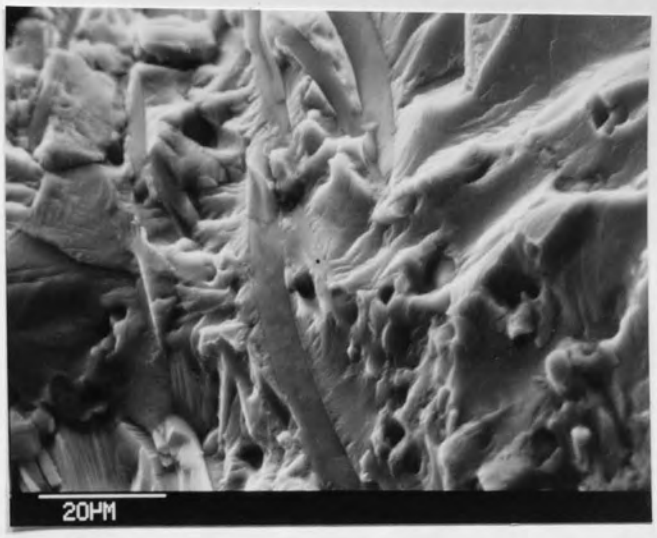

(b)

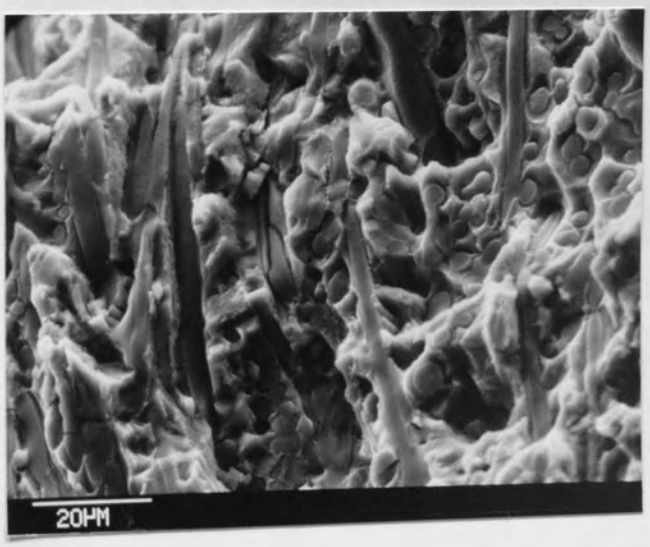

Figure 96: Typical fatigue fracture surfaces of Saffil/6061-T6 at low (a) and high (b) levels of ΔK.

(a)

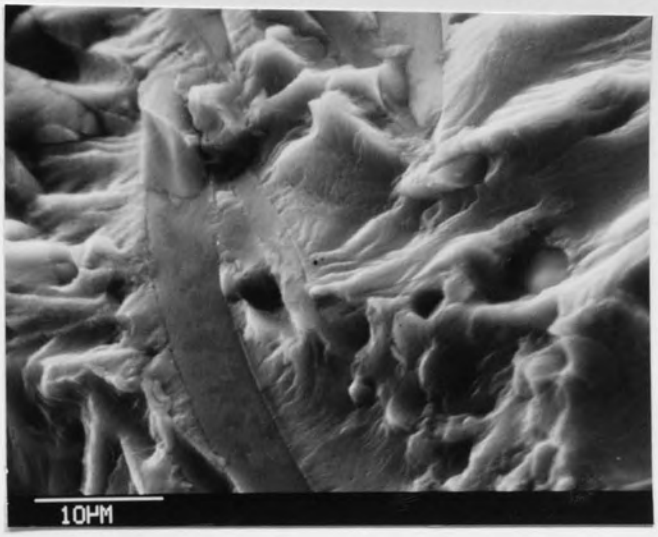

(b)

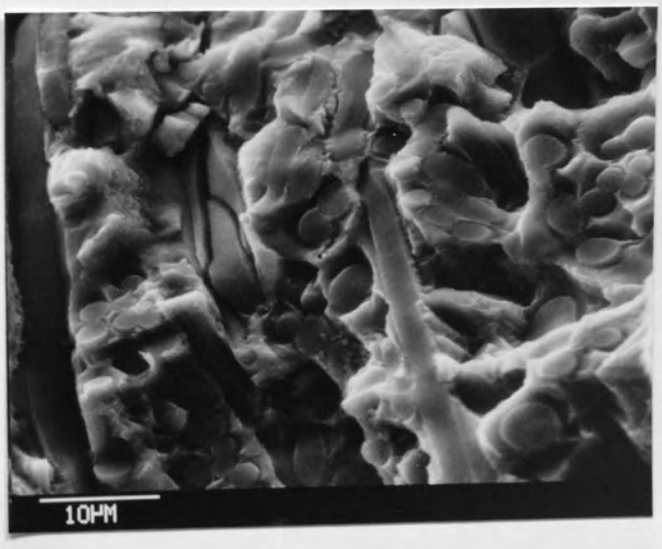

Figure 97: Fatigue fracture surfaces of Saffil/6061-T6 at low (a) and high (b) levels of ΔK.

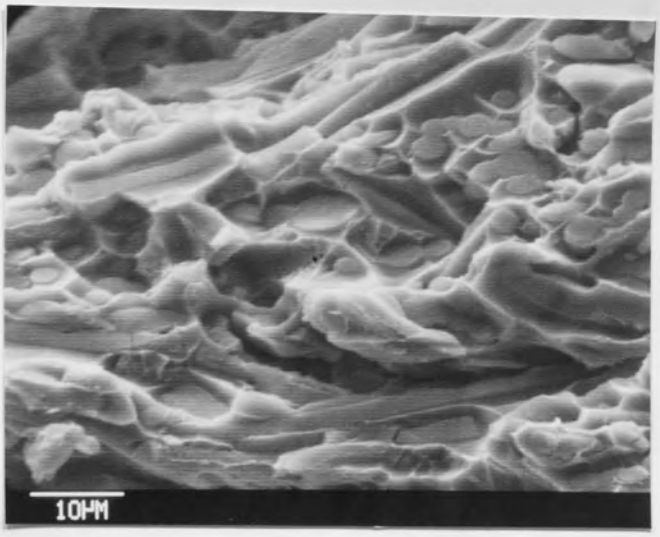

Figure 98: Typical fatigue fracture surface of a Saffil/6061-T6 (T) specimen.

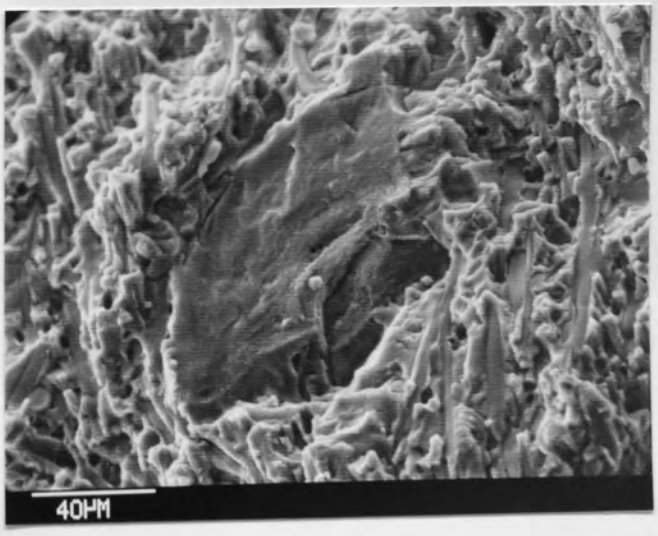

Figure 99: Large non-metallic inclusion found on Saffil/6061-T6 fatigue fracture surfaces.

(a)

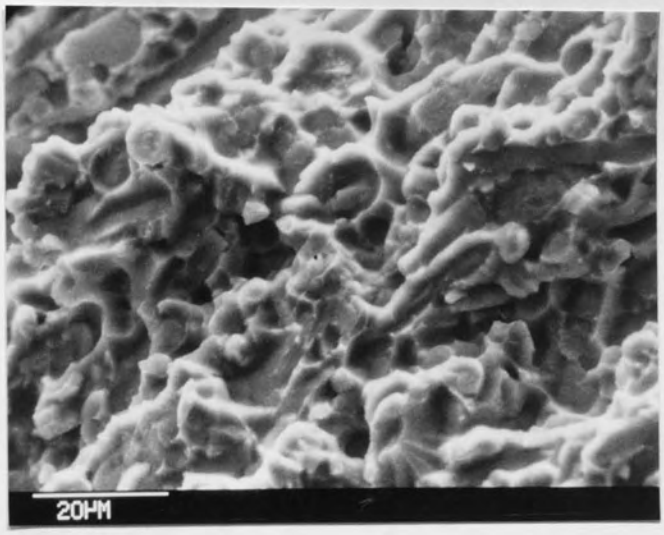

(b)

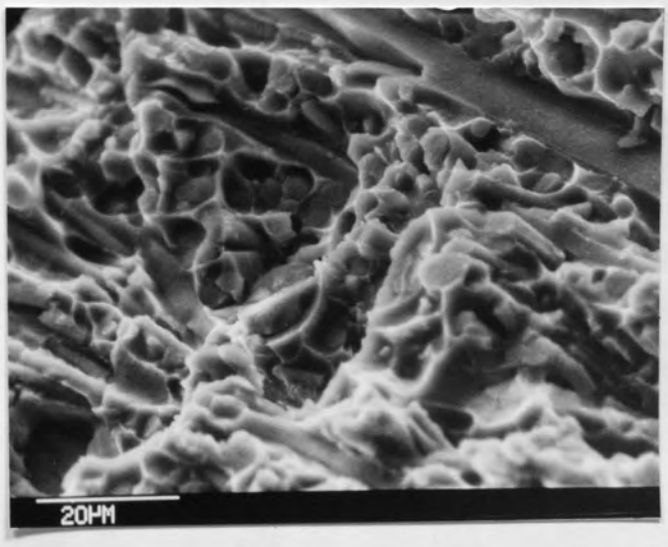

Figure 100: Saffil/6061-T6 tensile fracture surfaces, 20% (a) and 30% (b) Saffil.

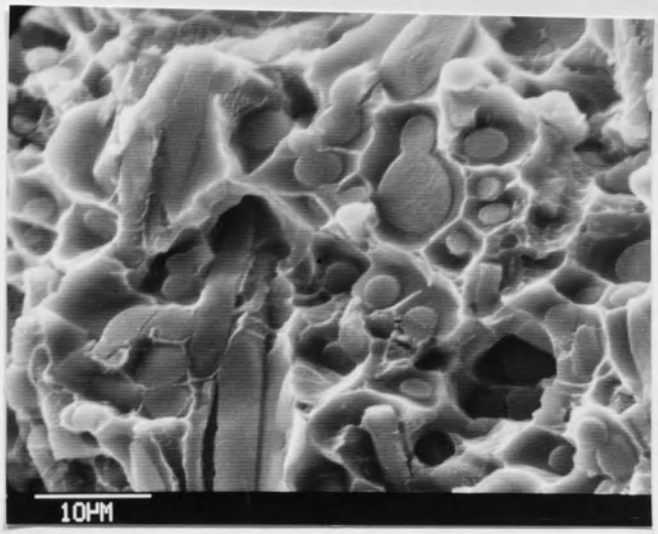

Figure 101: Fracture surfaces of Saffil/6061-T6 tensile specimens.

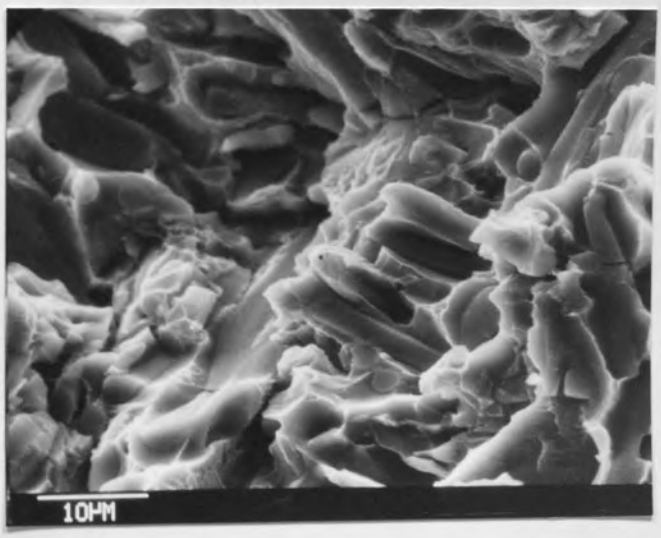

Figure 102: Fibre pullout in fracture surfaces of Saffil/6061-T6 tensile specimens.

8.DISCUSSION

8.1. ELECTRICAL POTENTIAL CALIBRATION

The results of the electrical potential calibration, figure 41a to 41i, show how important an experimental calibration is for the reliable measurement of crack length, especially with the smooth notched specimens. The theoretical electrical potential calibrations did not agree with the experimental calibrations for 2014-T6 and 8090-T6 smooth notched specimens, figures 41a, 41c, 41d and 41d, with slightly better agreement for the 2014-T6 and CZ20-T6 calibrations, figures 41b, 41f and 41g. This is to be expected, as the theoretical solution is based on the existence of an infinitely thin, sharp crack. The presence of a notch would therefore change the electrical potential distribution within the specimen, so bringing inaccuracies into the calculation. The larger the notch the greater the inaccuracy. The experimental electrical potential calibration for smooth notched specimens would therefore differ from the theoretical solution by a greater amount than in sharp notched specimens.

However, the theoretical calibration for 20% Saffil/6061-T6 agreed quite well with the experimental calibration (figure 41h), and agreement in the 30% Saffil/6061-T6 calibrations was almost exact over the range of crack lengths used to produce crack growth data (figure 41i). This suggests that plastic deformation at the notch root may also be affecting the experimental calibrations. The 2014-T6, 8090-T6 and CZ20-T6 specimens would have suffered appreciable plastic deformation at the crack tip, which may have had an effect on the experimental calibration. Plastic deformation would increase the resistance of the specimen slightly, and so the potential drop between the probes would increase correspondingly. This was noted to occur when cracked specimens were loaded, with increases of up to 10% in potential drop. Crack tip plastic deformation would be less in the Saffil-reinforced material, due to the presence of the high modulus fibres. For this reason the experimental calibrations in Saffil-reinforced 6061-T6 were either very close (20% Saffil) or identical (30% Saffil) to the theoretical calibrations.

Due to the effects of notch geometry and crack tip plastic deformation, the experimental electrical potential calibration was used to calculate crack length from values of potential drop. The results were presented in a non-dimensional form ($V_a/V_o.W$ versus a_o+c/W), rather than as a direct relationship between change in potential drop and crack length (ΔV versus c).

Apart from notch geometry and crack tip plastic deformation effects, a number of other factors could have affected the electrical potential calibration. Crack deviation would give an artificial value of crack length, as was found to occur in the 8090-T6 and CZ20-T6 (C-L) specimens. The crack length in the intended growth direction would be shorter than the recorded length, as the potential drop technique cannot describe the direction of crack growth and any crack branching could not be detected. Crack closure effects could also affect the potential calibration. Those specimens where crack deviation occurred would also be likely to have some crack closure occurring, which would reduce the potential drop for a certain crack length due to the effective surface area of the crack being reduced. Crack closure effects would therefore partially neutralise the effects of crack deviation on the potential calibration. Another factor found in 8090-T6 and CZ20-T6 (C-L) specimens that could have affected their potential calibrations was multiple crack growth. This would have given a higher value of potential drop than the potential that would correspond to the crack length in the intended direction. It is unlikely that crack front shape had any effect, as the potential drop technique can only detect the crack area and so an equivalent through thickness crack length would have been calculated.

Several factors can cause individual deviations from the experimental calibration; as shown in figure 41, not all of the points are on the experimental calibration curve. The position of the potential measurement probes was not identical for individual specimens, although every effort was made to spot weld them as close as possible to the edge of the notch on the top face. In practice, an error of ±0.5mm in probe spacing could not be avoided, which led to an error in potential drop readings of upto ±5μV. Also, the depths of

the machined notches were not exactly the same for individual specimens, and so the measurement of potential drop before cracking was slightly different. However, this would not affect fatigue crack propagation data as the total crack length (a) was used, which was the sum of notch depth (a_o) and crack length (c). Crack initiation data would also be effectively unaltered, as the change in potential drop was measured. Therefore, individual differences in notch depth should not have had an effect. Laboratory temperature may also have had an effect on individual specimens, as this would have fluctuated from test to test. However, it was considered that this effect would have been negligible, as any temperature fluctuations were small.

A corrosive environment did not affect the experimental electrical potential calibration of aluminium alloys in this investigation, which agrees with previous work on corrosion fatigue of steels (156). Values of V_a and V_o were the same in air and salt water for each specimen. The only effect of immersion in salt water was a temporary fall in electrical potential, due to the slight drop in temperature of the specimen. As the specimen returned to its original temperature the electrical potential stabilised, also to its original value.

8.2. ALUMINIUM-LITHIUM ALLOY

The structure of the 8090 alloy can be seen from figure 55 to consist primarily of elongated 'pancake' grains, as opposed to the almost equiaxed grain structure of 2014, as shown in figure 54. These elongated grains are outlined by particles, which are shown at higher magnification in figure 56. A very pronounced sub-grain structure could also be seen, which was approximately equiaxed. This recovery occurred during the T6 treatment, as no sub-grain structure could be seen in the 8090-T8 structure, as shown in figure 58. The amount of recovery seemed to vary with the orientation of the individual grains, as shown in figure 57, from a faint sub-grain structure to possibly full recrystallisation in some areas.

The results of the fatigue life testing, figure 42, showed that 2014-T6 offered better fatigue resistance than 8090-T6 at all but low levels of stress, close to the fatigue limit, in both air and salt water environments. However, this is contrary to recent work comparing the fatigue resistance of 8090 and 2XXX series alloys (160, 161), which show 8090 to be superior. There are several possible reasons for this difference. Firstly, the temper condition of 8090 in this investigation was T6, whereas a T8 condition was used in the referenced work. The T8 condition, which is basically a T6 temper with a cold stretch after solution treatment and prior to ageing, provides a greater tensile strength than the T6 condition. Therefore, fatigue strength would also be expected to be higher.

However, the main reason for the comparative drop in fatigue resistance of 8090 in this investigation is due to a combination of the state of the material and the testing conditions. Figure 48 shows that there is a difference in crack growth direction between the two materials under investigation, with transversely oriented crack growth in 2014-T6 (figure 48a) and a mixture of longitudinal and short transverse crack propagation directions in 8090-T6 (figure 48b) in these longitudinally-oriented specimens. In the referenced work (160, 161), 8090 specimens had a straight fracture path, similar to that of figure 48a. The referenced work used tension-tension fatigue specimens, whereas rotating beam specimens were used in this investigation, and this difference in stress state seems to have affected the

fracture mode. The tension-tension stress state involves an axial stress, whereas the bending occurring in the rotating beam specimens involves an axial stress plus small secondary stresses perpendicular to this axis. The effects of these small secondary stresses would only show if there were any weak interfaces along the specimen axis, which would be pulled apart if weak enough. This is the cause of the difference in fracture path, as these small secondary stresses are not present in tension-tension specimens. However, the presence of weak interfaces in transverse directions is also needed for this explanation to be acceptable. Figures 56 and 79 show that these do exist in the material investigated. The 8090 alloy supplied was pre-production material. The only difference between pre-production and present production material is that the pre-production material was not filtered at the casting stage. Present production material is either poured through porous filters on casting or bottom cast, so filtering out the non-metallic crust that forms on the top of the molten metal in the ladle. This crust consists of various oxides and calcium- or fluorine-containing compounds from the fluxing operation. As a result of not filtering this non-metallic material out, inclusions were strung out along the elongated grain boundaries in the 8090 alloy under investigation, as shown in figure 56 and 59. These non-metallic inclusions cause the longitudinal grain boundaries to be areas of weakness, and delamination of these boundaries is possible under even a small stress. For this reason, the 8090-T6 rotating beam specimens fractured along the path shown in figure 48b. The crack propagated by a combination of this longitudinal delamination and transgranular shear. A schematic illustration of the crack path is shown in figure 103. The ease of crack initiation and propagation in this manner would reduce the fatigue resistance of 8090-T6 when compared to other published data.

The same effect would have caused the reduction in corrosion fatigue resistance in 8090-T6, shown in figure 42. An additional reduction in fatigue life due to the corrosive environment would have been caused by salt water being able to penetrate the delaminated grain boundaries very easily.

The results of the fatigue crack initiation testing, figures 43 and 44, show similar trends

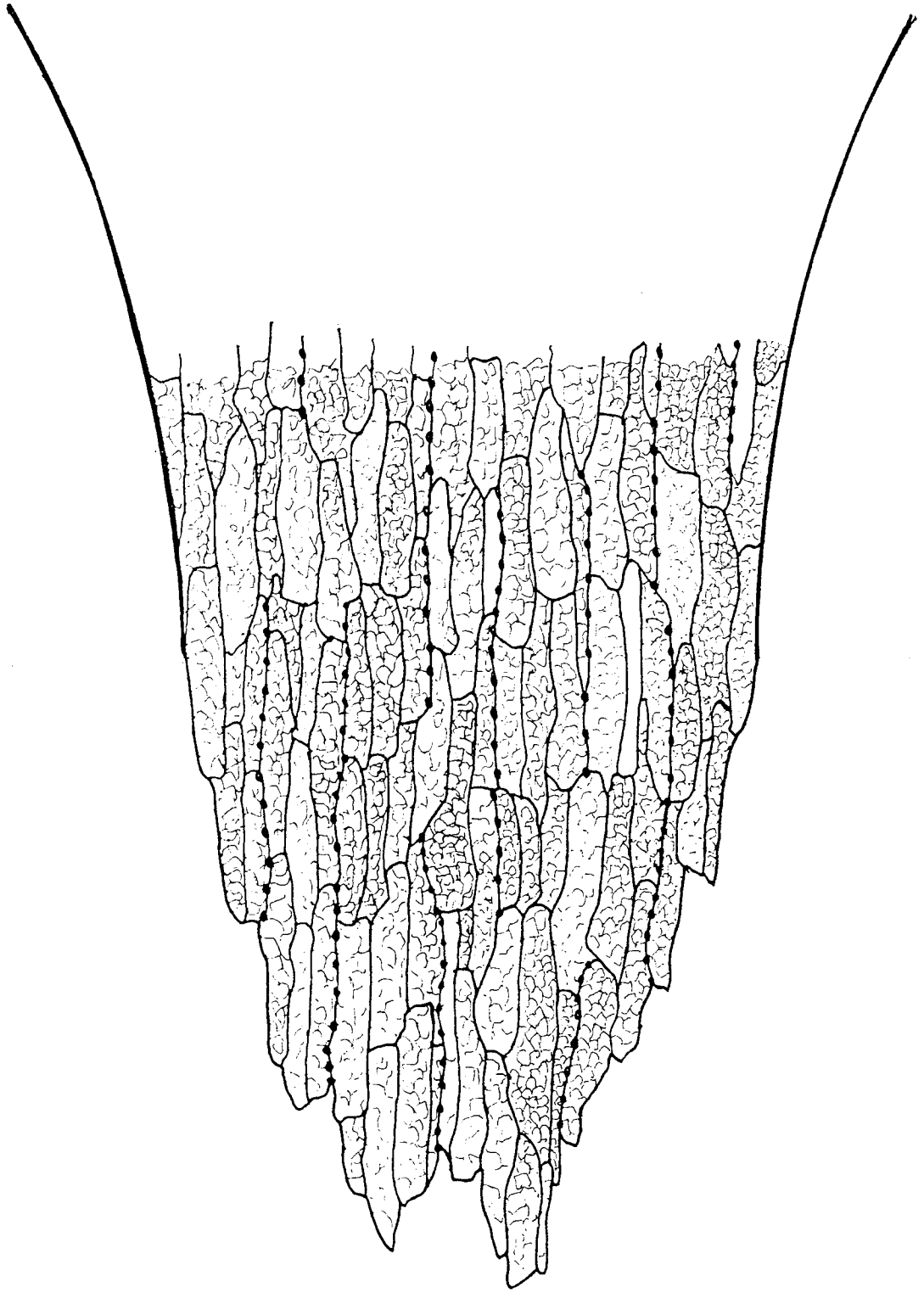

Figure 103: The Influence of non-metallic inclusions on the fracture path in 8090-T6 rotating beam specimens.

to the fatigue life testing results. Fatigue crack initiation results in air show 2014-T6 to be superior to 8090-T6, especially at higher stresses. Again, this is contrary to other published data (161), which quote superior crack initiation properties for 8090 over 2XXX series alloys. The reason for the drop in crack initiation properties in the 8090 in this investigation is the same as for the drop in fatigue life. The different temper conditions will have had an effect, the T6 condition having lower tensile strength properties than the T8 condition. However, the stress state and the cleanliness of the material would again have had the overriding effect. The tendency of the 'dirty' elongated grain boundaries to open up while under bending fatigue would reduce the crack initiation resistance of the material.

The crack initiation properties of 8090-T6 varied with orientation. The L-S orientation showed higher crack initiation resistance than the L-T and T-L orientations, which showed similar resistance. The unclean state of the material decreases the initiation life of L-S specimens, but not as much as L-T and T-L. This is because the weak longitudinal grain boundaries lie in a plane that is perpendicular to both the crack plane and the crack direction in L-S specimens, whereas these boundaries are in the same direction as the cracks in L-T and T-L specimens, as shown in figure 104. If an S-L specimen orientation had been tested, very poor fatigue crack initiation and propagation resistance would have been expected, as the weak longitudinal grain boundaries would be in the same plane as the crack plane.

The corrosion fatigue crack initiation resistance of 8090-T6 was superior to 2014-T6 in all but the T-L orientation. Again, an additional reduction in fatigue crack initiation resistance in a corrosive environment would have been caused by salt water being able to penetrate these weakened grain boundaries very easily, especially in the L-T and T-L specimens. However, the corrosion fatigue crack initiation resistance of 2014-T6 was reduced by an even greater amount. The most likely reason for this higher drop in fatigue crack initiation resistance due to the corrosive environment is the greater amount of pitting corrosion found with this alloy when compared to 8090-T6, as shown in figure 90. Corrosion pits can reduce fatigue crack initiation resistance, and so fatigue life, by introducing stress concentrations at their base.

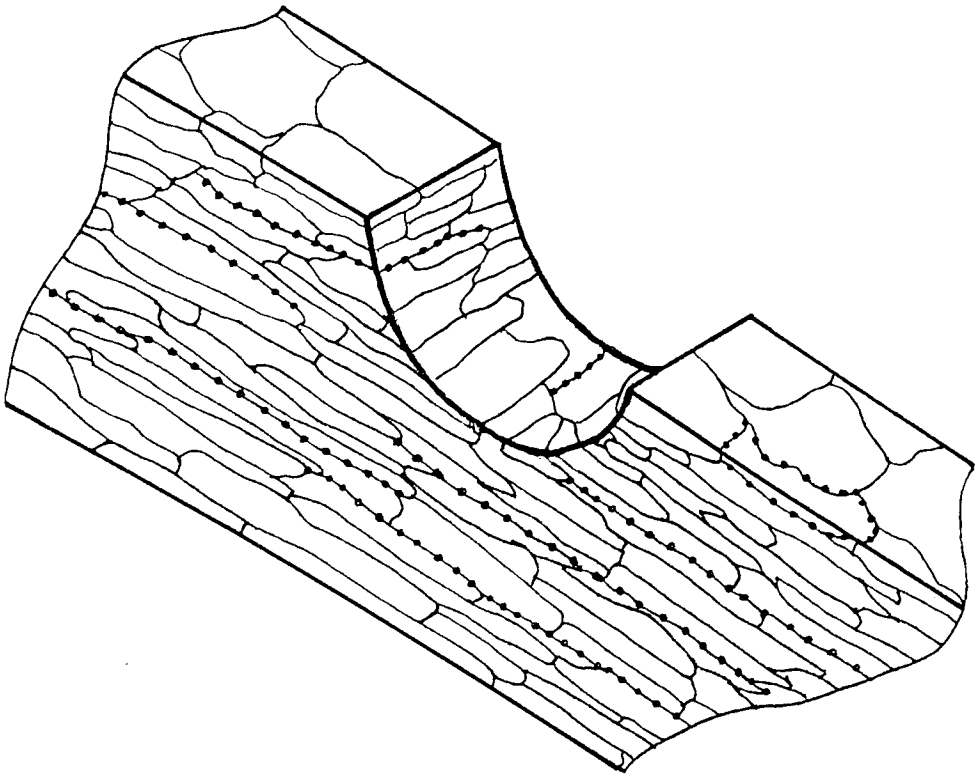

(a) L-S specimens.

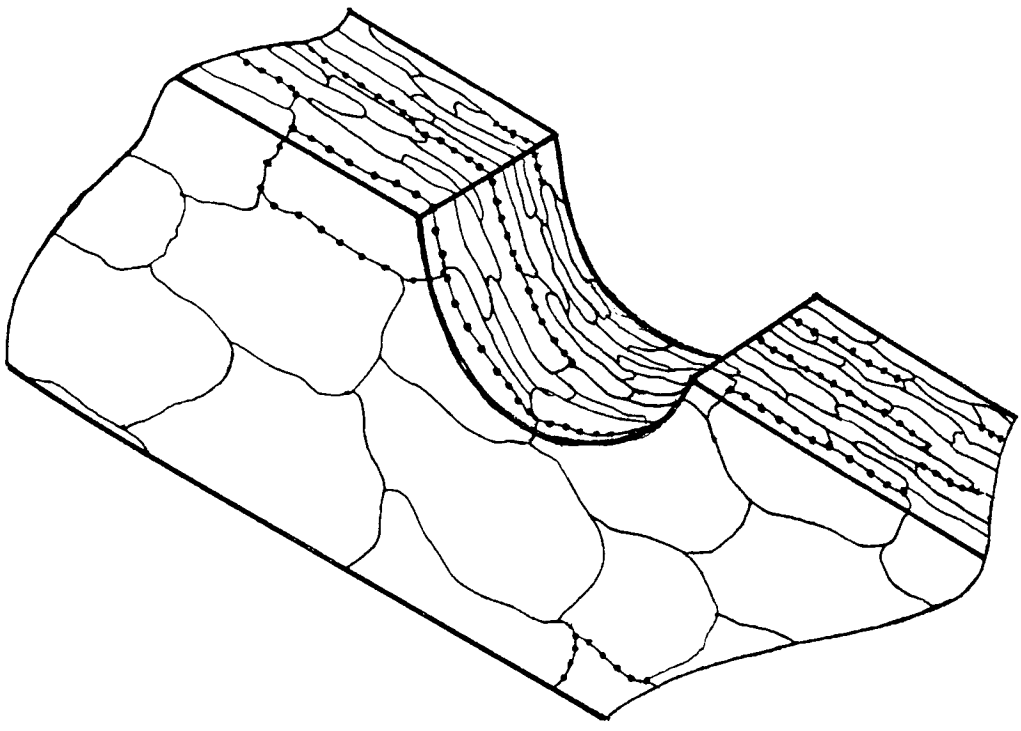

(b) L-T and T-L specimens.

Figure 104: Orientation of the weak longitudinal grain boundaries in relation to the direction of crack growth.

In terms of both fatigue life and fatigue crack initiation resistance, properties of 8090-T6 in this investigation are lower than those reported in other published data, for reasons already explained. The effects of the weak longitudinal grain boundaries were not shown up in the results of other work (161), also on pre-production material, because of the type of testpiece used. However, in a practical situation the effect of these 'dirty' boundaries would undoubtedly have been detrimental, and so the types of testpiece used in this investigation were considered to be more representative. This problem of testpiece selection would be less important in present production material, as the grain boundaries are much cleaner and so longitudinal delamination is less likely to occur.

The representation of the fatigue crack initiation results in the form shown in figure 44 suggests that a relationship between the number of cycles to initiation, N_i, and the effective stress intensity, ΔK_n, does exist. The straight line fit for the results shows a good representation of this relationship, similar to previous work in this area (101, 102) shown in equations 3.18 and 3.19. The power constant, n, in this relationship varied from -2.1 to -7.7, compared to -2 and -4 in equations 3.18 and 3.19.

The fatigue crack propagation data for 8090-T6 and 2014-T6, shown in figures 45 and 46, are comparable with published data (112, 113). However, the propagation resistance is slightly better for both 2014-T6 and 8090-T6 in this investigation than in the published data. The probable reason for this is the fact that both materials were in the T6 condition in this investigation, whereas the other work would have examined them in either the T651 or T8 (both stretched) conditions. The T6 condition has increased tolerance to crack growth, because the drop in strength associated with the lack of cold stretching treatment leads to an increase in fracture toughness, K_{IC}.

It can be seen from the specimen fracture surfaces, figure 50, that grain boundary delamination occurred during crack propagation. Closer examination of the fatigue fracture surfaces, figure 77, showed failure to be a combination of this intergranular rupture and transgranular failure involving large amounts of planar slip. In most cases planar slip was on

one set of planes, but a combination of slip systems could be seen in some cases, as shown in figure 83. Planar slip was seen to occur right across the elongated grains, as shown in figure 82, suggesting that the recovery seen within these grains, shown in figures 56 and 57, was indeed just recovery and had not developed into recrystallisation. The highly faceted crack path resulting from the extent of this planar slip would have led to an increase in crack propagation resistance, due to the larger amount of crack deviation involved. Only a small number of fatigue striations could be seen, shown in figure 84, as it was very difficult to distinguish any difference between striation formation and planar slip.

The delamination of longitudinal grain boundaries was a predominant feature of the fast fracture surfaces in L-T and T-L specimens, taking the form of fissures at right angles to the fracture surface, as shown in figure 85. This caused the fracture surfaces to be very coarse, with extensive crack deviation. Figure 105b shows how these delaminations relate to the grain structure. Figure 51 compares the coarse fracture surface of the pre-production 8090-T6 (T-L) specimen used in this investigation to one of a present production 8090 (T-L) specimen, where the fracture surface can be seen to be much smoother. The highly deviated crack path in this pre-production material could therefore have led to an improvement in fatigue crack propagation resistance in the orientations tested. Crack deflection and crack closure effects are possible causes of the increased crack growth resistance in these alloys, and would be another reason for the difference between fatigue crack propagation data in this investigation and in published data (160, 161). However, this is small compensation for the fact that fatigue crack propagation resistance would be very low in the S-L orientation for this pre-production material. It was noted that the superiority of 8090-T6 (L-T) and (T-L) specimen orientations over 2014-T6 was much less for an R-value of 0.45 in both air and salt water, as shown in figure 45. This would again suggest that crack closure was occurring in 8090-T6 specimens. The effects of crack closure would be much greater with a low R-value, such as 0.1, where the minimum stress would be closer to zero. With an R-value of 0.45 crack closure effects would be less, because the minimum stress in the fatigue

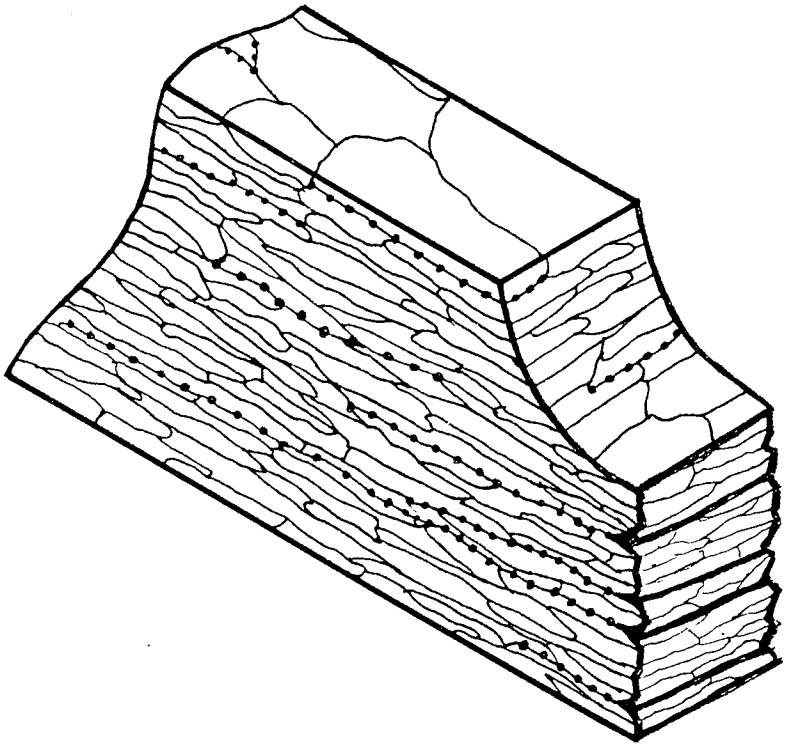

(a)

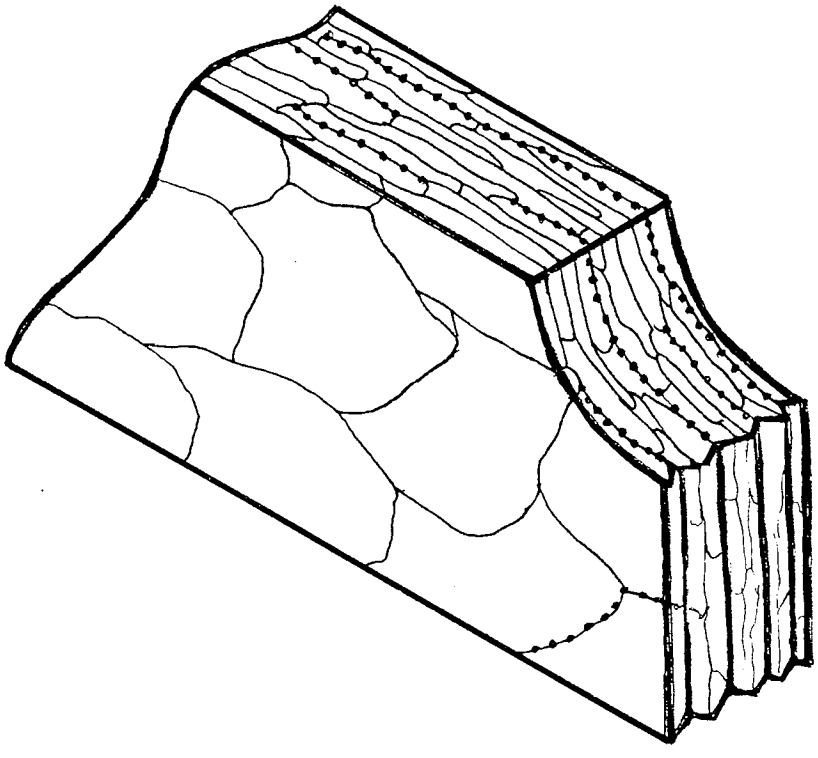

(b)

Figure 105: Fast fracture surfaces in 8090-T6 L-S (a) and L-T or T-L (b) specimens.

cycle would be higher.

It can be seen that the short transverse crack growth direction in 8090-T6 (L-S) specimens is a very unlikely crack growth direction with this pre-production material. A number of coinciding factors, in this case sharp grooves on three sides of the specimen, were needed to get the crack to grow in this direction. Side-grooves were needed to stop the L-S specimens from delaminating at longitudinal grain boundaries as soon as a crack was initiated, as shown in figure 78. Optical metallography showed these delaminations to be following lines of non-metallic inclusions on longitudinal grain boundaries (figure 79), with only small amounts of transgranular failure, as shown in figure 80. However, closer examination of this delamination showed it to be ductile (figure 81), with very fine dimples on the surfaces. It has been suggested that these dimples originate from particles of the equilibrium δ phase (160). Larger dimples originated from the larger (up to 5μm in size) non-metallic inclusions. Energy dispersive X-ray analysis of these inclusions on the grain boundaries showed them to be either aluminium-rich (presumably Al_2O_3) or aluminium and fluorine-containing, which would be fluxed material, as shown in figure 60. The side-grooved 8090-T6 (L-S) specimens still exhibited a large amount of longitudinal delamination, both in fatigue, shown in figure 77a, and fast fracture, shown in figure 85a, which is why L-S fracture surfaces were a lot more coarser than T-L or L-T surfaces. This would contribute to the superior fatigue crack propagation resistance of the L-S orientation. Figure 105a shows how these delaminations relate to the grain structure. However, some ductile failure was also seen to occur in fast fracture, as shown in figure 87.

The shape of the fatigue crack front in 8090-T6 specimens varied with their orientation, as shown in figure 50. In L-S specimens the crack front was bowed inwards, as opposed to the outwardly bowed crack front shape in 2014-T6 specimens, as shown in figure 49. This was due to the side-grooves used on these specimens. Crack propagation rates would have been slightly higher at the sides of the specimen, close to the side-grooves. The crack front in L-T and T-L specimen orientations was uneven, the crack length being longer on one side than the other, as shown in figure 50b. This was due to the grain size difference across the

thickness of the plate material, as shown in figure 58. The fine grained material from the edge of the rolled plate gave higher crack growth rates than the coarser grained material from its centre. This would agree with other work (162) which shows that the improvement in fatigue properties with increasing grain size can be attributed to a more highly faceted crack path. Crack closure effects and crack deflection would therefore have slowed the crack down in the coarser area of the specimen. One other effect of this difference in grain thickness across the specimen section would be that the texture and strength of the material would have varied also, which would have affected the crack propagation rates.

The fatigue crack propagation resistance of 8090-T6 did not show the same superiority over 2014-T6 in a salt water environment, as shown in figures 45b and 45d. Although the L-S specimen orientation showed superior corrosion fatigue crack propagation resistance over the whole range of ΔK, the L-T orientation was only equivalent to 2014-T6 and the T-L orientation was inferior in salt water. The most probable reason for this greater decrease in fatigue crack propagation resistance of L-T and T-L specimen orientations due to the salt water environment was the delamination of the longitudinal grain boundaries. As shown in figure 105, these delaminations are in the same direction as crack growth in L-T and T-L specimen orientations, but perpendicular to crack growth in L-S specimens. The superiority of the L-S specimen orientation would be more pronounced in corrosion fatigue, because the corrosive medium would be able to enter the material more easily and to a greater depth along delaminations in L-T and T-L specimens. This would account for the greater drop in fatigue crack propagation resistance due to a salt water environment in L-T and T-L specimen orientations than the L-S orientations.

However, a number of other effects may have caused this drop in crack growth resistance in salt water. It has been shown that planar bands of intense slip, caused in aluminum-lithium alloys by the coherent, shearable δ' precipitates, are more sensitive to localised corrosion (54). Some evidence of corrosive attack of these slip planes was found, as shown in figure 89. This may also have been the cause of the 'stepping' noticed on some slip

planes, as shown in figure 88. Corrosive attack may have restricted slip reversibility on a plane, causing this 'stepping'. However, it is unlikely that this would have had much effect on the corrosion fatigue crack propagation resistance. If it had, the crack growth resistance of L-S specimens would have been reduced by a larger amount than it actually was. Another possible explanation for the reduction in fatigue crack propagation resistance in salt water is the occurrence of hydrogen embrittlement ahead of the crack tip, which has been shown to occur in 8090 (146) and was suggested as a possible stress corrosion mechanism. However, it is likely that this mechanism would only occur at low frequencies, and the stress corrosion resistance of 8090 has also been shown to be equivalent to or better than 2014 (145, 146). At the testing frequency of 10Hz it is unlikely that hydrogen embrittlement would have had any effect, unless the weak longitudinal grain boundaries could have been embrittled in some way. The build-up of lithium-ion concentration in the electrolyte within the crack is a fourth possible reason for the reduction in fatigue crack propagation resistance of 8090 in a salt water environment, and would also explain the absence of a corresponding reduction in corrosion fatigue crack initiation resistance. Dissolution processes are accelerated by an increase in lithium-ion concentration (146), as may occur in the salt water solution close to the tip of a fatigue crack. Lithium ion concentration would not increase noticeably in the aerated bulk solution, so fatigue crack initiation would not be affected in this way.

The results of the tensile testing, table 23, shows that 8090-T8 had properties typical of plate material in this condition. These tensile properties were inferior to 2014-T6 in both longitudinal and transverse directions. However, the tensile properties of 8090-T6 were a lot lower than both 8090-T8 and 2014-T6. It is doubtful whether this reduction of 70-80MPa in tensile strength would allow 8090-T6 to be used in place of 2014-T6. For an application where a cold stretching treatment would be difficult, for example in an aircraft wheel forging, 8090 could not be used in the T8 condition. The low ductility in 8090 in both conditions can be attributed to the weakness of the longitudinal grain boundaries.

The aluminium-lithium alloy 8090 has shown several advantages over the conventional aluminium alloy 2014, but some problems still exist that would have to be rectified before this alloy could be used for aircraft structural purposes. The fatigue life and fatigue crack initiation properties of 8090-T6 were inferior to 2014-T6, although the fatigue crack propagation resistance was superior. The weak longitudinal grain boundaries in the pre-production material under investigation were shown to be one of the causes of this inferiority, along with the temper condition used. Present production material has reduced the occurrence of longitudinal grain boundary delamination found to occur in pre-production material. Fatigue crack initiation resistance, and so fatigue life, in 8090 would therefore be expected to be increased in the L-S, L-T and T-L specimen orientations, as has been found in pre-production material where delamination did not occur (160, 161). More importantly, fatigue resistance in the S-L specimen orientation would be greatly increased by elimination of the non-metallic inclusions along longitudinal grain boundaries, as in present production material. Fatigue resistance could not be measured in this orientation with the thickness of 8090 plate used, but values of strength and fracture toughness in the short transverse direction would indicate whether an improvement would occur. When comparing pre-production material properties, shown in table 8 (46), with present production material properties (169), in the T8 condition, it can be seen that the typical ultimate tensile strength has been increased from 435 to 453MPa and the fracture toughness from 16 to 19 $MN.m^{-3/2}$ in the short transverse direction, along with correspondingly high increases in the longitudinal and long transverse directions. It would therefore be expected that the fatigue resistance in the S-L orientation would also be improved. However, these short transverse properties are still inferior to the conventional 2XXX series aluminium alloys, with elongation to fracture being much poorer (10-11% in 2014-T6, compared with 3.2% in the short transverse direction and 4.3% in the longitudinal direction in 8090-T8). This is due to the elongated 'pancake' structure of the 8090 alloy, figure 55, compared to the almost equiaxed grain structure of 2014, figure 54.

The corrosion fatigue properties of 8090-T6 would also be greatly increased by the use of present production material. The superiority of corrosion fatigue crack initiation resistance would be enhanced slightly, and the corrosion fatigue crack propagation resistance would also be superior to 2014-T6, due to the elimination of longitudinal delaminations.

8.3. POWDER METALLURGICAL ALUMINIUM ALLOY

The structure of the CZ20 alloy forging can be seen from figure 61 to consist primarily of very fine, equiaxed grains. These grains were very difficult to resolve by optical metallography, mainly due to their size (2 to 3μm in diameter). It was clear from figure 61 that there was also a dispersion of particles in the structure but these were too fine to examine properly. It was presumed that these particles were mainly aluminium oxide, as a result of the break-up of prior particle boundaries. Al_3Zr particles would also be distributed throughout the structure. Figure 61 indicates that the material is fully dense. Eliminating porosity to obtain full density is necessary to develop good strength properties.

The results of fatigue crack propagation testing on CZ20-T6, figures 45 and 46, show that this PM variant of the IM alloy 2014 does not offer any improvement in terms of fatigue crack propagation resistance. This was expected, due to the extremely fine grain size in this alloy. Slip reversibility during fatigue would have been restricted by grain boundaries to a much greater extent than in 2014-T6, due to the fact that the plastic zone size was larger than the grain size (119). The drop in fatigue crack growth resistance that this caused would have been offset by the increase in resistance due to the smaller influence of impurities and intermetallic particles. In air, both CZ20-T6 (C-L) and (C-R) specimen orientations showed similar crack growth rates to 2014-T6 over the whole range of ΔK, at both R-values. In salt water, CZ20-T6 (C-L) and (C-R) specimen orientations were slightly inferior to 2014-T6 in terms of fatigue crack propagation resistance, over the whole range of ΔK. No difference in crack growth resistance could be seen between the C-L and C-R specimen orientations. Also, R-value does not seem to have made much difference to the fatigue crack growth rates of CZ20-T6. With both C-L and C-R specimen orientations, fatigue crack propagation resistance was similar for R-values of 0.1 and 0.45, as shown in figures 46e and 46f.

At low to medium levels of ΔK, fatigue fracture surfaces in C-L and C-R specimens looked identical, as shown in figure 92. It seems that the same mechanisms were occurring in both orientations, and so it is not surprising that fatigue crack growth resistance was

similar in both under all conditions of R-value and environment. Fatigue surfaces followed an irregular crack path, as shown in figure 94, with flat, almost featureless areas of roughly the same dimensions as the grain size.

The coarseness of the fatigue fracture surfaces increased with increasing levels of ΔK, as shown in figure 93. At high levels of ΔK no evidence of ductile fracture around particles, or dimpling, could be seen on fatigue fracture surfaces, as was seen in 2014-T6 fracture surfaces in figures 73c and 76. This is possibly due to the fact that the alumina particles in CZ20 were much finer than the intermetallic particles in 2014. The alumina particles in CZ20 were under 200nm in diameter, whereas the intermetallic particles in 2014 were at least 1μm in diameter and larger, as shown in figure 96. It is possible that the critical defect size for fracture of these particles ahead of the crack front at these high levels of ΔK is somewhere between these two sizes. However, fast fracture surfaces did show dimpling. The dimples were typically equiaxed, with the dimple size and distribution related to the initiating particle size. As shown in figure 96, the ductile dimpling fracture was a lot finer in CZ20-T6 than in 2014-T6, again due to the smaller size of the particles around which voiding occurred. It can therefore be seen that these alumina particles do take part in the fast fracture process, being sites for void nucleation ahead of the advancing crack. However, these particles do not seem to have had much effect on the fatigue fracture process. Other work has also suggested this, stating that the oxide particles do not influence the fatigue crack propagation rate in PM2XXX series alloys (163). The fatigue fracture appears instead to have been restricted to regions of smooth, flat matrix shear within individual grains, as shown in figure 94.

Although no certain judgement on the corrosion properties of CZ20 can be made, the slightly inferior corrosion fatigue crack propagation resistance of CZ20-T6 infers that its corrosion resistance is not particularly superior. Indeed, the stress corrosion resistance of CZ20-T6 is only equivalent to 2014-T6 (65). However, the superior pitting corrosion resistance of the PM alloy when compared to 2014-T6 suggests that its corrosion fatigue crack initiation resistance would be superior.

One phenomenon that is not fully understood in these alloys is the crack branching seen in CZ20-T6 (C-L) specimens. An example of this is shown on a typical facture surface of C-L oriented specimen in figure 53a. This branching of the fatigue crack was not seen in C-R oriented specimens, as shown in figure 53b. On closer examination of the fracture surfaces, these cracks could be seen to occur on both a large and a small scale, as shown in figure 95. It is difficult to decide whether these cracks were intergranular or transgranular, or whether the alumina particles have had any influence. However, some sort of weak interface would have been involved. As in the aluminium-lithium alloy, when a crack intersects a weak interface it will show a strong tendency to propagate along it. The extent of growth of this secondary crack depends upon the stress distribution in the vicinity of the crack tip. Again, small secondary stresses would be present in three-point bending, perpendicular to the axial stress. A tendency for out-of-plane crack branching has also been noted to occur in the PM alloy 7091 (164). The onset of cracking did not depend upon the attainment of a certain level of stress intensity, rather a certain crack length, which would again suggest the influence of secondary stresses. As soon as a crack length of 6 to 8mm (a/W of 0.5 to 0.6) had been reached, crack branching occurred. The effect of this crack branching on the fatigue crack propagation rate is shown in figure 47. It appears that the fatigue crack growth rate decreased with increasing ΔK, after a certain crack length. However, secondary cracks consume part of the energy normally available for propagation of the principal crack, effectively lowering the ΔK at the crack tip, which would explain the drop in fatigue crack growth rate. For this reason, fatigue crack propagation data was ignored after the ΔK when growth rates started to slow down in these CZ20-T6 (C-L) specimens.

As figure 25 shows, these weak interfaces in the C-L specimen orientation would be in the axial plane. During the forging operation the majority of the deformation would have been in this axial plane, in the radial direction.The powder particles would also have been deformed in this direction and so prior particle boundaries would be spread out on the axial plane if the amount of deformation was insufficient to completely disperse them. Therefore,

particles may have been aligned in these axial planes, which would be one possible cause of weak interfaces. The tensile results would tend to agree with the suggestion of weak interfaces on axial planes. Proof stress, ultimate tensile stress and elongation were lower in the axial direction than radial or tangential directions, as shown in figure 23.

Tensile properties in all directions in CZ20-T6 were inferior to 2014-T6, with the exception of elongation in the radial and tangential directions. A higher elongation would be expected in these wrought PM alloys, due to the lack of large intermetallic particles in their structure, which are present in IM aluminium alloys. Only the effect of weak interfaces in the axial plane caused the elongation in the axial direction to be lower.

The results of fatigue testing on CZ20-T6 have indicated poor properties, which may not be a true picture. Published literature all indicate inferior fatigue crack propagation resistance but superior fatigue crack initiation resistance for PM aluminium alloys when compared to their IM version, leading to a better S-N fatigue response. A more favourable picture of the potential of this alloy may therefore have been produced if fatigue and corrosion fatigue crack initiation data had also been produced.

8.4. SAFFIL - REINFORCED COMPOSITE MATERIAL

The structure of the Saffil-reinforced 6061-T6 composites consisted of a planar-random distribution of fibres in the aluminium alloy matrix, as shown in figure 62. This planar-random array of fibres can be seen more clearly by comparing figures 63 and 64. The plane of the as-cast disc, figure 63, shows fibres in a random orientation. A section through the thickness of the as-cast disc, figure 64, shows the directionality of the fibres in this plane. This planar-random array of fibres was essentially the same as the distribution in the uninfiltrated Saffil preform, shown in figure 72. Understandably, the fibre packing in the 30% Saffil material was denser than in the 20% Saffil composite, as shown in figures 64 and 65. A very fine distribution of precipitates could be seen within the etched 6061 matrix, as shown in figures 64b and 65b. It is presumed that this is magnesium silicide, Mg_2Si, precipitated out during the ageing treatment.

The results of the tensile testing on Saffil-reinforced 6061-T6, shown in table 24, show both improvements and reductions in properties when compared to typical values for unreinforced 6061-T6, shown in table 11. The ultimate tensile strength was improved by Saffil reinforcement. The improvement appeared to be linear, increasing by about 16MPa per 10% of Saffil reinforcement (UTS was 310MPa for 0% Saffil, 343MPa for 20% Saffil and 358MPa for 30% Saffil reinforcement). However, any increases in strength due to Saffil reinforcement were small, because randomly-oriented short fibre composites are not as effective in strengthening as unidirectional, continuous ones.

The 0.2% proof stress of 6061-T6 was also improved by Saffil reinforcement. This was to be expected, as an increase in proof stress would normally accompany any increase in tensile strength. The increase in proof stress with Saffil content appeared to be more complex than a simple linear relationship, with the greatest increase in the 20 to 30% Saffil range (0.2%PS was 280MPa for 0% Saffil, 305MPa for 20% Saffil and 328MPa for 30% Saffil). These increases in proof stress showed similar percentage improvements to the tensile strength for the same Saffil contents.

Other work (22, 30, 165) shows that Saffil reinforcement can either decrease or increase the strength properties of aluminium alloys, depending on the matrix alloy used. The general trend seems to be an increase in strength of low strength aluminium alloys and a decrease in high strength alloys due to Saffil reinforcement. However, a certain critical volume fraction of Saffil seems to be required before fibre reinforcement is effective in raising tensile strength. Other work (166) has shown that 3% Saffil-reinforced 6061-T6 has a lower tensile strength than unreinforced 6061-T6. This critical volume fraction of Saffil fibres for effective reinforcement has been shown to depend on matrix properties (167) and is higher in stronger alloys, varying from around 4% in a commercial purity aluminium matrix to 30-35% for high strength aluminium alloy matrices. The rate of work hardening of the matrix alloy is an important factor (167). A matrix with a low work hardening rate, like commercial purity aluminium, results in a low value of critical fibre volume fraction needed for an increase in material strength. It is likely that the critical volume fraction of Saffil fibres in a 6061-T6 matrix would be in the range of 10 to 20 %.

The elongation to fracture of Saffil-reinforced 6061-T6 was less than 1% in both cases, as shown in table 24, compared to a typical value of 13% for unreinforced 6061-T6. This can be attributed to the brittle nature of the fibres. Saffil fibres fracture at a very low elongation, around 0.67%, and the remaining 6061 matrix would fail soon afterwards at necked ligaments. Similar elongations to fracture have been recorded with other aluminium alloys reinforced with Saffil (165). These elongations to fracture decreased with increasing fibre volume fraction, closer to the fracture strain of the fibres (0.67%).

The Youngs Modulus was the property most improved by Saffil reinforcement. The typical Youngs Modulus of 71GPa in unreinforced 6061-T6 was increased by 21% with 20% Saffil reinforcement (to 86GPa) and by 41% with 30% Saffil reinforcement (to 100GPa). Similar percentage increases have been recorded by others on Saffil-reinforced aluminium alloys (30, 165). However, this improvement in modulus was still not as much as the theoretical increase calculated from the rule of mixtures, equation 2.3. This law is for

continuous, unidirectional fibre reinforcement, whereas Saffil fibres are discontinuous and planar-randomly oriented. Theoretical moduli of around 98GPa for 20% Saffil/6061-T6 and 111GPa for 30% Saffil/6061-T6 were calculated using the methods of other workers (23, 27) for the case of planar-randomly oriented composites, an adjusted form of the rule of mixtures. These represent modulus increases of 38% and 56%, respectively, which are much closer to the experimental results, suggesting that fibre-matrix bonding was quite good.

Tensile fracture surfaces showed dimple formation around fibres, figures 100 and 101. This indicated that the fibres failed first, by tensile fracture, followed by ductile failure of the matrix, necking to form dimples. On a macroscale, all tensile specimens deformed without appreciable plastic deformation before failure, resulting in low ductility. In general, fibre-matrix bonding appeared to be good, as shown in figure 101. This would lead to improved mechanical properties, due to the more effective transfer of load from the matrix to the fibres. However, some evidence of fibre pullout could also be seen where fibres were not on or near the stress axis, as shown in figure 102. This may explain why the experimental modulus values were below the theoretical ones.

The fatigue crack propagation resistance of the Saffil-reinforced material was inferior to all of the other materials under investigation, as shown in figures 45a and 45c. At low levels of ΔK the crack growth resistance was only slightly inferior to 2014-T6, but at higher levels of ΔK there was a much larger increase in crack propagation rates in Saffil-reinforced material. The low fracture toughness of Saffil-reinforced composites seems to be the major cause of this rapid increase in crack growth rate with increasing ΔK. The stress intensity range, ΔK, at fracture indicates a fracture toughness of around $10MN.m^{-3/2}$ for 20% Saffil/6061-T6 and $11MN.m^{-3/2}$ for 30% Saffil/6061-T6. Similar reductions in fracture toughness have been recorded by the addition of silicon carbide whiskers to 6061-T6 (168).The addition of 20 vol% SiC whiskers to 6061-T6 reduced the fracture toughness from $35MN.m^{-3/2}$ (unreinforced) to $7MN.m^{-3/2}$.

At low levels of ΔK, fatigue fracture occurred in the 6061-T6 matrix, as shown in figures

96a and 97a. No fatigue fracture occurred in the fibres. Fatigue fracture appeared to be restricted to the matrix , while the fibres failed by tensile fracture after the matrix had failed. At higher levels of ΔK the fibres appeared to have broken first, as shown in figures 96b and 97b. Again, no fatigue fracture occurred in the fibres, and so they must have failed by tensile fracture. The matrix necked around these broken fibres to form dimples. The crack would have advanced by jumps of fast fracture as the fibres break at the peak of the fatigue cycle. This would explain why the fatigue fracture surfaces at high levels of ΔK, shown in figures 96 and 97, were similar to fast fracture surfaces, shown in figures 100 and 101. Evidence of good fibre-matrix bonding was present on fatigue fracture surfaces, shown in figures 96 and 97, where fibre cleavage could be seen to occur rather than fibre pullout. This strong fibre-matrix bonding would reduce fatigue crack growth resistance, due to the preference of a crack to pass through the fibre, so cleaving it as soon as it enters the fibre, rather than along the fibre-matrix interface, which would cause crack deflection.

It was not clear from this investigation whether the fatigue crack propagation resistance of 6061-T6 was improved by Saffil reinforcement. However, other work has shown that Saffil reinforcement does improve the fatigue resistance of aluminium alloys if it increases the tensile strength also (165). This confirms the important role of tensile fracture in fatigue of Saffil reinforced aluminium alloys. It is likely that the Saffil reinforcement of 6061-T6 did bring about a slight increase in fatigue crack propagation resistance at low levels of ΔK, due to the increase in tensile strength. However, at high levels of ΔK the low fracture toughness of the reinforced alloys would reduce their fatigue crack growth resistance to below that of the unreinforced material. The slightly superior fatigue crack propagation resistance of 30% Saffil/6061-T6 over 20% Saffil/6061-T6 can be attributed to its higher tensile strength, as tensile fracture of the Saffil fibres takes part in the fatigue process, at both low and high levels of ΔK.

As shown in figures 45a and 45c, fatigue fracture in Saffil-reinforced 6061-T6 occurred over a very small range of ΔK (about $5MN.m^{-3/2}$ for R=0.1) when compared to 2014-T6

(about 20MN.m$^{-3/2}$ for R=0.1). This was partly due to the very low fracture toughness in this material, and partly due to the fact that fatigue fracture does not occur in the fibres. Fatigue crack growth rate would increase considerably once the peak stress in the fatigue cycle was high enough to cause tensile fracture of the fibres.

There does not appear to be any difference in fatigue crack propagation resistance between the two specimen orientations investigated. This is expected, as the proportion of fibres in the same direction as the specimen axis would have been similar in both orientations, and so the effectiveness of fibre-reinforcement the same.

A number of factors would have affected the tensile and fatigue properties of the Saffil-reinforced material. Firstly, a number of non-metallic inclusions were found within the composite structure, as shown in figures 66 and 67. These irregularly-shaped inclusions were upto 0.5mm in size, and looked to be surrounded by a fibre-depleted zone. It was discovered that these particles originated from the fibre production stage. Saffil fibres are produced by a spinning process, which occasionally produces non-fibrous material, which is filtered out. However, as figures 66 and 67 show, not all of these alumina inclusions are filtered out. Inclusions of these sizes would be dangerous defects to have in a structure. Indeed, they were found to be present on both fatigue and tensile fracture surfaces, as shown in figure 99. These alumina inclusions would therefore have had an effect on both the tensile and fatigue properties of Saffil-reinforced material, effectively reducing their fracture toughness. Crack initiation has been shown to take place at these particles in other Saffil-reinforced aluminium alloys (30, 165) where they have also been found to be involved in the crack propagation process.

The variable distribution of fibre reinforcement within the composite structure, shown in figure 68, would also have had an effect on material properties. This would have resulted in variable tensile properties within the material, and so selected areas of the structure would be weakened. Areas within the structure that appeared unreinforced, as shown in figure 69, would also have been areas of weakness. Local plastic deformation would take place in

these areas.

Evidence of cracking in the Saffil preforms prior to infiltration with 6061 alloy can be seen in figure 70. This was possibly due to too high an infiltration pressure being used. Again, the unreinforced area within the crack would be an area of weakness.

It is unlikely that any unusually large fibre diameters, as shown in figure 71, would have had much effect on mechanical properties. Most fibres were in a fibre diameter range of 2 to 4 μm, as shown in figure 72.

In terms of both tensile and fatigue properties, Saffil-reinforced 6061-T6 was the poorest of the materials under investigation, and would be an unlikely replacement for 2014-T6 in its applications.

8.5. APPLICABILITY OF THE MATERIALS INVESTIGATED TO AIRCRAFT STRUCTURES

The original reason for this investigation was to find a replacement for the existing conventional aluminium alloys used in aircraft structures, in this case 2014-T6 in aircraft wheel applications. It is obvious that none of the materials investigated have been developed sufficiently for them to be used in primary load-bearing aircraft structures in their present form.

The most promising of the materials investigated was the aluminium-lithium alloy. Present production 8090 material does not have the problems related to weakened longitudinal grain boundaries that have been shown to be apparent in the pre-production material investigated. When also taking into account the increase in Youngs Modulus (71GPa in 2014, compared with 79.5GPa in 8090) and decrease in density (2800 kg/m^3 in 2014, compared with 2540 kg/m^3 in 8090), this material is obviously a very attractive alternative to the 2XXX series alloy. However, several problems still exist with this alloy that need to be looked at. First of all, short transverse properties in 8090-T8 are still not satisfactory, especially elongation to fracture. Elongations in the longitudinal and long transverse directions are also much lower. The cause of this is still uncertain, and needs to be further investigated. Secondly, the cost of aluminium-lithium alloys is a prohibitive factor, mainly due to the difficulties in its production. It is hoped that the cost of 8090 will be reduced to around twice that of conventional alloys in the near future.

For the case of aircraft wheel applications, the added problem of temper condition exists. Mechanical properties of 8090-T8 match those of 2014-T6 or -T651 in terms of both static and fatigue strength, apart from short transverse properties. However, a controlled amount of cold stretching is not possible in such an intricate forging as an aircraft wheel, and so a T6 heat treatment would give the highest possible mechanical properties under these conditions. Therefore, before any future use of 8090 in aircraft wheels, present production material would have to be investigated in the form of a forging.

The powder metallurgical alloy, CZ20, has not been investigated thoroughly, but a judgement on its future use can be made. This investigation has shown that there is neither an increase nor a decrease in fatigue crack propagation resistance when comparing the IM alloy 2014-T6 with its PM variant, CZ20-T6. This would suggest that the increased cost involved in the PM route does not justify its use in place of 2014-T6 in aircraft applications. However, most other research on PM aluminium alloys has shown that their fatigue resistance is superior to their IM counterparts, even though their fatigue crack growth resistance is usually inferior. It is therefore likely that CZ20-T6 has superior fatigue resistance when compared to 2014-T6. Similarly, the corrosion fatigue resistance of the PM alloy is likely to be superior, due to the improvement in pitting corrosion resistance, even though its corrosion fatigue crack propagation resistance is slightly inferior to the IM alloy.

In other areas, CZ20 does not compare very favourably with 2014. Its density and Youngs Modulus would only be comparable to the IM alloy, which are the two properties where aluminium-lithium alloys compare most favourably. The strength levels attained by the PM route also appear to be inferior to those of the IM route, and lie in between the strength levels of 8090-T6 and 8090-T8, shown in table 23. When considering the increased cost of PM aluminium alloys when compared to their IM counterparts, it is unlikely that the replacement of 2014-T6 with CZ20-T6 in aircraft applications would be cost effective, except possibly in a fatigue-critical situation.

This investigation has shown that the Saffil reinforcement of aluminium alloys does not improve their properties sufficiently for their use in aircraft structural applications. Although 30% Saffil reinforcement of 6061-T6 brought about an increase of 15% in ultimate tensile strength over an unreinforced alloy, this was still around 170MPa short of the 526MPa attained in 2014-T6. Other work on the Saffil reinforcement of high strength aluminium alloys have produced results showing ultimate tensile strength levels of under 400MPa (165, 167). Other mechanical properties, such as elongation to fracture and fracture toughness are also reduced by Saffil reinforcement, to levels unacceptable in aircraft structures.

Although the fatigue resistance of 6061-T6 may be increased by Saffil reinforcement, it is still below that of conventional alloys. The fatigue crack growth resistance of Saffil-reinforced 6061-T6 was shown to be inferior to 2014-T6, especially at high levels of ΔK.

These deficiencies in both tensile and fatigue properties in Saffil-reinforced aluminium alloys suggest that they would be unacceptable in aircraft structural applications and would have restricted use in most ambient temperature applications, especially when the increased cost of these materials is considered. It seems as though the future of these materials lies in high temperature applications (14, 22). Their retention of strength and modulus at temperatures up to $300^{o}C$ would be of great advantage in certain automotive engine applications. This is where any future investigations on Saffil reinforcement should be aimed.

9. CONCLUSIONS

1. Differences between the theoretical and experimental electrical potential calibrations were due to the effects of notch geometry and notch root plastic deformation. Crack deviation, crack closure and multiple crack growth also had an effect on 8090 and CZ20 calibrations.

2. A corrosive environment did not affect the electrical potential calibrations of the materials under investigation.

3. The distribution of non-metallic inclusions along longitudinal grain boundaries in 8090-T6 caused these grain boundaries to be areas of weakness, leading to their delamination under even a small stress.

4. The fatigue resistance and fatigue crack initiation resistance of 8090-T6 is inferior to 2014-T6, due to the effect of the weakened longitudinal grain boundaries and temper condition used. The superiority of 2014-T6 was decreased in a salt water environment, due to the greater amount of pitting corrosion in this alloy.

5. The superior fatigue crack propagation resistance of 8090-T6 when compared to 2014-T6 can be partly attributed to the crack deflection and crack closure effects in the aluminium-lithium alloy, due to planar slip and delamination of longitudinal grain boundaries.

6. The superior fatigue crack propagation resistance of 8090 in this investigation when compared to other published data can be attributed to the temper condition and the larger amount of crack deflection and crack closure.

7. The bend specimens used in this investigation were considered to provide more meaningful fatigue data than tension-tension specimens, by revealing the effect of weakened

longitudinal grain boundaries in 8090-T6.

8. The superiority of 8090-T6 in terms of fatigue crack propagation resistance decreases in the L-T and T-L specimen orientations in a corrosive environment, due to the ease of penetration of the salt water solution along longitudinal grain boundaries, and possible build-up of lithium ion concentration in the electrolyte within the crack tip.

9. The powder metallurgical route offers no increase in fatigue or corrosion fatigue crack propagation resistance over the ingot metallurgy route as far as the 2014 alloy composition is concerned.

10. Cost considerations are likely to limit the future use of CZ20 PM aluminium alloy.

11. Inferior tensile and fatigue properties of Saffil-reinforced materials show that they would be unacceptable for use in aircraft structural applications, and would restrict their use in most ambient temperature applications. Further work on these materials should concentrate on high temperature applications.

12. Of the materials investigated, the most promising is the aluminium-lithium alloy. However, short transverse properties need to be increased and cost decreased before 8090 can be used in place of 2014 in aircraft structural applications.

APPENDIX 1

7-point polynomial method for the calculation of da/dN (159) and ΔK calculation.

```
REM astm 7 point polynomial data reduction
DIM  a(200),c(200),b(3),d(200),k(200),g(100),h(100),V(200)
PRINT:INPUT "no of data pairs?";n
PRINT:INPUT"PMAX (kN)";p1
INPUT "PMIN (kN)";p2
INPUT "BREADTH(mm)";b
b=b/1000
INPUT "WIDTH(mm)";w
w=w/1000
INPUT "Constant a1, in a = a1 + b1*V + c1*V^2 ";a1
INPUT "Constant b1";b1
INPUT "Constant c1";c1
PRINT
REM retrieve data
OPEN "clip:" FOR INPUT AS #1
FOR i=1 TO n
INPUT #1, c(i),V(i)
NEXT i
CLOSE #1
REM pd calibration
FOR i=1 TO n
a(i)=a1 + b1*V(i) + c1*V(i)*V(i)
a(i)= a(i)/1000
NEXT i
n=n-6
k = 0
FOR i=1 TO n
l=0
k=k+1
k1=k+6
FOR j=k TO k1
l=l+1
g(l)=a(j)
h(l)=c(j)
NEXT j
c1=.5*(h(1)+h(7))
c2=.5*(h(7)-h(1))
s1=0
s2=0
s3=0
s4=4
s5=0
s6=0
s7=0
FOR m=1 TO 7
x=(h(m)-c1)/c2
y=g(m)
s1=s1+x
s2=s2+x^2
```

```
s3=s3+x^3
s4=s4+x^4
s5=s5+y
s6=s6+x*y
s7=s7+y*(x^2)
NEXT m
d1=7*(s2*s4-s3^2)-s1*(s1*s4-s2*s3)+s2*(s1*s3-s2^2)
t1=s5*(s2*s4-s3^2)-s6*(s1*s4-s2*s3)+s7*(s1*s3-s2^2)
b(1)=t1/d1
t2=7*(s6*s4-s7*s3)-s1*(s5*s4-s7*s2)+s2*(s5*s3-s6*s2)
b(2)=t2/d1
t3=7*(s2*s7-s3*s6)-s1*(s1*s7-s3*s5)+s2*(s1*s6-s2*s5)
b(3)=t3/d1
y1=s5/7
r1=0
r2=0
FOR q=1 TO 7
x=(h(q)-c1)/c2
y2=b(1)+b(2)*x+b(3)*(x^2)
r1=r1+(g(q)-y2)^2
r2=r2+(g(q)-y1)^2
NEXT q
r3=1-(r1/r2)
d(i)=b(2)/c2+2*b(3)*(h(4)-c1)/(c2^2)
u=i+3
REM   k-calibration
com1=1.93*((a(u)/w)^.5) - 3.07*((a(u)/w)^1.5) + 14.53*((a(u)/w)^2.5)
com1=com1 - 25.11*((a(u)/w)^3.5) + 25.8*((a(u)/w)^4.5)
k(i)=  6*((p1-p2)/1000)*com1/(b*w^.5)
NEXT i
REM paste to clipboard
OPEN "clip:" FOR OUTPUT AS #1
FOR i=1 TO n
u=i+3
a(u)=a(u)*1000
d(i)=d(i)*1000
WRITE  #1,a(u),d(i),k(i)
NEXT i
CLOSE #1
PRINT "processing terminated . Data is residing in clipboard"
END
```

APPENDIX 2

Paper presented at the 4th International Aluminium-Lithium Conference, Paris, France.

10-12th June, 1987.

Aston University

Content has been removed for copyright reasons

Aston University

Content has been removed for copyright reasons